ISSN 2074-272X

науково-практичний
журнал
2023/6

Електротехніка і Електромеханіка

Electrical Engineering & Electromechanics

Електричні машини та апарати
Електротехнічні комплекси та системи
Промислова електроніка
Інженерна електрофізика.
Техніка сильних електричних та магнітних полів
Електричні станції, мережі і системи

Журнал включено до найвищої категорії «А»
Переліку фахових видань України

З 2019 р. журнал індексується у Scopus

З 2015 р. журнал індексується
у Web of Science Core Collection:
Emerging Sources Citation Index

Electrical Engineering & Electromechanics

Scientific Journal was founded in 2002
Founder – National Technical University «Kharkiv Polytechnic Institute» (Kharkiv, Ukraine)

EDITORIAL BOARD

Sokol Ye.I.	**Editor-in-Chief**, Professor, Corresponding member of NAS of Ukraine, Rector of National Technical University «Kharkiv Polytechnic Institute» (NTU «KhPI»), **Ukraine**
Korytchenko K.V.	**Deputy Editor,** Professor, NTU «KhPI», **Ukraine**
Rozov V.Yu.	**Deputy Editor,** Professor, Corresponding member of NAS of Ukraine, Anatolii Pidhornyi Institute of Mechanical Engineering Problems of NAS of Ukraine, Kharkiv, **Ukraine**
Bolyukh V.F.	**Deputy Editor,** Professor, NTU «KhPI», **Ukraine**
Abu-Siada A.	Professor, Curtin University, Perth, **Australia**
Aman M.M.	Professor, NED University of Engineering & Technology, Karachi, **Pakistan**
Babak V.P.	Professor, Corresponding member of NAS of Ukraine, General Energy Institute of NAS of Ukraine, Kyiv, **Ukraine**
Baltag O.	Professor, Grigore T. Popa University Medicine and Pharmacy, **Romania**
Baranov M.I.	Professor, Research and Design Institute «Molniya» of NTU «KhPI», **Ukraine**
Batygin Yu.V.	Professor, Kharkiv National Automobile and Highway University, **Ukraine**
Bíró O.	Professor, Institute for Fundamentals and Theory in Electrical Engineering, Graz, **Austria**
Bouktir T.	Professor, Ferhat Abbas University, Setif 1, **Algeria**
Buriakovskyi S.G.	Professor, NTU «KhPI», **Ukraine**
Butkevych O.F.	Professor, Institute of Electrodynamics of NAS of Ukraine (IED of NASU), Kyiv, **Ukraine**
Colak I.	Professor, Nisantasi University, Istanbul, **Turkey**
Cruz S.	Professor, University of Coimbra, **Portugal**
Doležel I.	Professor, University of West Bohemia, Pilsen, **Czech Republic**
Féliachi M.	Professor, Technological Institute of Saint-Nazaire, University of Nantes, **France**
Guerrero J.M.	Professor, Aalborg University, **Denmark**
Gurevich V.I.	PhD, Honorable Professor, Central Electrical Laboratory of Israel Electric Corporation, Haifa, **Israel**
Hajjar A.A.	Professor, Tishreen University, Latakia, **Syrian Arab Republic**
Hammarström T.	Professor, Chalmers University of Technology, **Sweden**
Ida N.	Professor, The University of Akron, Ohio, **USA**
Izykowski J.	Professor, Wroclaw University of Science and Technology, **Poland**
Kildishev A.V.	Associate Research Professor, Purdue University, **USA**
Klepikov V.B.	Professor, NTU «KhPI», **Ukraine**
Korzeniewska E.	Professor, Lodz University of Technology, **Poland**
Ktena A.	Professor, National and Kapodistrian University of Athens, **Greece**
Kuznetsov B.I.	Professor, Anatolii Pidhornyi Institute of Mechanical Engineering Problems of NAS of Ukraine, Kharkiv, **Ukraine**
Kyrylenko O.V.	Professor, Academician of NAS of Ukraine, IED of NASU, Kyiv, **Ukraine**
Malik O.P.	Professor, University Of Calgary, **Canada**
Maslov V.I.	Professor, National Science Center «Kharkiv Institute of Physics and Technology», **Ukraine**
Mikhaylov V.M.	Professor, NTU «KhPI», **Ukraine**
Miljavec D.	Professor, University of Ljubljana, **Slovenia**
Milykh V.I.	Professor, NTU «KhPI», **Ukraine**
Nacke B.	Professor, Gottfried Wilhelm Leibniz Universitat, Institute of Electrotechnology, Hannover, **Germany**
Oleschuk V.	Professor, Institute of Power Engineering of Technical University of Moldova, **Republic of Moldova**
Petrushin V.S.	Professor, Odessa National Polytechnic University, **Ukraine**
Podoltsev A.D.	Professor, IED of NASU, Kyiv, **Ukraine**
Reutskiy S.Yu.	PhD, Anatolii Pidhornyi Institute of Mechanical Engineering Problems of NAS of Ukraine, Kharkiv, **Ukraine**
Rezinkin O.L.	Professor, NTU «KhPI», **Ukraine**
Rezinkina M.M.	Professor, NTU «KhPI», **Ukraine**
Shcherbak Ya.V.	Professor, NTU «KhPI», **Ukraine**
Sikorski W.	Professor, Poznan University of Technology, **Poland**
Strzelecki R.	Professor, Gdansk University of Technology, **Poland**
Suemitsu W.	Professor, Universidade Federal Do Rio de Janeiro, **Brazil**
Trichet D.	Professor, Institut de Recherche en Energie Electrique de Nantes Atlantique, **France**
Vaskovskyi Yu.M.	Professor, National Technical University of Ukraine «Igor Sikorsky Kyiv Polytechnic Institute», Kyiv, **Ukraine**
Vazquez N.	Professor, Tecnológico Nacional de México en Celaya, **Mexico**
Vinnikov D.	Professor, Tallinn University of Technology, **Estonia**
Yagup V.G.	Professor, O.M. Beketov National University of Urban Economy in Kharkiv, **Ukraine**
Yatchev I.	Professor, Technical University of Sofia, **Bulgaria**
Zagirnyak M.V.	Professor, Member of NAES of Ukraine, Kremenchuk M.Ostrohradskyi National University, **Ukraine**
Zgraja J.	Professor, Lodz University of Technology, **Poland**
Grechko O.M.	**Executive Managing Editor,** PhD, NTU «KhPI», **Ukraine**

From no. 1 2019 Journal «Electrical Engineering & Electromechanics» is indexing in **Scopus**
and from no. 1 2015 Journal is indexing in **Web of Science Core Collection: Emerging Sources Citation Index (ESCI)**.

Also included in DOAJ (Directory of Open Access Journals), in EBSCO's database, in ProQuest's databases – Advanced Technologies & Aerospace Database and Materials Science & Engineering Database, in Gale/Cengage Learning databases.

Editorial office address:
National Technical University «Kharkiv Polytechnic Institute», Kyrpychova Str., 2, Kharkiv, 61002, Ukraine
phones: +380 57 7076281, +380 67 3594696, **e-mail:** a.m.grechko@gmail.com (**Grechko O.M.)**

ISSN (print) 2074-272X
ISSN (online) 2309-3404

© National Technical University «Kharkiv Polytechnic Institute», 2023

Printed 01 November 2023. Format 60 × 90 ⅛. Paper – offset. Laser printing. Edition 200 copies.
Printed by Printing house «Madrid Ltd» (18, Gudanova Str., Kharkiv, 61024, Ukraine)

Electrical Engineering & Electromechanics
Scientific Journal

no. 6, 2023

Table of Contents

Electrical Machines and Apparatus

Electrotechnical Complexes and Systems

Industrial Electronics

Engineering Electrophysics. High Electric and Magnetic Fields Engineering

Power Stations, Grids and Systems

UDC 621.313 https://doi.org/10.20998/2074-272X.2023.6.01

A. Aib, D.E. Khodja, S. Chakroune, H. Rahali

Fuzzy current analysis-based fault diagnostic of induction motor using hardware co-simulation with field programmable gate array

Introduction. *Presently, signal analysis of stator current of induction motor has become a popular technique to assess the health state of asynchronous motor in order to avoid failures. The classical implementations of failure detection algorithms for rotating machines, based on microprogrammed sequential systems such as microprocessors and digital signal processing have shown their limitations in terms of speed and real time constraints, which requires the use of new technologies providing more efficient diagnostics such as application specific integrated circuit or field programmable gate array (FPGA). The* ***purpose*** *of this work is to study the contribution of the implementation of fuzzy logic on FPGA programmable logic circuits in the diagnosis of asynchronous machine failures for a phase unbalance and a missing phase faults cases.* ***Methodology.*** *In this work, we propose hardware architecture on FPGA of a failure detection algorithm for asynchronous machine based on fuzzy logic and motor current signal analysis by taking the RMS signal of stator current as a fault indicator signal.* ***Results.*** *The validation of the proposed architecture was carried out by a co-simulation hardware process between the ML402 boards equipped with a Virtex-4 FPGA circuit of the Xilinx type and Xilinx system generator under MATLAB/Simulin*k. ***Originality.*** *The present work combined the performance of fuzzy logic techniques, the simplicity of stator current signal analysis algorithms and the execution power of ML402 FPGA board, for the fault diagnosis of induction machine achieving the best ratios speed/performance and simplicity/performance.* ***Practical value.*** *The emergence of this method has improved the performance of fault detection for asynchronous machine, especially in terms of hardware resource consumption, real-time online detection and speed of detection.* References 22, tables 3, figures 19.

Key words: **asynchronous machine, fuzzy current analysis, field programmable gate array, hardware co-simulation.**

Вступ*. В даний час аналіз сигналу струму статора асинхронного двигуна став популярним методом оцінки стану працездатності асинхронного двигуна, щоб уникнути відмов. Класичні реалізації алгоритмів виявлення несправностей машин, що обертаються, засновані на мікропрограмних послідовних системах, таких як мікропроцесори і цифрова обробка сигналів, показали свої обмеження з точки зору швидкості та обмежень у реальному часі, що вимагає використання нових технологій, що забезпечують більш ефективну діагностику. наприклад, інтегральна схема для конкретної програми або програмована вентильна матриця (FPGA).* ***Метою*** *даної є дослідження внеску реалізації нечіткої логіки на програмованих логічних схемах FPGA в діагностику відмов асинхронних машин при несиметрії фаз і обривах фази.* ***Методологія****. У цій роботі ми пропонуємо апаратну архітектуру на FPGA алгоритму виявлення відмов асинхронної машини на основі нечіткої логіки та аналізу сигналів струму двигуна, приймаючи середньоквадратичний сигнал статора струму як сигнал індикатора несправності.* ***Результати****. Валідація запропонованої архітектури проводилася шляхом апаратного моделювання між платами ML402, оснащеними схемою Virtex-4 FPGA типу Xilinx та генератором системи Xilinx під керуванням MATLAB/Simulink.* ***Оригінальність****. Дана робота поєднала в собі ефективність методів нечіткої логіки, простоту алгоритмів аналізу сигналів струму статора та виконавчу потужність плати ML402 FPGA для діагностики несправностей асинхронних машин, досягаючи найкращих співвідношень швидкість/продуктивність та простота/продуктивність.* ***Практична цінність****. Поява цього методу покращила продуктивність виявлення несправностей асинхронної машини, особливо з точки зору споживання апаратних ресурсів, онлайн-виявлення в реальному часі та швидкості виявлення.* Бібл. 22, табл. 3, рис. 19.

Ключові слова: **асинхронна машина, аналіз нечітких струмів, програмована вентильна матриця, апаратне спільне моделювання.**

Introduction. The advances in electronics, power electronics and control circuits have contributed to the growing use of asynchronous machines in electrical drive systems. The use of asynchronous machines is mainly linked to their robustness, their specific power and their manufacturing cost. Their maintenance and monitoring make it possible to make the installations profitable. It is therefore important to develop diagnostic tools for early detection of faults that may appear in these machines [1].

Usually, diagnostic methods require knowledge of the healthy state of the machine regardless of the physical quantity used. The detection of a fault is based on the comparison of the signature of a given state with a healthy state, by considering an indicator resulting from a measurement that is known to be sensitive to a particular fault [2]. Analysis and processing of measurable quantities in the electrical system, in particular stator currents, has taken a preponderant place in the approaches for detecting and diagnosing faults in electrical machines.

In the last decades, the diagnosis of the asynchronous machine has known a growing enthusiasm on the part of the scientific community. The model approach consists of the analytical modeling of machine [3]. The occupation of Lipo et al. [4] and Cornell et al. [5] all relate to the accurate modeling of the machine. Those of Toliyat are characterized by the winding function and the consideration of space harmonics [6]. On the other hand, Devanneaux et al. studies [7] are based on the multi-winding model. This work has greatly enriched the accurate modeling oriented towards diagnosis. Filippetti’s et al. research for the diagnosis defects in the induction motor by using the technique of artificial intelligence [8] and neural networks [9]. The signal approach consists in the detection of indicators or signatures of defects [10]. This operation is carried out by the extraction and quantification of measurable electrical or mechanical quantities of reliable indices related to defects. Work has been illustrated by the search for internal indicators (magnetic field, etc.) [2], others by external indicators (voltage, current, torque, speed) [6]. The system approach consists of extracting and classifying or interpreting the results. A form of automation of the diagnostic procedure from acquisition to decision-making has been developed and presented [11].

Intelligent techniques such as fuzzy logic and neural networks are increasingly integrated into algorithms for detecting the failure of electrical machines, particularly in the classification of faults. Filippetti et al. [9] introduced neural networks for the rotor faults diagnosis, in particular for the detection and estimation of the number of broken bars. In [12] presented a new method for on-line detection of faults in asynchronous machine by monitoring stator current based on artificial neural networks. His essays prove the interest of neural networks for classification and decision making. In [13] introduced the Kalman filter in a parametric study for detection of broken bars with estimation of rotor resistance. Another study [14], in which was presented a method for the diagnosis of electrical faults, based on Park vector approach using the technique of artificial neural networks as a decision criterion for the discrimination between healthy and failed cases. In [15] were proposed a system for identifying and classifying asynchronous machine faults. This system is based on radial function-based neural networks. The author [16] proposed a parameter selection method based on a genetic algorithm. It allows a notable reduction of the dimension of this vector without significant loss of information. In [17] was presented a new estimation model without sensors of inaccessible quantities of asynchronous machine for control and monitoring, based on artificial intelligence techniques, such as artificial neural networks and neuro-fuzzy networks. Furthermore, he gave the notion of neuro-fuzzy extended Kalman filters for the estimation of the internal parameters of asynchronous machine.

Online fault diagnosis plays a vital role in monitoring operation and provides early protection against faults in many industrial areas without stopping production lines. The use of field programmable gate array (FPGA) for implementing fault diagnosis algorithm solves the biggest obstacle of system complexity by reducing interconnections and wiring problems [18].

The condition monitoring and diagnosis of faults that occur in an asynchronous machine makes the machine highly reliable, helping to avoid unplanned downtime, which leads to more lost revenue and interrupted production. This can only be achieved when irregularities produced due to faults are detected as they occur and diagnosed quickly so that appropriate action to protect the equipment can be taken. This requires intelligent control with a performing scheme [19]. Therefore, FPGA architecture based on a hardware implementation of the motor current signal analysis (MCSA) failure detection algorithm and fuzzy logic is suggested in this article to diagnose the fault more efficiently and almost instantaneously.

The **purpose** of this work is to study the contribution of the implementation of fuzzy logic on FPGA programmable logic circuits in the diagnosis of asynchronous machine failures for a phase unbalance and a missing phase faults cases. In this study, we start with the adaptation of the fuzzy logic in order to allow an optimal implementation. This implementation must ensure efficiency, speed of execution and a minimum possible space on the FPGA circuit.

Basic calculation relationships and assumptions. A proposed system consists of a power supply block having an AC-DC inverter node and a DC-AC inverter node, an asynchronous machine, a flux and torque estimation block, a fault based on fuzzy MCSA, a controller block based on direct torque control (DTC) command. The input signals corresponding to the currents at the terminals of the asynchronous machine are transformed into output signals indicating the torque and the flux by the estimation block. These signals are fed into the controller block, which creates input signals for the DTC block, which processes and generates appropriate pulses for the bipolar transistor inverter. The fault diagnosis block receives signals corresponding to the stator currents of the asynchronous motor and gives the states (healthy or faulty) of the asynchronous machine.

The diagnostic block diagram of the asynchronous machine with a fuzzy MCSA implementation based on FPGA is shown in Fig. 1.

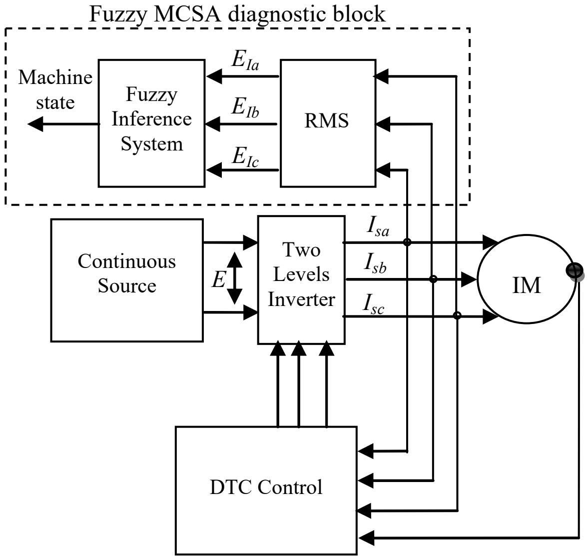

Fig. 1. Schematic of fuzzy-MCSA-based fault diagnosis drive system

Fuzzy inference system will automatically detect the fault of lack of phase, imbalance of the three phases and short circuit also between the turns as soon as it appears on the asynchronous motor.

RMS signal of the asynchronous motor stator phase current is used as a fault indicator signal

$$RMS=\sqrt{\frac{1}{t}\int_0^t u^2(t)\mathrm{d}t}\,. \tag{1}$$

For a periodic signal T, the relation will be:

$$RMS=\sqrt{\frac{1}{2T}\int_0^T u^2(t)\mathrm{d}t}\,. \tag{2}$$

The RMS values for the three phases of stator currents are compared with their nominal values. The results of this comparison give the three fault indicator signals: fault indicator of phase A current (E_{Ia}), fault indicator of phase B current (E_{Ib}) and fault indicator of phase C current (E_{Ic}) in the method proposed in this work.

Signals (E_{Ia}, E_{Ib} and E_{Ic}) represent the linguistic variables for the inputs of the proposed fuzzy inference system. These variables can take three linguistic values: N (negative), Z (zero) or P (positive). Figure 2 shows the fuzzification membership functions of the RMS error.

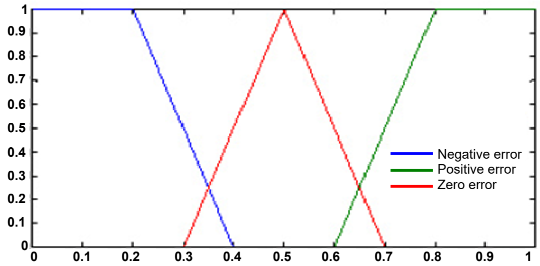

Fig. 2. The fuzzification membership functions of the RMS error

Output signal of the proposed fuzzy inference system is presented by the linguistic variable *EM*, which represents the state of the machine and can take the following linguistic values *S* (Healthy); *D*1 (Fault degree 1°); *D*2 (Fault degree 2°); *D*3 (Fault degree 3°). The fuzzification membership functions of the machine state *EM* is presented in Fig. 3.

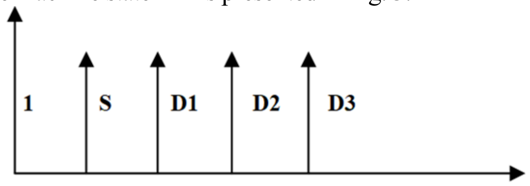

Fig. 3. The fuzzification membership functions of the *EM*

Fuzzy inference system decides according to the following rules:

- if all the fault indicators are zero then the state of the *EM* machine takes the value *S* (Healthy);
- if only one fault indicator is non-zero then the state of the *EM* machine takes the value *D*1 (Fault degree 1°);
- if only two fault indicators are non-zero then the state of the EM machine takes the value *D*2 (Fault degree 2°);
- if all the fault indicators are non-zero then the state of the *EM* machine takes the value *D*3 (Fault degree 3°).

FPGA implementation of RMS function. The RMS block is used to calculate the effective value of a signal using (1) [20]. Consider a signal form $u(t)$ in Fig. 4 a signal form $u^2(t)$ will be as in Fig. 5.

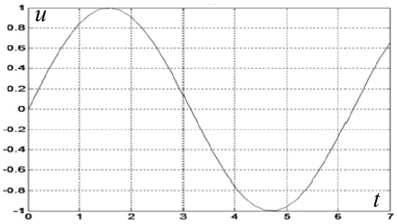

Fig. 4. Signal form $u(t)$

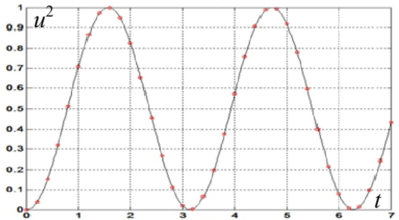

Fig. 5. Signal form $u^2(t)$

A signal sampled by a sampling steps T_e. Signal $u^2(t)$ will only be known at sampling instants. Figure 6 shows the signal $u^2(t)$ sampled. Signal $\int_0^t u^2(t)\mathrm{d}t$ can be approximated by the area between $u^2(t)$ discretized and the time axis as shown in Fig. 7.

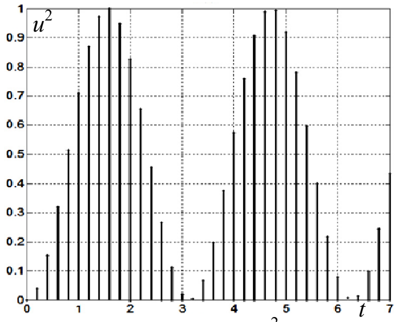

Fig. 6. Sampled $u^2(t)$

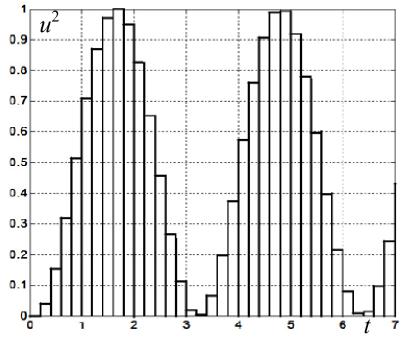

Fig. 7. Area between $u^2(t)$ discretized and the time axis

For *N* samples:

$$\int_0^t u^2(t)\mathrm{d}t \cong \sum_{i=0}^{N-1} u_i^2 \cdot T_e \,,$$

so

$$RMS \cong \sqrt{\frac{1}{N \cdot T_e}\sum_{i=0}^{N-1} u_i^2 \cdot T_e} \Rightarrow RMS \cong \sqrt{\frac{1}{N}\sum_{i=0}^{N-1} u_i^2} \,. \quad (4)$$

The hardware implementation on FPGA we used a counter to count the number of samples, a multiplier to calculate the square of a sampled signal u_i^2, an accumulator to cumulate the values of u_i^2, then multiply the value of the accumulator and the inverse of counter at the end make the square root of it to obtain the result.

The hardware architecture on FPGA of the RMS function is presented in Fig. 8.

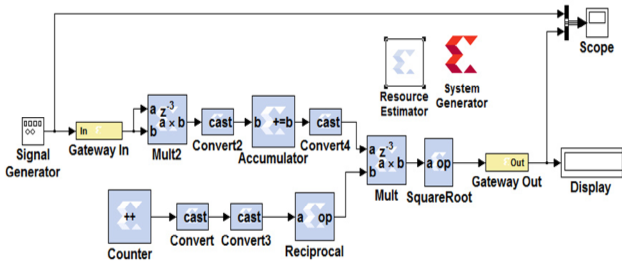

Fig. 8. Hardware architecture on FPGA of the RMS function

FPGA implementation of fuzzy inference system. The hardware implementation of a fuzzy inference system consists in implementing the three phases of a regulation by fuzzy logic: fuzzification, fuzzy inferences and defuzzification.

Fuzzification module implementation. In this study, we employ a memory-oriented approach for implementing the fuzzification module, which allows us to determine the degree of membership in a fuzzy set using a member ship function. This approach calculates the output values offline and stores them in memory. One advantage of this solution is that it simplifies the process of changing a member ship function [21].

To represent each linguistic input/output variable, we use tables that store the degree of membership for each linguistic value. These tables are implemented in hardware using Read Only Memory blocks that can be addressed with a single entry. These memory blocks contain the degree of membership for each linguistic value and provide a representation of the discrete speech universe. For instance, if we have a normalized discourse universe [0, 1] with 64 points of discretization, we would use an address space of

[0:63]. The hardware implementation of these functions is detailed in [22].

Implementation of rule inference and evaluation module. The implementation of rule inference and evaluation is shown in Fig. 9. This module takes three blocks from the fuzzification module as input. The rules selector block helps construct the rule base, which consists of 27 rules. The realization of all the possible combinations between the fuzzy values of «RMS error» makes it possible to obtain this base of rules.

The (min/max) operators are implemented by a 2-1 multiplexer and a comparator on XSG «Xilinx System Generator» hardware tool. If an operator (min/max) has more than two inputs, multiple two-input (min/max) operators are used. For instance, to implement a min operator with three inputs, two min operators with two inputs are employed.

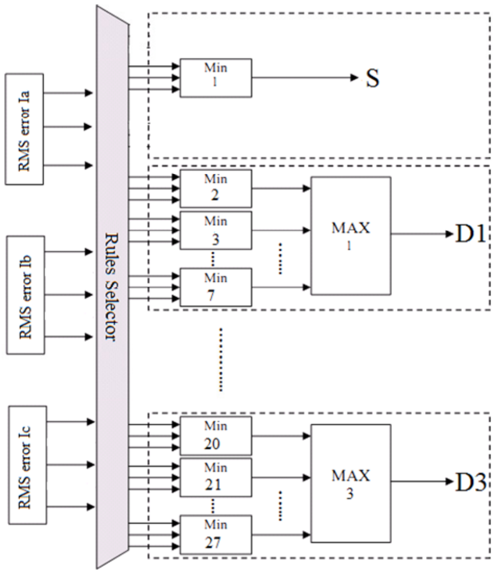

Fig. 9.Architecture of the inference engine module

Implementing the defuzzification module. The hardware description of the defuzzification module is performed by a MAX operator as shown in Fig. 10. The inputs of this module are the outputs of the inference module. The output of this block is representing the output of the entire EM fuzzy block, which represents the state of the machine.

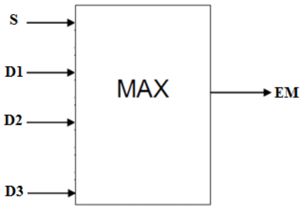

Fig. 10. Defuzzification architecture

Results, simulations and validation. This phase consists of the integration of a fuzzy inference system in the MCSA algorithm for diagnosis of asynchronous machine defects. During this part and similar to the simulation with MATLAB, we will simulate the proposed hardware architecture using the Xilinx generator system.

The diagnostic algorithm is applied to an induction motor, whose specifications are given in Table 1.

Table 1

Induction motor parameters

Stator resistance R_S, Ω	10
Rotor resistance R_r, Ω	6.3
Stator inductance L_S, H	0.4642
Rotor inductance L_r, H	0.4612
Mutual inductance L_m, H	0.4212
Moment of inertia j, kg·m^2	0.02
Machine pair pole number p	2

Synthesis results. Table 2 presents the performances in terms of resource consumption obtained during the implementation of the diagnostic algorithm proposed on the FPGA Virtex 4 given by the architecture presented in Fig. 1.

Note that the proposed architecture optimizes the use of the hardware resources of the FPGA card 4.8 % of slices and 13.7 % of look up tables (LUTs), moreover this architecture considerably reduces the logical components to be used compared to the architectures presented in [19, 21].

Table 2

FPGA proposed diagnostic algorithm

Target Device: ML402 Virtex-4 xc4vsx35-10ff668				
Logic utilization	RMS	Fuzzy system	Available	Utilization
Number of slice flip flops	170	1304	30720	4.8 %
Number of occupied slices	422	1685	15360	13.7 %
Total number of 4 Input LUTs	1286	2173	30720	11.25 %
Number of bonded input output block (IOBs)	65	58	448	27.4 %

Table 3 presents operating frequency comparison between our implementation and previous implementations of induction motor diagnostics algorithms.

Table 3

Operating frequency comparison

References	[21]	[21]	[19]	Proposed fuzzy MCSA
Device family	Intel Pentium Dual Core processor	FPGA Altera Cyclone-II	FPGA Xilinx Spartan-3E	FPGA Xilinx Virtex-4
Maximum clock frequency	2.95 kHz	45.45 kHz	92.1 MHz	231.64 MHz
Minimum period	338 μs	22 μs	10.857 ns	4.317 ns

The synthesis tool sets the maximum clock frequency at 231.64 MHz, corresponding to a minimum period of 4.317 ns. Table 3 presents a comparative study of the operating frequencies among various references within the same research axis.

MATLAB/Simulink and XSG/Xilinx simulations. The structure of the fuzzy MCSA diagnostic algorithm block is shown in Fig. 1. This proposed algorithm consists of two modules. RMS module is used to calculate the effective value for the three phases of stator currents. This signal is used as the signal fault indicator and the diagnostic module based on a fuzzy inference system, we simulated these modules separately on MATLAB/Simulink with Xilinx generator system. Simulation results of the RMS module for the different types of input signals are illustrated in Fig. 11.

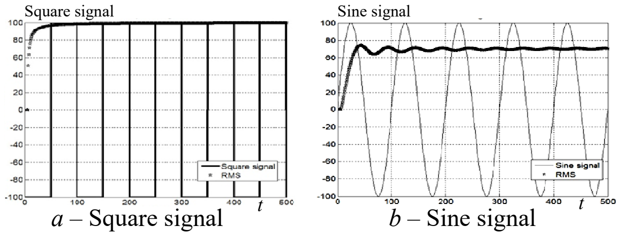

a – Square signal *b* – Sine signal

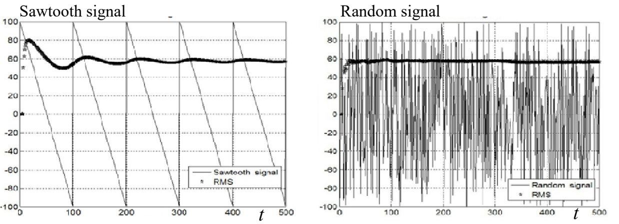

c – Sawtooth signal *d* – Random signal

Fig. 11. RMS function for different types of input signals

FPGA hardware co-simulation validation. After a simulation step, the proposed hardware architecture was validated by co-simulation on the target device ML402 equipped with a Virtex4 FPGA circuit. This last is dedicated to the implementation of the proposed diagnostic algorithm on a development board integrating an FPGA component. It is mainly intended for the verification and validation of the digital implementation of control and diagnostic algorithms on FPGA targets in a «Hardware in the loop» simulation environment.

Figure 12 shows the principle of validation of the architecture proposed by Hardware co-simulation.

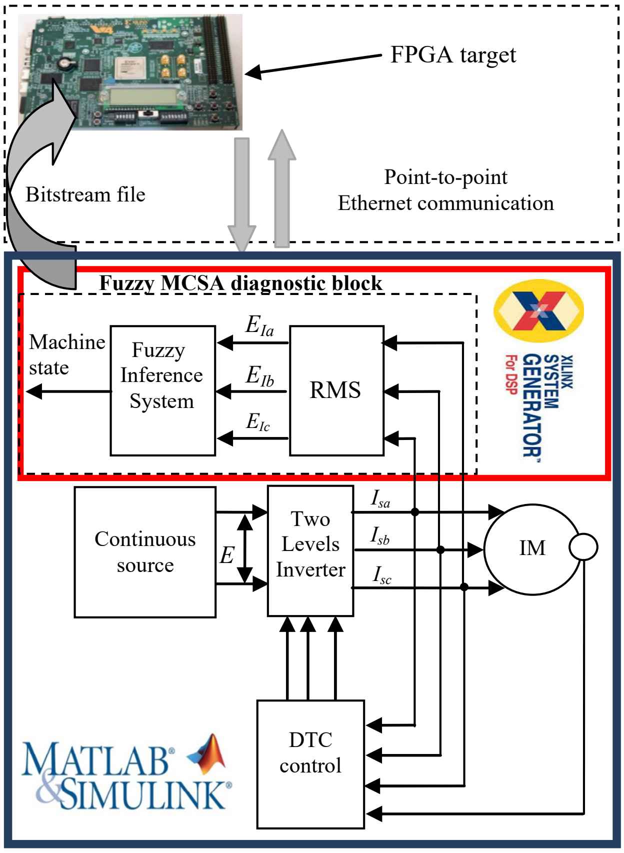

Fig. 12.Hardware in the loop validation of fuzzy MCSA diagnostic algorithm

Upon completion of the simulation and timing analysis, the hardware co-simulation process in XSG follows a procedure to generate a bitstream file from the prototype and a point-to-point Ethernet block. This facilitates the Hardware-in-the-Loop (HIL) procedure. The generated block (Fig. 13) replaces the previously constructed hardware architecture for the fuzzy MCSA diagnostic algorithm.

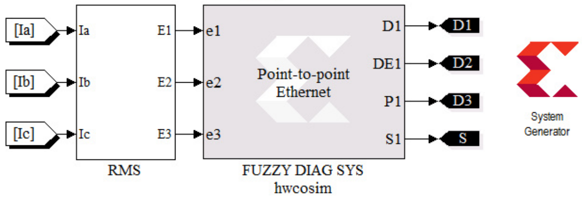

Fig. 13. Fuzzy MCSA diagnostic algorithm HIL point-to-point Ethernet block

During the HIL validation process, the point-to-point Ethernet blocks are connected to both the inverter and the induction motor. In this setup, the motor model, DTC control, and inverter models are simulated in the MATLAB/Simulink environment, while the XSG architectures of the fuzzy MCSA diagnostic algorithm are implemented on the ML402 FPGA device.

To perform the HIL validation, the target device is connected to a PC using an Ethernet cable. This allows for real-time communication and interaction between the simulated models running on the PC and the hardware implementation running on the FPGA device.

1. *For phase unbalance*: phase *A* voltage V_{sa} = 40 % V_{sa} at t = 0.5 s the waveform responses of the induction motor speed, torque, phase voltages and currents are shown in the Fig. 14, 15.

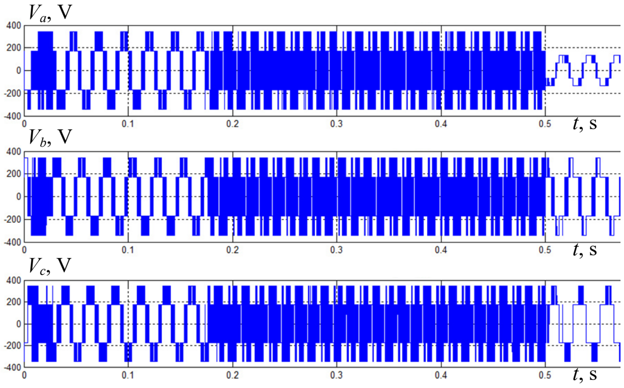

Fig. 14. Behavior of induction motor phase voltages

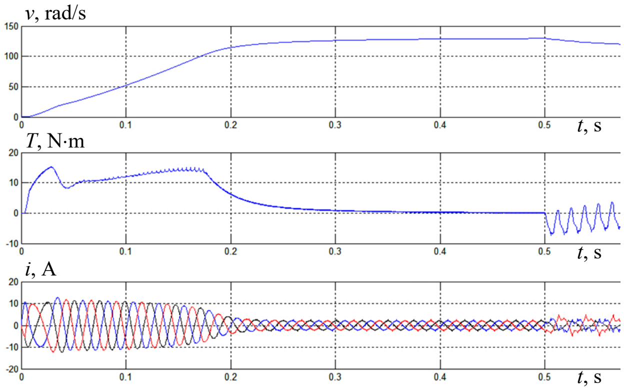

Fig. 15. Behavior of induction motor speed, torque and phase currents

Figure 16 presents the results of the analysis by the fuzzy MSCA algorithm proposed for the phase currents of the previous Fig. 15.

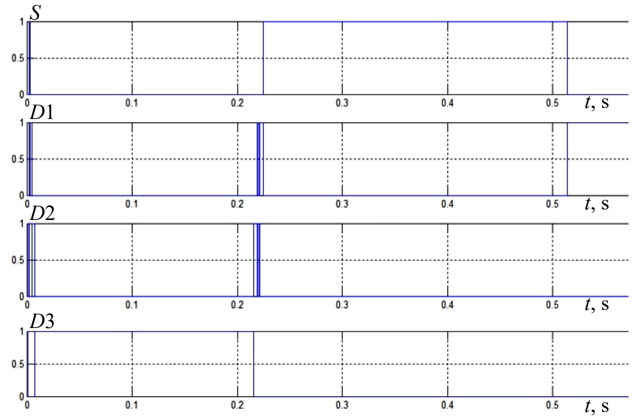

Fig. 16. Proposed fuzzy MSCA analysis of the phase currents

In the machine start-up phase (transient regime) from 0 to 0.2 s the three current phases are greater than their nominal values so it is obvious to have a class *D*3 fault in this time interval.

In the interval 0.2 to 0.5 s the machine reaches their permanent regime and the three current phases resume their nominal values so the state of the machine takes the value Healthy.

At instant 0.5 s a fault appeared and the state of the machine changes from the *S* value to the value *D*1.

The fault does not have a great influence on the dynamic response of the machine speed; this is due to the robustness of the DTC command.

2. *For missing of a phase*: $V_{sa} = 0$ at $t = 0.5$ s the waveform responses of the induction motor speed, torque, phase voltages and currents are shown in the Fig. 17 and 18.

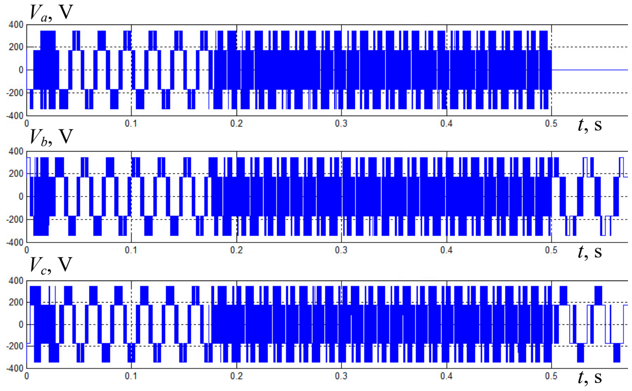

Fig. 17. Behavior of induction motor phase voltage

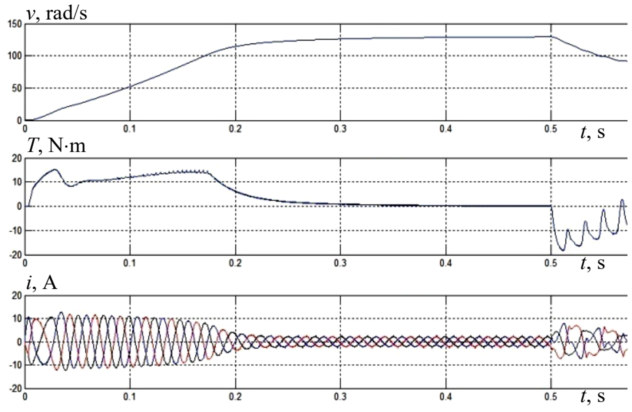

Fig. 18.Behavior of induction motor speed, torque and phase currents

Figure 19 presents the results of the analysis by the fuzzy MSCA algorithm proposed for the phase currents of the previous Fig. 18.

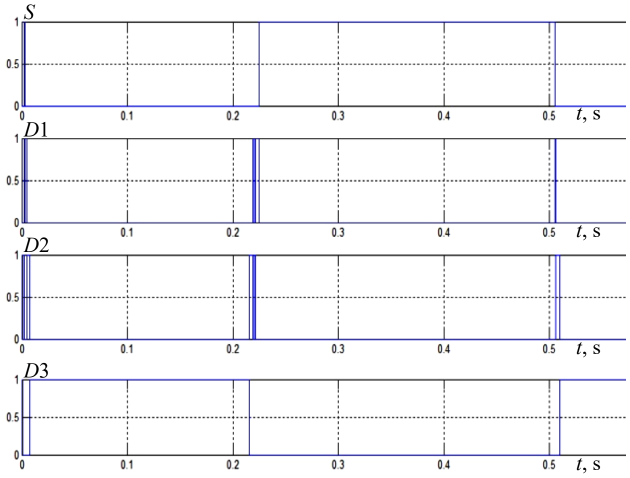

Fig. 19. Proposed fuzzy MSCA analysis of the phase currents

In the machine start-up phase (transient regime) from 0 to 0.2 s the three current phases are greater than their nominal values so it is obvious to have a class *D*3 fault in this time interval.

In the interval 0.2 to 0.5 s the machine reaches their permanent regime and the three current phases resume their nominal values so the state of the machine takes the value Healthy.

At instant 0.5 s a fault appeared and the state of the machine changes from the *S* value to the value *D*3.

The lack of phase fault has a great influence on the dynamic response of the machine speed, this is due to the catastrophic nature of the lack of phase fault.

Conclusions.

1. The purpose of this work was, firstly, to evaluate the performance of the use of field programmable gate array programmable logic circuits for the diagnosis of faults in an asynchronous machine by introducing a fuzzy inference system into the algorithm of the analysis of the motor current signal analysis by taking the RMS signal of the stator phase current as the fault indicator signal. Secondly, to implement and validate the proposed hardware detection algorithm.
2. The originality of our work has been to combine the performance of artificial intelligence techniques, the simplicity of motor current signal analysis algorithms and the execution power of programmable logic circuits, for the definition of a fault diagnosis structure for the asynchronous machine achieving the best simplicity/performance and speed/performance ratios.
3. Finally, we believe that the proposed solution has improved the performance of fault detection for the asynchronous machine, especially in terms of hardware resource consumption, real-time online detection and speed of detection.

Conflict of interest. The authors of the article declare that there is no conflict of interest.

REFERENCES

1. Sakhara S., Brahimi M., Nacib L., Layadi T.M. Application of a wavelet neural network approach to detect stator winding short circuits in asynchronous machines. *Electrical Engineering & Electromechanics*, 2023, no. 3, pp. 21-27. doi: https://doi.org/10.20998/2074-272X.2023.3.03.

2. Moussaoui L., Aouaouda S., Rouaibia R. Fault tolerant control of a permanent magnet synchronous machine using multiple constraints Takagi-Sugeno approach. *Electrical Engineering & Electromechanics*, 2022, no. 6, pp. 22-27. doi: https://doi.org/10.20998/2074-272X.2022.6.04.

3. Da Costa C., Santin C.O. FPGA design approach of digital control of three-phase induction motor. *2017 Brazilian Power Electronics Conference (COBEP)*, 2017, pp. 1-6. doi: https://doi.org/10.1109/COBEP.2017.8257221.

4. Lipo T.A., Consoli A. Modeling and Simulation of Induction Motors with Saturable Leakage Reactances. *IEEE Transactions on Industry Applications*, 1984, vol. IA-20, no. 1, pp. 180-189. doi: https://doi.org/10.1109/TIA.1984.4504392.

5. Cornell E.P., Lipo T.A. Modeling and Design of Controlled Current Induction Motor Drive Systems. *IEEE Transactions on Industry Applications*, 1977, vol. IA-13, no. 4, pp. 321-330. doi: https://doi.org/10.1109/TIA.1977.4503414.

6. Toliyat H.A., Lipo T.A. Transient analysis of cage induction machines under stator, rotor bar and end ring faults. *IEEE Transactions on Energy Conversion*, 1995, vol. 10, no. 2, pp. 241-247. doi: https://doi.org/10.1109/60.391888.

7. Devanneaux V., Dagues B., Faucher J., Barakat G. An accurate model of squirrel cage induction machines under stator faults. *Mathematics and Computers in Simulation*, 2003, vol. 63, no. 3–5, pp. 377-391. doi: https://doi.org/10.1016/S0378-4754(03)00083-1.

8. Filippetti F., Franceschini G., Tassoni C., Vas P. Recent developments of induction motor drives fault diagnosis using AI techniques. *IEEE Transactions on Industrial Electronics*, 2000, vol. 47, no. 5, pp. 994-1004. doi: https://doi.org/10.1109/41.873207.

9. Filippetti F., Franceschini G., Tassoni C. Neural networks aided on-line diagnostics of induction motor rotor faults. Conference Record of the *1993 IEEE Industry Applications Conference Twenty-Eighth IAS Annual Meeting*, 1993, pp. 316-323. doi: https://doi.org/10.1109/IAS.1993.298942.

10. Abu Ibaid O.Z.I., Belhamdi S., Abid M., Chakroune S., Mouassa S., Al-Sagar Z.S. Wavelet packet analysis for rotor bar breakage in an inverter induction motor. *Electrical Engineering & Electromechanics*, 2023, no. 3, pp. 3-11. doi: https://doi.org/10.20998/2074-272X.2023.3.01.

11. Bellini A., Filippetti F., Franceschini G., Tassoni C. Closed-loop control impact on the diagnosis of induction motors faults. *IEEE Transactions on Industry Applications*, 2000, vol. 36, no. 5, pp. 1318-1329. doi: https://doi.org/10.1109/28.871280.

12. Schoen R.R., Lin B.K., Habetler T.G., Schlag J.H., Farag S. An unsupervised, on-line system for induction motor fault detection using stator current monitoring. *IEEE Transactions on Industry Applications*, 1995, vol. 31, no. 6, pp. 1280-1286. doi: https://doi.org/10.1109/28.475698.

13. Said M.S.N., Benbouzid M.E.H., Benchaib A. Detection of broken bars in induction motors using an extended Kalman filter for rotor resistance sensorless estimation. *IEEE Transactions on Energy Conversion*, 2000, vol. 15, no. 1, pp. 66-70. doi: https://doi.org/10.1109/60.849118.

14. Nejjari H., Benbouzid M.E.H. Monitoring and diagnosis of induction motors electrical faults using a current Park's vector pattern learning approach. *IEEE Transactions on Industry Applications*, 2000, vol. 36, no. 3, pp. 730-735. doi: https://doi.org/10.1109/28.845047.

15. Kral C., Pirker F., Pascoli G. Detection of rotor faults in squirrel-cage induction machines at standstill for batch tests by means of the Vienna monitoring method. *IEEE Transactions on Industry Applications*, 2002, vol. 38, no. 3, pp. 618-624. doi: https://doi.org/10.1109/TIA.2002.1003409.

16. Hsu J.S. Monitoring of defects in induction motors through air-gap torque observation. *IEEE Transactions on Industry Applications*, 1995, vol. 31, no. 5, pp. 1016-1021. doi: https://doi.org/10.1109/28.464514.

17. Lehtoranta J., Koivo H.N. Fault Diagnosis of Induction Motors with Dynamical Neural Networks. *2005 IEEE International Conference on Systems, Man and Cybernetics*, 2005, vol. 3, pp. 2979-2984. doi: https://doi.org/10.1109/ICSMC.2005.1571603.

18. Karim E., Memon T.D., Hussain I. FPGA based on-line fault diagnostic of induction motors using electrical signature analysis. *International Journal of Information Technology*, 2019, vol. 11, no. 1, pp. 165-169. doi: https://doi.org/10.1007/s41870-018-0238-5.

19. Rajeswaran N., Thangaraj R., Mihet-Popa L., Krishna Vajjala K.V., Özer Ö. FPGA Implementation of AI-Based Inverter IGBT Open Circuit Fault Diagnosis of Induction Motor Drives. *Micromachines*, 2022, vol. 13, no. 5, art. no. 663. doi: https://doi.org/10.3390/mi13050663.

20. Chouidira I., Khodja D., Chakroune S. Induction Machine Faults Detection and Localization by Neural Networks Methods. *Revue d'Intelligence Artificielle*, 2019, vol. 33, no. 6, pp. 427-434. doi: https://doi.org/10.18280/ria.330604.

21. Romero-Troncoso R.J., Saucedo-Gallaga R., Cabal-Yepez E., Garcia-Perez A., Osornio-Rios R.A., Alvarez-Salas R., Miranda-Vidales H., Huber N. FPGA-Based Online Detection of Multiple Combined Faults in Induction Motors Through Information Entropy and Fuzzy Inference. *IEEE Transactions on Industrial Electronics*, 2011, vol. 58, no. 11, pp. 5263-5270. doi: https://doi.org/10.1109/TIE.2011.2123858.

22. Aib A., Khodja D.E., Chakroune, S. Field programmable gate array hardware in the loop validation of fuzzy direct torque control for induction machine drive. *Electrical Engineering & Electromechanics*, 2023, no. 3, 28-35. doi: https://doi.org/10.20998/2074-272X.2023.3.04.

Received 02.03.2023
Accepted 23.05.2023
Published 02.11.2023

Abdelghani Aib [1], *Doctor of Electrotechnical,*
Djalal Eddine Khodja[2], *Doctor of Electrotechnical, Professor,*
Salim Chakroune[1], *Doctor of Electrotechnical, Professor,*
Hilal Rahali [1], *Doctor of Electrotechnical,*
[1] Research Laboratory on the Electrical Engineering,
Faculty of Technology,
University of M'Sila, BP 166, Ichbilia 28000, Algeria,
e-mail: abdelghani.aib@univ-msila.dz;
salim.chakroun@univ-msila.dz (Corresponding Author);
Hilal.rahali@univ-msila.dz
[2] Signals & Systems Lab,
Institute of Electrical and Electronic Engineering,
Boumerdes, 35000, Algeria,
e-mail: djalaleddine.khodja@univ-msila.dz

How to cite this article:
Aib A., Khodja D.E., Chakroune S., Rahali H. Fuzzy current analysis-based fault diagnostic of induction motor using hardware co-simulation with field programmable gate array. *Electrical Engineering & Electromechanics*, 2023, no. 6, pp. 3-9. doi: https://doi.org/10.20998/2074-272X.2023.6.01

UDC 621.313 https://doi.org/10.20998/2074-272X.2023.6.02

B. Larbi, M. Hatti, K. Kouzi, A. Ghadbane

Axial flux machine with non-slotted TORUS-NS rotor type. Design and investigate for electric traction

Introduction. *The drive electric motor is one of the key components in the traction chain of an electric vehicle. Traditional radial flux motors used in electric vehicles, which use permanent magnets or induction motors in an electric field, are experiencing significant development aimed at optimizing their weight and cost. However, it can only go so far, so switching to a completely different type of machine, such as an axial flow, might be a good alternative. The* ***novelty*** *to this item is an axial flux permanent magnet motorization with non-slotted TORUS-NS rotor (single interior stator with two external rotors North-South) type housed in the wheel of the vehicle; this allows power to pass directly from the motor to the wheel, increasing the efficiency of the motor. System complexity is also less, as the transmission, differentials and driveshaft are eliminated.* ***Purpose*** *is to equip the electric car and choose the motor adapted to the application and the available space. The smaller size and weight allows for a lighter vehicle and more batteries, thus increasing range. The focus on customization is because vehicle performance is so dependent on the quality of the vehicle architecture , battery pack and axial flux motor design. The* ***results*** *obtained are in good agreement of accuracy, in particular the flux density at the air gap. The investigation is carried out by the finite element method. Machine model was run on Maxwell 16.0 business code.* References 22, table 1, figures 10.

Key words: **axial flux permanent magnet machine, electric vehicle, finite element method, TORUS-NS.**

Вступ. *Привідний електродвигун є одним із ключових компонентів тягового кола електромобіля. Традиційні двигуни з радіальним магнітним потоком, що використовуються в електромобілях, в яких використовуються постійні магніти або асинхронні двигуни в електричному полі, переживають значний розвиток, спрямований на оптимізацію їхньої ваги та вартості. Однак це не межа, тому гарною альтернативою може бути перехід на зовсім інший тип машини, наприклад, з осьовим потоком.* ***Новизною*** *у цьому питанні є машина з постійним магнітом з осьовим магнітнім потоком та безпазовим ротором TORUS-NS (один внутрішній статор з двома зовнішніми роторами північ-південь), розміщеним у колесі транспортного засобу; це дозволяє потужності передаватися безпосередньо від двигуна до колеса, підвищуючи ефективність двигуна. Складність системи також знижується, оскільки відсутні трансмісія, диференціали та карданний вал.* ***Мета*** *полягає в тому, щоб обладнати електромобіль та вибрати двигун, адаптований до застосування та доступного простору. Найменші розмір і вага дозволяють використовувати більш легкий автомобіль та більше батарей, що збільшує пробіг. Особлива увага приділяється індивідуальному настроюванню, оскільки продуктивність автомобіля багато в чому залежить від якості його архітектури, акумуляторної батареї та конструкції двигуна з осьовим магнітним потоком. Отримані* ***результати*** *перебувають у добрій згоді за точністю, зокрема за густиною потоку у повітряному зазорі. Дослідження проводиться методом скінченних елементів. Модель машини була досліджена з використанням комерційного програмного продукту Maxwell 16.0.* Бібл. 22, табл. 1, рис. 10.

Ключові слова: **машина з постійним магнітом з осьовим потоком, електромобіль, метод скінченних елементів, електрична машина типу TORUS-NS.**

1. Introduction. Road transport is one of the biggest emitters of greenhouse gases in the world and one of the main sources of air pollution. Faced with this colossal challenge, the world has embarked on an ambitious transition policy towards cleaner and more efficient energy, improving performance, efficiency, safety and sustainability [1] with less polluting transport judged as a strong requirement. One of the solutions for reducing polluting gas emissions is the development of electric vehicles, while the traction of electric vehicles is entirely provided by electric motors. Unfortunately, electric vehicles have several disadvantages compared to internal combustion vehicles: for example; very limited autonomy, and high manufacturing costs.

On the might of these points, it is obvious that the motor for this vehicle must be very efficient. Due to its disc-shaped structure and high compactness, the topology of the axial flux permanent magnet (AFPM) machine is well suited for direct drive motor applications in the wheels [2]. Innovative solutions for emerging low-speed vehicles each providing a wide range of benefits in the areas these vehicles move through. The use of low-speed vehicles helps users enjoy the benefits of low-speed electric vehicles even more. For this purpose, a mode for low-speed vehicles was chosen for this study where the nominal speed of the wheels is 200 rpm.

The objective of this paper is to design the twin rotor axial flux synchronous motor without slot with internal stator (TORUS) according to the dimensioning equation. 3D finite element analysis is used for the accuracy of the electromagnetic air gap density.

2. Axial flux permanent magnet machine.

A. Presentation of the axial flux machine. A radial flux motor generates flux perpendicular to the axis of rotation, where the rotor is made of permanent magnets located inside a stator that contains support known as a yoke, which is outfitted with «teeth» containing electromagnetic coils that work as alternating magnetic poles. These poles interact with the alternating magnetic flux of the stator coils, which produces rotation of the rotor and therefore of the motor. An axial flux motor design has a different geometry from a radial machine, since its stator disc sandwiched between two rotor discs distinguishes the motor. In this design, the flux is generated parallel to the axis of rotation. This carries has the advantage of simplifying the fabrication of the motor (Fig. 1).

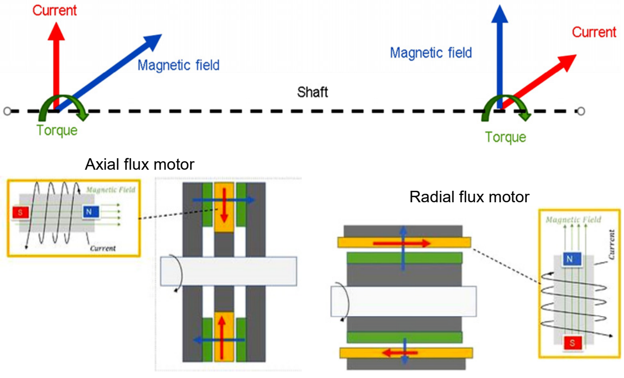

Fig. 1. Operating principles of the machine

B. Topologies of axial flux machines. Several axial flux machine configurations are shown in Fig. 2. Are classified into several categories [3, 4] according to:

- *construction*: number of stators and rotors, and their locations to each others.
- *winding support*: slotted, unslotted.
- *type of winding produced*: distributed, concentrated, Gramme ring.
- *arrangement of magnets*: on the surface, buried radially, buried tangentially.

Moreover, in literature, 4 main families are classified according to the type of structure:

1. «Single face» machine or a machine with 1 rotor and 1 stator.
2. «TORUS» (single interior stator with two external rotors) machine, where the stator is between 2 rotors.
3. «AFIR» (axial flux internal rotor) machine, where the rotor is between 2 stators.
4. Multi-stage machine with several stators and rotors.

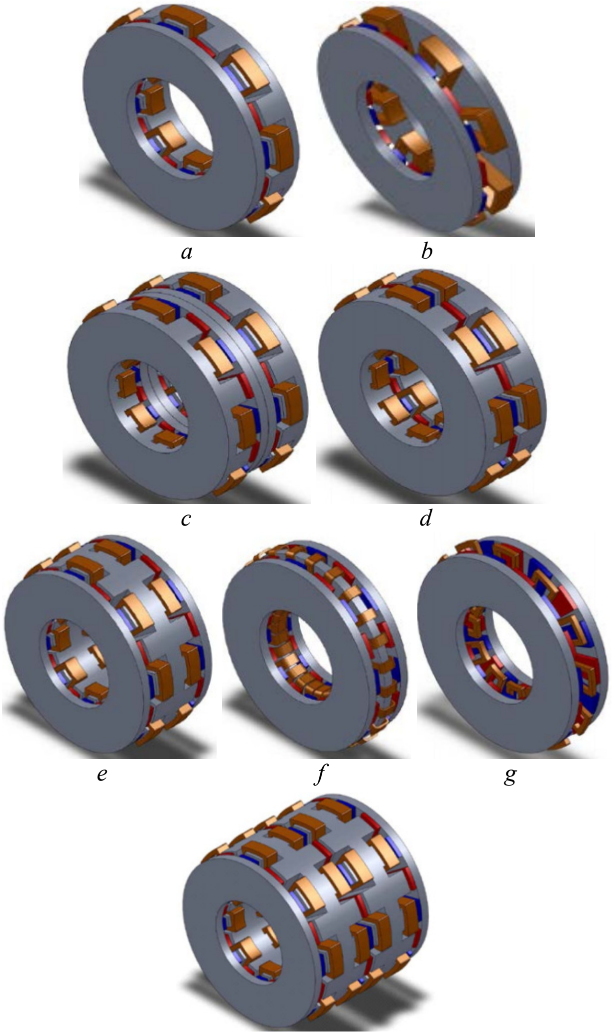
a *b* *c* *d* *e* *f* *g* *h*

Fig. 2. AFPM synchronous motor topologies:
a, *b* – single stator-single rotor [5]; *c*, *d* – dual stator-single rotor; *e*, *f*, *g* – dual rotor-single stator; *h* – multistage structure

3. Geometrical modeling, and dimensioningof the AFPM machine.

A. Machine suitable for automotive application. In order to be able to select the best machine meeting the needs of our application, a small comparison between the different topologies of the AFPM machine illustrated in Fig. 2 is made to extract the advantages and disadvantages of each machine in order to be able to select the most suitable topology and meeting the different requirements of our application. Firstly, single air gap structures of the 1 stator/1 rotor type are eliminated in favor of multiple air gap structures because the objective is to have a mechanically balanced structure where the axial forces in operation compensate each other. In addition, a multiple air gap structure allows us to use a larger electromechanical conversion surface than the single air gap structure and, therefore, to hope to meet the performance required for our application. However, the reduced axial size imposed by the wheel and the obligation to work with discs of significant thickness prohibits multi-disc structures with more than two air gaps. The choice made among the symmetrical structures with two air gaps, we eliminate the structure with two stator and one rotor because of volume in favor of a structure with two rotor and one stator, therefore the selection remains between the TORUS-NN machine a magnetic flux emanates from a permanent magnet (PM), passes through the air gap, passes through the stator core and completes the circuit at the opposite polarity PM [6], stator and TORUS-NS or the direction of the flux changes such that the flux moves along the axis of the stator; in other words, the flux moves from the first rotor to the stator towards the second rotor without circulating along the stator yoke. In this case, the winding is placed on a disk of non-conductive and non-magnetic material [7], which implies a considerable reduction in iron losses and the elimination of the cogging torque which can be responsible for annoying torque ripples. Thus, this machine has a fairly advantageous mass torque [8]. In addition, the windings are placed at the level of the air gap and are in direct exposure to the magnetic field. At the end of this comparison and according to the criteria required for our application the TORUS machine where the stator is located between 2 mild steel rotors, carrying axially polarized magnets [9, 10] reaching relatively large dimensions air gap associated with a winding without an air gap [11]. The laminated stator strip wound toroid has a slotless toroidal winding that carries three phases. The geometric design of the TORUS-NS engine is shown in Fig. 3 [12]. The arrangement of the three-phase windings, the polarity of the magnet and the current path in the magnetic circuit through the diameter of the machine are shown in Fig. 4 [13].

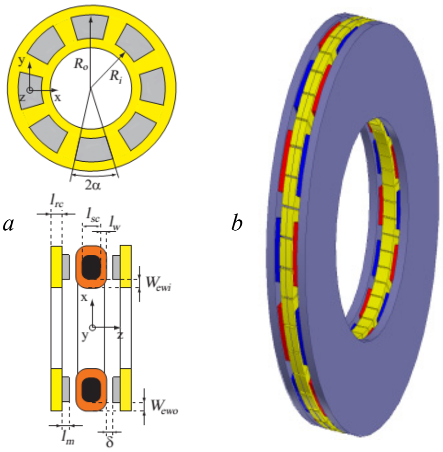

Fig. 3. *a* – definition of the geometrical parameters for the AFPM TORUS-NS motor [10]; *b* – configuration of the PM machine with axial flux TORUS without slot (TORUS-NS)

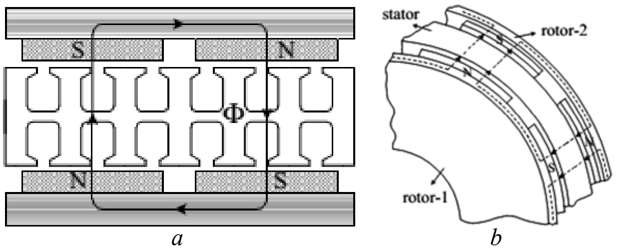

a *b*

Fig. 4. PM polarities and magnetic flux paths of a TORUS-NS machine [5]: *a* – 2D; *b* – 3D

B. Sizing equation for the AFPM machine. Two models of analytical modeling of electromagnetic phenomena are described, a simplified modeling was developed in order to set up dimensioning equations [14]. It is based on a reasoning on the power balance of the machine tha allows possibility to analyze, compare and pre-dimension machines of different structures. These models are fast, however, compromises must be made in terms of solution accuracy. The established sizing rules link input quantities such as geometry and power supply to output quantities which are the performance of these machines in terms of torque, losses, and efficiency. The sizing equations of machines with TORUS axial flow have the following form:

$$P_{out} = \eta \cdot \frac{m}{T} \cdot \int_0^T e(t) \cdot i(t) \mathrm{d}t = m \cdot K_p \cdot \eta \cdot E_{pk} \cdot I_{pk}\ , \quad (1)$$

where $e(t)$ is the electromotive force (EMF) due to PM; $i(t)$ is the supply current; E_{pk} is the maximum value of EMF in air gap; I_{pk} is the maximum value of current; K_p is the power coefficient; η is the motor efficiency; m is the phases number of motor [6, 15].

The power coefficient K_p is defined as:

$$K_p = \frac{1}{T} \cdot \int_0^T \frac{e(t) \cdot i(t)}{E_{pk} \cdot I_{pk}} \mathrm{d}t = \frac{1}{T} \cdot \int_0^T fe(t) \cdot fi(t) \mathrm{d}t . \quad (2)$$

The normalized EMF and current are defined as:

$$fe(t) = e(t) / E_{pk}\ ; \quad fi(t) = i(t) / I_{pk}\ .$$

The form factor of the current is K_i defined as:

$$K_i = \frac{I_{pk}}{I_{rms}} = \left[\frac{1}{T} \cdot \int_0^T \left(\frac{i(t)}{I_{pk}} \right)^2 \mathrm{d}t \right]^{-0.5} , \quad (3)$$

where I_{rms} is the average square value of the phase current.

The maximum value of the phase air gap EMF for the AFPM in (1) is given as:

$$E_{pk} = K_e \cdot N_{ph} \cdot B_g \cdot \frac{f}{p} \left(1 - \lambda^2\right) \cdot D_0^2 , \quad (4)$$

where K_e is the factor form voltage into account the type of winding; N_{ph} is the turns per phase number; B_g is the air gap magnetic flux density taken as a parameter to increase the mass moment [16]; f is the frequency of machine; p is the pole pairs number of machine; $\lambda = D_0 / D_0$, which is taken as a parameter to improve performance of motor [17]; D_0 is the outer diameter of motor; D_0 is the inside diameter of motor.

The maximum current value is given by:

$$I_{pk} = A \cdot \pi \cdot K_i \cdot \frac{1 + \lambda}{2} \cdot \frac{D_0}{2_{m1} \cdot N_{ph}} , \quad (5)$$

where m_1 is the number of phases in stator; A is the electrical load of machine.

Combining (1) to (5), we obtain measuring equation:

$$P_{out} = \frac{m}{m_1} \cdot \frac{\pi}{2} \cdot K_e \cdot K_p \cdot K_i \cdot A \cdot B_g \cdot \eta \cdot \frac{f}{p} \cdot \left(1 - \lambda^2\right) \cdot \left(\frac{1 + \lambda^2}{2} \right) \cdot D_0^3 , (6)$$

with introduction the aspect factor of the axial current machine [16]: $K_i = D_0 / L_e$, where L_e is the axial height of the machine, which is based on certain considerations of physical and geometrical quantities.

Using this parameter, second expression of the sixth dimensional equation (6) is deduced:

$$P_{out} = K_e \cdot K_i \cdot K_p \cdot K_L \cdot \eta \cdot B_g \cdot A \cdot \frac{f}{p} \cdot \left[\left(1 - \lambda^2\right) \cdot \frac{1 + \lambda}{2} \cdot D_0^2 \right] \cdot L_e . (7)$$

The torque density of machine for total volume is:

$$\tau_{dem} = \frac{P_{out}}{w_m \cdot \frac{\pi}{4} \cdot D_{tot}^2 \cdot L_{tot}} , \quad (8)$$

where w_m is the angular speed of rotor; D_{tot} and L_{tot} are the total outer diameter and the total length of machine respectively, including the outer diameter winding end [2, 6, 17].

A general approximation of the size equation can be easily applied to TORUS surface-mounted PM motors [6]. The diameter of the outer surface D_0 can be specified as:

$$D_0 = \left(\frac{P_{out}}{\frac{\pi \cdot m}{2 \cdot m_1} \cdot K_e \cdot K_p \cdot K_i \cdot A \cdot B_g \cdot \eta \cdot \frac{f}{p} \cdot \left(1 - \lambda^2\right) \cdot \left(\frac{1 + \lambda}{2} \right)} \right)^{\frac{1}{3}} . (9)$$

Axial height of active parts L_e (7) is expressed as a function of geometric and magnetic parameters of axial flux machine, the axial height of active parts can be expressed by:

$$L_e = L_s + 2 \cdot L_r + 2 \cdot g , \quad (10)$$

where L_r is the active length of the rotor:

$$L_r = L_{cr} + L_{PM} , \quad (11)$$

where L_{cr}, L_{PM} are the axial height of a rotor yoke and magnets respectively; g is the axial thickness of machine air gap; L_s is the height of the toroidal stator without notch. This height is made up of a laminated ferromagnetic yoke to height L_{cr}, and that of the windings in the axial direction, denoted W_{cu}:

$$L_s = L_{cs} + 2 \cdot W_{cu} . \quad (12)$$

In order to evaluate W_{cu} in [17] was developed a method based on volume considerations. By introducing the effective surface current density J_s in the copper wire, and the winding factor K_{cu} simple considerations on the volume of copper allow us to write that:

$$W_{cu} = \frac{D_i - \sqrt{D - \left(2 \cdot A \cdot D_g / K_{cu} \cdot J_s\right)}}{2} . \quad (13)$$

This size is also useful not only for the axial size, but also for radial dimensions, because it can then write the total exterior diameter of the machine in the form:

$$D_{tot} = D_0 + 2W_{cu} . \quad (14)$$

The thickness of the yoke of the stator is obtained as:

$$L_{cs} = \frac{B_g \cdot \pi \cdot \alpha_p \cdot D_0 \cdot (1 + \lambda)}{4 \cdot p \cdot B_{cs}} , \quad (15)$$

where B_{cs} is the flux density in the stator core.

For the rotor thickness, the previous expression must be divided by a factor of two, since the rotor yoke must only channel the magnetic flux present on one side:

$$L_{cr} = \frac{B_u \cdot \pi \cdot D_0 \cdot (1+\lambda)}{8 \cdot p \cdot B_{cr}}, \qquad (16)$$

where B_u is the average magnetic flux density on a pole at surface of magnets. Axial height of magnets L_{PM} as function of maximal required magnetic flux density B_g is:

$$L_{PM} = \frac{K_f \cdot B_g}{B_r - \frac{1}{\beta_\alpha} \cdot B_u} \cdot (g + W_{cu}), \qquad (17)$$

where β_α is the relative opening angle of the magnet with respect to the pole pitch; K_f is the ratio of the mean value of the air gap magnetic flux density under a pole B_u to its maximum value B_g [19], and must be determined by three-dimensional finite elements in the axial flux machine.

The form factor of an axial flux machine, whose expression [20]:

$$K_L = \frac{1}{\left[\begin{array}{l} \frac{\pi \cdot (1+\lambda)}{4 \cdot p}\left(\frac{K_f \cdot B_g}{B_{cs}} + \frac{B_u}{B_{cs}}\right) + \\ + \frac{1}{D_0}(2 \cdot W_{cu} + 2 \cdot g)\left(1 + \frac{K_f \cdot B_g}{B_r - \frac{1}{\beta_\alpha} \cdot B_u}\right) \end{array}\right]}. \qquad (18)$$

C. 3D finite element modeling. The complexity of AFPM on surfaces with a single stator double rotor structure requires 3D finite element numerical analysis. In general, finite element modelling and simulation are used to take into account non-linear and three-dimensional aspects of electrical machines [21]. However, this type of simulation is becoming increasingly common in industry. Figure 5 shows the assembled machine using Ansys Maxwell 3D 16.0 Software (the machine design has been modelled here). Meshing is an important step in numerical modeling [22]. Improper meshing can lead to incorrect results. It is therefore important to develop a mesh in combination between smoothness and computation time. This machine was initially designed to meet the conditions for integration in the wheels of electric cars.

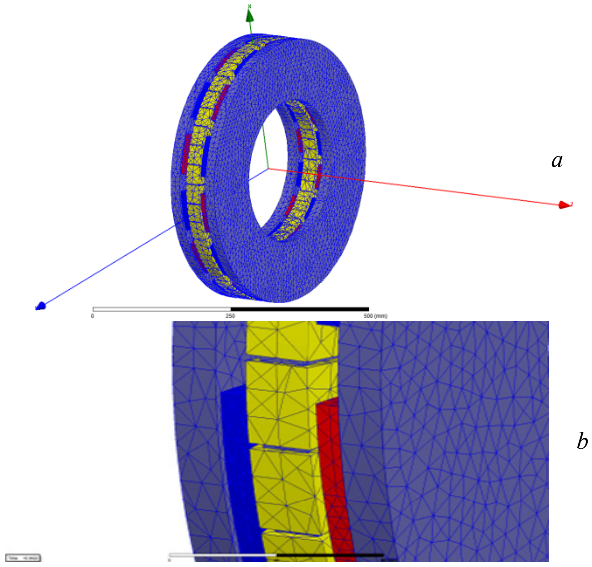

Fig. 5. Illustration and mesh of a double rotor axial magnet machine with internal stators TORUS-NS:
a – general geometry of machine; *b* – part of machine

The geometrical and electrical parameters are detailed in Table 1.

Table 1
Geometrical and electrical parameters of the TORUS-NS AFPM

Parameter	Value
Main voltage V_L, V	219.05
Phase voltage V_P, V	126.47
Number of pole pair p	14
Electrical loading A, A/m	10500
Current density J, A/mm^2	7.8
Air-gap flux density B_g, T	0.74
Diameter ratio λ	0.5745
Electrical power wave factor K_p	0.777
Current wave form factor K_i	0.134
EMF factor K_e	Π
Copper fill factor K_{Cu}	0.33
Residual magnetic flux density of PM material B_r, T	1.17
Leakage flux factor K_d	0.533
Specific magnetic loading B_u, T	1.125
Outside diameter D_o, mm	470
Internal diameter D_i, mm	270
Average diameter D_g, mm	370
Air-gap length g, mm	1.5
Flux density in the stator core B_{cs}, T	1.245
Axial span of the stator core L_{cs}, mm	20
Winding width at internal thickness W_{cui}, mm	5.5
Winding width at external diameter W_{cuo}, mm	3.2
Interior diameter along side width W_{cu}, mm	4.3
Stator core length L_s, mm	28.8
Rotor core length L_{cr}, mm	20
Magnet thickness-to-pole field ratio α_i	0.72
Average diameter magnet breadth WP_{Mg}, mm	29.9
Axial length of the rotor L_r, mm	32.7
Axial length of the machine L_e, mm	97
Number of winding turns per phase N_t	160
Phase current rms value I_{ef}, A	12.71
Axial thickness of the winding l_w, mm	4.4
Cross-section area of wire S_w, mm^2	0.396
Wire conductor diameter d_w, mm	0.71
Effective axial length of machine L_i, mm	100
Average length of the armature turn L_{1av}, mm	257.6
Nominal power P_R, W	5000
Number of phase m	3
DC voltage V_{DC}, V	210
Frequency f, Hz	46.67
Nominal speed, rpm	200
Connection	Y

Figure 6 in 3D model shows the distribution of magnetic flux density ***B*** of yoke vector distribution. In magnetic analysis, the motor is simulated at a certain time to obtain the magnetic field distribution. In this way, it is possible to check whether the design geometry is correct, by observing flux density distribution in air gap, in which central radius is obtained.

The results are shown in Fig. 7, 8.

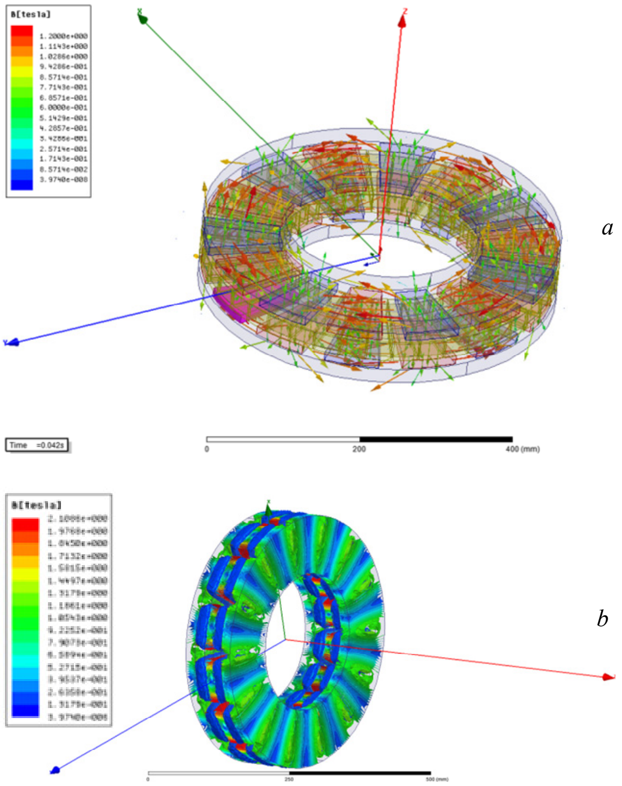

Fig. 6. *a* – magnetic field strength with vectors;
b – magnetic flux density distribution in the motor

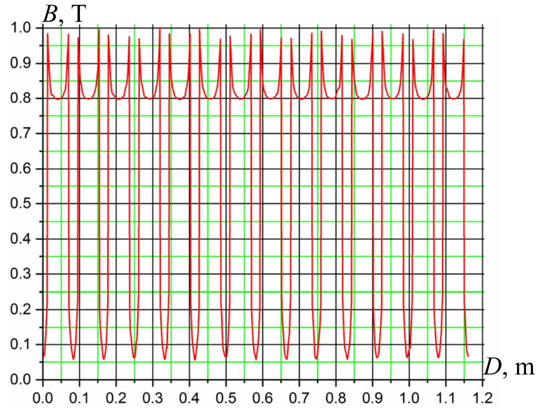

Fig. 7. Air gap flux density magnetic distribution for average radius (average diameter $D_g = (D_i + D_o)/2$)

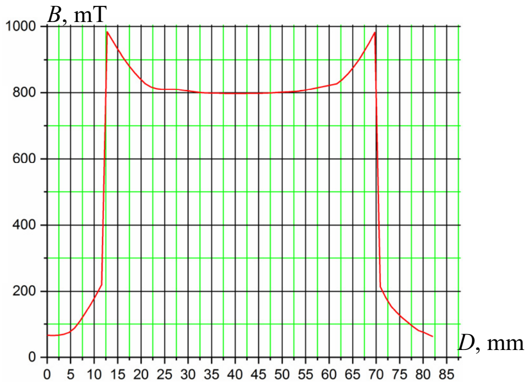

Fig. 8. TORUS-NS air gap flux densityunder one pole

The expositions of the stator core and rotor to time-varying flux densities were studied. The results are illustrated in Fig. 9, 10.

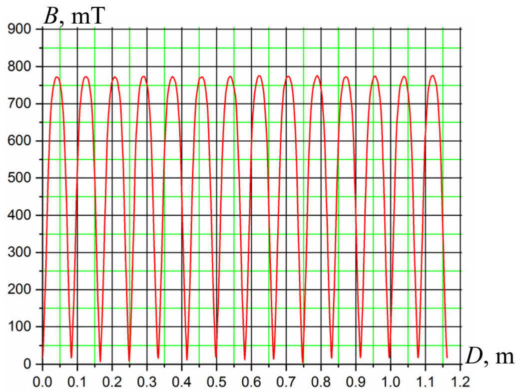

Fig. 9. Stator yoke flux density magnetic distribution for average radius

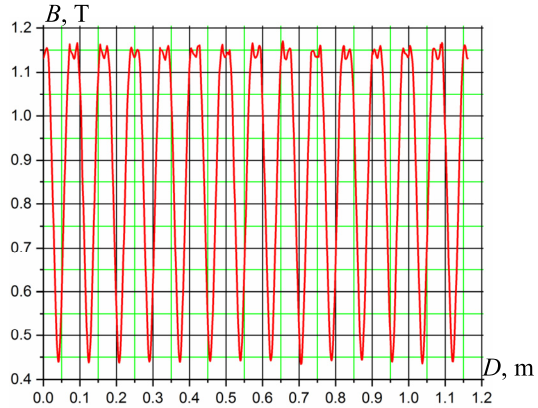

Fig. 10. Rotor yoke flux density magnetic distribution for average radius

4. Conclusions. The current global context has prompted car manufacturers to electrify their vehicles. In order to reduce the cost, which is still high, various technical solutions need to be implemented in these types of vehicles to reduce the cost of the power-train/electric transmission components, particularly the electric machines.The main objective of this article is to study an electric machine that can satisfy severe constraints in terms of performance and size for an application in a direct drive system for electric vehicles.

It is important to achieve optimum performance: high torque density with maximum efficiency over a wide speed range, which would impact the use of analytical models based on the sizing equationsin order to identify the best geometry of the machines application. Therefore, at the end of this study, axial flux machine with non-slotted TORUS-NS rotor type was selected due to its advantages. The numerical results using finite elements have given satisfied resukts to evaluate the potential of this machine.

For further study this machine, three-dimensional features are considered using the Maxwell Ansys finite element model. The results concerning the magnetic flux density in the air gap, obviousmy shown that it is necessary to improve the overall operation: in the end wheel motors begin to make their way to the automobile.

The effect of buried permanent magnet axially in the rotor has been planned as a perspective task and radial split of each permanent magnet into small pieces.

Conflict of interest. The authors declare that they have no conflicts of interest.

REFERENCES

1. Lasocki J., Krawczyk P., Kopczyński A., Roszczyk P., Hajduga A. Analysis of the strategies for managing extended-range electric vehicle powertrain in the urban driving cycle. *Electrical Engineering & Electromechanics*, 2022, no. 1, pp. 70-76. doi: https://doi.org/10.20998/2074-272X.2022.1.10.

2. Caricchi F., Crescimbini F., Mezzetti F., Santini E. Multi-stage axial-flux PM machine for wheel direct drive. *IAS '95. Conference Record of the 1995 IEEE Industry Applications Conference Thirtieth IAS Annual Meeting*, 1995, vol. 1, pp. 679-684. doi: https://doi.org/10.1109/IAS.1995.530365.

3. Vun S.T., McCulloch M.D. Optimal Design Method for Large-Scale YASA Machines. *IEEE Transactions on Energy Conversion*, 2015, vol. 30, no. 3, pp. 900-907. doi: https://doi.org/10.1109/TEC.2015.2397342.

4. Fan J., Lee Y. Sensorless control of switched reluctance motor based on a simple flux linkage model. *Electrical Engineering & Electromechanics*, 2023, no. 3, pp. 36-39. doi: https://doi.org/10.20998/2074-272X.2023.3.05.

5. Si J., Zhang T., Hu Y., Gan C., Li Y. An Axial-Flux Dual-Rotor Slotless Permanent Magnet Motor With Novel Equidirectional Toroidal Winding. *IEEE Transactions on Energy Conversion*, 2022, vol. 37, no. 3, pp. 1752-1763. doi: https://doi.org/10.1109/TEC.2021.3138465.

6. Patel A.N. Slot opening displacement technique for cogging torque reduction of axial flux brushless DC motor for electric two-wheeler application. *Electrical Engineering & Electromechanics*, 2023, no. 2, pp. 7-13. doi: https://doi.org/10.20998/2074-272X.2023.2.02.

7. Jacekf G., Rong W., Maarten K. *Axial Flux Permanent Magnet Brushless Machines. 2nd Ed.* Springer, 2008.

8. Caricchi F., Crescimbini F., Honorati O. Low-cost compact permanent magnet machine for adjustable-speed pump application. *IEEE Transactions on Industry Applications*, 1998, vol. 34, no. 1, pp. 109-116. doi: https://doi.org/10.1109/28.658730.

9. Gonzalez-Lopez D.A., Tapia J.A., Wallace R., Valenzuela A. Design and Test of an Axial Flux Permanent-Magnet Machine With Field Control Capability. *IEEE Transactions on Magnetics*, 2008, vol. 44, no. 9, pp. 2168-2173. doi: https://doi.org/10.1109/TMAG.2008.2000543.

10. Abu Ibaid O.Z.I., Belhamdi S., Abid M., Chakroune S., Mouassa S., Al-Sagar Z.S. Wavelet packet analysis for rotor bar breakage in an inverter induction motor. *Electrical Engineering & Electromechanics*, 2023, no. 3, pp. 3-11. doi: https://doi.org/10.20998/2074-272X.2023.3.01.

11. Profumo F., Zheng Zhang, Tenconi A. Axial flux machines drives: a new viable solution for electric cars. *IEEE Transactions on Industrial Electronics*, 1997, vol. 44, no. 1, pp. 39-45. doi: https://doi.org/10.1109/41.557497.

12. Liu C.-T., Lee S.-C. Magnetic field modeling and optimal operational control of a single-side axial-flux permanent magnet motor with center poles. *Journal of Magnetism and Magnetic Materials*, 2006, vol. 304, no. 1, pp. e454-e456. doi: https://doi.org/10.1016/j.jmmm.2006.02.065.

13. Gholamian S.A., Ardebil M., Abbaszadeh K., Mahmodi Charati S. Optimum Design of 1 kW Axial Flux Permanent Magnet Slotted TORUS Motor. *European Journal of Scientific Research*, 2008, vol. 21, no. 3, pp. 488-499.

14. Dlala E. Comparison of Models for Estimating Magnetic Core Losses in Electrical Machines Using the Finite-Element Method. *IEEE Transactions on Magnetics*, 2009, vol. 45, no. 2, pp. 716-725. doi: https://doi.org/10.1109/TMAG.2008.2009878.

15. Gholamian S.A., Ardebili M., Abbaszadeh K. Analytic and FEM evaluation of power density for various types of double-sided axial flux slotted PM motors. *International Journal of Applied Engineering Research (IJAER)*, 2008, vol. 3, no. 7, pp. 927-939.

16. Aydin M., Huang S., Lipo T.A. Optimum design and 3D finite element analysis of nonslotted and slotted internal rotor type axial flux PM disc machines. *2001 Power Engineering Society Summer Meeting. Conference Proceedings (Cat. No.01CH37262)*, 2001, vol. 3, pp. 1409-1416. doi: https://doi.org/10.1109/PESS.2001.970283.

17. Huang Y., Zhu J., Guo Y., Hu Q. Development of a High-Speed Claw Pole Motor with Soft Magnetic Composite Core. *2007 IEEE International Electric Machines & Drives Conference*, 2007, pp. 1564-1568. doi: https://doi.org/10.1109/IEMDC.2007.383661.

18. Surong Huang, Jian Luo, Leonardi F., Lipo T.A. A comparison of power density for axial flux machines based on general purpose sizing equations. *IEEE Transactions on Energy Conversion*, 1999, vol. 14, no. 2, pp. 185-192. doi: https://doi.org/10.1109/60.766982.

19. Jiang C., Qiao M., Zhu P., Zheng Q. Design and Verification of High Speed Permanent Magnet Synchronous Motor for Electric Car. *2018 2nd IEEE Advanced Information Management,Communicates,Electronic and Automation Control Conference (IMCEC)*, 2018, pp. 2371-2375. doi: https://doi.org/10.1109/IMCEC.2018.8469398.

20. Aydin M., Huang S., Lipo T.A. Axial flux permanent magnet disc machines: A review. *Conf. Record of SPEEDAM*, 2004, vol. 8, pp. 61-71.

21. Yatchev I., Balabozov I., Hinov K., Hadzhiev I., Gueorgiev V. Influence of the shape of the input pulses on the characteristics of hybrid electromagnetic system with magnetic flux modulation. *Electrical Engineering & Electromechanics*, 2021, no. 3, pp. 3-7. doi: https://doi.org/10.20998/2074-272X.2021.3.01.

22. Belkacem L., Mustapha H., Katia K., Ahmed G. Design and Investigation of Axial Flux Permanent Magnet Synchronous Machine for electric vehicles. *2018 International Conference on Communications and Electrical Engineering (ICCEE)*, 2018, pp. 1-6. doi: https://doi.org/10.1109/CCEE.2018.8634529.

Received 04.03.2023
Accepted 10.07.2023
Published 02.11.2023

Belkacem Larbi $^{1, 2}$*, PhD,*
Mustapha Hatti ^{3}*, Professor,*
Katia Kouzi ^{2}*, Doctor,*
Ahmed Ghadbane ^{1}*, Doctor,*
^{1} Nuclear Research Center of Birnie,
p.o. box 180 Ain Oussera, Algeria,
e-mail: l.belkacem.eln@lagh-univ.dz (Corresponding Author);
ghadbane_ahmed12@yahoo.com
^{2} University Amar Telidji, Laghouat, Algeria,
e-mail: k.kouzi@lagh-univ.dz
^{3} Solar Equipments Development Unit, UDES/CDER,
B.P. 386, 42004, Bou Ismail, Tipasa, Algeria,
e-mail: musthatti@ieee.org

How to cite this article:
Larbi B., Hatti M., Kouzi K., Ghadbane A. Axial flux machine with non-slotted torus-ns rotor type. Design and investigate for electric traction. *Electrical Engineering & Electromechanics*, 2023, no. 6, pp. 10-15. doi: https://doi.org/10.20998/2074-272X.2023.6.02

UDC 621.313 https://doi.org/10.20998/2074-272X.2023.6.03

A.N. Patel, P.J. Doshi, S.C. Mahagaokar, T.H. Panchal

Optimization of cogging torque in interior permanent magnet synchronous motor using optimum magnet v-angle

Introduction. *At present, the most important requirement in the field of electrical engineering is the better utilization of electrical power, due to its increasing demand and not-so-increasing availability. A permanent magnet synchronous motor (PMSM) is increasingly gaining popularity in various household and industrial applications because of its superior performance compared to conventional electrical motors.* ***Purpose.*** *PMSM is designed based on the selection of various design variables and optimized to fulfill the same. Being superiorly advantageous over other motors, PMSM has the major disadvantage of higher cogging torque. Higher cogging torque generates torque ripple in the PMSM motor leading to various problems like vibration, rotor stress, and noisy operation during starting and steady state. The designer should aim to reduce the cogging torque at the design stage itself for overall better performance.* ***Methods.*** *An interior rotor v-shaped web-type PMSM is designed and its performance analysis is carried out using finite element analysis (FEA). Magnet v-angle is optimized with the objective of cogging torque reduction. Performance comparison is carried out between the optimized motor and the initially designed motor with FEA.* ***Novelty.*** *Magnet v-angle analysis is performed on the same keeping all other parameters constant, to obtain minimum cogging torque. The proposed method is practically viable as it does not incur extra costs and manufacturing complexity.* ***Practical value.*** *It is observed that the magnet v-angle is an effective technique in the reduction of cogging torque. Cogging torque is reduced from 0.554 N·m to 0.452 N·m with the application of the magnet v-angle optimization technique.* References 19, tables 2, figures 10.

Key words: **cogging torque, finite element analysis, interior v-shape web, magnet spread angle, magnet v-angle, permanent magnet synchronous motor.**

Вступ. *В даний час найважливішою вимогою в галузі електротехніки є найкраще використання електроенергії через зростаючу потребу в ній і не настільки зростаючу доступність. Синхронний двигун з постійними магнітами (СДПМ) набуває все більшої популярності в різних побутових та промислових застосуваннях завдяки своїм чудовим характеристикам у порівнянні зі звичайними електродвигунами.* ***Мета***. *СДПМ, спроєктований на основі вибору різних конструктивних змінних та оптимізований для їх виконання. Будучи чудовим у порівнянні з іншими двигунами, СДПМ має головний недолік: вищий крутний момент. Вищий крутний момент викликає пульсації крутного моменту в двигуні з постійними магнітами, що призводить до різних проблем, таких як вібрація, напруга ротора і шумна робота під час запуску і режиму. Проєктувальник повинен прагнути зменшити крутний момент зубчастого колеса на стадії проєктування для підвищення загальної продуктивності.* ***Методи***. *Розроблено СДПМ з внутрішнім ротором v-подібної форми та стрижневого типу, та аналіз його характеристик виконаний з використанням аналізу методом скінченних елементів (FEA). Кут v-подібного магніту оптимізовано з метою зниження зубчастого моменту. Порівняння продуктивності здійснюється між оптимізованим двигуном та двигуном, спочатку спроєктованим за допомогою FEA.* ***Новизна***. *Аналіз кута v-подібного магніту виконується таким же чином, зберігаючи решту всіх параметрів постійними, щоб отримати мінімальний зубчастий крутний момент. Запропонований спосіб практично життєздатний, оскільки не вимагає додаткових витрат та складності виготовлення.* ***Практична цінність***. *Помічено, що v-подібний кут магніту є ефективним способом зниження зубчастого моменту. Зубчастий крутний момент зменшений з 0,554 Н·м до 0,452 Н·м за рахунок застосування методу оптимізації v-подібного кута магніту.* Бібл. 19, табл. 2, рис. 10.

Ключові слова: **крутний момент зубчатої передачі, аналіз методом скінченних елементів, внутрішнє v-подібне полотно, кут розкриття магніту, v-подібний кут магніту, синхронний двигун із постійними магнітами.**

1. Introduction. The permanent magnet synchronous motor (PMSM) is increasingly gaining popularity in recent times because of its stellar performance with its smaller size. The moment of inertia and the dynamic response time is reduced due to its lesser size. It also turns out to be beneficial when there are spatial limitations. Its initial cost is higher compared to the induction motor, but thanks to its superior performance, its extra cost is paid back within just some time. It was developed keeping in view the elimination of synchronous machine exciters, which eventually decreases field winding losses and enhances performance and thermal conditions [1, 2]. Based on the magnet location, the two most common rotor configurations available for PMSM are surface permanent magnet (SPM) and interior permanent magnet (IPM). Among both of these, IPM beats SPM in terms of advantages. Because of the interior configuration of the magnets, they can be easily mounted in grooves, without the use of any binding material, which simplifies the manufacturing process and increases stability. As the magnets are not close to the air gap, the possibilities for demagnetization are also minimized. The increased saliency ratio also adds to the reluctance torque, which further enhances the average torque [3].

However, the concern with this motor is the cogging torque. It is an undesirable phenomenon. Cogging torque is inherent in permanent magnet motors due to the presence of a permanent magnet and slotted stator. Cogging torque is the result of the interaction of magnetomotive force harmonics and air gap permeance harmonics. It degrades the motor performance and adds instability to the shaft movement, rendering the motion shaky. So, this unnecessary torque has to be reduced in torque-sensitive applications like traction, robotics, etc. The cogging torque can be minimized by choosing the appropriate magnet length. The equation involving optimum magnet length and slot pitch is given. By shifting the pole pairs, and creating an asymmetric distribution of the magnet pole, further reduction is also possible [4]. The same equation is improved, taking into account, the effects of the rotor curvature [5]. But the approach involves changes in the design of the rotor. The probability of asymmetry in flux distribution also exists. Another solution is to reduce the cogging torque by determining the optimal ratio of pole arc to pole pitch using no. of slots, no. of poles, and the goodness factor [6]. Simulations as well as experimental methods were used to validate the approach [7]. A novel approach consisting of torque ripple modeling and its use of the genetic algorithm to minimize cogging torque is also presented [8]. The parameters needed as well as the calculations performed are more in this method. It's quite time-consuming. It also does not provide an angular spread of the magnets relative to the center of the rotor. Thus, magnet placement in an interior-type rotor has not yet been specified. The cogging torque can be minimized using skewing techniques. Recent developments also suggest step skewing of the rotor in which the rotor is axially skewed [3, 9]. V-shape skewing is also implemented in which, the skew is added in a v-shape to the axial rotor length [10]. But these are very complicated, exhaustive, and time-consuming approaches. Various rotor skewing techniques are compared for the generation of cogging torque, excitation torque ripple, average torque, and axial force [11]. The opening width of the slot and the shape of the magnet edge can also have an impact on the cogging torque [12].

Various types of rotor geometries are used for the flux barrier synchronous reluctance motor. The equation is given for the determination of the angular spread of flux barriers. It can also be used in the case of v-shape web type PMSM, as the magnet spread, because the principle behind the equation is the reduction of torque ripple by employing uniformity of reluctance only [13]. An approach to minimizing cogging torque using flux barriers is also presented [14]. The design of concentrated wound interior permanent magnet synchronous motor (IPMSM) with symmetrically positioned flux barriers to address smaller sensorless operating regions and significant torque ripples is proposed [15]. The Machaon structure having flux barriers, ending at some specific angles is also introduced, which can improve the cogging torque profile. The Taguchi method has been employed for shape design optimization [16]. The axial pole shaping of IPM machines to reduce the cogging torque as well as to obtain uniform distribution of flux density all over the surface is presented [17]. A hybrid rotor design, consisting of both circumferential as well as radial magnets, and having consequent rotor poles are also introduced to achieve an optimum synchronous performance of the motor [18]. But, the difficulties and expenses of manufacturing such kinds of rotors are very significant. Keeping uniformity and symmetry needs to be utmost considered.

So, in all the previous developments, it is either time-consuming and involves indirect calculations (in the case of the equation for optimum magnet length or optimum pole arc to pole pitch ratio or genetic algorithm using torque ripple modeling) or complicated and involves constructional changes (in the case of skewing), or affected by complexity and expenditure (in the case of axial pole shaping or step skewing). The v-angle is one of the major factors that influence the performance of IPMSM. The v-angle variation technique is straightforward, practically implantable hence suitable for the mass production of IPMSM. The proposed technique is more viable where cogging torque has relatively less effect on vibration and losses. Therefore, an approach is presented here, to find out the optimum magnet placement for cogging torque minimization.

The advantages of a PMSM are explained in section 1. The harmful impact of cogging torque and the limitations of its reduction techniques invented to date are also mentioned. Section 2 focuses on designing a PMSM. In section 3, the finite element analysis (FEA) of the same is carried out and different performance characteristics such as cogging torque profile and torque-angle profile are analyzed. In section 4, the optimization of the designed motor is carried out for the magnet v-angle. The plot of the variation of cogging torque with respect to the magnet v-angle is also analyzed. From the attained results, the optimum magnet v-angle is found. The cogging torque, average torque, back electromotive force (EMF) spectrum, back EMF profile, and flux density plot are compared for both initial as well as the optimized model and the discussion of the same is carried out in section 5. In section 6, the conclusion from the exercise is drawn.

2. Design of PMSM. Owing to the many advantages of IPM over SPM, as evident from Section 1, IPM is selected for research purposes. Figure 1 shows the illustrative figure of the same which can help to understand terminology better. Figure 2 is the magnified view of the same.

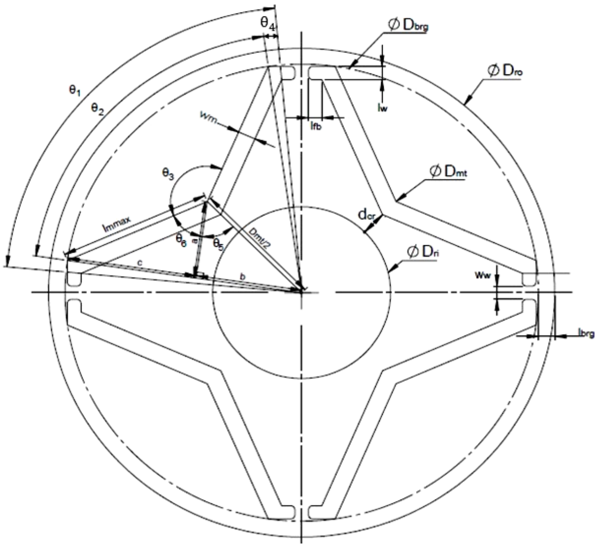

Fig. 1. Illustrative figure of interior v-shaped web type PMSM

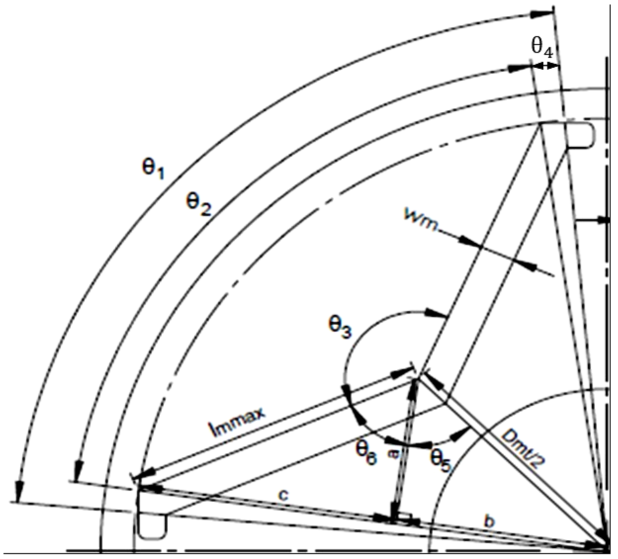

Fig. 2. Magnified view of Fig. 1

There are two magnet angles in the design of IPMSM. The first one is the magnet spread angle. This is known as the angular spread of a magnet pole in relation to the center of the rotor. This angle is shown as θ_1 in Fig. 1, 2. The other one is magnet v-angle, which is defined as the angular spread of a magnet pole in relation to the pole center. This angle is shown as θ_3 in Fig. 1, 2. Magnet spread angle at the magnet top is θ_2 and the offset angle due to magnet thickness is θ_4 as shown in Fig. 1, 2.

PMSM of rating 4 kW, 415 V, 3-phase, and 50 Hz is designed. Necessary assumptions for specific magnetic loading, specific electric loading, number of poles, number of stator slots, aspect ratio, conductor packing factor, current density, tooth flux density, etc. are made. The design outcomes of this design are shown in Table 1.

Table 1
Design outcomes

Parameter	Value
Stator outer diameter D_o, mm	175
Stator inner diameter D, mm	120
Rotor outer diameter D_{ro}, mm	118
Core length L, mm	150
No. of stator slots S_S	36
Magnet width W_m, mm	5
Slot pitch λ, mm	10.46
Magnet spread angle θ_1	72°
Magnet v-angle θ_3	125°
Magnet length $l_{m\max}$, mm	33
Air gap thickness l_g, mm	0.5
Permanent magnet material	N38SH
Core material	M530-50A

3. FEA of the designed machine. The FEA of the designed machine is carried out using commercially available FEA software for design validation. Performance characteristics exhibited by this machine are observed, such as the cogging torque profile and torque-angle profile.

A two-dimensional (2D) finite element model of the designed machine is shown in Fig. 3.

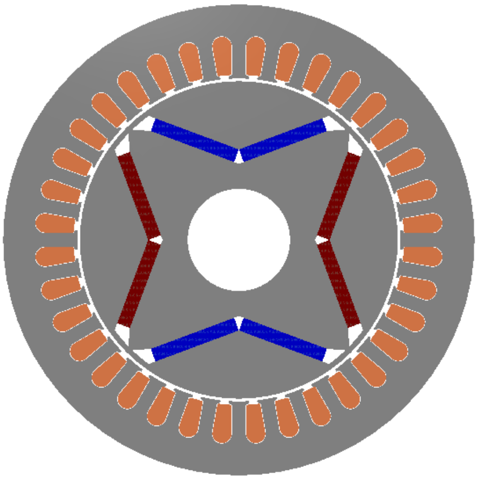

Fig. 3. 2D finite element model of the designed IPMSM

The dimensions to create this model are as per the analytical design. Each pole of the v-shape IPMSM consists of two magnet segments, to make v-shape poles. For different parts of the motor, appropriate materials are used. Figure 4 reveals that the peak cogging torque is 0.554 N·m. The cogging torque profile can be shown for one slot pitch only because of its repetitive nature for each slot pitch. Figure 5 dictates the variation of torque with respect to angular rotation. The maximum and minimum values are 36.1 N·m and 22.3 N·m respectively.

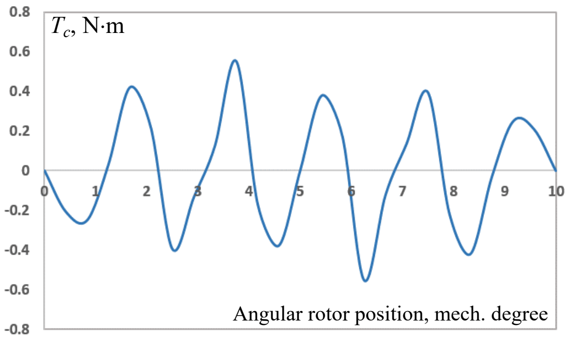

Fig. 4. Cogging torque profile

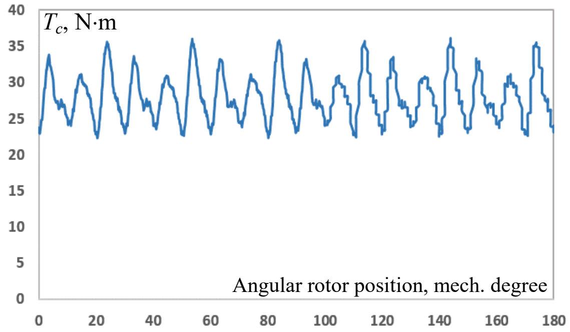

Fig. 5. Torque-angle profile

4. Optimization of the designed machine. As described earlier, cogging torque is an unwanted phenomenon. Therefore, it is necessary to reduce this torque. There is some specific relationship between cogging torque and reluctance variations. When the reluctance variation with respect to angular displacement increases, the cogging torque also increases. An equation is stated in [19], which describes this relationship as:

$$T_c = -\frac{1}{2} \cdot \Phi_g^2 \cdot \frac{\mathrm{d}R}{\mathrm{d}\theta}, \tag{1}$$

where T_c is the cogging torque; Φ_g is the air-gap flux; R is the reluctance of air-gap; θ is the angular displacement of the rotor.

As per the equation, the cogging torque can be reduced if the reluctance is made as uniformly as possible. This torque is the result of harmonic components present in the torque harmonic spectrum. So, it can also be represented in the Fourier series form, as mentioned in [8]:

$$T_c = \sum_{k=1}^{\infty} T_{ck} \cdot \sin\left(k \cdot \theta + \phi_k^c\right), \tag{2}$$

where T_{ck} is the magnitude of k^{th} cogging torque harmonic; k is the integer; ϕ_k^c is the phase angle of k^{th} cogging torque harmonic.

In this section, the cogging torque is optimized. The effort is made to achieve minimum cogging torque using magnet v-angle optimization. The magnet v-angle is changed and its effects on cogging torque are observed. During this entire optimization process, magnet volume, magnet length, magnet width, magnet spread angle, winding design, and slot dimensions have been kept constant.

Magnet v-angle is varied from 121° to 149°, above and below which the design fails to keep magnet dimensions constant due to geometrical constraints. During the entire process, the magnet spread angle is kept constant at the initial value of 72°. To achieve this, the magnet v-angle is increased by pushing the magnet segments away from the shaft. The geometrical constraint is that the original magnet length has to be retained while pushing it upwards. This becomes necessary as, when the magnets are pushed upwards, the maximum allowed length ($l_{m\max}$ in Fig. 2), which the geometry can afford, reduces. At one point, it reaches the boundary, and further increment of magnet v-angle becomes impossible. The results of this analysis are shown in Fig. 6.

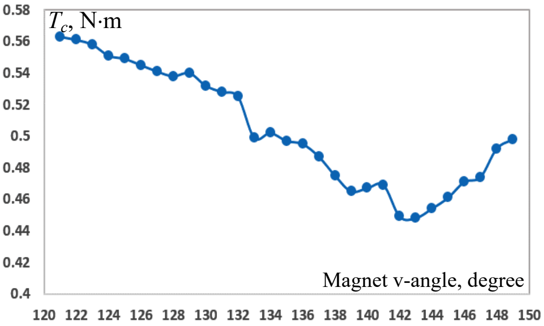

Fig. 6. Cogging torque vs. magnet v-angle

The figure dictates that the cogging torque reduces from 121° to 143° and then starts increasing. At 143°, the cogging torque is minimum. On both sides of 143°, it is increasing. So, this angle can be said as the optimum magnet v- angle for this design.

5. Result table and observations. FEA is carried out to obtain the peak cogging torque of the initial design and optimized design. The cogging torque period obtained for the designed 4 kW IPMSM is 10° mechanical. Cogging torque waveform period can be calculated as:

$$\theta_{cog-period} = \frac{360°}{LCM\left(N_p, N_s\right)}, \tag{3}$$

where N_p is the number of poles; N_s is the number of stator slots; LCM is the least common multiplier.

Figure 7 shows the comparison of cogging torque profile for both, the initial as well as the optimized models. The peak cogging torque reduces from 0.554 Nm to 0.452 N·m.

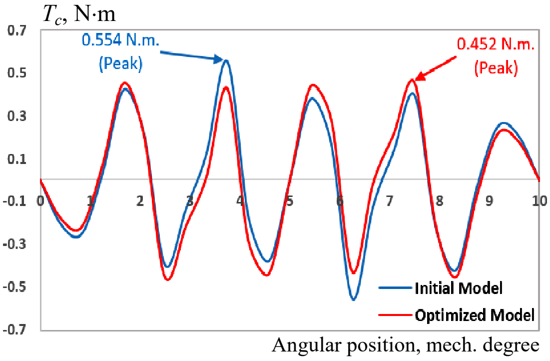

Fig. 7. Cogging torque profile of initial and optimized model

The performance comparison of the initial design and the optimized design is shown in Table 2.

Table 2

Comparison of initial and optimized design

Design	Cogging torque, N·m	Average torque, N·m
Initial	0.554	28
Optimized	0.452	28.2
Change, %	–18.41	0.71

Compared to the initial design, the optimized model shows an 18.41 % reduction in cogging torque and a 0.71 % increase in average torque. The back EMF profile comparison for the initial model, optimized model, and model having skewing of rotor poles is shown in Fig. 8.

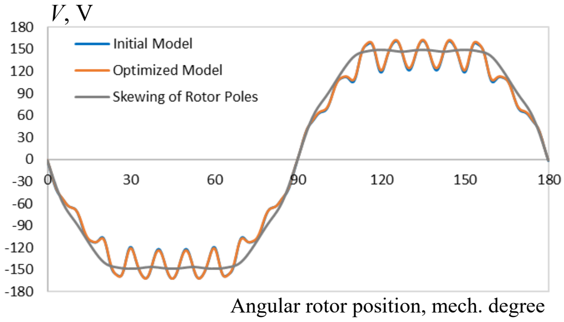

Fig. 8. Comparison of back EMF profiles of different models

It is evident from the same that there isn't much difference in the back EMF profile of the initial and optimized models. Both are looking almost similar to each other. It is analyzed that the back EMF profile obtained with a skewed rotor is smooth without any dips. Skewing is a known method to reduce cogging torque. However, there are some well-known disadvantages of skewing as well. For instance, the skewing of rotor magnets results in more axial thrust, more flux leakage, and a low winding factor. The skewed rotor of PM machines normally requires a magnet with a specific shape which complicates the design and increases the manufacturing difficulty as well as the cost. Skewing makes the rotor mechanically weak also. Skewing imposes limitations in mass production due to low manufacturability.

Figure 9 shows the comparison of the back EMF harmonics spectrum. Again, there isn't any appreciable change in the spectrum. The fundamental component of the back EMF is increased by 1 V. This slight increment has contributed to the minor increment of average torque achievable from the design. It is observed that after optimization, the even-order harmonics are eliminated and the other odd-order harmonics are decreased. The total harmonic distortions (THD) of the back EMF spectrum are also reduced slightly from 5.13 % to 5.04 % due to this spectrum improvement.

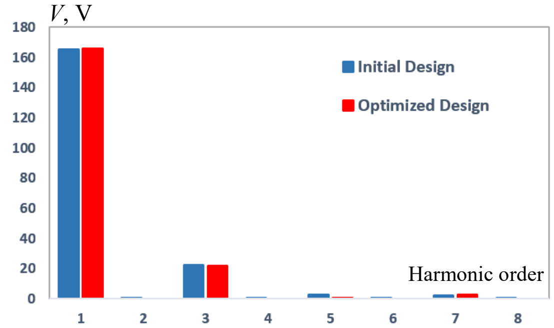

Fig. 9. Back EMF harmonic spectrum of the initial and optimized model

Figure 10 shows the flux density plot of both, the initial as well as the optimized models. In both cases, flux density at all parts is the same as that of the analytical design.

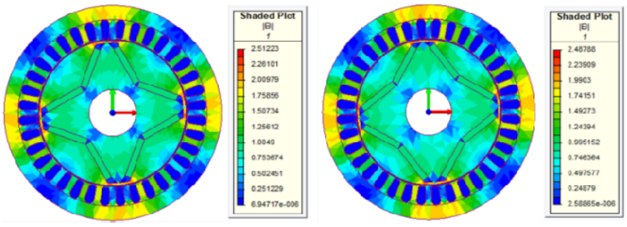

a *b*

Fig. 10. Flux density plot of initial model (*a*) and optimized model (*b*)

From all these observations it can be said that the magnet v-angle has a major impact on cogging torque of the PMSM. It also has some minor impact on average torque, back EMF spectrum, and THD. Only by changing the placement of the magnet, cogging torque can be reduced. There is no need to change any other parameters or any other structural modifications required, which makes this technique practically viable and implementable, as it will not increase the complexity or initial cost of the motor. This is the novelty of the proposed methodology.

The reason behind this behavior can be stated as the uniformity of reluctance, at all times. As it is well-known, the cogging torque is the outcome of non-uniform reluctance distribution offered to magnet flux. But if we place the magnet such that, it faces nearly equal reluctance at all times, during the rotor rotation, it will face minimum reluctance, eventually resulting in minimum cogging torque.

6. Conclusions. The design of a permanent magnet synchronous motor and its finite element analysis is conducted for performance analysis. This initial design is considered a reference for further comparative performance analysis. Design optimization is performed with the objective of cogging torque minimization by optimization of magnet v-angle, and keeping all other dimensions constant. From the results obtained, it is analyzed that the magnet v-angle has a major impact on cogging torque. The cogging torque is reduced up to 18.41 % compared to the reference design. In addition to that, the average torque is increased by 0.71 % and the total harmonic distortions of back electromotive force reduces from 5.13 % to 5.04 % by application of magnet v-angle optimization.

Conflict of interest. The authors declare that they have no conflicts of interest.

REFERENCES

1. Pillay P., Krishnan R. Application characteristics of permanent magnet synchronous and brushless DC motors for servo drives. *IEEE Transactions on Industry Applications*, 1991, vol. 27, no. 5, pp. 986-996. doi: https://doi.org/10.1109/28.90357.

2. Panchal T.H., Patel A.N., Patel R.M. Reduction of cogging torque of radial flux permanent magnet brushless DC motor by magnet shifting technique. *Electrical Engineering & Electromechanics*, 2022, no. 3, pp. 15-20. doi: https://doi.org/10.20998/2074-272X.2022.3.03.

3. Ge X., Zhu Z.Q., Kemp G., Moule D., Williams C. Optimal Step-Skew Methods for Cogging Torque Reduction Accounting for Three-Dimensional Effect of Interior Permanent Magnet Machines. *IEEE Transactions on Energy Conversion*, 2017, vol. 32, no. 1, pp. 222-232. doi: https://doi.org/10.1109/TEC.2016.2620476.

4. Touzhu Li, Slemon G. Reduction of cogging torque in permanent magnet motors. *IEEE Transactions on Magnetics*, 1988, vol. 24, no. 6, pp. 2901-2903. doi: https://doi.org/10.1109/20.92282.

5. Ishikawa T., Slemon G.R. A method of reducing ripple torque in permanent magnet motors without skewing. *IEEE Transactions on Magnetics*, 1993, vol. 29, no. 2, pp. 2028-2031. doi: https://doi.org/10.1109/20.250808.

6. Zhu Z.Q., Howe D. Influence of design parameters on cogging torque in permanent magnet machines. *IEEE Transactions on Energy Conversion*, 2000, vol. 15, no. 4, pp. 407-412. doi: https://doi.org/10.1109/60.900501.

7. Zhu Q., Ruangsinchaiwanich S., Schofield N., Howe D. Reduction of cogging torque in interior-magnet brushless machines. *IEEE Transactions on Magnetics*, 2003, vol. 39, no. 5, pp. 3238-3240. doi: https://doi.org/10.1109/TMAG.2003.816733.

8. Lai C., Feng G., Iyer K.L.V., Mukherjee K., Kar N.C. Genetic Algorithm-Based Current Optimization for Torque Ripple Reduction of Interior PMSMs. *IEEE Transactions on Industry Applications*, 2017, vol. 53, no. 5, pp. 4493-4503. doi: https://doi.org/10.1109/TIA.2017.2704063.

9. Luu P.T., Lee J.-Y., Hwang W., Woo B.-C. Cogging Torque Reduction Technique by Considering Step-Skew Rotor in Permanent Magnet Synchronous Motor. *2018 21st International Conference on Electrical Machines and Systems (ICEMS)*, 2018, pp. 219-223. doi: https://doi.org/10.23919/ICEMS.2018.8549086.

10. Park G.-J., Kim Y.-J., Jung S.-Y. Design of IPMSM Applying V-Shape Skew Considering Axial Force Distribution and Performance Characteristics According to the Rotating Direction. *IEEE Transactions on Applied Superconductivity*, 2016, vol. 26, no. 4, pp. 1-5. doi: https://doi.org/10.1109/TASC.2016.2543267.

11. Jiang J.W., Bilgin B., Yang Y., Sathyan A., Dadkhah H., Emadi A. Rotor skew pattern design and optimisation for cogging torque reduction. *IET Electrical Systems in Transportation*, 2016, vol. 6, no. 2, pp. 126-135. doi: https://doi.org/10.1049/iet-est.2015.0021.

12. Nur T., Mulyadi M. Improve cogging torque method in inset-permanent magnet synchronous machine. *2018 IEEE International Conference on Applied System Invention (ICASI)*, 2018, pp. 1211-1213. doi: https://doi.org/10.1109/ICASI.2018.8394506.

13. Jae Yoon Oh, Dal Ho Jung. *Flux Barrier Synchronous Reluctance Motor*. USA Patent no. 6239526B1, May 29, 2001.

14. Kawaguchi Y., Sato T., Miki I., Nakamura M. A reduction method of cogging torque for IPMSM. *2005 International Conference on Electrical Machines and Systems*, 2005, vol. 1, pp. 248-250. doi: https://doi.org/10.1109/ICEMS.2005.202522.

15. Kano Y. Sensorless-oriented design of IPMSM. *2014 International Power Electronics Conference (IPEC-Hiroshima 2014 - ECCE ASIA)*, 2014, pp. 2457-2464. doi: https://doi.org/10.1109/IPEC.2014.6869934.

16. Rahimi Monjezi S., Kiyoumarsi A., Mirzaeian Dehkordi B., Sabahi M.-F., Vafaie M.-H. Shape Design Optimization of Interior Permanent-Magnet Synchronous Motor with Machaon Flux Barriers for Reduction of Torque Pulsation. *Electric Power Components and Systems*, 2016, vol. 44, no. 19, pp. 2212-2223. doi: https://doi.org/10.1080/15325008.2016.1199611.

17. Du Z.S., Lipo T.A. Reducing Torque Ripple Using Axial Pole Shaping in Interior Permanent Magnet Machines. *IEEE Transactions on Industry Applications*, 2020, vol. 56, no. 1, pp. 148-157. doi: https://doi.org/10.1109/TIA.2019.2946237.

18. Ugale R.T., Chaudhari B.N., Baka S., Pramanik A. A Hybrid Interior Rotor High-performance Line Start Permanent Magnet Synchronous Motor. *Electric Power Components and Systems*, 2014, vol. 42, no. 9, pp. 901-913. doi: https://doi.org/10.1080/15325008.2014.903539.

19. Hanselman D.C. *Brushless Permanent Magnet Motor Design*. Magna Physics Publ., Ohio, 2006. 411 p.

Received 19.10.2022
Accepted 27.06.2023
Published 02.11.2023

A.N. Patel[1]*, PhD, Associate Professor,*
P.J. Doshi[2]*, Traction Control Software Engineer,*
S.C. Mahagoakar[3]*, R&D Group Manager,*
T.H. Panchal[1]*, PhD, Assistant Professor,*
[1] Department of Electrical Engineering, Institute of Technology, Nirma University, Ahmedabad, Gujarat, India,
e-mail: amit.patel@nirmauni.ac.in;
tejas.panchal@nirmauni.ac.in (Corresponding Author)
[2] Alstom Transport India Ltd., Bangalore, Karnataka, India,
e-mail: 18meep03@nirmauni.ac.in
[3] Rotomotive Powerdrive India Limited, Anand, Gujarat, India,
e-mail: s.mahagaokar@rotomotive.com

How to cite this article:
Patel A.N., Doshi P.J., Mahagaokar S.C., Panchal T.H. Optimization of cogging torque in interior permanent magnet synchronous motor using optimum magnet v-angle. *Electrical Engineering & Electromechanics*, 2023, no. 6, pp. 16-20. doi: https://doi.org/10.20998/2074-272X.2023.6.03

UDC 621.313.333 https://doi.org/10.20998/2074-272X.2023.6.04

V.V. Rymsha, I.N. Radimov, M.V. Gulyy, I.P. Babych, A.A. Kalinichenko, N.P. Demenko

Modeling and research of a magnetoelectric converter for hydro and pneumo actuators

Purpose. *Presentation of the results of modeling and practical implementation of a magnetoelectric converter for hydraulics and pneumatics systems of the aerospace industry.* ***Methodology.*** *Calculations of three-dimensional magnetic fields are carried out with the Finite Element Method by JMAG program. The solution of the differential equations connecting the input voltage, current, magnetic flux and torque is performed by numerical integration.* ***Results.*** *As a result of calculations, the converter configuration was obtained. Tests of the prototype model of the converter confirmed the principle workability of the adopted design and design solutions in its development.* ***Practical value.*** *Tests of the converter prototype sample confirmed the fundamental performance of the adopted design and constructive solutions.* References 9, tables 3, figures 14.

Key words: **magnetoelectric converter, three-dimensional magnetic field, mechanical characteristic, prototype sample.**

Наведено результати моделювання та практичної реалізації магнітоелектричного перетворювача для гідро- та пневмоприводів аерокосмічної галузі. На основі серії проектних розрахунків при різноманітній конфігурації магнітної системи перетворювача обрано варіант з чотирма зубцями на полюсі статору і отримані його основні характеристики. Результати розрахунків зіставлені з результатами експерименту на макетному зразку магнітоелектричного перетворювача. Бібл. 9, табл. 3, рис. 14.

Ключові слова: **магнітоелектричний перетворювач, тривимірне магнітне поле, механічна характеристика, макетний зразок.**

Introduction. In modern aircraft control systems, guidance and tracking systems, hydraulic and pneumatic drives are widely used, the component of which is a contactless magneto-electric converter (MEC) [1-3]. The MEC is designed to convert the input electrical signal (current) supplied to the control winding into a proportional angular displacement of the output shaft.

The first and currently the only theoretical work devoted to the development of MEC in Ukraine is the work [4]. Regarding the development of similar devices abroad, any information is missing or unavailable in open sources.

Currently, MECs for aviation and space technology are not produced in Ukraine. In this regard, the development and introduction into production of domestic MECs is urgent. This goal is solved within the framework of scientific and technical cooperation between State Design Office «Pivdenne» (Dnipro) and Ltd. «Electrical Engineering – New Technology» (Odesa).

According to the design of the magnetic system, MECs can be performed with electromagnetic excitation and excitation from permanent magnets. The MECs type MP-220B with permanent magnets of the UNDK brand became the most popular. The design of this MEC is based on the principle of a double polarized relay (Fig. 1) [5].

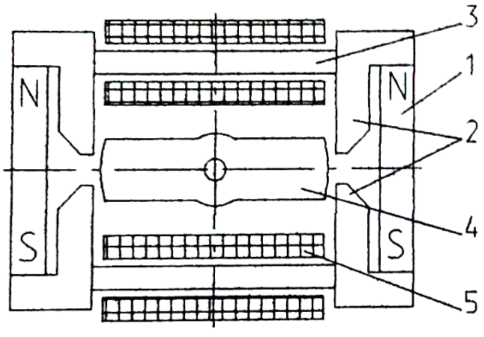

Fig. 1. MEC type MP-220B: 1 – permanent magnet; 2 – pole tips; 3 – core; 4 – armature; 5 – control winding

The design of this type ensures a stable neutral position, as well as the occurrence of a torque proportional to the angular deviation from the neutral position and directed in the direction opposite to this deviation (magnetic spring effect).

At the same time, MECs in this design have a number of disadvantages associated with the structural and technological difficulty of their manufacture [4].

The influence of the above-mentioned shortcomings can be eliminated by changing the topology of the MEC magnetic circuit from a rectangular to a concentric one, while preserving the principle of interaction of the excitation and control magnetic fluxes [4].

To solve this problem, it is proposed to implement the magnetic system of the MEC similar to the magnetic system of the hybrid stepper motor [4, 6, 7]. This implementation of the MEC magnetic system, in comparison with the MP-220B magnetic system, is characterized by a much better use of the volume of the active space, specific mass-dimensional indicators and adaptability to the use of rare earth magnets [4]. For the first time, the study of the MEC with such a topological structure of the magnetic system was carried out in [4] on the basis of magnetic substitute circuits, followed by the determination of magnetic conductivities by the modified method of probable paths of the magnetic flux. Without questioning the results obtained in [4], it should be noted that the method of probable magnetic flux paths has low accuracy and limitations in use [8]. Considering the fact that in the design of the MEC, which is built similarly to the magnetic system of a hybrid stepper motor, the complex path of closing the magnetic flux in the volume of the active part, in this case it is necessary to solve the problem of calculating the magnetic field in a 3D formulation using one of the modern numerical methods.

The goal of the article is to develop 3D mathematical models and analyze the characteristics of a magnetoelectric converter, the magnetic system of which is made similar to the magnetic system of a hybrid stepper motor.

Basic technical requirements for the electromechanical parameters of the MEC.

1. The MEC must ensure the linearity and necessary rigidity of the mechanical characteristics at different currents in the control winding. The mechanical characteristic is the dependence of the torque M created by the MEC on the angle of rotation of its shaft θ, i.e. $M = f(\theta)$.

2. The MEC must ensure the linearity and necessary rigidity of the mechanical characteristic $M = f(\theta)$ when the control current in its windings is equal to zero (characteristic of the magnetic spring). The slope of this mechanical characteristic determines the stiffness of the magnetic spring, which must be at least 0.0106 Nm/degree.

3. With the nominal control current I = 50 mA and the zero position of the shaft, the torque on the MEC shaft should be at least 0.0624 Nm, and when loaded by an external spring with stiffness of 0.0236 Nm/degree and shaft rotation angle of 1.5°, the torque should be not less than 0.0354 Nm.

Description and principle of operation of the selected MEC design. By analogy with the hybrid stepper motor, the magnetic system of the developed MEC consists of toothed stator and rotor (Fig. 2). Stator 1 is made in the form of a salient pole structure with coils 4 on toothed poles. Rotor 2 is divided into two parts, between which there is a cylindrical permanent magnet magnetized in the axial direction. The upper and lower parts of the rotor 2 are offset relative to each other by 90° and have tooth zones with gaps, which distinguishes them from the tooth zones of a stepper motor, which are performed without gaps. To eliminate magnetic hysteresis, the MEC magnetic core is made of permalloy grade 50N.

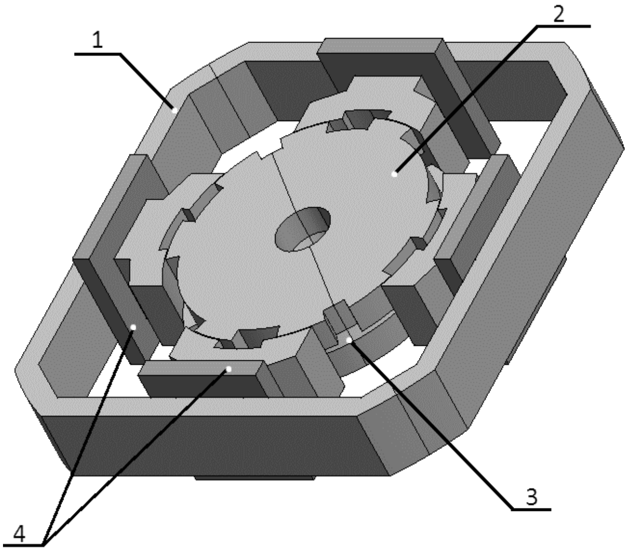

Fig. 2. Active part of the MEC: 1 – stator; 2 – rotor; 3 – permanent magnet; 4 – winding

The principle of operation of the MEC under consideration is as follows. In the absence of current in the excitation winding, the magnetized rotor occupies the zero position, in which half of the upper and lower rotor teeth are symmetrically located opposite the stator teeth.

When the rotor deviates from the zero position, the overlapping area between the stator teeth and the teeth of the upper and lower parts of the rotor changes (for example, it decreases from above, increases from below depending on the direction of rotation of the rotor) and the magnetic flux in the corresponding air gaps changes. At the same time, magnetic attraction forces tend to return the rotor to a stable zero position. Thus, the MEC magnetic system has the properties of a mechanical spring.

When the current flows in the control winding, a magnetomotive force is created, which leads to a change in the distribution of the magnetic flux in the air gap between the stator and the rotor halves. As a result, electromagnetic forces and torque arise which tend to deviate the rotor from the central position.

The design of the MEC of this type can be completed with a different number of teeth and poles on the stator and rotor. For example, a design with two teeth on the stator pole is shown in Fig. 2, and with three and four teeth – respectively in Fig. 3, 4.

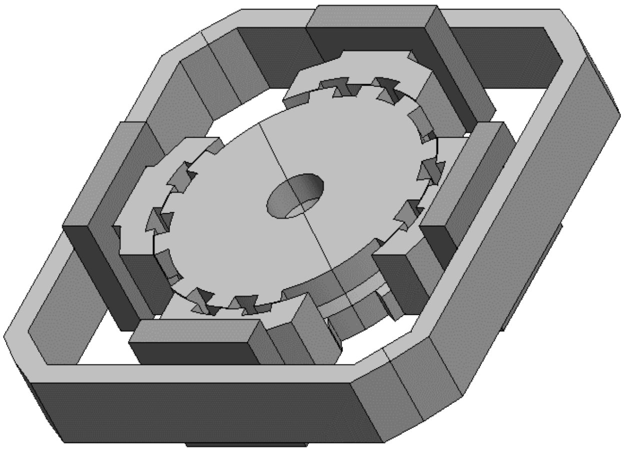

Fig. 3. Active part of the MEC with three teeth on the stator pole

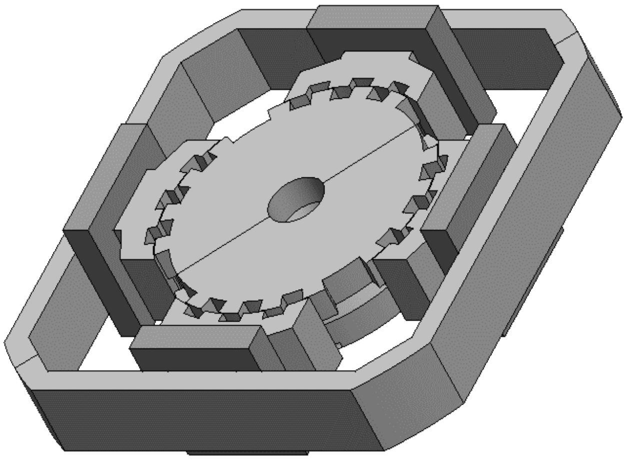

Fig. 4. Active part of the MEC with four teeth on the stator pole

To choose a constructive implementation of the active part of the MEC, presented in Fig. 2–4, and to calculate the characteristics of the selected design, it is necessary to conduct simulation of the magnetic field for each of the variants of the active part of the MEC.

Field models of MEC and results of design calculations. Calculations of the 3D magnetic field were carried out using the Finite Element Method for four variants of the four-pole active part of the MEC with two, three, four and five teeth on the stator pole. In all calculation variants, the number of elements of the finite element mesh of the 3D model was on average 240,000. With such a number of mesh elements, a sufficiently detailed approximation of the geometry of the MEC is achieved.

As an example, Fig. 5 shows the 3D field mathematical model of the MEC with three teeth on the pole, which was developed in the license program JMAG-Designer [9], and in Fig. 6 – the results of calculating the magnetic field in the form of magnetic lines of force.

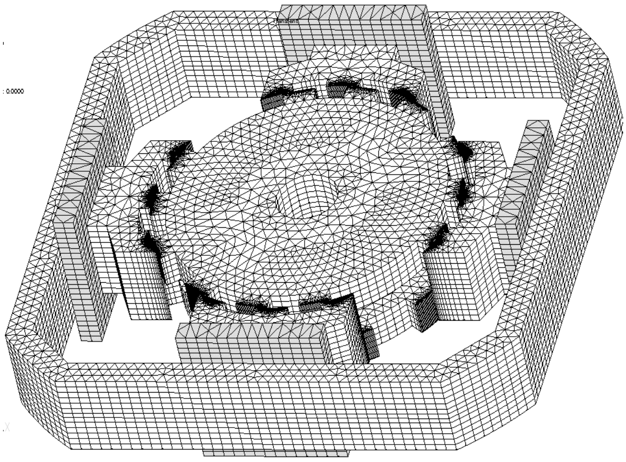

Fig. 5. 3D finite element model of the active part of the MEC with three teeth on the stator pole

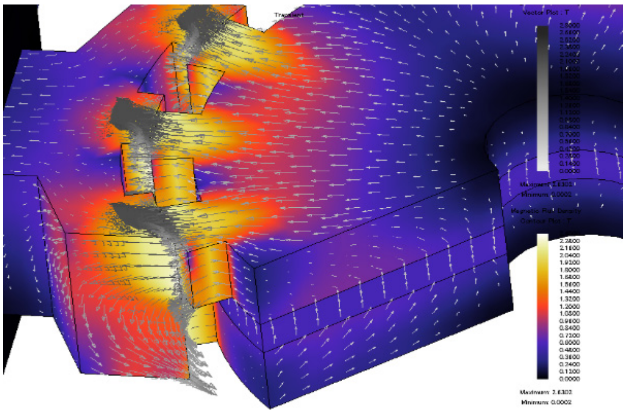

Fig. 6. Lines of force of the magnetic field in the active part of the MEC with three teeth on the stator pole

Based on the results of a series of calculations of the magnetic field of the considered four-pole variants, a family of characteristics of magnetic springs and mechanical characteristics of the MEC was obtained. The analysis of the obtained characteristics showed the following:

- with an increase in the number of teeth, the stiffness of the magnetic spring increases;
- the torque at the nominal current and the zero position of the rotor practically does not depend on the number of teeth on the stator pole;
- the slope of the mechanical characteristics increases as the number of teeth on the stator pole increases.

The results of the calculations are summarized in Table 1.

Table 1

Results of MEC calculations

Number of teeth on the stator pole	Stiffness of the magnetic spring, Nm/degree	Torque at zero position of the rotor, Nm
2	0,00059	0,055
3	0,0063	0,0617
4	0,0117	0,067
5	0,0183	0,0676

From the data in the Table 1, it can be seen that the version of the active part of the MEC with four teeth on the stator pole and a high coercive permanent magnet of the NdFeB brand fully meets the basic technical requirements for the electromechanical parameters of the MEC, and its manufacture is more technological than the manufacture of the active part of the MEC with five teeth on the stator pole.

The construction of the proposed MEC is shown in Fig. 7. The main geometric dimensions and materials of the active part of the selected version of the MEC are given in Table 2.

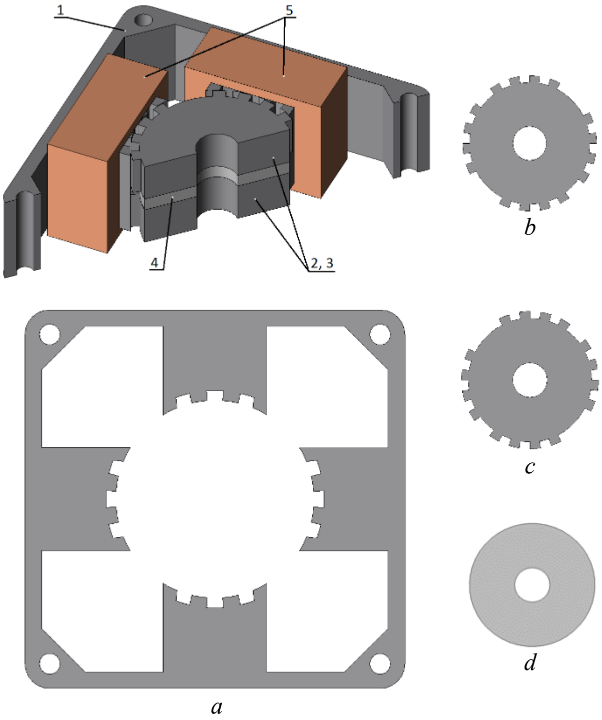

Fig. 7. Structural elements of the active part of the MEC:
a – general view (1 – magnetic core of the stator, 2, 3 – magnetic cores of parts of the rotor, 4 – permanent magnet, 5 – coils of the control winding) and section of the magnetic core of the stator;
b, *c* – cross-section of parts of the magnetic core of the rotor;
d – cross-section of the permanent magnet

Table 2

Geometric dimensions and materials of the active part of the MEC

Name	Value
Overall dimensions of the active part, mm	46×46×14
Internal diameter of the stator, mm	24
Length of the active part, mm	14
Air gap, mm	0,1
Magnet thickness, mm	2
Material of the magnetic core of the stator and rotor	Permalloy 50N
Permanent magnet material	N38EH
Magnetomotive force of the coil, A	20
Operating range of rotor rotation angles, mech. degrees	±2
Number of coil turns	200

Taking into account the symmetry of the constructive implementation of the active part of the MEC when solving the 3D field problem, the boundary conditions of the periodicity of the change of the magnetic vector potential were adopted, which made it possible to limit the calculation area to half of the 3D model of the MEC and reduce the time of magnetic field analysis.

Figure 8 shows a 3D finite element model of the MEC with four teeth on the stator pole, and Fig. 9 – distribution of the magnetic field in its active part.

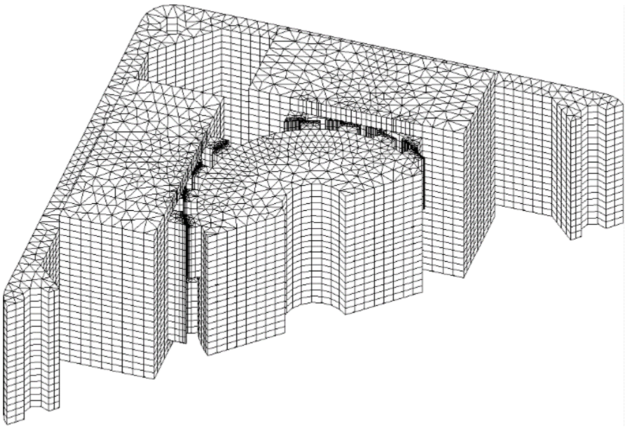

Fig. 8. 3D finite element model of the active part of the MEC with four teeth on the stator pole

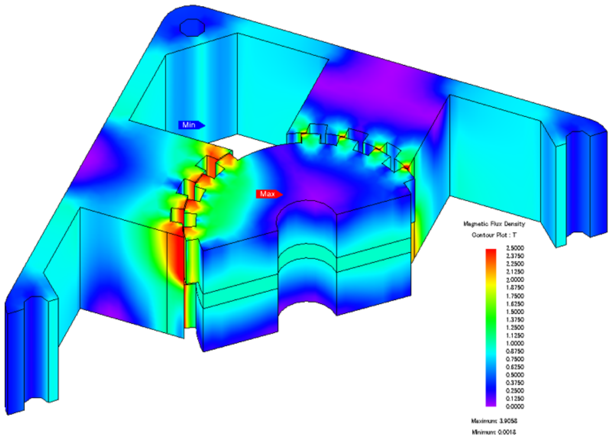

Fig. 9. Distribution of magnetic flux density in the active part of the MEC with four teeth on the stator pole

As a result of a series of calculations of the magnetic field, a family of mechanical characteristics of the MEC was obtained (Fig. 10).

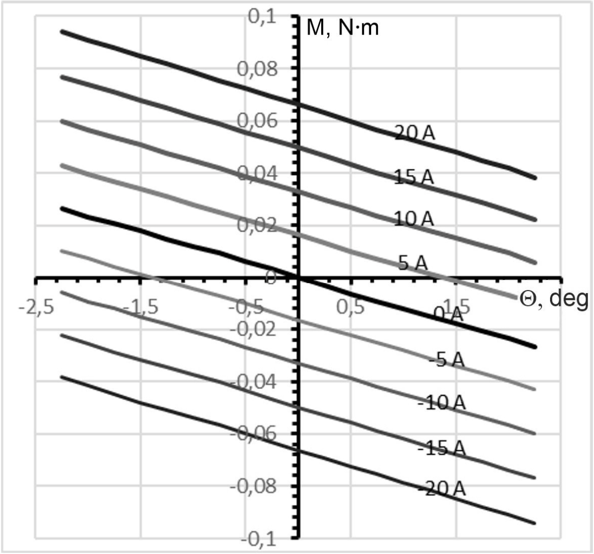

Fig. 10. Mechanical characteristics of the MEC with four teeth on the stator pole

The mechanical characteristics were calculated when the MMF of the coils of the control winding was changed from 0 to 20 A. Here, the MMF of the coil of 20 A corresponds to the nominal MEC control current of 50 mA.

Figure 10 shows that the mechanical characteristics of the MEC are linear. With nominal control current of 50 mA and a shaft braked in the zero position, the torque developed by the MEC is 0.067 Nm, which meets the requirements (not less than 0.0624 Nm). When rotating the rotor by 1.5°, the MEC torque is 0.0476 Nm, which also meets the requirements (not less than 0.0354 Nm). The stiffness of the magnetic spring is 0.0117 Nm/degree. (0.668 Nm/rad) and meets the specified requirements (at least 0.0106 Nm/degree).

The calculation of the characteristics of the selected design of the active part of the MEC with four teeth on the stator was also performed, using instead of the permanent magnet of the NdFeB brand, a permanent magnet of the SmCo brand, which has a higher temperature limit of operation, but somewhat worse magnetic and energy characteristics. Figure 11 shows the mechanical characteristics of the compared MEC variants. From the given data, it can be seen that the MEC with a permanent magnet of the SmCo brand has a lower stiffness of the magnetic spring and a lower torque at the zero position of the rotor and nominal control current of 50 mA.

A comparison of the calculated characteristics of the proposed MEC with the characteristics of the MP-220B prototype was also carried out (Fig. 12).

It can be seen that the compared characteristics are close to each other. However, if total magnetomotive force of 300 A is required to control the MP-220B in the nominal mode, then for the MEC proposed in this article only 80 A, that is, the power consumption of the MEC under development is significantly less than in the prototype.

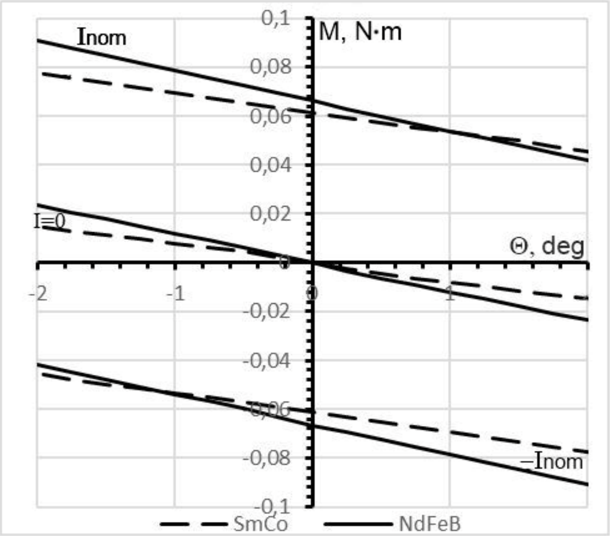

Fig. 11. Mechanical characteristics of the MEC with four teeth on the stator pole with SmCo and NdFeB magnets

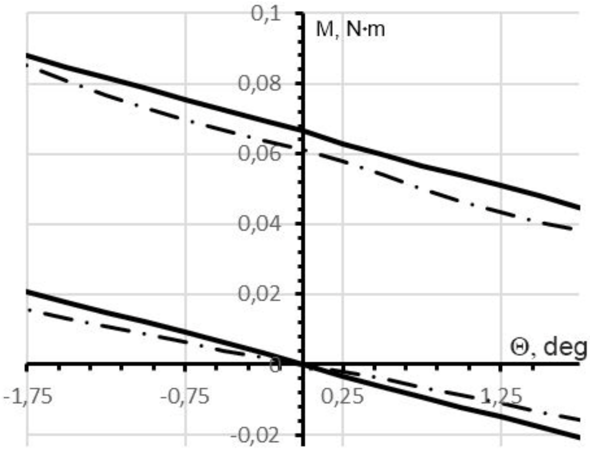

Fig. 12. Comparison of the calculated mechanical characteristics of the proposed MEC (———) with four teeth on the stator pole and MEC MP-220B (– · – · –)

Thus, based on the analysis of the results of the obtained calculations, the construction of the active part of the MEC was adopted in the form of a four-pole magnetic system with four teeth on the stator pole, the main geometric dimensions and materials given in Table 2.

MEC layout. In order to confirm the functionality and the possibility of implementing the main technical characteristics, a mock-up sample of the MEC was made, the external view of which is shown in Fig. 13.

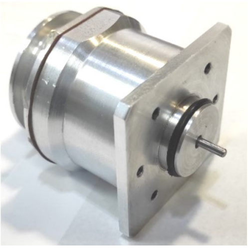

Fig. 13. External view of the MEC mock-up sample

The following were evaluated when prototyping the MEC Indicators:

1. Stiffness of the magnetic spring.
2. Torque at the zero position of the rotor.
3. The rotation angle of the rotor at a load torque of 0.0354 Nm.

A test stand was developed to evaluate the above-mentioned MEC indicators (Fig. 14).

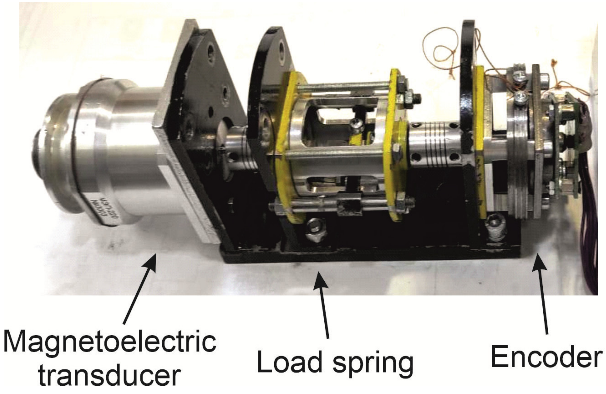

Fig. 14. MEC test stand

The stand consists of two units mechanically connected to the MEC shaft: a loading spring and an encoder. The loading spring is designed to create a load on the MEC shaft as a function of its angle of rotation. The magnetic encoder implemented on the AEAT-6600 sensor is designed to measure the MEC shaft rotation angle. The resolution of the encoder is 16 bits, which allows to determine the position of the shaft with an accuracy of 1 arc minute.

The results of tests of the MEC mock-up sample are shown in Table 3.

Table 3

Results of MEC tests

	Stiffness of the magnetic spring, Nm/degree	Torque at the zero position of the rotor, Nm	Angle of rotation of the rotor at the moment of loading 0,0354 Nm, degree
MEC layout	0,0115	0,064	1,7
Technical requirements	not less than 0,0106	not less than 0,0624	1,5

Conclusions.

1. The possibility of creating an MEC with the necessary technical characteristics and parameters is shown. On the basis of design calculations carried out on the basis of magnetic field modeling in a 3D formulation, the construction of the active part of the MEC in the form of a four-pole magnetic system with four teeth on the stator pole is substantiated.

2. The mechanical characteristics of the developed MEC are linear in the given range of the rotor rotation angle change. With nominal control current of 50 mA and the shaft braked in the zero position, the calculated torque developed by the designed MEC is 0.064 Nm, which satisfies the technical requirements (not less than 0.0624 Nm). The stiffness of the magnetic spring is

0.0115 Nm/degree and corresponds to the value specified in the technical requirements (not less than 0.0106 Nm/degree).

3. Tests of the mock-up sample of the MEC confirmed the basic efficiency of the adopted design and construction decisions.

Conflict of interest. The authors of the article declare that there is no conflict of interest.

REFERENCES

1. Reshetnikov E.M., Sablin Yu.A., Grigoriev V.E. *Electromechanical converters of hydraulic and gas drives.* Moscow, Mashinostroeniye Publ., 1982. 144 p. (Rus).

2. Kanuk G.I., Shuvanov A.N., Bliznichenko L.N. Hydraulic executive mechanisms for highspeed precision electronic hydraulic servomechanisms (EHSM). *Electrical Engineering & Electromechanics*, 2005, no. 1, pp. 44-46. (Rus).

3. Karnaukhov N.F. *Electromechanical and mechatronic systems*. Rostov-on-Don, Phoenix Publ., 2006. 320 p. (Rus).

4. Kharchishyn B.M. *Designing and researching of new type of electromechanical converters for pneumatic and hydraulic amplifiers*. PhD Thesis, Lviv Polytechnic National University, 2003. 19 p. (Ukr).

5. Tolmachev V.A., Demidova G.L. Mathematical models and dynamic characteristics of electromechanical converters with a limited angle of rotation. *Journal of Instrument Engineering*, 2008, vol. 51, no. 6, pp. 18-23. (Rus).

6. Stolov L.I., Afanasiev A.Y. *DC torque motors*. Moscow, Energoatomizdat Publ., 1989. 223 p. (Rus).

7. Emelyanov A.V., Shilin A.N. *Stepper motors. Textbook.* Volgograd, VolgGTU Publ., 2005. 48 p. (Rus).

8. Bul O.B. *Methods for calculating the magnetic systems of electrical devices. Magnetic circuits, fields and the FEMM program*. Moscow, Academy Publ., 2005. 336 p. (Rus).

9. *JMAG-Designer*. Available at: https://www.jmag-international.com/products/jmag-designer (accessed 10.01.2023).

Received 07.03.2023
Accepted 13.05.2023
Published 02.11.2023

V.V. Rymsha[1]*, Doctor of Technical Science, Professor,*
I.N. Radimov[1]*, PhD, Assistant Professor,*
M.V. Gulyy[1]*, PhD,*
I.P. Babych [2]*,*
A.A. Kalinichenko[2]*,*
N.P. Demenko [2]*,*
[1] Ltd. «Electrical Engineering – New Technology», Ukraine,
26/2, Melnytska Str., Odesa, 65005, Ukraine,
e-mail: rimsha61@gmail.com (Corresponding Author);
igor.radimov@gmail.com;
mv.skbss@gmail.com; office@ukrainemotors.com.ua
[2] State Design Office «Pivdenne»,
3, Kryvorizka Str., Dnipro, 49008, Ukraine,
e-mail: igorbabich@hotmail.com; alex_kalinichenko@i.ua
info@yuzhnoe.com

How to cite this article:
Rymsha V.V., Radimov I.N., Gulyy M.V., Babych I.P., Kalinichenko A.A., Demenko N.P. Modeling and research of a magnetoelectric converter for hydro and pneumo actuators. *Electrical Engineering & Electromechanics*, 2023, no. 6, pp. 21-26. doi: https://doi.org/10.20998/2074-272X.2023.6.04

UDC 621.3 https://doi.org/10.20998/2074-272X.2023.6.05

Y.A. Mabrouk, B. Mokhtari, T. Allaoui

Frequency analysis of stator currents of an induction motor controlled by direct torque control associated with a fuzzy flux estimator

Introduction. *The best way to control the torque of an induction motor is conventional direct torque control (DTC); this control method is the most used approach in the industrial sector due to its many advantages. Its main advantages are its simplicity and its exclusive dependence on the stator resistance of the induction motor. However, the use of hysteresis comparators reduces its effectiveness, causing more torque ripple. Additionally, this results in variable operating frequency and limited frequency sampling, resulting in pseudo-random overshoot of the hysteresis band.* ***Purpose****. For these reasons, this article presents a new study aimed at confirming its shortcomings and improving the effectiveness of the control.* ***Novelty****. We propose to use fuzzy logic methods to estimate the two components of the stator flux.* ***Methods****. In traditional DTC the flux components are estimated from an equation relating the stator resistance to the stator voltage and current. In the proposed method, only stator currents and voltages are used for this evaluation, which eliminates the dependence of DTC on stator resistance. The aim of this proposal is to make DTC robust to parametric changes.* ***Results****. General harmonic distortions, rotational speed of the induction motor, electromagnetic moment, magnetic flux and stator currents are analyzed.* ***Practical value****. With this proposed technique, validated in Simulink/MATLAB, several improvements in motor behavior and control are endorsed: torque fluctuations are reduced, overshoot is completely eliminated, and total harmonic distortion is significantly reduced by 48.31 % for stator currents. This study also confirmed the robustness of DTC to changes in stator resistance.* References 26, table 3, figures 11.

Key words: **direct torque control, fuzzy logic controller, fuzzy logic estimator, induction motor, spectral analysis, total harmonic distortion.**

Вступ*. Найкращим способом управління крутним моментом асинхронного двигуна є традиційне пряме управління крутним моментом (DTC); цей метод управління є найбільш використовуваним у промисловому секторі через його численні переваги. Його основними перевагами є простота та виключна залежність від опору статора асинхронного двигуна. Однак використання гістерезисних компараторів знижує його ефективність, викликаючи велику пульсацію крутного моменту. Крім того, це призводить до зміни робочої частоти та обмеження вибірки частоти, що призводить до псевдовипадкового виходу за межі смуги гістерезису.* ***Мета****. З цих причин у цій статті представлено нове дослідження, спрямоване на підтвердження його недоліків та підвищення ефективності контролю.* ***Новизна****. Ми пропонуємо використовувати методи нечіткої логіки з метою оцінки двох компонентів потоку статора.* ***Методи****. У традиційному DTC компоненти потоку оцінюються за рівнянням, що зв'язує опір статора з напругою та струмом статора. У запропонованому методі цієї оцінки використовуються лише струми і напруги статора, що виключає залежність DTC від опору статора. Мета цієї пропозиції – зробити DTC стійким до параметричних змін.* ***Результати****. Аналізуються загальні гармонічні спотворення, швидкість обертання асинхронного двигуна, електромагнітний момент, магнітний потік та струми статору.* ***Практична цінність****. За допомогою цього запропонованого методу, перевіреного в Simulink/MATLAB, підтверджено кілька покращень у поведінці та управління двигуном: коливання крутного моменту зменшуються, перерегулювання повністю усувається, а загальні гармонічні спотворення значно зменшуються на 48,31% для струмів статора. Це дослідження підтвердило стійкість DTC до змін опору статора.* Бібл. 26, табл. 3, рис. 11.

Ключові слова: **пряме управління крутним моментом, контролер нечіткої логіки, пристрій оцінки нечіткої логіки, асинхронний двигун, спектральний аналіз, повне гармонійне спотворення.**

Introduction. Owing to their affordability and ease of construction, induction motors (IM) are widely used in variable-speed drive systems [1]. IM compared to DC motors, are more durable, easier to maintain, and more economical [2]. Additionally, they are sturdy and resistant to big loads [3]. These many benefits, however, are not without drawbacks. The motor's dynamic behavior is frequently quite complicated [4], as a result of the strongly coupled, multivariable, nonlinear equations that come from its modeling. Furthermore, some of its state variables, including flux, cannot be measured or quantified [5-7]. To continuously control the torque and flux of these motors under these limits, more sophisticated control algorithms are needed [8]. Academic and commercial research has been conducted for a number of years to address the IM's control issue and create reliable controls [9]. For high-performance applications, there are two types of control used to control the electromagnetic torque of AC drives:

- Vector Control based on pulse width modulation inverter control for stator current regulation in the field rotational reference;
- Direct Torque Control (DTC) was proposed as an alternative to field-oriented control for high-performance AC drives. The fundamental idea behind this control method is the direct control of electromagnetic torque and flux by direct selection of the control sequence to be used with voltage inverters. This control strategy was proposed for the 1st time in the 1980s [10, 11]. The idea of torque control in the DTC scheme [12] is to increase the torque angle (angle between the stator and rotor flux) in case torque output needs to be increased. To reduce torque, one performs the reverse. However, it is maintained at the desired magnitude for the stator-linked flux [13].

Among the advantages of DTC control, it depends only on the motor stator resistance (R_s). Unfortunately, this solution can degrade the control's robustness because the resistance value varies over time due to heating. For this reason, we propose in this paper to replace the «classic estimator» of the two flux components which is described in equation (5) with another fuzzy one, in this fuzzy estimation we eliminate the dependence of the flux estimator to the R_s, and the only quantities used in this operation are the stator currents and voltages. This technique allowed us to improve the DTC control performance by minimizing the undulations of the controlled quantities.

To date, several studies have investigated the fuzzy estimator in DTC control. Khadar et al. in [14] propose a method for stator resistance estimation of a double-fed induction motor (DFIM) by a three-level neutral point-clamped inverter based on the DTC technique. Also, Zidani et al. in [15] propose a new stator resistance estimator using fuzzy logic. While in [13], Kamalapur et al. implement the estimation method using the proportional-integral (PI) control and fuzzy logic control schemes. Also, El Ouanjili et al. in [9] for a DFIM driven by two voltage source inverters operating at two levels, show an improved DTC technique.

Model of the IM in the stationary frame. In the literature, there are several mathematical models representing the dynamic behavior of IMs. In the following, a state space model related to α and β axes, for electrical variables, is considered [4]:

$$\begin{cases} \dfrac{d\varphi_{\alpha s}}{dt} = V_{\alpha s} - R_s I_{\alpha s}; & \dfrac{d\varphi_{\beta s}}{dt} = V_{\beta s} - R_s I_{\beta s}; \\ \dfrac{d\varphi_{\alpha r}}{dt} = -R_r I_{\alpha r} - \omega_m \varphi_{\beta r}; & \dfrac{d\varphi_{\beta r}}{dt} = -R_r I_{\beta r} + \omega_m \varphi_{\alpha r}, \end{cases} \qquad (1)$$

where $\omega_m = p\Omega_m = \omega_s - \omega_r$, where p is the pole pairs; subscripts s and r refer to the stator and rotor; α and β refer to components in (α, β) frame; V, I, φ are used to describe respectively voltage, current, and flux; R_s and R_r refer to the stator and rotor resistances; Ω_m is the mechanical speed; ω_s is the rotation speed of the stator field; ω_r is the rotation speed of the rotor one.

Currents and flux relationships are [16]:

$$\begin{bmatrix} \varphi_{\alpha s} \\ \varphi_{\alpha r} \end{bmatrix} = \begin{bmatrix} L_s & M \\ M & L_r \end{bmatrix} \begin{bmatrix} I_{\alpha s} \\ I_{\alpha r} \end{bmatrix}, \begin{bmatrix} \varphi_{\beta s} \\ \varphi_{\beta r} \end{bmatrix} = \begin{bmatrix} L_s & M \\ M & L_r \end{bmatrix} \begin{bmatrix} I_{\beta s} \\ I_{\beta r} \end{bmatrix}; \qquad (2)$$

where L and M are respectively the inductance of motor and the mutual one.

The next equation represents the mechanical part of the motor [16]:

$$\frac{d\Omega_m}{dt} = \frac{1}{J} \cdot \left(T_{em} - T_L\right); \qquad (3)$$

where T_{em} and T_L are respectively the electromagnetic torque and load one; J is the motor inertia.

Presentation of the DTC control. The DTC principle was first developed by Takahashi and Depenbrock [10, 11] around the end of the 1980s. It accomplishes decoupled control of the electromagnetic torque and stator flux, allowing IMs to respond to electromagnetic torque accurately and quickly in the stationary frame (α, β). A switching table is used to select the proper voltage vector. The choice of switching states has a direct impact on changes in the stator flux and torque of the motor. As a result, the choice is made by keeping the magnitudes of the flux and torque within two hysteresis bands. These controllers ensure that these two quantities are controlled separately [17, 18]. The flux and torque errors are the inputs of hysteresis controllers, and the voltage vector that is appropriate for each commutation period is determined by the controllers' outputs [19]. In DTC, the inverter voltage and frequency are adjusted based on the measured stator current and voltage. The torque and flux of the motor are then estimated based on these measurements, and the inverter voltage and frequency are adjusted to maintain the desired torque and flux. The schema of direct torque control is shown in Fig. 1.

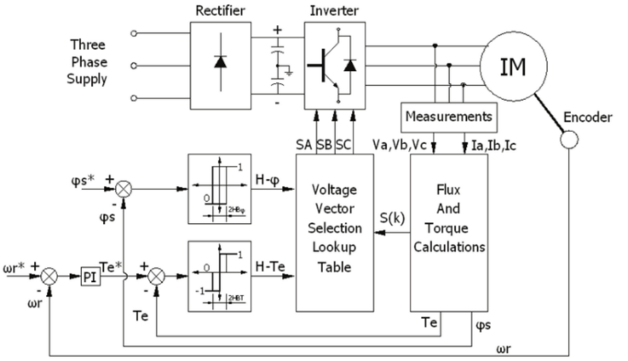

Fig. 1. Basic diagram of DTC control of IM

a) electromagnetic torque and flux estimation equations. To control the IM, a DTC loop is selected. First, the principal motor inputs, stator voltages, and currents are used to determine the T_{em} and φ_s. Then, the selection of the optimal voltage vector is applied inside the inverter. It is mandatory to express the used mathematical models for estimating the T_{em} and φ_s. The expressions of the flux into the stator can be evaluated as:

$$\varphi_s = \sqrt{\left(\varphi_{\alpha s}^2 + \varphi_{\beta s}^2\right)}, \qquad (4)$$

where the variables in (4) are given in (5):

$$\begin{aligned} \varphi_{\alpha s} &= \int \left(V_{\alpha s} - R_s I_{\alpha s}\right); \\ \varphi_{\beta s} &= \int \left(V_{\beta s} - R_s I_{\beta s}\right), \end{aligned} \qquad (5)$$

where $\varphi_{\alpha s}$ and $\varphi_{\beta s}$ represent the two components of flux in (α, β) reference frame.

The angle θ between $\varphi_{\alpha s}$ and $\varphi_{\beta s}$ is calculated as follows:

$$\theta = \arctan\left(\varphi_{\beta s} / \varphi_{\alpha s}\right). \qquad (6)$$

The cross-product of the stator quantities (stator flux and stator currents) can be used to calculate the IM's produced electromagnetic torque as:

$$T_{em} = \frac{3}{2} p \left(\varphi_{\alpha s} I_{\beta s} - \varphi_{\beta s} I_{\alpha s}\right). \qquad (7)$$

b) presentation of the conventional switching DTC table. Table 1 displays the switching table for the conventional DTC control [13].

Table 1

DTC switching table*

Sector		1	2	3	4	5	6	
Flux	Torque							
$\Delta\varphi_s = 1$	ΔT_{em}=1	V2	V3	V4	V5	V6	V1	2 level
	ΔT_{em}=0	V7	V0	V7	V0	V7	V0	
	ΔT_{em}= –1	V6	V1	V2	V3	V4	V5	3 level
$\Delta\varphi_s = 0$	ΔT_{em}= 1	V3	V4	V5	V6	V1	V2	2 level
	ΔT_{em}= 0	V0	V7	V0	V7	V0	V7	
	ΔT_{em} = –1	V5	V6	V1	V2	V3	V4	3 level

*$\Delta\varphi_s$ is the difference between the reference flux and the estimated one, $\Delta\varphi_s = \varphi_s^* - \varphi_s$; ΔT_{em} is the difference between the reference electromagnetic torque and the estimated one, $\Delta T_{em} = T_{em}^* - T_{em}$.

DTC with a fuzzy estimator. Principle of the fuzzy logic controller. A fuzzy logic controller (FLC) is a type of control system that uses fuzzy logic (FL) to control a system or process. FL is a mathematical approach that deals with uncertainty and imprecision, allowing for more flexible and robust control than traditional control techniques. In an FLC, the inputs to the system are represented as fuzzy sets, which are defined by membership functions (MF) that assign degrees of membership to each input. These MFs allow for a more natural representation of inputs that may be difficult to define using traditional crisp sets.

The output of the FLC is then determined using a set of fuzzy rules, which define the relationship between the inputs and the output. These rules are typically defined by expert knowledge or by analyzing data from the system [20, 21].

The output of the FLC is then defuzzified to produce a crisp value that can be used to control the system. This defuzzification process can be done using a variety of techniques, such as centroid or max-min.

One of the advantages of FLC is its ability to deal with complex and nonlinear systems, which may be difficult to control using traditional control techniques. FLCs can also adapt to changing system conditions, making them suitable for systems that may experience changes in operating conditions. FLCs are commonly used in a variety of applications, such as process control, robotics, and intelligent transportation systems. They have also been used in many consumer products, such as washing machines, air conditioners, and cameras, to provide intelligent control and improve performance [22, 23].

In summary, FLCs provide a flexible and robust approach to control systems and processes, using fuzzy logic to deal with uncertainty and imprecision. Their ability to deal with complex and nonlinear systems makes them suitable for a wide range of applications, from industrial control to consumer.

Inference and formulation of rules. In most cases, fuzzy systems translate input fuzzy sets into output fuzzy sets. Relations between input and output fuzzy sets are known as fuzzy rules. Any one of the following can be used to derive fuzzy rules:

- master insight and control designing information;
- control actions were taken by the operator;
- gaining knowledge from the training examples [24].

The fuzzy rules in this study are created by learning from the training instances. In this instance, the fuzzy control rules' general form is: if x and y are A_i and B_i, respectively, then $z = f_i(x, y)$ denotes the linguistic variables that, in turn, denote the control variable and the process state variables. A first-order Sugeno (FOS) fuzzy model is the outcome of a fuzzy inference system (FIS) that takes the form of a FOS fuzzy model. A_i and B_i are the language-specific values of the linguistic variables, $f_i(x, y)$ is a function of the process state variables x, y [25, 26].

The proposed flux estimator In our research we propose the use of fuzzy logic to estimate the components of the stator flux ($\varphi_{\alpha s}$, $\varphi_{\beta s}$), such that we use as inputs of the fuzzy system the stator voltages V_s and currents I_s of the motor, and the outputs of this system are the components of the flux without having introduced the stator resistance (R_s) in this estimate. The outputs of the fuzzy system are used to calculate the electromagnetic torque T_{em} and the position of the flux θ. Figure 2 shows the proposed estimation block.

The range of fuzzy controller inputs (V_s, I_s) are characterized into three MFs, and two constants MFs are defined for output. There are 9 rules based on which the FIS infers the gains, these rules represented in Table 2. MFs used for inputs are Negative (Ne), Zero (Z), Positive (Po), and for outputs we choose: flux exists (exist), and flux doesn't exist (no).

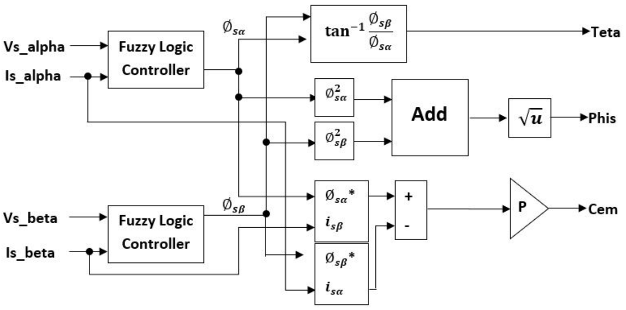

Fig. 2. Fuzzy flux estimator block

Table 2

Inference matrix

V_s, I_s	Ne	Z	Po
Ne	exist	no	exist
Z	no	no	no
Po	exist	no	exist

Trapezoidal MFs are chosen for the three fuzzy sets (P), (N) and (Z) as shown in Fig. 3, 4, and we choose constant MF for the output (Fig. 5).

The FIS used in this work is a FOS fuzzy model, its principle of operation is given as: if V_s is Po and I_s is Po then flux exist.

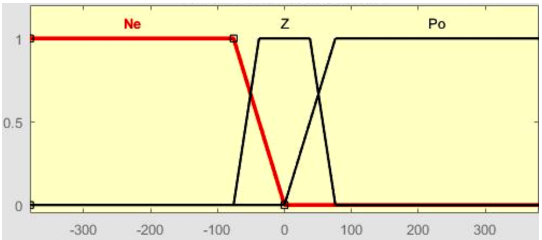

Fig. 3. Trapezoidal MFs used for the voltage input

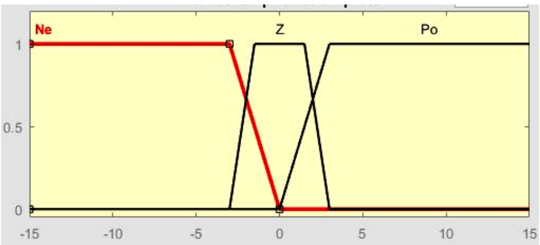

Fig. 4. Trapezoidal MFs used for the current input

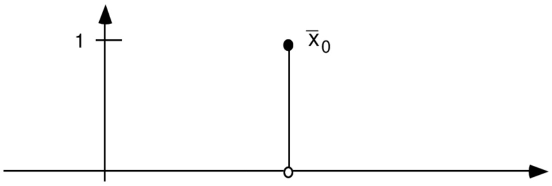

Fig. 5. MFs used for the decision output

Results and discussion. In this section, we are going to present and discuss the simulation results of conventional DTC of an IM, and the simulation results of the proposed strategy with the analysis spectral of the current. Motor and simulation parameters are listed in Appendix.

The simulation results in Fig. 6-9 show that the proposed strategy improved the performance of the DTC, minimizing torque ripples, the overshoot is absolutely removed and decreasing important values of total harmonic distortion (THD) by 48.31 %, and rotation with some oscillations.

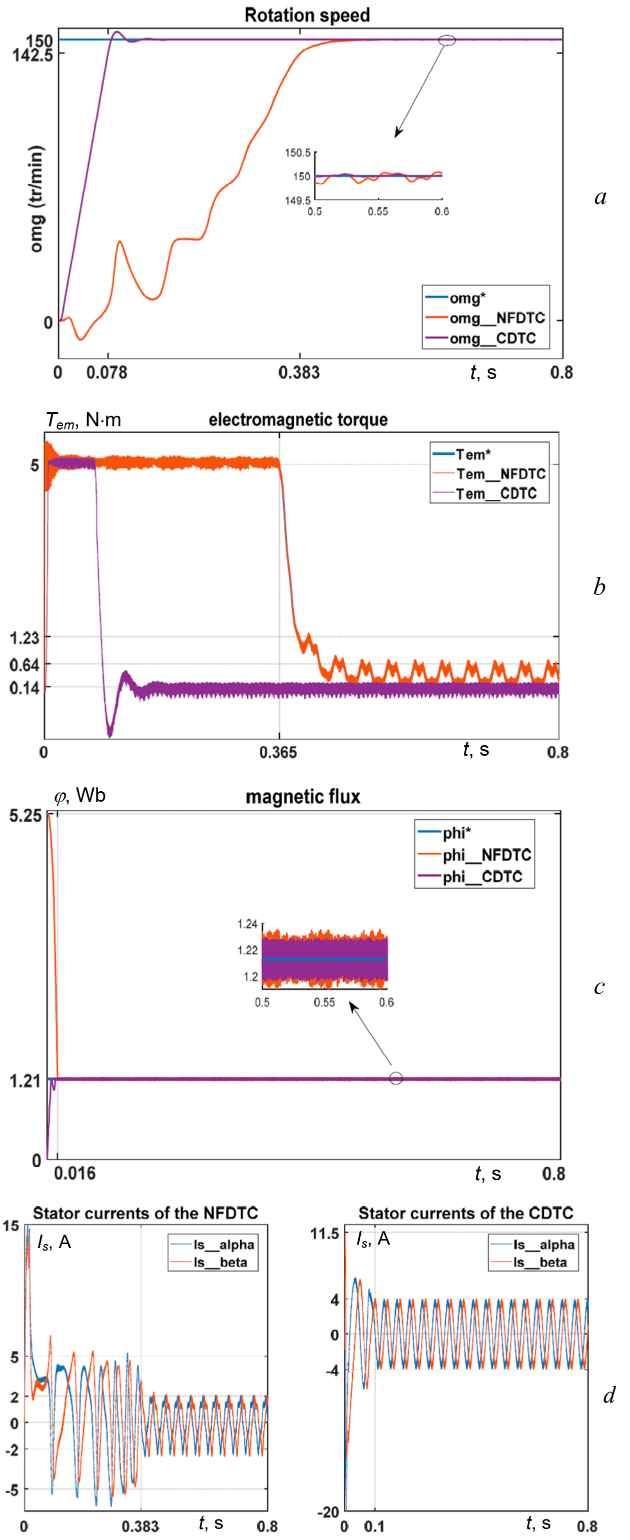

Fig. 6. Simulation results of conventional and the proposed DTC of an IM: *a* – rotation speed; *b* – electromagnetic torque; *c* – magnetic flux; *d* – stator current

From the analysis of Fig. 7, 8, we can notice the influence of the proposed method on the waveform of the current. The use of a fuzzy estimator also makes it possible to reduce the effect of harmonics of orders 3, 5, and 7. Figure 9 shows that the two components of flux obtained by a fuzzy estimator have a perfectly sinusoidal shape as desired. Table 3 presents a comparative study between the classic DTC and the proposed strategy.

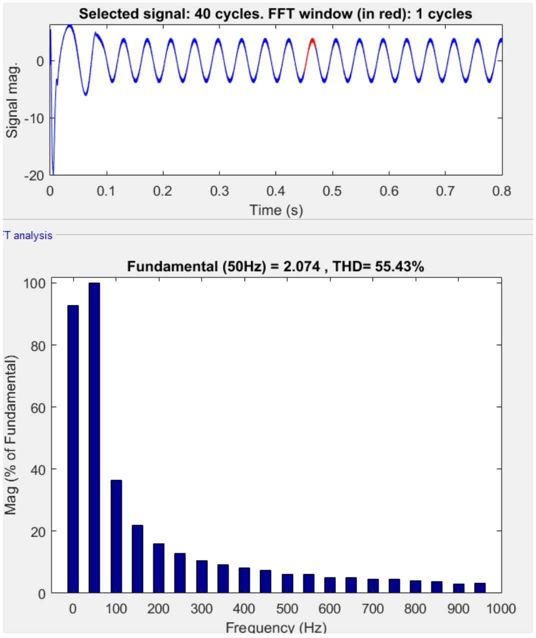

Fig. 7. The current spectral analysis of the conventional DTC control

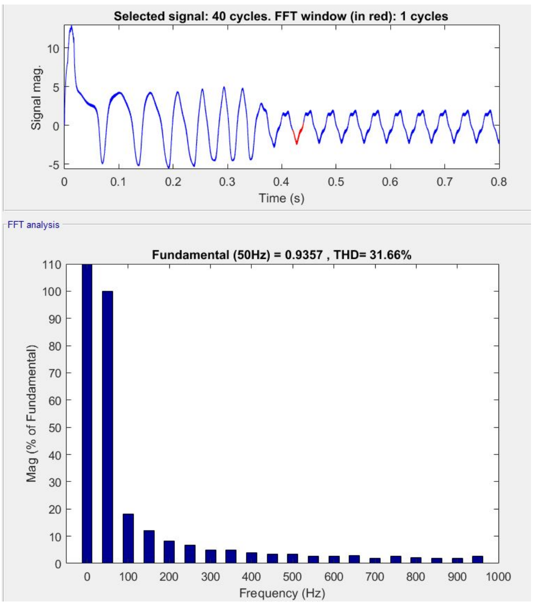

Fig. 8. The current spectral analysis of the proposed DTC control

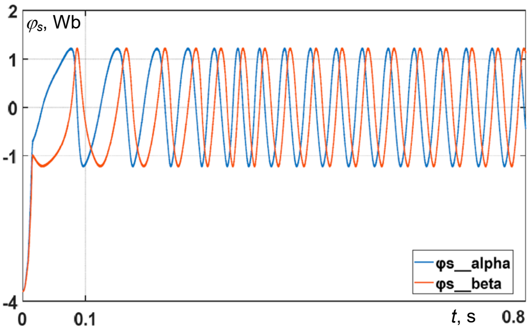

Fig. 9. The two components of flux obtained with fuzzy estimator

Table 3

Comparative study between the CDTC and the proposed one

	Dynamic response	Parameter sensitivity R_s	Current THD
Conventional DTC	fast	sensitive	important distortion
DTC with fuzzy observatory	slow	insensitive	less distortion

Robustness test. As shown in the introduction, the propose FLC-DTC, is independent of the stator resistance, to check the performance and the robustness of this proposed control, we propose to vary the value of the resistance R_s (increase it and decrease it) and see its influence on the behavior of the motor.

In the following, we show the simulation results of the FLC-DTC control, we increase the value of the resistance by 50 % of its nominal value (Fig. 10) and decrease it by 25 % of its nominal value (Fig. 11). These results confirm the effectiveness of the proposed strategy when we have a stator resistance variation.

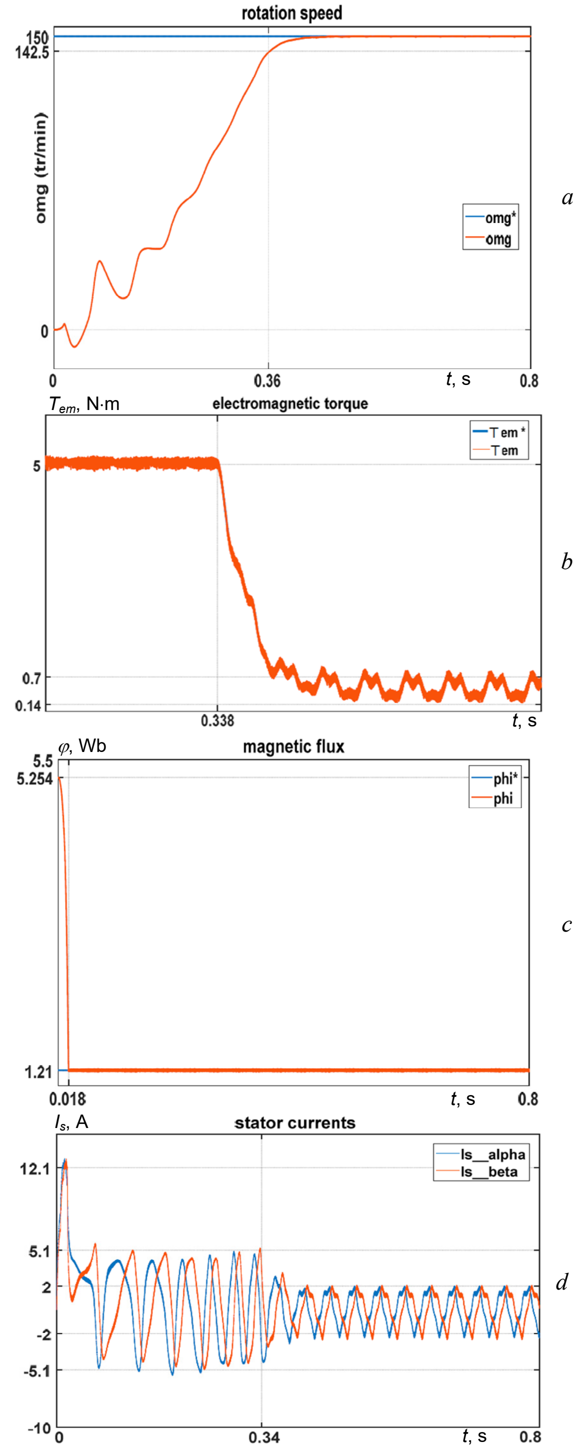

Fig. 10. Simulation results of the proposed DTC of an IM decreasing R_s by 50 % of its nominal value: *a* – rotation speed; *b* – electromagnetic torque; *c* – magnetic flux; *d* – stator current

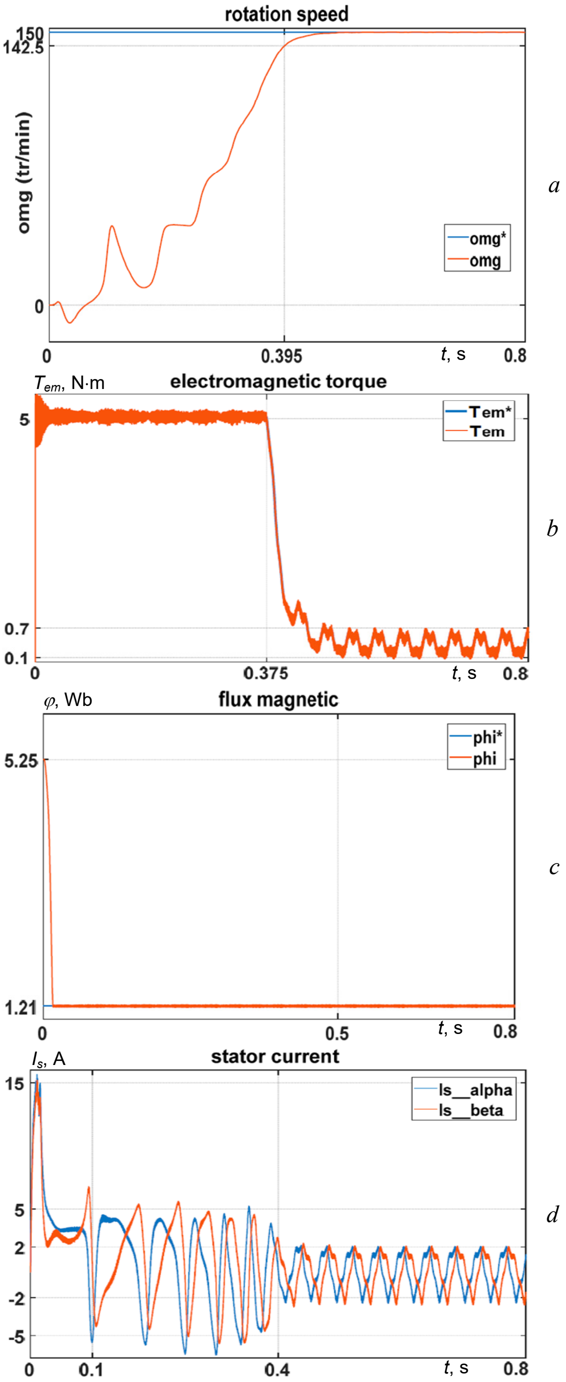

Fig. 11. Simulation results of the proposed DTC of an IM decreasing R_s by 25 % of its nominal value: *a* – rotation speed; *b* – electromagnetic torque; *c* – magnetic flux; *d* – stator current

Conclusions. In this paper, we suggested a new approach to the direct torque control of an induction motor, we used fuzzy logic to estimate the two components of the stator flux this strategy brought improvements to this control and the behavior of the motor. On the other hand, the simulation results demonstrated the stability of direct torque control to stator resistance variations, but it also has some drawbacks such as a speed response time that is a bit slow with some speed oscillations. We, therefore, propose in future studies to replace the fuzzy logic controller with a neuro-fuzzy controller and to use techniques to improve the dynamic response of the system.

Conflict of interest. The authors of the article declare that there is no conflict of interest.

Appendix

Pole pairs p	1
Stator resistance, Ω	4.7333
Power, W	1000
Moment of inertia, kg·m^2	0.0026
Coefficient of viscous friction	$6.1704\cdot10^{-4}$
Fuzzy logic gains	k_1 = 18,25; k_2 = 3.71

REFERENCES

1. Malyar V.S., Malyar A.V., Andreishyn A.S. A method for calculating mechanical characteristics of induction motors with squirrel-cage rotor. *Electrical Engineering & Electromechanics*, 2019, no. 2, pp. 9-13. doi: https://doi.org/10.20998/2074-272X.2019.2.02.

2. Lallouani H., Saad B., Letfi B. DTC-SVM based on Interval Type-2 Fuzzy Logic Controller of Double Stator Induction Machine fed by Six-Phase Inverter. *International Journal of Image, Graphics and Signal Processing*, 2019, vol. 11, no. 7, pp. 48-57. doi: https://doi.org/10.5815/ijigsp.2019.07.04.

3. Ben Slimene M. Performance analysis of six-phase induction machine-multilevel inverter with arbitrary displacement. *Electrical Engineering & Electromechanics*, 2020, no. 4, pp. 12-16. doi: https://doi.org/10.20998/2074-272X.2020.4.02.

4. Fathy Abouzeid A., Guerrero J.M., Endemaño A., Muniategui I., Ortega D., Larrazabal I., Briz F. Control Strategies for Induction Motors in Railway Traction Applications. *Energies*, 2020, vol. 13, no. 3, art. no. 700. doi: https://doi.org/10.3390/en13030700.

5. Fekik A., Denoun H., Azar A.T., Kamal N.A., Zaouia M., Benyahia N., Hamida M.L., Benamrouche N., Vaidyanathan S. Direct power control of three-phase PWM-rectifier with backstepping control. *Backstepping Control of Nonlinear Dynamical Systems*, 2021, pp. 215-234. doi: https://doi.org/10.1016/B978-0-12-817582-8.00017-9.

6. El Ouanjli N., Derouich A., El Ghzizal A., Motahhir S., Chebabhi A., El Mourabit Y., Taoussi M. Modern improvement techniques of direct torque control for induction motor drives - a review. *Protection and Control of Modern Power Systems*, 2019, vol. 4, no. 1, art. no. 11. doi: https://doi.org/10.1186/s41601-019-0125-5.

7. Aktas M., Awaili K., Ehsani M., Arisoy A. Direct torque control versus indirect field-oriented control of induction motors for electric vehicle applications. *Engineering Science and Technology, an International Journal*, 2020, vol. 23, no. 5, pp. 1134-1143. doi: https://doi.org/10.1016/j.jestch.2020.04.002.

8. Bounar N., Boulkroune A., Boudjema F., M'Saad M., Farza, M. Adaptive fuzzy vector control for a doubly-fed induction motor. *Neurocomputing*, 2015, vol. 151, pp. 756-769. doi: https://doi.org/10.1016/j.neucom.2014.10.026.

9. El Ouanjli N., Taoussi M., Derouich A., Chebabhi A., El Ghzizal A., Bossoufi B. High performance direct torque control of doubly fed induction motor using fuzzy logic. *Gazi University Journal of Science*, 2018, vol. 31, no. 2, pp. 532-542.

10. Takahashi I., Noguchi T. A New Quick-Response and High-Efficiency Control Strategy of an Induction Motor. *IEEE Transactions on Industry Applications*, 1986, vol. IA-22, no. 5, pp. 820-827. doi: https://doi.org/10.1109/TIA.1986.4504799.

11. Depenbrock M. Direct self-control (DSC) of inverter-fed induction machine. *IEEE Transactions on Power Electronics*, 1988, vol. 3, no. 4, pp. 420-429. doi: https://doi.org/10.1109/63.17963.

12. Pragati A., Ganthia B.P., Panigrahi B.P. Genetic Algorithm Optimized Direct Torque Control of Mathematically Modeled Induction Motor Drive Using PI and Sliding Mode Controller. *Lecture Notes in Electrical Engineering*, 2021, vol. 707, pp. 351-366. doi: https://doi.org/10.1007/978-981-15-8586-9_32.

13. Kamalapur G., Aspalli M.S. Direct torque control and dynamic performance of induction motor using fractional order fuzzy logic controller. *International Journal of Electrical and Computer Engineering (IJECE)*, 2023, vol. 13, no. 4, pp. 3805-3816. doi: https://doi.org/10.11591/ijece.v13i4.pp3805-3816.

14. Khadar S., Kouzou A., Benguesmia H. Fuzzy Stator Resistance Estimator of Induction Motor fed by a Three Levels NPC Inverter Controlled by Direct Torque Control. *2018 International Conference on Applied Smart Systems (ICASS)*, 2018, pp. 1-7. doi: https://doi.org/10.1109/ICASS.2018.8651999.

15. Zidani F., Diallo D., Benbouzid M.E.H., Nait-Said R. Direct Torque Control of Induction Motor With Fuzzy Stator Resistance Adaptation. *IEEE Transactions on Energy Conversion*, 2006, vol. 21, no. 2, pp. 619-621. doi: https://doi.org/10.1109/TEC.2006.874251.

16. Djamila C., Yahia M. Direct Torque Control Strategies of Induction Machine: Comparative Studies. *Direct Torque Control Strategies of Electrical Machines*. IntechOpen. 2021. doi: https://doi.org/10.5772/intechopen.90199.

17. Agha Kashkooli M.R., Madani S.M., Lipo T.A. Improved Direct Torque Control for a DFIG under Symmetrical Voltage Dip With Transient Flux Damping. *IEEE Transactions on Industrial Electronics*, 2020, vol. 67, no. 1, pp. 28-37. doi: https://doi.org/10.1109/TIE.2019.2893856.

18. Kodumur Meesala R.E., Thippiripati V.K. An Improved Direct Torque Control of Three-Level Dual Inverter Fed Open-Ended Winding Induction Motor Drive Based on Modified Look-Up Table. *IEEE Transactions on Power Electronics*, 2020, vol. 35, no. 4, pp. 3906-3917. doi: https://doi.org/10.1109/TPEL.2019.2937684.

19. Dos Santos T.H., Goedtel A., Da Silva S.A.O., Suetake M. Scalar control of an induction motor using a neural sensorless technique. *Electric Power Systems Research*, 2014, vol. 108, pp. 322-330. doi: https://doi.org/10.1016/j.epsr.2013.11.020.

20. Ikhe A., Pahariya Y. Voltage regulation using three phase electric spring by fuzzy logic controller. *Electrical Engineering & Electromechanics*, 2023, no. 4, pp. 14-18. doi: https://doi.org/10.20998/2074-272X.2023.4.02.

21. Aib A., Khodja D.E., Chakroune S. Field programmable gate array hardware in the loop validation of fuzzy direct torque control for induction machine drive. *Electrical Engineering & Electromechanics*, 2023, no. 3, pp. 28-35. doi: https://doi.org/10.20998/2074-272X.2023.3.04.

22. Maghfiroh H., Saputro J.S., Adriyanto F., Sujono A., Lambang R.L. Performance Evaluation of Fuzzy-PID in Speed Control of Three Phase Induction Motor. *IOP Conference Series: Materials Science and Engineering*, 2021, vol. 1096, no. 1, art. no. 012071. doi: https://doi.org/10.1088/1757-899X/1096/1/012071.

23. Saifi R. Implementation of a new flux rotor based on model reference adaptive system for sensorless direct torque control modified for induction motor. *Electrical Engineering & Electromechanics*, 2023, no. 2, 37-42. doi: https://doi.org/10.20998/2074-272X.2023.2.06.

24. Saidi A., Naceri F., Youb L., Cernat M., Guasch Pesquer L. Two Types of Fuzzy Logic Controllers for the Speed Control of the Doubly-Fed Induction Machine. *Advances in Electrical and Computer Engineering*, 2020, vol. 20, no. 3, pp. 65-74. doi: https://doi.org/10.4316/AECE.2020.03008.

25. Derbane A., Tabbache B., Ahriche A. A fuzzy logic approach based direct torque control and five-leg voltage source inverter for electric vehicle powertrains. *Revue Roumaine des Sciences Techniques Série Electrotechnique et Energétique*, 2021, vol. 66, no. 1, pp. 15-20.

26. Paranchuk Y.S., Paranchuk R.Y. Research of arc furnace electrical mode with a fuzzy control model. *Electrical Engineering & Electromechanics*, 2020, no. 4, pp. 30-36. doi: https://doi.org/10.20998/2074-272X.2020.4.05.

Received 26.03.2023
Accepted 10.07.2023
Published 02.11.2023

Younes Abdelbadie Mabrouk[1]*, PhD Student,*
Bachir Mokhtari[1]*, Lecturer,*
Tayeb Allaoui[2]*, Full Professor,*
[1] Electrotechnics Department, LEDMASD Laboratory,
University of Laghouat, Algeria,
e-mail: mab.younes@lagh-univ.dz (Corresponding Author);
ba.mokhtari@lagh-univ.dz
[2] Department of Electrical Engineering, L2GEGI Laboratory,
University of Tiaret, Algeria,
e-mail: tayeb.allaoui@univ-tiaret.dz

How to cite this article:
Mabrouk Y.A., Mokhtari B., Allaoui T. Frequency analysis of stator currents of an induction motor controlled by direct torque control associated with a fuzzy flux estimator. *Electrical Engineering & Electromechanics*, 2023, no. 6, pp. 27-32. doi: https://doi.org/10.20998/2074-272X.2023.6.05

UDC 621.314 https://doi.org/10.20998/2074-272X.2023.6.06

A. Abdellah, M. Larbi, D. Toumi

Open circuit fault diagnosis for a five-level neutral point clamped inverter in a grid-connected photovoltaic system with hybrid energy storage system

Introduction. *Recently, the number of high and medium voltage applications has increased dramatically. The connection between these different applications requires series-parallel combinations of power semiconductors. Multilevel converter topologies provide major advantages to these applications. In this paper, a grid-connected photovoltaic system with a hybrid energy storage system using a five-level neutral point clamped inverter is studied. Although the multilevel inverter has many advantages over the two-level inverter, it has a high probability of experiencing an open circuit fault. In this context, the five-level inverter has 24 controllable switches, one of which may experience an open circuit fault at any time. Therefore, it plays an important part in the reliability and robustness of the whole system. The* ***novelty*** *of this paper presents an approach to accurately detect the open circuit fault in all insulated gate bipolar transistors of a five-level neutral point clamped inverter in a photovoltaic power generation application with a hybrid energy storage system.* ***Purpose.*** *Before using fault-tolerant control to ensure service continuity, fault diagnosis techniques must first be used, which are the crucial phase of reliability.* ***Methods.*** *A detection method based on the maximum and minimum error values is proposed. These errors are calculated using the expected and measured line-to-line pole voltages.* ***Results.*** *The open circuit fault detection method is implemented using MATLAB/Simulink. Simulation results showed the accuracy of detecting the open circuit fault in all insulated gate bipolar transistors in a short time. Moreover, this method is adaptable to several applications and is also robust to transient regimes imposed by solar irradiation and load variations.* References 26, table 3, figures 16.

Key words: **photovoltaic, fault diagnosis, five-level neutral point clamped inverter, line-to-line pole voltages.**

Вступ. *Останнім часом різко зросла кількість застосувань високої та середньої напруги. З'єднання між цими різними використаннями вимагає послідовно-паралельних комбінацій силових напівпровідників. Топології багаторівневих перетворювачів надають цим додаткам великі переваги. У цій статті вивчається фотоелектрична система, підключена до мережі, з гібридною системою зберігання енергії, яка використовує п'ятирівневий інвертор із фіксуванням нейтральної точки. Хоча багаторівневий інвертор має багато переваг, порівняно з дворівневим інвертором, він має високу ймовірність виникнення обриву кола. У зв'язку з цим п'ятирівневий інвертор має 24 керовані перемикачі, один з яких будь-якої миті може зіткнутися з обривом кола. Таким чином, він відіграє важливу роль у надійності та стійкості всієї системи.* ***Новизна*** *цієї статті являє собою підхід до точного виявлення несправності розімкнутого кола у всіх біполярних транзисторах із ізольованим затвором п'ятирівневого інвертора з фіксуванням нейтральної точки у фотоелектричних додатках для вироблення електроенергії з гібридною системою зберігання енергії.* ***Мета***. *Перш ніж використовувати відмовостійкий контроль для забезпечення безперервності обслуговування, необхідно спочатку використовувати методи діагностики несправностей, які є вирішальним етапом надійності.* ***Методи***. *Запропоновано метод виявлення, заснований на максимальному та мінімальному значеннях помилок. Ці помилки розраховуються з використанням очікуваних та виміряних міжфазних напруг на полюсах.* ***Результати***. *Метод виявлення обриву кола реалізовано з використанням MATLAB/Simulink. Результати моделювання показали точність виявлення обриву кола у всіх біполярних транзисторах із ізольованим затвором за короткий час. Більш того, цей метод адаптується до кількох застосувань, а також стійкий до перехідних режимів, викликаних сонячним випромінюванням та змінами навантаження.* Бібл. 26, табл. 3, рис. 16.

Ключові слова: **фотогальванічна система, діагностика несправностей, п'ятирівневий інвертор із зажимом нейтралі, лінійна напруга на полюсах.**

1. Introduction. Photovoltaic (PV) system is increasingly important as it is easy to set up and requires low maintenance. Currently, the energy demand in the public domain has been fulfilled through the implementation of stand-alone, grid-connected and hybrid PV system configurations [1]. However, like other renewable energy sources, solar energy tends to be intermittent because it is influenced by meteorological conditions [2]. Hence, the Energy Storage System (ESS) is typically needed in renewable energy based microgrid system to serve as a buffer between production and load. In microgrid systems, the incoming and outgoing power of the ESS elements varies considerably depending on the instantaneous power production and load status [3]. These intermittent variations negatively impact ESS performance, reduce ESS life and increase the cost of battery replacement, as batteries are featured with high-energy density, but have low-power density, low charge/discharge rates and slow dynamic response. One way around these problems is to combine multiple types of energy storage elements to create a Hybrid Energy Storage System (HESS). Currently, batteries and supercapacitors (SCs) are the most popular choices for many systems because SCs have high-power densities, offer a long life cycle with high efficiency and fast charge/discharge response [4, 5].

The grid-connected PV system with a HESS was widely studied in the literature [6, 7]. Moreover, this system must be equipped with an inverter that presents the connection between the generator and the AC side. The inverter, which is based on power semiconductors, including insulated gate bipolar transistors (IGBTs) and diodes, is one of the most vulnerable components, and therefore plays an important role in the reliability and robustness of the overall system. According to a study, 34 % of faults in power converters are related to power semiconductors and mainly to controllable switches, while diodes have a lower failure rate [8].

The multi-level Neutral Point Clamped (NPC) inverter is increasingly used in grid-connected PV systems because it has many advantages over two-level inverters, including lower harmonic distortion of the output voltage, the best choice for medium to high power and low switching loss [9, 10]. However, the high number of power switching devices increases the chance of failure. The most common power semiconductor failures are open circuit (OC), short circuit (SC), which can occur due to high thermal or electrical strain, wire disconnection or gate driver failure [11]. In most cases, a short-circuit fault results in an overcurrent, which is very destructive and can immediately damage the IGBTs. Therefore, protection against short-circuit faults is often achieved through hardware solutions. In addition, industrial gate drivers protect the system against short circuits [12]. However, when an OC fault occurs, the system continues to operate, but the line current and DC bus voltage fluctuate, which may result in a secondary fault in the power converter or other devices. One of the most important ways to boost system reliability is through fault-tolerant techniques. Currently, fault tolerance methods for inverters are mainly classified into two categories: software-based approaches without additional hardware and hardware-based approaches [13]. However, fault diagnosis is a crucial phase of service continuity, because without it, it is impossible to reconfigure the converter correctly [14].

Literature review. Fault diagnosis methods for multilevel converters are still not widely studied in the literature due to their more recent development than two-level converters. Moreover, the diagnostic methods validated for two-level converters are not directly applicable to multilevel converters due to their large number of power components. These methods are classified into two categories: voltage-based methods and current-based methods. For methods based on currents [15] proposes a method using the Average Current Park Vector for a three level NPC inverter. Although this method can detect the OC fault in two switches, the possibility of the failure of two IGBTs at the same time is rare. In [16], the authors contribute to the improvement of the previously mentioned study by accurately detecting the faulty switch. However, this study is only dedicated to AC drive applications. A study based on the extension theory method to locate faults in a three-level NPC inverter supplying an AC motor is proposed in [17]. The inputs used for this method are the frequency spectra of the line current waveforms. For an AC motor drive, the frequency spectra are different depending on the faulty switch. However, for a grid-connected system, it is impossible to detect the OC fault because the frequency spectrum is the same for the upper half arm as well as for the lower half arm. The authors of [18] accurately locate the OC fault in a three-level NPC converter associated with a wind power system using the neural network. The inputs used in this study are the magnitude and phase angle of the generator currents. However, this method is limited to AC drive applications and requires large data storage and computing capacity.

For voltage-based methods, the authors of [19] propose a method based on the evaluation of pole voltages and motor line currents to detect the fault in a three-level NPC inverter. Although this method has the ability to detect multiple OC faults in all IGBTs and clamp diodes, it is not suitable for grid-connected systems. In [20] the authors contributed significantly to the accurate location of the faulty IGBT in a three-level NPC rectifier without adding additional hardware. The estimated voltage errors are represented by the expected value of the converter line voltage and its estimated value. However, this estimation generates a lot of noise, and the choice of thresholds and minimum detection time depends on each system, which reduces the robustness of this method. Fault detection of a five-level NPC inverter is not studied at all in the literature. The authors in [21] focused on the reconfiguration of this inverter without specifying the diagnostic method.

The goal of the paper. To remedy the previously mentioned drawbacks, this study presents an approach to accurately detect the OC fault in all IGBTs of a five-level NPC inverter. This inverter is used in a grid-connected PV system with a HESS to improve the power quality and to be able to support high power. The detection method is based on the maximum and minimum error values resulting from the comparison between the measured line-to-line pole voltages and their expected values. The fault monitoring is well achieved regardless of the load type (resistive or inductive) and power state (transient or steady-state), which amplifies the reliability of this algorithm. In addition, the proposed method can quickly detect the OC fault.

2. System description. The global system architecture is depicted in Fig. 1, which comprises three main functions: generation of electrical energy, HESS and energy management, connection to the grid.

2.1 PV generation. PV panels have been installed to produce electrical energy (Fig. 1,*a*). The PV generator is formed by PV panels connected in series for increasing the voltage and in parallel for increasing the current, and a DC/DC boost converter which transmits the produced power P_{pv} to the DC bus. The voltage V_{pv} at the terminals of the bank of panels, and the current I_{pv} passing through them, follow a $I_{pv}(V_{pv})$ characteristic which depends on the exogenous inputs which are the solar irradiation, and the atmospheric temperature. The electrical behavior of a PV cell can be described with good precision by a model called «single diode» [22].

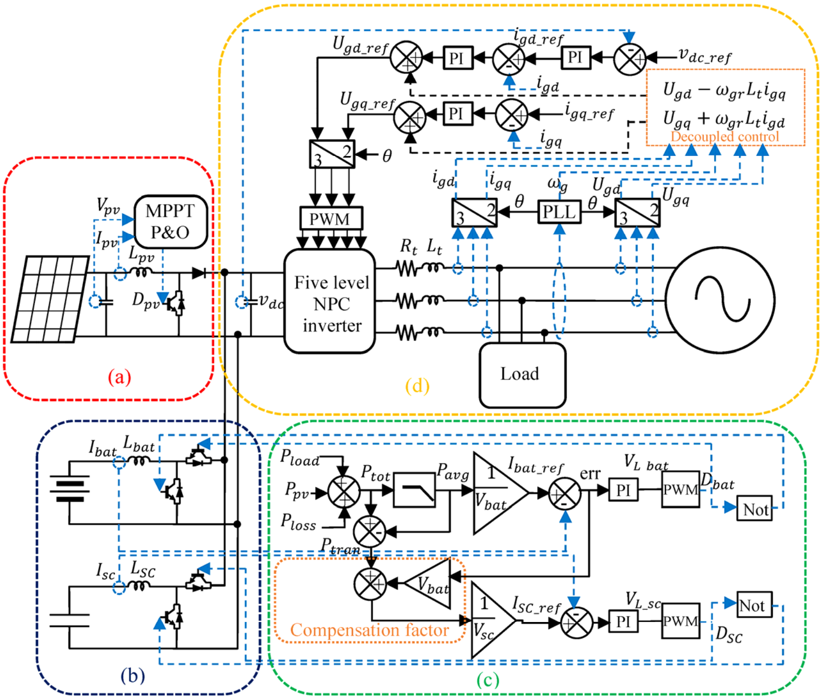

Fig. 1. Schematic diagram of grid-connected PV system with AC load

The Perturb & Observe method is used for extracting the maximum power of PV panels. It is an iterative method, allowing acquiring the maximum power point. It depends on measuring the characteristics $I_{pv}(V_{pv})$ of the PV modules, then induces a slight disturbance of the voltage (or the current) to analyze the resulting power change [23].

2.2 Configuration of the HESS and energy management. Figure 1,*b* presents the HESS, which includes batteries and SCs. Each bank of SCs and batteries is connected to a DC/DC buck-boost converter, which connects it to the DC bus. There must be a complementarity between these hybrid storage systems. The batteries providing the «energy» function are sized in terms of average power, while the SCs having the «power» function are sized in transient power. The implementation of SCs is to improve battery life.

The energy management is presented in Fig. 1,*c*. To determine the total power P_{tot}, it is necessary to calculate the power of the PV generation P_{pv}, the power of the load P_{load} and the power dissipated in the grid filter P_{loss}. Then a low-pass filter is used to split the total power into two components: the transient power component P_{tran} and the average power component P_{avg}. Consequently, the part containing the high frequencies (transient power) is supplied to the SCs and those of the low frequencies to the batteries [24]. The power balance equation is stated as follows:

$$P_{tot} = P_{load} + P_{loss} - P_{pv} = P_{avg} + P_{tran}\,. \qquad (1)$$

Since the components P_{tran} and P_{avg} are based on a reference current on the DC bus side, two gains are used to estimate the reference currents on the SC side (I_{SCref}) and battery side ($I_{bat\ ref}$). The measured values of the SC and battery current (I_{SC} and I_{bat}) are taken in order to compare them with their reference values. In addition, a compensation factor is used to increase system performance by recovering uncompensated battery power due to its slow dynamics [25]. This uncompensated power is added to the transient power to be recovered by SC. Finally, the PI controllers are concerned with the generation of adequate control signals via the duty cycles of the converters (D_{SC} and D_{bat}), which allow the measured currents to follow their references.

2.3 Control of grid connection. The grid connection consists of a five-level NPC inverter, an *R-L* filter at each phase, a load and a power grid as shown in Fig. 1,*d*. To control the grid side, Voltage Oriented Control (VOC) is proposed in this paper using the PI controller. The purpose of the VOC is to keep the DC bus voltage constant regardless of the amplitude and direction of the power. This control technique needs to calculate the angle using a phase locked loop for the Park transform. The control strategy comprises an outer loop to control the DC bus voltage and two internal loops to control the direct and quadrature components of the current (*d*-axis and *q*-axis). The external loop is then produced employing a regulation loop, making it possible to maintain a constant DC bus voltage, with a PI regulator generating the current reference $I_{gd\ ref}$. Concerning the internal loop, the direct and quadrature components are used to regulate active and reactive power, respectively. Furthermore, a decoupled control for direct and quadrature components is implemented to tackle the problem of the relationship between the *d*-axis and *q*-axis [26].

3. Open circuit fault analysis. This section presents the analysis of the OC fault in a five-level NPC inverter, which is shown in Fig. 2 by the arm of the *A* phase. The five-level NPC inverter arm consists of four capacitors of equal capacity dividing the input voltage V_{dc} into four identical voltage levels and eight switches (IGBTs) mounted in antiparallel with diodes. In addition, six clamp diodes are present to have five additional voltage levels, as shown in Table 1 [9].

This analysis is only dedicated to the switches of the upper half arm of phase *A* S_{A1}, S_{A2}, S_{A3}, S_{A4} due to its symmetrical shape. Therefore, the switches of the lower half arm S_{A5}, S_{A6}, S_{A7}, S_{A8} have the same analysis as those of the upper half arm, except for the path and the sign of the phase current.

3.1 Open circuit fault in S_{A1}. When the OC fault arises in the switch S_{A1}, then the current path is D_1, S_{A2}, S_{A3}, S_{A4} and the switching state P_2 is impossible as shown in Fig. 3,*a*. Figure 4,*a* represents when an OC fault occurs in S_{A1} at the instant $t = 0.5$ s, from this instant a part of the positive phase current (I_{Ma}) flows. Furthermore, the diode D_1 is reverse biased due to the grid voltage, which is greater than the DC bus voltage $V_{dc}/4$. The control increases the amplitude of the currents of other phases (I_{Mb} and I_{Mc}) to balance the power.

3.2 Open circuit fault in S_{A2}. When the OC fault has appeared at the switch S_{A2}, the switching states P_2 and P_1 are impossible. Therefore, the current path of the faulty phase (I_{Ma}) is formed by D_2, S_{A3} and S_{A4} as shown in Fig. 3,*b*. Then the diode D_1, which blocks the majority of the positive phase current, is reverse biased. Therefore, the positive phase current is 0, as shown in Fig. 4,*b*.

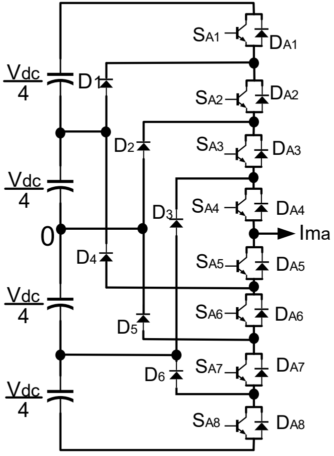

Fig. 2. The *A*-phase arm of a five-level NPC inverter

Table 1

Switching states in phase *X*

State of leg *X*	IGBT's states $X \in \{A, B, C\}$								Pole voltage V_{XO}
	S_{X1}	S_{X2}	S_{X3}	S_{X4}	S_{X5}	S_{X6}	S_{X7}	S_{X8}	
P_2	1	1	1	1	0	0	0	0	$+V_{dc}/2$
P_1	0	1	1	1	1	0	0	0	$+V_{dc}/4$
0	0	0	1	1	1	1	0	0	0
N_1	0	0	0	1	1	1	1	0	$-V_{dc}/4$
N_2	0	0	0	0	1	1	1	1	$-V_{dc}/2$

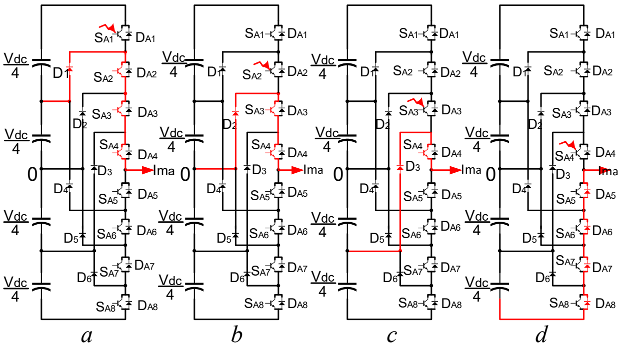

Fig. 3. Current paths in the case of an OC fault

3.3 Open circuit fault in S_{A3}. When S_{A3} is open-circuited, the impossible switching states are P_2, P_1 and 0. Therefore, the current path is formed by D_3, S_{A4} as shown in Fig. 3,*c*. However, because of the negative DC bus voltage and the positive grid voltage, diode D_3 is always reverse biased. So, the positive current corresponding to the faulty phase cannot flow, as shown in Fig. 4,*c*.

3.4 Open circuit fault in S_{A4}. When S_{A4} is open-circuited, the impossible switching states are P_2, P_1, 0 and N_1. Therefore, the current path is formed by D_{A8}, D_{A7}, D_{A6} and D_{A5} as shown in Fig. 3,*d*. However, due to negative DC bus voltage and positive mains voltage, diode D_{A8}, D_{A7}, D_{A6} and D_{A5} are always reverse biased. So, the positive phase current cannot flow as shown in Fig. 4,d.

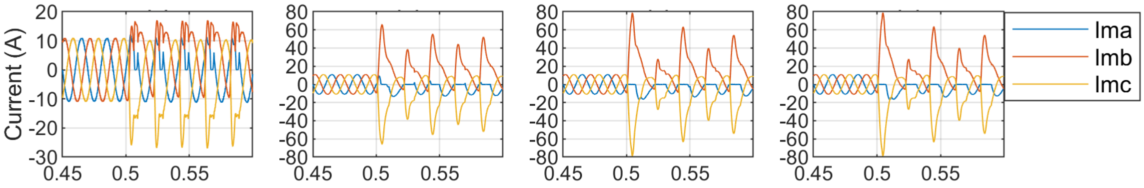

a *b* *c* *d*

Fig. 4. Current waveforms under OC fault in switches (*a*) S_{A1}, (*b*) S_{A2}, (*c*) S_{A3}, (*d*) S_{A4}

From the previous analysis, the phase current is 0 in both situations when the switch S_{A3} or S_{A4} is faulty. The phase current when the fault occurs in S_{A5} or S_{A6} is also equal to each other. Therefore, if the load is not reactive, it is difficult or impossible to distinguish the OC fault from the switches mentioned above. Unless there are additional algorithms added to the detection technique. This will add a large computational capacity and slow down the detection time.

4. Diagnostic technique. In this section, a technique for detecting an OC fault of one of the switches of a five-level NPC inverter is proposed. This method is based on the comparison between the measured and expected line-to-line pole voltages, denoted V_{XY} and V^*_{XY}, respectively ($XY \in \{AB, BC, CA\}$). The five-level NPC inverter is controlled by the sine-triangle PWM control, which generates the control commands δ_{Xi}($i \in \{1, 2, ..., 8\}$) to control the DC-bus voltage and the active and reactive power. Using these control commands those of the upper half arm of each phase, it is possible to estimate each pole voltage V^*_{XO}($X \in \{A, B, C\}$) according to the following relation:

$$V^*_{XO} = (\delta_{X1} + \delta_{X2} + \delta_{X3} + \delta_{X4} - 2)\frac{V_{dc}}{2}. \quad (2)$$

The expected line-to-line pole voltages are:

$$V^*_{XY} = V^*_{XO} - V^*_{YO}. \quad (3)$$

To precisely locate the OC fault in each phase and each switch, the fault was analyzed using the deference between the expected and measured line-to-line pole voltages ΔV_{XY}. The diagnostic errors are calculated by:

$$\Delta V_{XY} = V^*_{XY} - V_{XY}. \quad (4)$$

The diagnostic errors must be normalized so that the diagnostic algorithm is independent of the DC bus voltage using the following formula:

$$\varepsilon_{XY} = \Delta V_{XY} / V_{dc}. \quad (5)$$

In healthy conditions, the diagnostic errors are 0, which means the measured and expected line-to-line pole are equal. On the other hand, if the OC fault has occurred in any switch, two-line voltage errors are affected by the OC fault, because each phase is linked to two line-to-line pole voltages. The third error, which has nothing to do with the faulty phase, remained 0.

Therefore, it is possible to accurately detect the defective half arm. For example, if the fault appeared in the upper half arm of phase *X*, the errors are as follows:

$$\begin{cases} \varepsilon_{XY} = \text{threshold;} \\ \varepsilon_{YZ} \approx 0; \\ \varepsilon_{ZX} = -\text{threshold.} \end{cases} \quad (6)$$

The diagnostic errors linked to defective phase *X* take symmetrical values. If the fault appeared in the lower half arm of phase *X*, the errors are the same, but the values of those linked to the defective phase are reversed.

After detecting the fault and determining the faulty phase and half-arm, it is necessary to identify with precision the faulty switch by determining the values of the errors corresponding to each switch. To calculate the maximum error value when S_{X1} is in OC, the current passes through D_1, S_{X2}, S_{X3} and S_{X4} instead as explained in section (3), connecting the DC bus mid-point (O) to the AC terminal and generating a pole voltage of value P_1. This results in a pole voltage error ΔV_{XY} of $V_{dc}/4$. From (5), the normalized diagnostic error applied to the identification process (ε_{XY}) reaches a magnitude of 0.25 when the switching state is P_2. Furthermore, the second normalized diagnostic error (ε_{ZX}) affected by the fault obtains a symmetrical value of –0.25 when the switching state is N_2. The third error (ε_{YZ}), which is completely unrelated to the faulty phase, is 0. Using the analysis done in section (3), a similar process is employed to compute the normalized diagnostic error values for all switches, and the results are listed in Table 2.

However, these errors are not fixed at those values which vary at each cycle between 0 and the maximum value for the high error and between 0 and the minimum value for the low error. For this, it is only necessary to capture the maximum and minimum error values using an algorithm that calculates at any time the maximum and minimum error values, resulting in six errors {max(ε_{XY}), min(ε_{XY}), max(ε_{YZ}), min(ε_{YZ}), max(ε_{ZX}), min(ε_{ZX})}. Therefore, the fault detection of each switch relies on the behavior of these six errors and the threshold ranges in which these errors may exist. Table 3 summarizes the proposed OC fault detection method.

The diagnostic algorithm is recapitulated in the block diagram in Fig. 5. In summary, the algorithm begins with a step of calculating the expected pole voltages, and a line-to-line pole voltage measurement from which the necessary diagnostic errors are calculated. Then, as shown in Table 2, the maximum and minimum values of each normalized diagnostic error are extracted, since the errors don't have a fixed value. An OC fault is recognized by checking (6), which identifies the faulty phase. In the event of a fault, the conditions in Table 3 immediately locate the faulty IGBT.

5. Simulation results and discussion. The simulation results of a grid-connected PV system with a hybrid storage system were performed via MATLAB. All the parameters of the studied system are presented in the Appendix. Power is injected via a balanced three-phase grid (220 V / 50 Hz). Before the system is subjected to an OC type fault, it is simulated in its healthy state to check the energy management. The PV generation power and the load power are shown in Fig. 6,*a*. From Fig. 6,*b*, it is evident that when the PV generation is higher than the demand the battery and the SC are charged by the deference of the two powers, and when the generation is lower than the load demand the battery and the SC discharge to provide the rest of the required power. In the same figure, the SC supplies or absorbs the transient component of the current, while the battery supplies or absorbs the average component of the current. Figure 6,*c* shows the DC bus voltage following its reference (630 V). There are small fluctuations that are corrected by the PI regulator when the generation power or the load demand is changed. Figure 6,*d* illustrates the three-phase currents coming out of the five-level NPC inverter. The quality of the currents is very good thanks to this inverter. From Fig. 6,*e*, it is clear that the active power coming out of the inverter is the same as that of the load, which means that the energy management is working well. Since the load is purely active, the grid side controller maintains the reactive power around 0, as shown in Fig. 6,*f*.

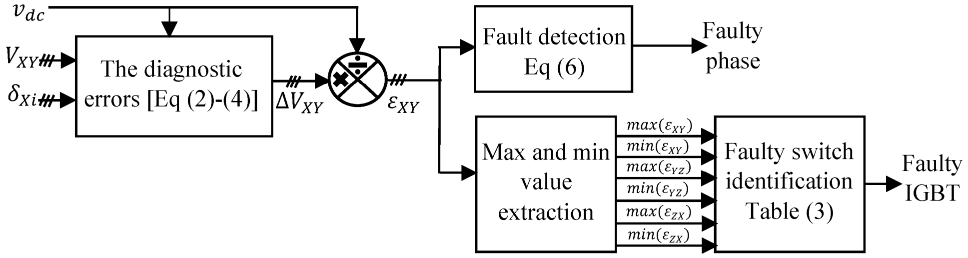

Fig. 5. Proposed diagnostic algorithm block diagram

Table 2

Normalized diagnostic errors with OC fault in phase *X*

Faulty switch	ε_{XY}					ε_{YZ}					ε_{ZX}				
	P_2	P_1	0	N_1	N_2	P_2	P_1	0	N_1	N_2	P_2	P_1	0	N_1	N_2
S_{X1}	0.25	0	0	0	0	0	0	0	0	0	0	0	0	0	–0.25
S_{X2}	0.5	0.25	0	0	0	0	0	0	0	0	0	0	0	–0.25	–0.5
S_{X3}	0.75	0.5	0.25	0	0	0	0	0	0	0	0	0	–0.25	–0.5	–0.75
S_{X4}	1	0.75	0.5	0.25	0	0	0	0	0	0	0	–0.25	–0.5	–0.75	–1
S_{X5}	–1	–0.75	–0.5	–0.25	0	0	0	0	0	0	0	0.25	0.5	0.75	1
S_{X6}	–075	–0.5	–0.25	0	0	0	0	0	0	0	0	0	0.25	0.5	0.75
S_{X7}	–0.5	–0.25	0	0	0	0	0	0	0	0	0	0	0	0.25	0.5
S_{X8}	–0.25	0	0	0	0	0	0	0	0	0	0	0	0	0	0.25

Table 3

Look-up table for detection of the faulty IGBT of phase *X*

Faulty switch	max(ε_{XY})	min(ε_{XY})	max(ε_{YZ})	min(ε_{YZ})	max(ε_{ZX})	min(ε_{ZX})
S_{X1}	[0.05 0.25]	≈0	≈0	≈0	≈0	[–0.25 –0.05]
S_{X2}	[0.25 0.5]	≈0	≈0	≈0	≈0	[–0.5 –0.25]
S_{X3}	[0.5 0.75]	≈0	≈0	≈0	≈0	[–0.75 –0.5]
S_{X4}	[0.75 1]	≈0	≈0	≈0	≈0	[–1 –0.75]
S_{X5}	≈0	[–1 –0.75]	≈0	≈0	[0.75 1]	≈0
S_{X6}	≈0	[–0.75 –0.5]	≈0	≈0	[0.5 0.75]	≈0
S_{X7}	≈0	[–0.5 –0.25]	≈0	≈0	[0.25 0.5]	≈0
S_{X8}	≈0	[–0.25 –0.05]	≈0	≈0	[0.05 0.25]	≈0

To verify the effectiveness of the proposed detection technique, an OC type fault is imposed on the switches by forcing the switching states to 0. For the same parameters (irradiation and load) used previously, the OC type fault is generated at 0.55 s in switches S_{A3}, S_{B4} and S_{C7}, as shown in Fig. 7–9. From Fig. 7, the three fault cases show significant oscillations on the output currents of the faulty five-level NPC inverter. Consequently, the active power supplied to the load and the grid is no longer stable as well as the reactive power supplied to the grid is no longer equal to 0 and is oscillating, as shown in Fig. 8. Figure 9 shows a comparison between an ESS with and without SCs when the OC type fault occurs on the same switches mentioned previously. When the OC fault appeared, it turned out that the SCs absorb the power peaks that are harmful to the batteries. These show small ripples as if nothing had happened. On the other hand, the system without hybrid storage (without SCs) forces the batteries to absorb the power peaks, which will reduce its lifespan.

The normalized diagnostic errors with which the fault can be detected are shown in Fig. 10. After t = 0.55 s, the behavior of these errors for the three fault cases is changed, which means that there is a fault. From Fig. 10,*a*, the ε_{AB} and ε_{CA} errors vary at 0.75 and –0.75 respectively, and ε_{BC} is around 0. From Table 2, the fault is in the S_{A3} switch. The fault can be easily detected using the same reasoning for Fig. 10,*b*,*c*. Furthermore, when the load changes at t = 0.75 s, these errors remain stable at maximum and minimum values.

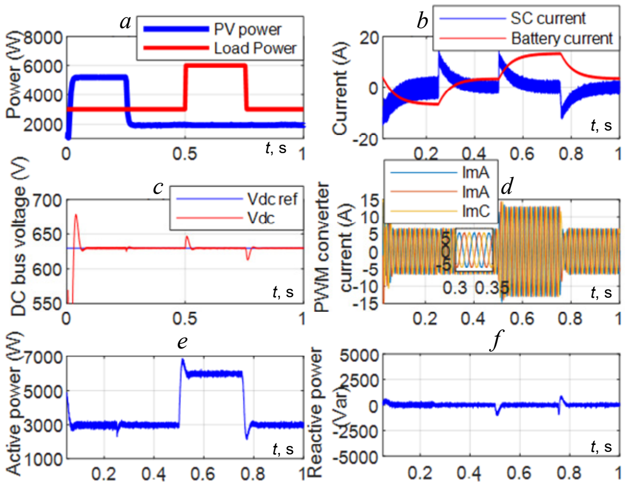

Fig. 6. The overall system behavior without OC fault

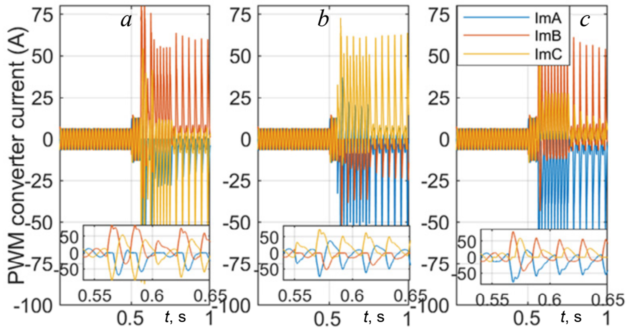

Fig. 7. The output currents of the PWM converter: *a*) OC fault in S_{A3}; *b*) OC fault in S_{B4}; *c*) OC fault in S_{C7}

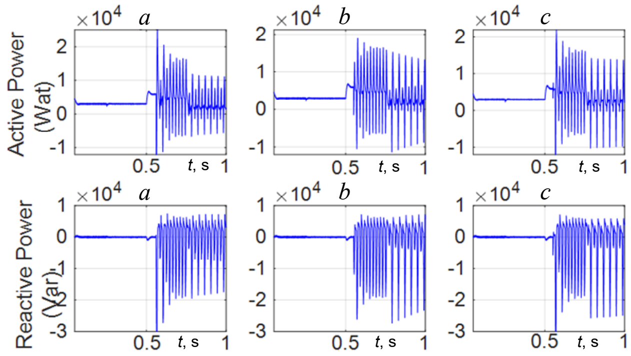

Fig. 8. Effects of an OC fault on active and reactive power: *a*) S_{A3}; *b*) S_{B4}; *c*) S_{C7}

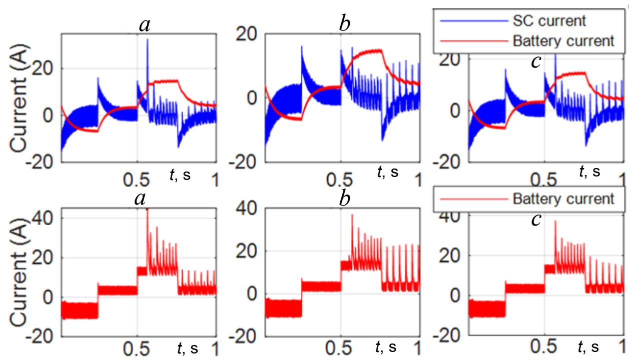

Fig. 9. Comparison between a storage system with and without SC under an OC fault: *a*) S_{A3}; *b*) S_{B4}; *c*) S_{C7}

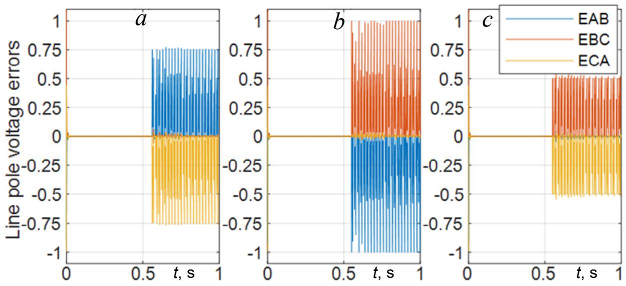

Fig. 10. Normalized diagnostic errors: *a*) S_{A3}; *b*) S_{B4}; *c*) S_{C7}

However, these errors switch between 0 and their maximum and minimum values. For this, Fig. 11 shows after using an algorithm to calculate the maximum and minimum point of each error. It is now easy to locate the fault using Table 3. The fault detection signals are presented in Fig. 12. Note that when the amplitude of the faulty phase detection signal is equal to «1» the fault is in phase *A*, «2» the fault is in phase *B*, and «3» the fault is in phase *C*. When the amplitude of the faulty switch detection signal is equal to «1» the fault is in switch S_{X1}, «2» the fault is in switch S_{X2} and so on, and «8» the fault is in switch S_{X8}. After the occurrence of an OC fault at 0.55 s in a five-level NPC inverter, the proposed method accurately detected it thanks to the six-normalized diagnostic errors. In addition, the time to identify each faulty switch is fast.

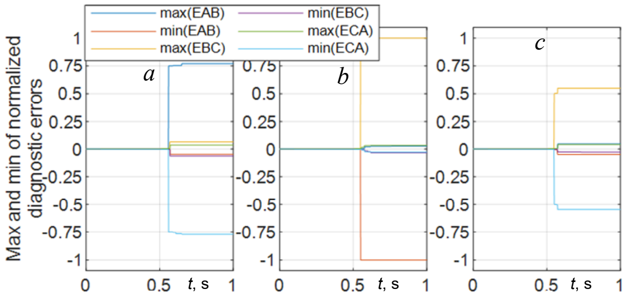

Fig. 11. Maximum and minimum values of the normalized diagnostic errors: *a*) S_{A3}; *b*) S_{B4}; *c*) S_{C7}

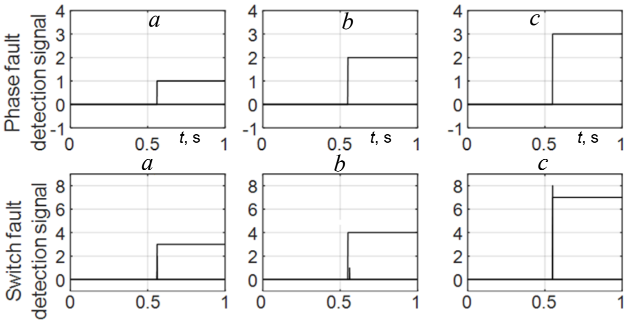

Fig. 12. Fault detection signals for phase and switch: *a*) S_{A3}; *b*) S_{B4}; *c*) S_{C7}

To test the robustness under transient conditions, the fault is shifted to $t = 0.5$ s which is the same time as the load variation. The OC fault is now applied to the switches S_{A5}, S_{B2}, S_{C3}. From Fig. 13,*a*–*c*, the maximum and minimum errors are the same values of Table 3 to detect the fault in switches S_{A5}, S_{B2}, S_{C3}. Therefore, the detection results are shown in Fig. 14,*a*–*c*. Moreover, for an active load fixed at a value of 2 kW with a reactive power of 2 kVAr, it is obvious that the OC fault is well detected, according to Fig. 15, 16.

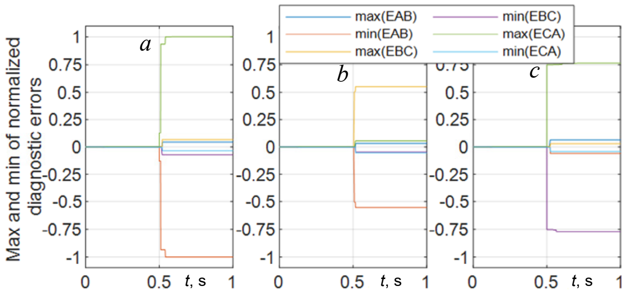

Fig. 13. Max and min values of the normalized diagnostic errors under transient conditions: *a*) S_{A5}; *b*) S_{B2}; *c*) S_{C3}

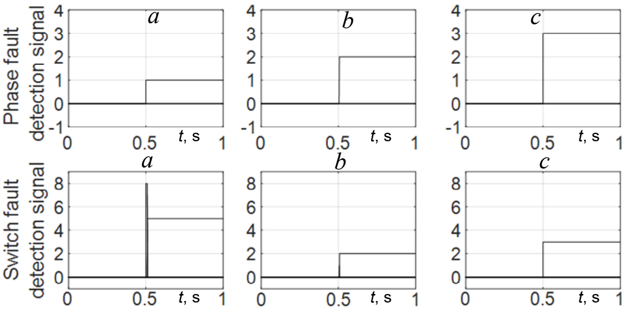

Fig. 14. Fault detection signals for phase and switch under transient conditions: *a*) S_{A5}; *b*) S_{B2}; *c*) S_{C3}

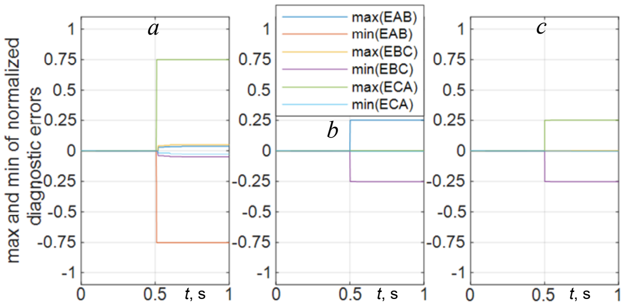

Fig. 15. Max and min values of the normalized diagnostic errors with active (2 kW) and reactive (2 kVAR) load: *a*) S_{A6}; *b*) S_{B8}; *c*) S_{C1}

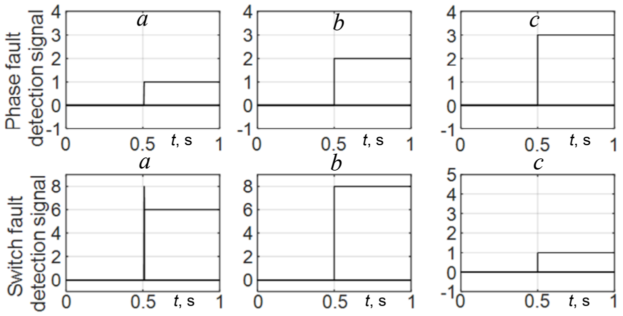

Fig. 16. Fault detection signals for phase and switch with active (2 kW) and reactive (2 kVAR) load: *a*) S_{A6}; *b*) S_{B8}; *c*) S_{C1}

6. Conclusions. A method for detecting an open circuit fault in a five-level neutral point clamped inverter has been proposed. This inverter has been used in a grid-connected photovoltaic system with a Hybrid Energy Storage System. The combination of the battery and supercapacitor improves the overall battery performance in terms of lifetime. Even when the open circuit fault occurs, the supercapacitor absorbs the ripples that are harmful to the battery. The detection method is mainly based on the calculation of the maximum and minimum point of each normalized diagnostic error, which results in six. These six errors are determined by comparing the three measured line-to-line pole voltages with their expected values. The fault in each switch is related to the behavior of all six faults at once. Therefore, it is possible to discriminate the fault in each insulated-gate bipolar transistor through the lookup table. Furthermore, this method can identify the open circuit fault no matter what type of load. It is also robust to transient regimes imposed by solar irradiation and load variations, ensuring system reliability.

Appendix.

PV array parameters: MPPT power P_m = 165 W; inductor filter L_{pv} = 10 mH; cells in series N_s = 8; cells in parallel N_p = 4.

Battery parameters: terminal voltage V_{bat} = 12 V; inductor filter L_{bat} = 8 mH; A·h capacity 100 A·h; internal resistance 1.2 mΩ; batteries in series – 25.

SC parameters: maximum voltage V_{SC} = 2.5 V; inductor filter L_{SC} = 8 mH; internal resistance 3.2 mΩ; nominal capacity 350 F; SC in series – 120.

Utility grid parameters: DC bus capacitance C = 900 µF; coupling inductance L_f = 6.8 mH; grid voltage V_g = 380 V; grid frequency f = 50 Hz.

Conflict of interest. The authors of the article declare that there is no conflict of interest.

REFERENCES

1. Cabrane Z., Kim J., Yoo K., Ouassaid M. HESS-based photovoltaic/batteries/supercapacitors: Energy management strategy and DC bus voltage stabilization. *Solar Energy*, 2021, vol. 216, pp. 551-563. doi: https://doi.org/10.1016/j.solener.2021.01.048.

2. Teleke S., Baran M.E., Bhattacharya S., Huang A.Q. Rule-Based Control of Battery Energy Storage for Dispatching Intermittent Renewable Sources. *IEEE Transactions on Sustainable Energy*, 2010, vol. 1, no. 3, pp. 117-124. doi: https://doi.org/10.1109/TSTE.2010.2061880.

3. Jing W., Hung Lai C., Wong S.H.W., Wong M.L.D. Battery-supercapacitor hybrid energy storage system in standalone DC microgrids: a review. *IET Renewable Power Generation*, 2017, vol. 11, no. 4, pp. 461-469. doi: https://doi.org/10.1049/iet-rpg.2016.0500.

4. Javed K., Ashfaq H., Singh R., Hussain S.M.S., Ustun T.S. Design and Performance Analysis of a Stand-alone PV System with Hybrid Energy Storage for Rural India. *Electronics*, 2019, vol. 8, no. 9, art. no. 952. doi: https://doi.org/10.3390/electronics8090952.

5. Khaligh A., Li Z. Battery, Ultracapacitor, Fuel Cell, and Hybrid Energy Storage Systems for Electric, Hybrid Electric, Fuel Cell, and Plug-In Hybrid Electric Vehicles: State of the Art. *IEEE Transactions on Vehicular Technology*, 2010, vol. 59, no. 6, pp. 2806-2814. doi: https://doi.org/10.1109/TVT.2010.2047877.

6. Roy P.K.S., Karayaka H.B., Yan Y., Alqudah Y. Investigations into best cost battery-supercapacitor hybrid energy storage system for a utility scale PV array. *Journal of Energy Storage*, 2019, vol. 22, pp. 50-59. doi: https://doi.org/10.1016/j.est.2018.12.024.

7. Kong L., Yu J., Cai G. Modeling, control and simulation of a photovoltaic /hydrogen/ supercapacitor hybrid power generation system for grid-connected applications. *International Journal of Hydrogen Energy*, 2019, vol. 44, no. 46, pp. 25129-25144. doi: https://doi.org/10.1016/j.ijhydene.2019.05.097.

8. Choi U.-M., Lee J.-S., Blaabjerg F., Lee K.-B. Open-Circuit Fault Diagnosis and Fault-Tolerant Control for a Grid-Connected NPC Inverter. *IEEE Transactions on Power Electronics*, 2016, vol. 31, no. 10, pp. 7234-7247. https://doi.org/10.1109/TPEL.2015.2510224.

9. Himour K., Ghedamsi K., Berkouk E.M. Supervision and control of grid connected PV-Storage systems with the five level diode clamped inverter. *Energy Conversion and Management*, 2014, vol. 77, pp. 98-107. doi: https://doi.org/10.1016/j.enconman.2013.09.001.

10. Yang G., Fu C., Yi H., Chai C., Huang B., Hao S., Chen Z. Direct power control of three-level NPC grid-connected system combined with fault-tolerant technology. *Microelectronics Reliability*, 2018, vol. 88-90, pp. 1057-1062. doi: https://doi.org/10.1016/j.microrel.2018.07.140.

11. Jlassi I., Estima J.O., Khojet El Khil S., Mrabet Bellaaj N., Marques Cardoso A.J. Multiple Open-Circuit Faults Diagnosis in Back-to-Back Converters of PMSG Drives for Wind Turbine Systems. *IEEE Transactions on Power Electronics*, 2015, vol. 30, no. 5, pp. 2689-2702. doi: https://doi.org/10.1109/TPEL.2014.2342506.

12. Zhou D., Yang S., Tang Y. A Voltage-Based Open-Circuit Fault Detection and Isolation Approach for Modular Multilevel Converters With Model-Predictive Control. *IEEE Transactions on Power Electronics*, 2018, vol. 33, no. 11, pp. 9866-9874. doi: https://doi.org/10.1109/TPEL.2018.2796584.

13. Rehman H., Tariq M., Sarwar A., Alhosaini W., Hossain M.A., Batiyah S.M. Single-Phase Fault Tolerant Multilevel Inverter Topologies – Comprehensive Review and Novel Comparative Factors. *Energies*, 2022, vol. 15, no. 24, art. no. 9319. doi: https://doi.org/10.3390/en15249319.

14. Li H., Guo Y., Xia J., Li Z., Zhang X. Open-circuit fault diagnosis for a fault-tolerant three-level neutral-point-clamped STATCOM. *IET Power Electronics*, 2019, vol. 12, no. 4, pp. 810-816. doi: https://doi.org/10.1049/iet-pel.2018.5802.

15. Abadi M.B., Mendes A.M.S., Cruz S.M.A. Three-level NPC inverter fault diagnosis by the Average Current Park's Vector approach. *2012 XXth International Conference on Electrical Machines*, 2012, pp. 1893-1898. doi: https://doi.org/10.1109/ICElMach.2012.6350140.

16. Mendes A.M.S., Abadi M.B., Cruz S.M.A. Fault diagnostic algorithm for three-level neutral point clamped AC motor drives, based on the average current Park's vector. *IET Power Electronics*, 2014, vol. 7, no. 5, pp. 1127-1137. doi: https://doi.org/10.1049/iet-pel.2013.0416.

17. Chao K.-H., Ke C.-H. Fault Diagnosis and Tolerant Control of Three-Level Neutral-Point Clamped Inverters in Motor Drives. *Energies*, 2020, vol. 13, no. 23, art. no. 6302. doi: https://doi.org/10.3390/en13236302.

18. Abid M., Laribi S., Larbi M., Allaoui T. Diagnosis and localization of fault for a neutral point clamped inverter in wind energy conversion system using artificial neural network technique. *Electrical Engineering & Electromechanics*, 2022, no. 5, pp. 55-59. doi: https://doi.org/10.20998/2074-272X.2022.5.09.

19. Abadi M.B., Mendes A.M.S., Cruz S.M.A. Method to diagnose open-circuit faults in active power switches and clamp-diodes of three-level neutral-point clamped inverters. *IET Electric Power Applications*, 2016, vol. 10, no. 7, pp. 623-632. doi: https://doi.org/10.1049/iet-epa.2015.0644.

20. Caseiro L.M.A., Mendes A.M.S. Real-Time IGBT Open-Circuit Fault Diagnosis in Three-Level Neutral-Point-Clamped Voltage-Source Rectifiers Based on Instant Voltage Error. *IEEE Transactions on Industrial Electronics*, 2015, vol. 62, no. 3, pp. 1669-1678. doi: https://doi.org/10.1109/TIE.2014.2341558.

21. Yu Y., Li X., Wei L. Fault Tolerant Control of Five-Level Inverter Based on Redundancy Space Vector Optimization and Topology Reconfigruation. *IEEE Access*, 2020, vol. 8, pp. 194342-194350. doi: https://doi.org/10.1109/ACCESS.2020.3033805.

22. Abdellah A., Toumi D., Larbi M., Moreau S. Zero-Compensator Filter for Power Sharing Between Battery/Supercapacitor in a Grid-Connected Photovoltaic System. *Advances in Electrical and Electronic Engineering*, 2022, vol. 20, no. 2, pp. 154-169. doi: https://doi.org/10.15598/aeee.v20i2.4321.

23. Mostafa H.H., Ibrahim A.M., Anis W.R. A performance analysis of a hybrid golden section search methodology and a nature-inspired algorithm for MPPT in a solar PV system. *Archives of Electrical Engineering*, 2019, vol. 68, no. 3, pp. 611-627. doi: https://doi.org/10.24425/aee.2019.129345.

24. Jing W., Lai C.H., Wong W.S.H., Wong M.L.D. Dynamic power allocation of battery-supercapacitor hybrid energy storage for standalone PV microgrid applications. *Sustainable Energy Technologies and Assessments*, 2017, vol. 22, pp. 55-64. doi: https://doi.org/10.1016/j.seta.2017.07.001.

25. Manandhar U., Tummuru N.R., Kollimalla S.K., Ukil A., Beng G.H., Chaudhari K. Validation of Faster Joint Control Strategy for Battery- and Supercapacitor-Based Energy Storage System. *IEEE Transactions on Industrial Electronics*, 2018, vol. 65, no. 4, pp. 3286-3295. doi: https://doi.org/10.1109/TIE.2017.2750622.

26. Ali A.I.M., Mohamed H.R.A. Improved P&O MPPT algorithm with efficient open-circuit voltage estimation for two-stage grid-integrated PV system under realistic solar radiation. *International Journal of Electrical Power & Energy Systems*, 2022, vol. 137, art. no. 107805. doi: https://doi.org/10.1016/j.ijepes.2021.107805.

Received 24.11.2022
Accepted 03.03.2023
Published 02.11.2023

Abderrahmane Abdellah[1], *PhD Student,*
M'hamed Larbi[1], *Full Professor,*
Djilali Toumi[1], *Senior Lecturer,*
[1] Department of Electrical Engineering,
L2GEGI Laboratory, University of Tiaret, Algeria,
e-mail: abderrahmane.abdellah@univ-tiaret.dz (Corresponding Author);
larbi_mh@yahoo.fr; toumi_dj@yahoo.fr

How to cite this article:

Abdellah A., Larbi M., Toumi D. Open circuit fault diagnosis for a five-level neutral point clamped inverter in a grid-connected photovoltaic system with hybrid energy storage system. *Electrical Engineering & Electromechanics*, 2023, no. 6, pp. 33-40. doi: https://doi.org/10.20998/2074-272X.2023.6.06

UDC 621.314 https://doi.org/10.20998/2074-272X.2023.6.07

O.I. Khrysto

Current-voltage characteristics of single-stage semiconductor magnetic pulse generators with a distinctive structure of the conversion link in the input circuit

***Introduction**. The main feature of the semiconductor magnetic pulse generators (SMPGs) is a slow accumulation of energy in the primary capacitor and its rapid introduction into the load by using a series of sequentially connected magnetic compression stages. Initially, these devices were mainly used for pumping gas lasers, but over the last decade SMPGs have been increasingly used in electric discharge technologies for water purification and air ionization to remove toxic impurities. At the same time, along with the practice of using these devices, development has also been achieved in the principles of their design and methods of mathematical modeling. **Problem**. The main drawback of the existing theory of SMPG's stationary oscillations mode is an adoption of the saturable reactor (SR) model in approximation of the static magnetization curve of its core, as well as unidirectional nature of the energy transfer from the generator to the load. In most publication the exchange processes between the power source and SR are still not covered. **Goal**. Study of electrical and energy characteristics of low-voltage single-stage SMPG devices with series and parallel conversion stages in the charging circuit. **Methodology**. To achieve the set goal, this work uses comprehensive approach relayed on technical tools of setting up the experiment, numerical methods for processing measurement results, as well as an analytical method for describing electromagnetic processes in single-stage SMPG circuits. **Results**. The closed current-voltage characteristics of the SR are obtained, according to which the numerical calculations of the integral magnetic and energy characteristics of the proposed models are carried out. The features of the longitudinal capacitance charging process in a SMPG's circuit with a parallel conversion stage, which occurs simultaneously in two adjacent circuits, are explained. Analytical expressions to describe the dynamics of magnetic flux density in the SR's core as a time-depended function are derived. Based on the obtained hysteresis curve of the core, the exchange processes of energy transfer between the power source and the SR are explained. **Practical value**. The results of the research can be applied in the development of low-voltage SMPG circuits with improved energy-dynamic parameters.* Reference 15, figures 8.

Key words: **semiconductor magnetic pulse generator, commutating choke, conversion link, electrical and energy characteristics, displacement current, energy losses dynamics.**

У роботі проведено експериментальне дослідження одноступеневих магнітно-напівпровідникових генераторів імпульсів з відмітною структурою зарядно-розрядного перетворювача у вхідному контурі. Наведено електричні параметри кожної схеми, відмічено фізичні й конструктивні особливості комутуючого дроселя вихідної ланки компресії імпульсів, та описано технічні засоби проведення експерименту. Отримано замкнуті вольт-амперні характеристики комутуючого дроселя, відповідно до яких проведено числові розрахунки інтегральних магнітних та енергетичних характеристик запропонованих моделей. Виведено аналітичні вирази для опису динаміки магнітної індукції в осерді дроселя за часом. На основі кривої гістерезису осердя роз'яснено обмінні процеси передачі енергії між джерелом живлення та комутуючим дроселем. Розглянуто енергетичні характеристики магнітно-напівпровідникових генераторів імпульсів в залежності від струму підмагнічування. Пояснено особливості заряду повздовжньої ємності у схемі з паралельною перетворювальною ланкою, що відбувається одночасно у двох суміжних колах. Отримано залежності споживаної потужності від напруги джерела живлення та виконано аналіз цих характеристик за різним співвідношенням між повздовжньою та поперечною ємністю суміжних ланок компресії імпульсів. Результати досліджень можуть бути застосовані при розробці низьковольтних магнітно-напівпровідникових генераторів імпульсів з поліпшеними енергодинамічними параметрами. Бібл. 15, рис. 8.

Ключові слова: **магнітно-напівпровідниковий генератор імпульсів, комутуючий дросель, перетворювальна ланка, електричні та енергетичні характеристики, зсувний струм, динаміка втрат енергії.**

Problem definition. The research presented is a continuation of the author's previous cycle of works on this topic [1, 2], which highlights the principles of construction, physical and mathematical modelling of semiconductor magnetic pulse generators (SMPGs), both high and low voltage, with the aim of finding more rational circuit solutions, special modes of their operation and methods of efficient energy transfer from the generator to the load.

Analysis of recent research and publications. SMPGs belong to the class of converting technology devices that serve to amplify the peak power of the pulse on the load [3, 4]. They are widely used in a number of electric discharge technologies, where it is necessary to have powerful current pulses of submicrosecond duration with a sharp leading edge, for example, for powering microwave devices or pumping gas lasers on metal vapors [5, 6]. In recent years, the relevance of using these devices has increased significantly with the need for air purification from sulfur dioxide [7, 8] and wastewater disinfection [9, 10]. The steady-state mode of electromagnetic oscillations in SMPGs is mainly achieved under the condition of amplitude asymmetry between the main and return pulses, while the energy transfer processes between pulse compression links are usually considered assuming their unidirectionality from the generator to the load [11]. Mathematical modelling allows the application of approximation by the magnetization curve of the commutating choke (saturable reactor, SR*)*, however, it still remains «static» [12, 13], i.e. in approximation to the slow process of magnetization of its core, and allows to obtain only an indirect judgment about the characteristics of the magnetic flux density and the dynamics of losses energy for remagnetization in the SR core. As is known from [14], the conversion link of the charging circuit and the first link of pulse compression determine the mode of operation of the generator, while the role of the following magnetic compression elements is to bring the pulse to a certain duration. Therefore, in the current work, attention is focused on the experimental study of single-stage SMPGs, which differ in the conversion link in the input circuit. Moreover, in contrast to previous mathematical models of various variants of SMPG, these studies are defined as experimental, as superior in terms of their availability and effectiveness.

Separation of the previously unsolved part of the tasks. Despite the large number of publications on this topic, the processes of energy exchange between the power source and the SR, which noticeably increase with the increase of the displacement currents caused by the asymmetric mode of electromagnetic oscillations in various SMPG circuits, have remained aside.

The goal of the work is to study the electrical and energy characteristics of single-stage SMPGs with a distinctive converting link (serial or parallel) of electricity in the input circuit.

Research methods. Physical modelling of electromagnetic processes using appropriate technical means; numerical and analytical modelling; data processing by means of Excel.

Main material. In the work, an analysis of low-voltage (up to 1 kV output voltage) SMPGs with a series pulse compression link on the load, which differ in the structure of the charge-discharge converter in the input circuit and the method of restoring the magnetic flux density in the core of the SR to the initial state, is carried out. Based on the theoretical models of high-voltage SMPGs, considered in the previous work of the author [15], the basis of this study was precisely various options for the construction of the input converter of electricity, separating the part of the device that contains the voltage increase link (high-voltage transformer). These converters can be conventionally divided into one- and two-key, containing a series, parallel, or series-parallel link in the input circuit of the SMPG. The main advantage of a parallel energy conversion link over a serial one is that in order to achieve remagnetization of the SR, it is not necessary to use an additional source of energy that generates a magnetizing current in its main winding, but on the contrary, the process of forming a reverse pulse occurs at the expense of the energy of the main power supply.

The circuit of the first version of the SMPG, which contains a series conversion link C_0-VT_0-VD_0-L_0 in the charging circuit and an additional source of displacement current E_b is shown in Fig. 1.

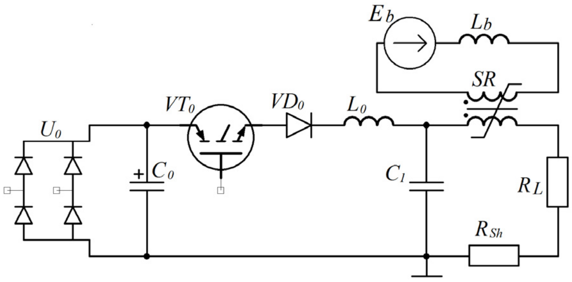

Fig. 1. Magnetic generator with series link in the charging circuit

The input of the device also contains a diode rectifier U_0 and a battery of capacitors C_0 with total capacity of 1 mF. Mains voltage to the diode rectifier is supplied through a step-down autotransformer, which allows for smooth adjustment of the input DC voltage. The charging choke L_0 must provide constant inductance, so it is designed on a ring magnetic core made of sprayed iron. The circuit was calculated based on the maximum accumulated energy stored in C_1, the duration of the input pulse and the compression ratio of the SR. For the parameters of the charging circuit of 32 μH and 1 μF, the duration of the current in this link is 10 μs. As the core of the SR, a ribbon magnetic core made of cobalt alloy (overall dimensions 50×34×30 mm) was used, which has high coefficient of rectangularity of the magnetic hysteresis loop. Taking into account the volume of the magnetic core – $V_m = 3.2\cdot10^{-5}$ m^3, the range of the magnetic flux density – $\Delta B = 0.8$ T, and the relative magnetic permeability in its saturated state – $\mu_S = 5$, the compression ratio of the output link was $x_k = 3.4$ The generator was loaded with linear resistance $R_L = 12$ Ω, consisting of two parallel-connected low-inductance resistors, with total power of 120 W. The power supply sets the displacement current in the additional winding of the SR, which is connected through the decoupling choke L_b, which is designed to eliminate the variable component of the secondary winding of the SR. The inductance of the decoupling choke is 10 mH. The displacement current I_{bc} was set constant at the level of 1.5 A to ensure fast enough remagnetization of the SR.

A bifilar R_{Sh} current shunt with resistance of 0.16 Ω and a 1:10 voltage divider of a mixed type (resistive-capacitive) were used to measure the current-voltage characteristics of the SR. All measurements were made relative to the negative bus of the device, so the current shunt was located in the cut between C_1 and R_L. As indicated in Fig. 1, according to this variant of the SR placement, to measure the voltage on it, it is necessary to have a voltage difference between C_1 and R_L, but this complicates the calculation process due to the need for exact synchronization of three signals at once (SR current, voltage on R_L, voltage on C_1). If we place the SR in series near the shunt on the negative bus, then the voltage on its winding will be determined by subtracting the voltage drop on the shunt itself, which will facilitate further numerical calculations. Current signals on the shunt U_{Sh} and voltage on the SR U_{SR} are supplied through coaxial lines to the inputs of a two-channel memory oscilloscope SDS1022, which has a common negative terminal between its channels. Digitized data were stored in text format and transferred to Excel for mathematical calculations. The number of sampling points provided by the oscilloscope on each channel is 10^3 with interval of 40 ns and amplitude value in millivolts. Since the signals have an asymmetric shape, for their correct output on the oscilloscope screen, it is necessary to ensure the deviation of the position of the rays of these signals from the zero position, so the digitization results were transformed taking into account the vertical shift on each channel of the oscilloscope and the transmission coefficient on each signal according to the appropriate formulas:

$$U_c = (U_i - U_b)/100\,, \qquad (1)$$

$$I_c = (I_i - I_b)/160\,, \qquad (2)$$

where U_i, I_i are the discretized values of the voltage and current signals of the SR; U_b, I_b are shifts to compensate for the deviation in mV; U_c, I_c are the normalized values of the voltage and current of the SR.

Below are the main formulas for calculation (analysis) of one-stage SMPG, which are applied in the Excel program.

Formulas for calculating SR with toroidal core:

Cross section of the core:

$$S_c = h \cdot (D - d)/2 \,, \tag{3}$$

where D, d, h are, respectively, the outer and inner diameters and height of the core.

The length of the middle line:

$$\ell_c = \pi \cdot (D + d)/2 \,. \tag{4}$$

The magnetic field strength:

$$H = (w \cdot I_c)/\ell_c \,, \tag{5}$$

where I_C is the current through the choke winding, w is the number of its turns.

The inductance of the choke with a uniformly distributed winding on the core:

$$L_{SR} = \mu_r \mu_0 \frac{w^2 \cdot S_c}{\ell_c} \,. \tag{6}$$

The magnetic flux density is proportional to the integral of the voltage on its winding and is defined as:

$$B = B_0 + \frac{1}{w \cdot S_c} \int U_c \mathrm{d}t \,, \tag{7}$$

where U_c is the voltage on the choke winding, B_0 is the initial magnetic flux density in the SR core.

The energy of the external power source spent on remagnetization of the core can be determined by the following equivalent expressions:

$$E_m = \int_0^{\tau} U_c \cdot I_c \cdot \mathrm{d}t = V_m \cdot \int_{-B}^{+B} \mathrm{d}B \cdot H \,, \tag{8}$$

where τ is the time at which a complete cycle of the passage of the hysteresis curve $B(H)$ occurs; V_m is the volume of the magnetic core of the SR.

For the integrals in the specified expressions, it is possible to approximate using the trapezoidal approximation method:

$$E_m = \frac{V_m}{2} \sum_{k=0}^{k=n} \left(H^{k+1} + H^k\right) \cdot \left(B^{k+1} + B^k\right), \tag{9}$$

where H^k, B^k are the discrete values of the magnetic field strength and the magnetic flux density in the core of the SR.

On the basis of the converted current and voltage signals of the SR, closed current-voltage characteristics were constructed for three values of the input voltage (U_{in} =120, 150, 180 V), which are shown in Fig. 2,*a*. A common feature of the obtained curves is their positive shift relative to the current axis and the same contour of the negative loop of the 3rd quadrant, which reproduces the process of forming the reverse polarity pulse. A distinctive feature is the growing contour of the hysteresis loops located in the 1st quadrant. The integral calculation of these curves takes place according to the time arrow starting from the zero position of the coordinate system. The area of each curve is proportional to the energy consumed by the power source, therefore, it can be argued that the difference between the areas of the 1st and 3rd quadrants will be directly proportional to the energy dissipated on the SR. The dependence of the magnetic flux density on the magnetic field strength and the dynamics of energy losses in the SR core was calculated according to the formulas indicated above, and the results are shown in Fig. 2,*b*. According to the obtained graphs, it is possible to note the tendency of the gradual expansion of the hysteresis area of the SR core with an increase in the input voltage, which is associated with an increase in the charge rate of C_1.

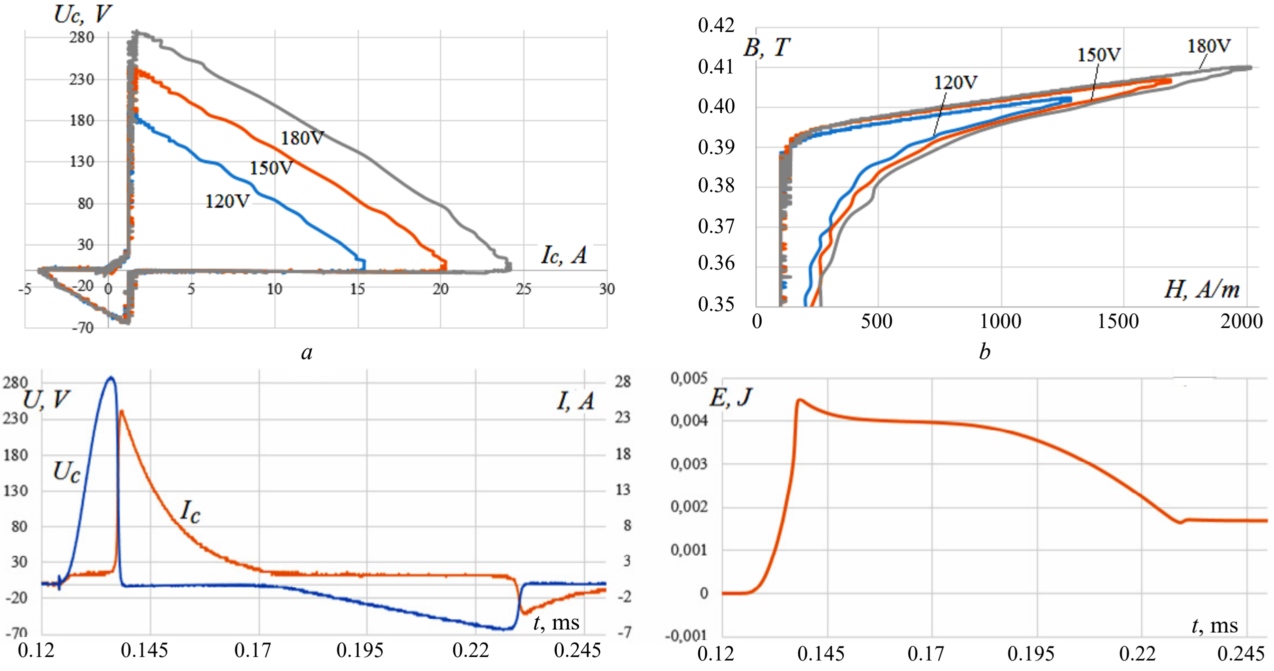

Fig. 2. Electromagnetic characteristics of the SR: *a*) current-voltage characteristics; *b*) magnetic flux density in the core; *c*) voltage and current oscillograms; *d*) dynamics of remagnetization energy

The maximum amplitude of the charge of the capacity C_1 from the capacity of the power source C_0 is determined according to the derived expression:

$$U_{\max}(t_1) = U_{C1} + \frac{U_{c0} - U_{c1}}{L_0 \cdot \omega_1 \cdot C_1} \cdot \left(\frac{\omega_1}{\alpha_1^2 + \omega_1^2} \cdot \exp(\alpha_1 \cdot t_1) \right), \quad (10)$$

where the cyclic frequency of oscillations of the charging circuit ω_1, the duration of its half-wave t_1 and the attenuation decrement α are determined respectively as

$$\omega_1 = \frac{\sqrt{\left| R_0^2 \cdot C_0^2 \cdot C_1^2 - 4 \cdot L_0 \cdot C_0 \cdot C_1 \cdot (C_0 + C_1) \right|}}{2 \cdot L_0 \cdot C_0 \cdot C_1}; \quad (11)$$

$$t_1 = \pi / \omega; \quad \alpha = -R_0 / 2 \cdot L_0 .$$

If we assume that the current through the SR on the main magnetization curve has a sufficiently small value compared to the current in its saturation, then the law of change of magnetic flux density in its core will be determined by the voltage on the capacitor C1 and can be written as:

$$B(t) = -B_s + \frac{1}{S_m \cdot w_1} \cdot \left(\begin{array}{l} U_{C0} \cdot t + \\ + \dfrac{U_{c1} - U_{c0}}{L_0 \cdot \omega_1 \cdot C_1} \cdot \dfrac{\omega_1^2}{\left(\alpha_1^2 + \omega_1^2 \right)^2} \times \\ \times \exp(\alpha_1 \cdot t) \cdot \sin(\omega_1 \cdot t) \end{array} \right). \quad (12)$$

The process of returning the magnetic flux density to the initial state occurs due to the action of the magnetization current I_{bc} from the source E_b in its additional winding w_2, which accordingly transforms the displacement current into the main winding w_1 equal to:

$$i_b = -I_{bc} \cdot w_1 / w_2 . \quad (13)$$

This current will create linearly increasing voltage on C_1 of reverse polarity before the appearance of an operating pulse, which is described by a linear law:

$$U_{C1} = -\frac{I_{bc} \cdot w_1}{C_1 \cdot w_2} t . \quad (14)$$

Integrating this equation over time in accordance with (7), we obtain the expression for the magnetic flux density on the reverse remagnetization interval:

$$B(t) = B_s - \frac{I_{bc} \cdot w_1}{2 \cdot S_c \cdot w_1 \cdot C_1 \cdot w_2} t^2 , \quad (15)$$

where B_s is the magnetic flux density of the SR core saturation.

That is, in the reverse process, the magnetic flux density will change according to the parabolic law, and its full dynamics is shown in Fig. 3,*b*.

As noted in Fig. 3,*a*, the hysteresis loop has a positive shift along the axis of the magnetic field strength due to the magnetization current, which affects the energy interaction between the power source and the SR core, which stores the energy of the magnetic field. According to the obtained graph of energy losses due to remagnetization of the core (Fig. 2,*d*), the hysteresis curve can be divided into sections where the work of the external power source has both positive and negative values. In the field section from residual magnetic flux density to positive saturation magnetic flux density (curve 1–2 in Fig. 3,*a*), the work of the external power source (energy of capacitor C_1) is performed due to magnetization of the core, with dB>0 and H>0, so the resulting energy gain according to (9) dE_m>0. At the moment of saturation of the SR and the introduction of energy into the R_L load, a slight its increase is observed in the graph of the dynamics of energy loss (Fig. 2,*d*). But already at the stage of formation of the reverse voltage, a significant part of the energy accumulated in the core of the SR will return to the power source (curve 2–3 in Fig. 3,*a*), because in this section the fields dB<0 and H>0, and the resulting increase in energy losses, respectively, is dE_m<0. At the moment of reaching the magnetic flux density of the opposite value –B_s, the work of the power source will also be positive (dB<0, H<0), because the magnetic field strength becomes negative, which is noted on the curve (Fig. 2,*d*) by its slight increase (curve 3–4), but this increase will be compensated at the stage of formation of a new operating pulse (curve 4–3).

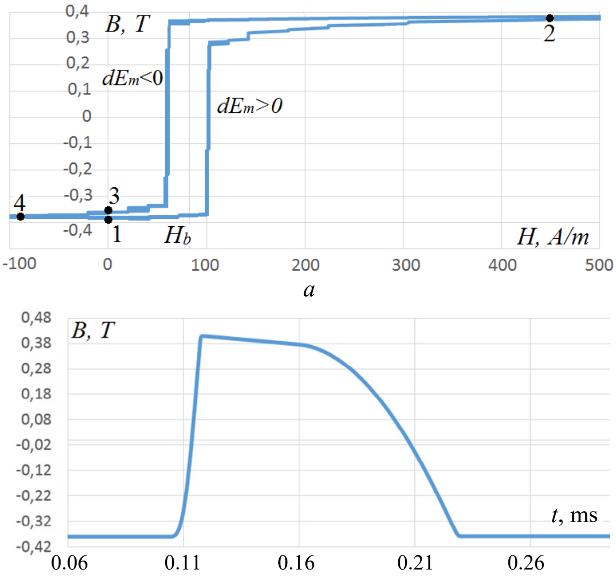

Fig. 3. *a* – magnetic hysteresis loop with shift by H;
b – dynamics of magnetic flux density B over time

The principle of operation of the SMPG circuit in the absence of magnetization current differs in that the amplitude of the output pulse decreases, but at the same time the power consumption increases depending on the input rectified voltage on the C_0 capacitor, which is shown in Fig. 4. In this mode, the SR operates by a partial magnetization curve, therefore the working drop of the magnetic flux density in the core is reduced and, accordingly, the delay in its saturation, which gradually disappears completely, and the characteristic of the peak pulse voltage reaches its saturation. Since there is no time delay between the closing of the transistor VT_0 and the saturation of the SR, the discharge current will be closed not only along the C_1–SR–R_L circuit but also along the C_0–VT_0–SR–R_L circuit, which will additionally increase the energy of the pulse at its amplitude even lower for the input one.

The following SMPG circuit is already based on a parallel conversion element and a charging choke in the input circuit. This version of the device allows to avoid the use of an additional source of displacement current, but with the difference from the previous version of the SMPG that it generates pulses of inverse polarity on the load. In the circuit (Fig. 5), the mains alternating voltage from the autotransformer, the diode rectifier and the electrolytic capacitor are combined into one element and represented by a constant voltage source E_0.

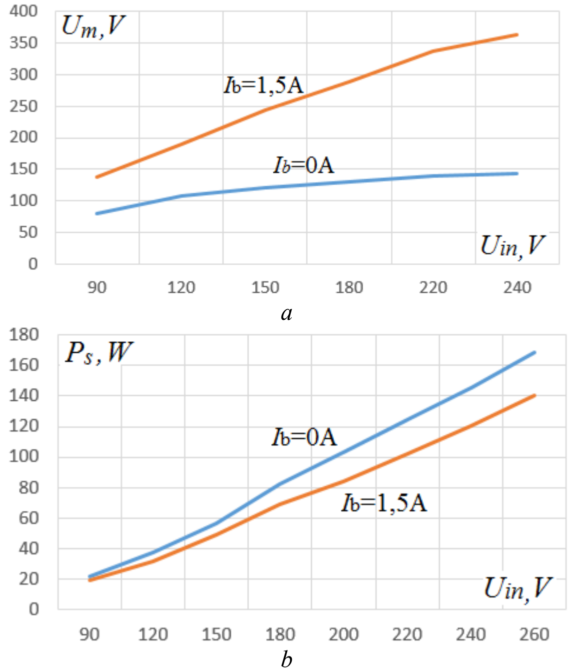

Fig. 4. Characteristics of the amplitude value of the pulse voltage U_m on the load (*a*) and the power consumption of the device P_s (*b*) depending on the constant input voltage U_{in} on C_0

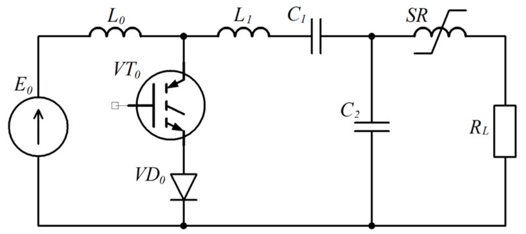

Fig. 5. SMPG circuit with parallel conversion link in the input circuit

A distinctive feature of the SR circuit with parallel conversion link is that its closed current-voltage characteristics (Fig. 6) become directly opposite to the characteristics of the first version of the SMPG, namely, the working and return pulses are described in the 3rd quadrant and the 1st quadrant of the system coordinates, respectively. The characteristics have a negative current shift, but unlike the previous SMPG model, this shift turns out to be dependent on the input voltage of the power supply E_0.

When approaching the ideal model of the SR, the charge-discharge processes in the circuit can be considered separately and divided into several intervals along separate circuits. When VT_0 is unlocked in the circuit C_1–L_1–VT_0–C_2, the discharge process of C_1 to C_2 begins with partial energy transfer, due to the presence of charging current from the power source, therefore, after locking VT_1, there will be residual voltage on C_1. This process is shown in Fig. 7,*a*, where the voltage on the capacitor C_1 is obtained as a result of the calculation, as the difference between the numerical data of the voltages on VT_0 and C_2.

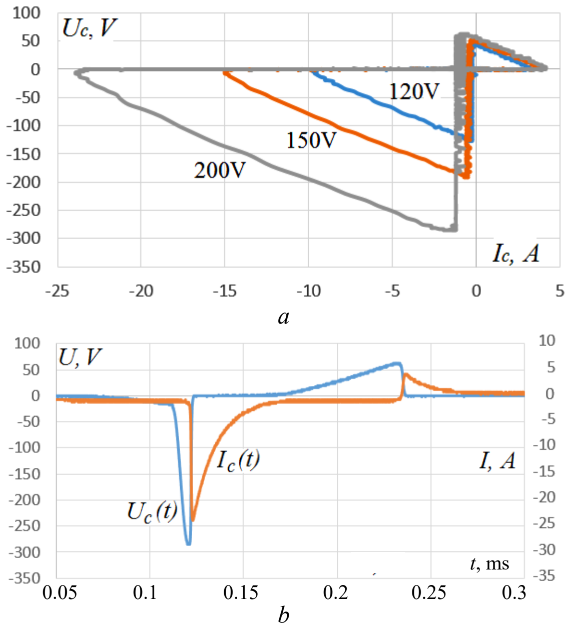

Fig. 6. Electrical characteristics of the SR: *a* – closed current-voltage characteristics; *b* – oscillograms of voltage and current

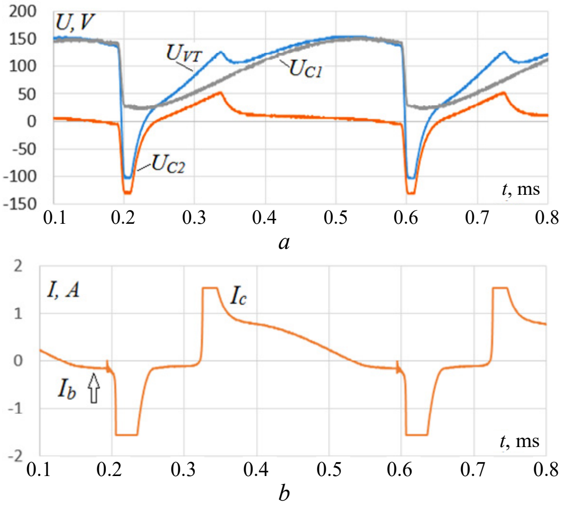

Fig. 7. *a* – voltage characteristics on capacitors; *b* – characteristic of the current through the SR

After blocking VT_0, the charging phase of series-connected C_1 and C_2 in the circuit E_0–L_0–L_1–C_1–C_2 begins. Due to the relatively low natural frequency of oscillations of this circuit, the voltage on C_2 increases almost linearly. At the same time, the magnetic flux density in the core of the SR changes its value to the opposite, and when saturation magnetic flux density is reached, C_2 energy is reset to the load. At this stage, the charging current will be closed to the load through the inductance of the saturated SR winding within the circuit E_0–L_0–L_1–C_1–SR–R_L. Here, the capacity C_1 continues to charge according to the oscillating law to its maximum value, and the voltage on C_2 will remain at the residual level due to its shunting to the load by the SR winding. The current in the SR winding as shown in Fig. 7,*b*, also displays part of the charge current of capacitor C_1. When the voltage on C_1 reaches its maximum value, the current through the SR changes its direction and relatively small displacement biasing current I_b is formed, which, as it turns out, depends on the voltage of the power source.

At this stage, the SR core leaves the state of reverse saturation and, in the process of charging C_2, is magnetized along the main curve to the opposite saturation limit. Since the C_1 charge process occurs simultaneously in two circuits, for the analytical determination of the displacement current through the SR winding, it is necessary to solve the characteristic equation of the 4th order and find the unknown coefficients of the harmonic equations, which complicates the calculation process enough. Considering the fact that the inductance of the outer circuit consists of L_0 and the inductance of the SR in its unsaturated state, when the relative permeability of its core is sufficiently large ($\mu = 10^5$), its oscillation frequency will be lower than the frequency of the inner circuit. In addition, the initial voltage difference between C_0 and C_1 will be higher for the inner circuit, so the displacement current through the SR will be a smaller part of the charging current of C_1. Therefore, it can be assumed that the displacement current of the external circuit will modulate the charging current of C_1 until the moment of saturation of the SR from the linearly increasing voltage on C_2. Thus, the oscillatory processes in the considered circuits can be described by similar analytical expressions specified above, taking into account the parameters of each circuit. For example, for the above charging circuit with E_0–L_0–L_1–C_1–SR–R_L, its cyclic frequency ω_2 and attenuation decrement α_2 can be found by the formulas:

$$\omega_2 = \frac{\sqrt{\left| \begin{aligned} & R_L^2 \cdot C_0^2 \cdot C_1^2 \cdot C_2^2 - 4 \cdot (L_0 + L_1 + L_{SR}) \times \\ & \times C_0 \cdot C_1 \cdot C_2 \cdot (C_0 \cdot C_1 + C_1 \cdot C_2 + C_0 \cdot C_2) \end{aligned} \right|}}{2 \cdot (L_0 + L_1 + L_{SR}) \cdot C_0 \cdot C_1 \cdot C_2}; \quad (16)$$

$$\alpha_2 = -\frac{R_L}{2 \cdot (L_0 + L_1 + L_{SR})}.$$

The maximum voltage on each capacitor is determined according to (10), but taking into account the algebraic sum of the initial values of the voltages on the three capacitors U_{C0}–U_{C1}–U_{C2} and the sum of the inductances L_0+L_1+L_{SR} of this circuit. The value of the displacement current through the SR is approximately determined as:

$$i_b(t) = \frac{U_{C0} - U_{C1}}{(L_0 + L_{SR}) \cdot \omega_2} \sin(\omega_2 \cdot t) \cdot \exp(\alpha_2 \cdot t), \quad (17)$$

where the inductance L_{SR} is determined by the formula, as for the toroidal core (6). It was determined that the initial voltage U_{C1} on the capacitor C_1 is the maximum voltage when the core is magnetized L_{SR}.

It was established that due to the fact that the C_1 charge occurs according to the oscillatory law, the dependence of the output pulse amplitude on the switching frequency of the transistor is observed. In the frequency range from 1.2 to 1.8 kHz, the amplitude of the main pulse is significantly weakened, which is accompanied by a decrease in power consumption. By the time of the new switching of VT_0 due to the oscillating charge of C_1, the capacity C_2 has time to recharge again and therefore another pair of pulses of the main and reverse polarity is formed. It was found that if the switching region of VT_0 coincides with the moment of formation of the demagnetization pulse, then the charging current of C_2 will be shunted by the inductance of the saturated SR, which causes a significant decrease in the working pulse. In another case, when the moment of switching coincides or occurs before the moment of recharging C_2, the amplitude of the pulse on it only increases. According to this study, it was established that for the correct operation of the device, the generation frequency should be at least 2-2.5 kHz.

The dependencies of the power consumption characteristics and the output pulse amplitude on the input voltage of the power source at the generation frequency of 2.5 kHz for 3 values of the transverse capacitance C_2 and the fixed capacitance C_1 = 1 μF are shown in Fig. 8.

The obtained graphs can be analyzed as follows, namely: an increase in the capacity C_2 from 0.5 to 1.5 μF leads to a deeper discharge of the capacitor C_1, therefore the charging voltage drop on it becomes more significant, which causes an increase in the charging current and power consumption of the SMPG. When C_1<C_2, the pulses on the load become longer and are characterized by a decrease in their amplitude (Fig. 8,*b*). On the contrary, for C_1>C_2, the capacity C_1 is no longer completely discharged, therefore, a significant residual voltage is formed on it, which reduces the jump in the charging current. It can be noted that the power characteristic grows according to quadratic laws and corresponds to the energy accumulated in C_1 at the time of switching VT_0. Calculations also showed that the dependencies of energy losses in the core on the input supply voltage are characterized by the presence of their threshold value, after which the energy losses stop increasing, which can occur in the case of the hysteresis loop of the SR core reaching its maximum expansion. The maximum energy losses in the SR core during one magnetization cycle for this SMPG circuit at input voltage of 280 V do not exceed 1.5 mJ. The considered circuit solutions of low-voltage semiconductor magnetic pulse generators are expedient to be used in modern advanced electroimpulse material processing technologies.

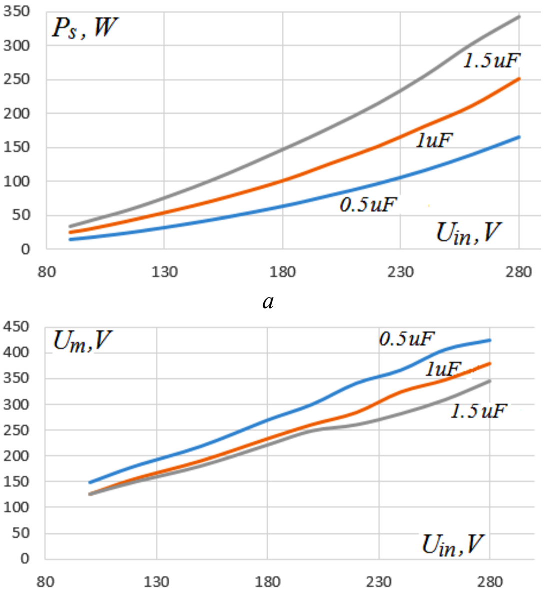

b

Fig. 8. Characteristics of: *a* – power consumption;
b – output pulse amplitude for 3 values of capacitance C_2

Conclusions.

1. According to the numerical analysis performed on the experimental current-voltage characteristics of the single-stage SMPG circuit with a series conversion link in the input circuit, it was determined that a significant part of the energy at the stage of the remagnetization process of the SR core is returned to the power source. In contrast to the symmetrical hysteresis loop, which is characteristic of two-stroke circuits of magnetic pulse generators without external biasing, the presence of a significant fraction of negative energy in the magnetization characteristic of the SR is caused by the presence of constant displacement current through its winding, which increases the area of the magnetic field where its flux density and strength have opposite values.
2. On the basis of the experimentally obtained closed current-voltage characteristics of the commutating choke for the SMPG circuit with a parallel conversion link in the input circuit, the presence of displacement current, the value of which depends on the input supply voltage, was established for the first time. Based on the considered oscillatory processes in adjacent charging circuits, an analytical equation is proposed for estimating the displacement current, which plays an important role at the stage of energy return from the commutating choke to the power source.
3. It is established that the power consumption of the SMPG with a parallel conversion link in the input circuit depends on the ratio of capacities in the adjacent pulse compression links. A decrease in the residual voltage on the longitudinal capacitance leads to an increase in the charging current and power consumption. When the condition $C_1 > C_2$ is met, the generator generates pulses with larger amplitude and shorter duration on the load.

Acknowledgments. The author expresses sincere gratitude to Dr. V.I. Zozulev for his unique understanding of practical ways of improving power converters of electricity and valuable recommendations provided during the discussion of the results of this work.

Conflict of interest. The author declares no conflict of interest.

REFERENCES

1. Khrysto O. Energy transfer processes in high-voltage circuits based on magnetic pulse compression. *Acta Electrotechnica et Informatica*, 2020, vol. 20, no. 3, pp. 3-10. doi: https://doi.org/10.15546/aeei-2020-0013.

2. Volkov I.V., Zozulev V.I., Khrysto O.I. Increasing of the efficiency of power electronics devices by the control of charging time of the capacitors in their circuits. *Technical Electrodynamics*, 2019, no. 2, pp. 15-18. (Ukr). doi: https://doi.org/10.15407/techned2019.02.015.

3. Golubev V.V., Zozulov V.I., Marunia Yu.V., Storozhuk A.I. Development of principles of construction and improvement of magnetic-semiconductor pulse devices of power converter technology. *Proceedings of the Institute of Electrodynamics of the National Academy of Sciences of Ukraine*, 2022, no. 62, pp. 34-40. (Ukr). doi: https://doi.org/10.15407/publishing2022.62.034.

4. Li S., Gao J., Yang H., Zhu D., Qian B., Cui Y., Wu Q., Zhang J. Investigation on Adjustable Magnetic Pulse Compressor in Power Supply System. *IEEE Transactions on Power Electronics*, 2019, vol. 34, no. 2, pp. 1540-1547. doi: https://doi.org/10.1109/TPEL.2018.2830106.

5. Boyko N.I. Powerful generators of high-voltage pulses with nanosecond fronts. *Electrical Engineering & Electromechanics*, 2018, no. 1, pp. 59-61. doi: https://doi.org/10.20998/2074-272X.2018.1.09.

6. Ghodke D.V., Muralikrishnan K., Singh B. New multiplexed all solid state pulser for high power wide aperture kinetically enhanced copper vapor laser. *Review of Scientific Instruments*, 2013, vol. 84, no. 11, art. no. 113102. doi: https://doi.org/10.1063/1.4829075.

7. Bozhko I.V., Zozulev V.I., Kobylchak V.V. SOS-generator for the electric discharge technology used pulse barrier discharge. *Technical Electrodynamics*, 2016, no. 2, pp. 63-67. (Ukr). doi: https://doi.org/10.15407/techned2016.02.063.

8. Pokryvailo A., Yankelevich Y., Wolf M. A High-Power Pulsed Corona Source for Pollution Control Applications. *IEEE Transactions on Plasma Science*, 2004, vol. 32, no. 5, pp. 2045-2054. doi: https://doi.org/10.1109/tps.2004.835952.

9. Guo X., Zheng D., Blaabjerg F. Power Electronic Pulse Generators for Water Treatment Application: A Review. *IEEE Transactions on Power Electronics*, 2020, vol. 35, no. 10, pp. 10285-10305. doi: https://doi.org/10.1109/TPEL.2020.2976145.

10. Akiyama H., Akiyama M. Pulsed Discharge Plasmas in Contact with Water and their Applications. *IEEJ Transactions on Electrical and Electronic Engineering*, 2021, vol. 16, no. 1, pp. 6-14. doi: https://doi.org/10.1002/tee.23282.

11. Balcerak M., Hołub M., Pałka R. High voltage pulse generation using magnetic pulse compression. *Archives of Electrical Engineering*, 2013, vol. 62, no. 3, pp. 463-472. doi: https://doi.org/10.2478/aee-2013-0037.

12. Choi J. Introduction of the magnetic pulse compressor (MPC) – fundamental review and practical application. *Journal of Electrical Engineering and Technology*, 2010, vol. 5, no. 3, pp. 484-492. doi: https://doi.org/10.5370/JEET.2010.5.3.484.

13. Nejadmalayeri A.H., Bali Lashak A., Bahrami H., Soltani I. A high voltage isolated pulse generator using magnetic pulse compression and resonant charging techniques for dielectric barrier discharge applications. *Journal of Electrical and Computer Engineering Innovations*, 2021, vol. 9, no. 2, pp. 239-248. doi: https://doi.org/10.22061/jecei.2021.7519.400.

14. Volkov I.V., Zozulov V.I., Golubev V.V., Paschenko V.V., Storozhuk A.I. Optimization of structural units of magnetic - semiconductor pulse generators. *Proceedings of the Institute of Electrodynamics of the National Academy of Sciences of Ukraine*, 2019, no. 53, pp. 65-74. (Ukr). doi: https://doi.org/10.15407/publishing2019.53.065.

15. Khrysto O.I. Electrical and energy characteristics of the serial-parallel converter unit of a high-voltage semiconductor - magnetic pulse generator. *The Bulletin of National Technical University «KhPI». Series: Techniques and Electrophysics of High Voltage*, 2015, no. 51, pp. 99-106. (Ukr).

Received 11.03.2023
Accepted 04.05.2023
Published 02.11.2023

O.I. Khrysto[1]*, PhD, Senior Researcher,*
[1] Institute of Pulse Processes and Technologies of NAS of Ukraine,
43-A, Bogoyavlenskij Avenue, Mykolayiv, 54018, Ukraine,
e-mail: alexander.khristo@gmail.com

How to cite this article:
Khrysto O.I. Current-voltage characteristics of single-stage semiconductor magnetic pulse generators with a distinctive structure of the conversion link in the input circuit. *Electrical Engineering & Electromechanics*, 2023, no. 6, pp. 41-47. doi: https://doi.org/10.20998/2074-272X.2023.6.07

UDC 621.314 https://doi.org/10.20998/2074-272X.2023.6.08

D.S. Krylov, O.I. Kholod

Active rectifier with a fixed modulation frequency and a vector control system in the mode of bidirectional energy flow

Goal. *Creation of a vector control system with improved characteristics for an active rectifier-voltage source operating in the bidirectional energy flow mode with a with a fixed modulation frequency.* ***Methodology***. *The physical prerequisites for the active rectifier - voltage source operation in the system of a medium-power frequency electric drive are considered. A vector control system with a fixed modulation frequency is constructed, the principles of forming the signals acting in it and the influence on its operation of the converter power circuit parameters and the power consumed by it are considered. Mathematical modeling of the converter with the developed control system in MATLAB/Simulink made it possible to verify the correctness of the operation of the power circuit and the control system.* ***Results***. *A new structure of a vector control system operating with a fixed modulation frequency is proposed, and the performance characteristics of the circuit in a wide range of changes in the magnitude and sign of the output power are obtained. The advantages of the new control system over the existing ones are shown.* ***Originality***. *The physical prerequisites for the functioning of the power scheme and the vector control system of the ARVS proposed by the authors with a fixed frequency of modulation, the principles of forming the signals operating within it are considered in detail.* ***Practical significance.*** *New structure of the vector control system operating with a fixed modulation frequency is proposed and the advantages of the new control system over the existing ones are shown.* References 17, tables 1, figures 9.

Key words: **active rectifier, fixed modulation frequency, vector control system, bidirectional energy flow, vector diagram, coordinate transformation, pulse width modulation.**

В статті розглянуто роботу активного випрямляча-джерела напруги, що працює з фіксованою частотою модуляції в режимі двонаправленого потоку енергії, запропоновано нову структуру векторної системи управління, та отримано характеристики роботи схеми в широкому діапазоні зміни величини та знаку вихідної потужності. Розглянуті фізичні передумови функціонування силової схеми АВДН, запропонованої авторами векторної системи управління та принципи формування діючих усередині неї сигналів в складі частотного перетворювача середньої потужності. Показано переваги нової системи управління над існуючими та отримано залежності, що демонструють коректність застосування запропонованих у статті технічних рішень. Результати математичного моделювання показали, що АВДН, який працює з фіксованою частотою модуляції та запропонованою системою управління, дозволяє підтримувати задане значення вихідної напруги та близький до синусоїди струм мережі живлення при нульовому споживанні реактивної потужності в усталеному режимі в широкому діапазоні зміни параметрів схеми та величини і знаку потужності навантаження. Бібл. 17, табл. 1, рис. 9.

Ключові слова: **активний випрямляч, фіксована частота модуляції, векторна система управління, двонаправлений потік енергії, векторна діаграма, перетворення координат, широтно-імпульсна модуляція.**

Introduction. The frequency converter is an integral part of industrial installations that use an induction motor (IM) as part of their composition. By changing the effective value and frequency of the three-phase alternating voltage supplied to the stator windings, it allows to implement various strategies for controlling the speed and torque on the shaft of this type of electric machine. In the range of small and medium powers when powered from an industrial network of 380-400 V, the converter structure based on an autonomous voltage inverter (AVI) has become the most widespread. It contains two main components: a converter of three-phase alternating voltage into direct one – a rectifier and an inverter powered by its output voltage, most often made according to a three-phase bridge circuit on alternating current switches.

The use of various modulation algorithms allows such an inverter to generate a voltage with the necessary parameters on the load and to adjust them within wide limits. Among the possible options, pulse-width, frequency-pulse, time-pulse and vector-pulse modulation [1-3] can be distinguished, each of which has its own advantages and disadvantages.

For AVIs operating in the range of small and medium powers, pulse width modulation (PWM) has become the most common. Having a relative simplicity of implementation, it provides a fixed switching frequency of valves switching in the circuit, which significantly simplifies their thermal calculation, and also facilitates the calculation of filters at the output of the circuit [4, 5].

A three-phase bridge diode circuit can act as a rectifier in the considered structure. Simple and reliable, here it has a number of significant disadvantages: it distorts the shape of the power network current; does not form a sufficient level of voltage at the input of the AVI when it operates in the sinusoidal PWM mode; does not ensure the return of energy from the load to the power network [1, 6].

Modern requirements for the quality of energy consumed from the industrial network force us to consider other topologies of rectifiers that are devoid of the mentioned disadvantages. Among them, we can single out a diode rectifier with various circuits of power factor correction modules, a rectifier according to the Vienna circuit and an active rectifier-voltage source (ARVS) circuit made, similarly to AVI, according to a three-phase bridge circuit on alternating current switches [1, 7, 8].

It is worth noting that only the ARVS circuit allows to simultaneously eliminate all the shortcomings inherent in the diode rectifier in the structure of the frequency converter based on AVI. Its effectiveness will also depend on the modulation algorithm used and the structure of the control system that implements it. For the same power circuits of ARVS and AVI in a single converter, it is advisable to use the same modulation algorithms and structures of control systems built on similar principles.

In modern practice, the strategies for controlling speed and torque on the shaft of an induction motor, built on the principles of presenting stator currents and voltages in the form of generalized vectors in different coordinate systems, have shown the greatest efficiency. They are implemented by the so-called «vector» control systems of autonomous inverters [7, 9].

ARVS control systems can be built according to a similar principle [10-13].

The goal of the work is to create a vector control system with improved characteristics for an active rectifier-voltage source operating in the mode of bidirectional energy flow with a fixed modulation frequency.

Power circuit of the converter. Figure 1 shows a generalized functional diagram of a frequency converter with an ARVS in the input circuit. It consists of the following components: *AC* – three-phase network of sinusoidal variable voltage u_S; phase inductance *L*, including additional input reactors; active rectifier *AR*, made according to a three-phase bridge circuit on alternating current switches; direct current section of the converter *DC* with capacitive energy storage *C*, which smoothes out voltage ripples and creates an operating mode for the load that is close in characteristics to the voltage source; load *Load*, which is an AVI with PWM, which powers an induction motor.

The physical processes in each phase of the ARVS input circuit are similar to the other two with a shift of 120 electrical degrees. Consider them on the example of the equivalent circuit shown in Fig. 2.

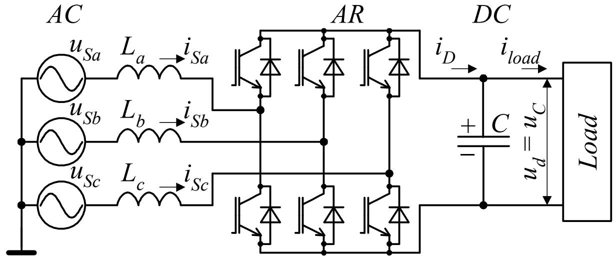

Fig. 1. Functional diagram of the converter with ARVS

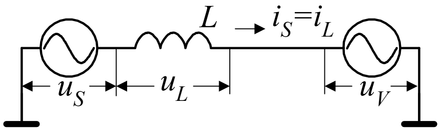

Fig. 2. Equivalent circuit of the ARVS input circuit phase

It contains: the source of sinusoidal alternating phase voltage with instantaneous value u_S; the instantaneous phase voltage at the input of the ARVS u_V, which is formed during the operation of the semiconductor switch of the circuit in PWM mode, by periodically connecting to the phase of the power supply network the voltage on the capacitor of the DC link $u_C = u_d$ with different polarity. As a result, during the modulation period, the sign of the voltage drop u_L on the input inductance of the phase *L* and the dynamics of the current i_L flowing through it change. This allows to form the required shape and phase of the current of the power source.

According to Kirchhoff law, at any moment in time, the instantaneous circuit voltages (Fig. 2) will be related to each other by the expression

$$u_S = u_L + u_V . \qquad (1)$$

The generalized vector diagram for the input circuit of the ARVS phase while maintaining a unit power factor is shown in Fig. 3,*a* for the energy consumption mode, and in Fig. 3,*b* – for the energy recovery mode from the load to the power supply network.

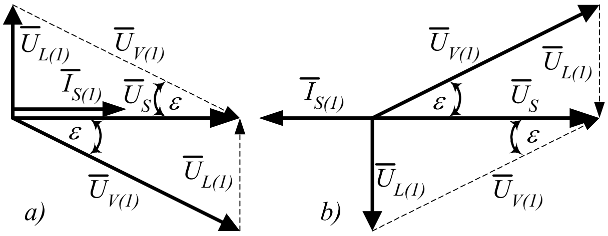

Fig. 3. Generalized vector diagram of the ARVS input circuit at a unit power factor for: *a* – energy consumption by the load; *b* – energy recovery from the load to the power supply network

The presence of the inductance *L* gives the ARVS input circuit the properties of a current source, which allows the circuit to operates in the boost PWM mode and maintain the voltage on the capacitor $u_C = u_d$ of the DC link above the mains voltage.

By controlling the amplitude and phase shift angle ε of the voltage u_V, it is possible to control the amplitude and phase of the source current i_S by varying the voltage drop across the input inductance u_L. Here, the average value and sign of the current at the output of the ARVS will be proportional to the active power at the input of the circuit. The reactive power can be controlled independently by shifting the current of the fundamental harmonic i_S with respect to the voltage u_S.

Control system. If we talk about the strategy of building the ARVS control system, it is often based on the dual identity of its power circuits with the AVI circuit as part of the general frequency converter. Indeed, the power circuits of both converters are exactly the same. Both have a common DC link that has the properties of a voltage source and their own circuits of three-phase alternating voltage, which, due to the serial connection of inductances in their phases, have the properties of current sources. Both provide a bidirectional flow of energy, because they operate as a step-down pulse width converter when transferring it from a DC link to an AC link and as a step-up one when transferring it from an AC link to a DC link. Therefore, it is possible to use the concepts of building AVI control systems to regulate an induction electric motor during the creation of ARVS control systems.

The main concepts of induction motor control are *Direct Torque Control* (DTC) and *Field Oriented Control* (FOC) [10, 11, 14]. They are matched with the strategy of *Direct Power Control* (DPC) and *Voltage Oriented Control* (VOC), which are used in ARVS [10, 11, 14, 15]. Each of them has many implementation options that have their own advantages and disadvantages.

Note that only ARVS vector control systems built on the basis of the *VOC* concept operate with a fixed modulation frequency. They are based on the principle of presenting generalized network current and voltage vectors in rotating (for example, *d-q*) coordinates, in which the regulated values are constant signals, which allows for the elimination of static control errors. Here, the structure of separate control of the «active» i_d and «reactive» i_q components of the network current is used using its own, usually proportional-integral (PI) regulators for each of the channels. By adjusting the d-component of the current, it is possible to control the flow of energy between the source and the load, as well as to maintain the required voltage level on the capacitor of the DC link. The regulator of the q-component relies only on the function of maintaining a zero or other specified shift angle between the current and the voltage of the power supply network. This fully corresponds to the principle of operation of ARVS power circuits described above.

Vector control systems of ARVS using separate control structures are widely presented in [9-14]. Their essential drawback is the need for a direct and inverse transformation of the coordinates of the generalized current and voltage vectors with the calculation of the trigonometric function of their angle of rotation. This complicates the physical implementation of such systems and places increased demands on its element base.

It is possible to simplify the ARVS vector control system, which operates with a fixed modulation frequency, if we use the above-described principle of the converter operation.

To form the required shape and phase shift of the network current $i_S = i_L$, it is necessary to control the voltage drop on the input inductance of the circuit u_L by adjusting the value and phase shift of the input voltage u_V. Its first harmonic, in turn, repeats the control voltage at the input of the *PWM* generator with some given transmission ratio.

Representing (1) in relative units, it is possible to obtain an expression for determining the *PWM* control voltage of the generator, which forms a given shape of the network current in the form

$$u_V^* = u_S^* - u_L^* = u_S^* - L\frac{\mathrm{d}i_L^*}{\mathrm{d}t}, \tag{2}$$

where u_S^*, u_V^*, u_L^* and i_L^* are the relative phase voltages and current of the input circuit of the ARVS according to Fig. 2, for which the amplitudes of the nominal phase voltage and current of the power source are taken as the basic values, respectively.

Thus, with unchanged voltage of the power source, the task of the control system is reduced to the generation of the task signal of the phase current of the ARVS input circuit with the necessary parameters. It can be solved using the principle of separate regulation described above.

Figure 4 shows the structural diagram of the ARVS vector control system proposed by the authors, which operates with fixed modulation frequency.

Instantaneous values of three phase currents i_S^* and voltages u_S^* of the power supply network, reduced to relative units, are supplied to the *abc-dq* coordinate conversion unit. In it, using the Clark matrix, currents and voltages are converted from coordinates *abc* to coordinates *α-β* according to the expressions

$$\begin{bmatrix} i_\alpha^* \\ i_\beta^* \end{bmatrix} = \sqrt{\frac{2}{3}} \begin{bmatrix} 1 & -\frac{1}{2} & -\frac{1}{2} \\ 0 & \frac{\sqrt{3}}{2} & -\frac{\sqrt{3}}{2} \end{bmatrix} \cdot \begin{bmatrix} i_{Sa}^* \\ i_{Sb}^* \\ i_{Sc}^* \end{bmatrix}; \tag{3}$$

$$\begin{bmatrix} u_\alpha^* \\ u_\beta^* \end{bmatrix} = \sqrt{\frac{2}{3}} \begin{bmatrix} 1 & -\frac{1}{2} & -\frac{1}{2} \\ 0 & \frac{\sqrt{3}}{2} & -\frac{\sqrt{3}}{2} \end{bmatrix} \cdot \begin{bmatrix} u_{Sa}^* \\ u_{Sb}^* \\ u_{Sc}^* \end{bmatrix}. \tag{4}$$

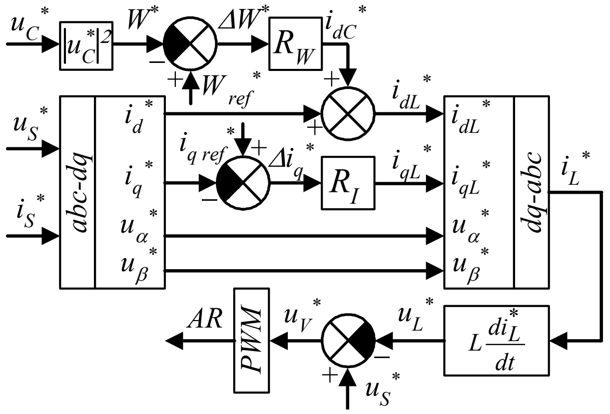

Fig. 4. Structural diagram of the ARVS control system

Then the relative instantaneous network currents are transformed from *α-β* coordinates to *d-q* coordinates. If the Park matrix [16] is used directly for this, it will be necessary to calculate the trigonometric functions of the rotation angle of the generalized voltage vector of the power source. This increases the requirements for the hardware part of the control system. Therefore, it is advisable to obtain projections of the generalized network current vector on the *d-q* axis through the coordinates of the generalized network voltage vector in the *α-β* system according to the expression [16]

$$\begin{bmatrix} i_d^* \\ i_q^* \end{bmatrix} = \frac{1}{\sqrt{u_\alpha^{*2} + u_\beta^{*2}}} \begin{bmatrix} u_\alpha^* & u_\beta^* \\ -u_\beta^* & u_\alpha^* \end{bmatrix} \cdot \begin{bmatrix} i_\alpha^* \\ i_\beta^* \end{bmatrix}. \tag{5}$$

In the mode of full reactive power compensation, the value of the q-projection of the generalized network current vector should tend to zero. This condition is valid both for the mode of energy consumption by the load and for the mode of energy recovery from the load to the power network. Therefore, the relative instantaneous value of the q-component of the network current i_q^* is compared with the task $i_{q\,ref}^* = 0$. The mismatch signal Δi_q^* is fed to the input of the PI current regulator R_I, which forms the q-component of the task current signal of the choke of the ARVS input circuit i_{qL}^*.

The flow of energy consumed or generated by the load depends on the operating modes of the load itself and in the structure under consideration (Fig. 1), controlled by the AVI control system. Therefore, there is no need to introduce any additional regulator of the d-component current of the ARVS network i_d^* into the shown in Fig. 4 structure of the control system. In this way, the proposed structure differs from most structures built on the basis of the concept of *VOC* [9-15].

The regulator is necessary to maintain the constant value of the voltage on the capacitor of the DC link at the level higher than the amplitude of the line voltage of the source. It needs to form the component i_{dC}^*, which complements i_d^* depending on the value and direction of the energy transmitted in the converter. At the same time, the capacitor itself is a store of energy, the value of which can be determined as

$$E_C = C \cdot u_C^2 / 2\,, \tag{6}$$

where C is the capacitor capacity; u_C is the voltage on the capacitor in the DC link of the circuit (Fig. 1).

The instantaneous power in it, determined by the superposition of the instantaneous active powers in the source and the load, can be obtained as the derivative of (6) in time

$$\frac{\mathrm{d}E_C}{\mathrm{d}t} = \frac{C}{2}\frac{\mathrm{d}u_C^2}{\mathrm{d}t} = p_S - p_{load}\,. \tag{7}$$

Expression (7) is non-linear with respect to u_C, which complicates the operation of the regulator. It can be facilitated by linearization of the feedback by introducing a new variable $W = u_C^2$ in (7). Then we will get a linear dependence relative to W

$$\frac{C}{2}\frac{\mathrm{d}W}{\mathrm{d}t} = p_S - p_{load}\,. \tag{8}$$

Now we can use a linear regulator, taking the amount of energy as a variable to adjust the voltage of the DC link. In it, according to Fig. 4, the instantaneous DC link voltage u_C^*, reduced to relative units by the nominal amplitude value of the line voltage of the source, is squared and compared with the squared relative reference voltage of the capacitor. The mismatch signal ΔW^* is fed to the input of the PI regulator R_W, which forms the signal i_{dC}^*, which supplements the current value of the *d*-component of the current of the ARVS network i_d^* to the required level i_{dL}^*.

The obtained i_{dL}^* and i_{qL}^* values, together with the previously calculated u_α^* and u_β^*, enter the *dq-abc* coordinate converter. In it, the reverse transformation of d-*q* current components into *α*-*β* coordinates takes place according to the expression

$$\begin{bmatrix} i_{\alpha L}^* \\ i_{\beta L}^* \end{bmatrix} = \frac{1}{\sqrt{u_\alpha^{*2} + u_\beta^{*2}}} \begin{bmatrix} u_\alpha^* & -u_\beta^* \\ u_\beta^* & u_\alpha^* \end{bmatrix} \cdot \begin{bmatrix} i_{dL}^* \\ i_{qL}^* \end{bmatrix}, \tag{9}$$

and then from *α*-*β* coordinates to *abc* coordinates according to the expression

$$\begin{bmatrix} i_{aL}^* \\ i_{bL}^* \\ i_{cL}^* \end{bmatrix} = \sqrt{\frac{2}{3}} \begin{bmatrix} 1 & 0 \\ -\frac{1}{2} & \frac{\sqrt{3}}{2} \\ -\frac{1}{2} & -\frac{\sqrt{3}}{2} \end{bmatrix} \cdot \begin{bmatrix} i_{\alpha L}^* \\ i_{\beta L}^* \end{bmatrix}. \tag{10}$$

The instantaneous relative voltage drop at the input choke of the circuit u_L^* is obtained as the derivative of the current i_L^* multiplied by the current value of the inductance of the source phase. Next, according to (2), we subtract u_L^* from u_S^* and the thus obtained relative input voltage u_V^* is supplied to the *PWM* input of the generator as a control voltage.

Thus, the control system proposed by the authors has, compared to the known, the following advantages: it reduces the number of regulators in the system to two; does not require calculation of *d-q* voltage components; does not require the calculation of trigonometric functions in the process of coordinate transformation.

Mathematical modelling. Figure shows a virtual model of the converter based on ARVS, which corresponds to the structure in Fig. 1. It is performed in the MATLAB/Simulink software environment.

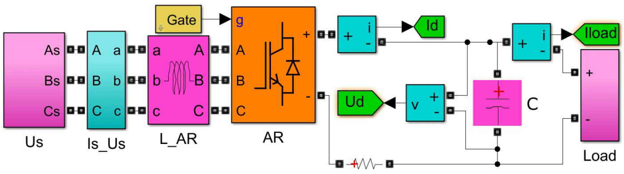

Fig. 5. MATLAB model of ARVS power circuits

The model has the same parameters that were adopted by the authors in previous studies [4], namely: the three-phase AC voltage source with short-circuit power of 150 MVA and the linear voltage at the converter input of 400 V; the value of the input inductance of the phase is taken equal to 400 μH; the DC link capacity 28 mF; the ARVS operates in sinusoidal PWM mode with fixed modulation frequency of 4 kHz and the vector control system made according to the structure (Fig. 4). To test the possibility of operation of the circuit with bidirectional flow of energy, the link with the series connection of the resistor limiting the maximum current and the source of adjustable EMF is accepted as the load. The automatic load control system allows to maintain the level of power consumption on it in the range of ±315 kW, i.e. up to the nominal in both directions.

Figure 6 presents the MATLAB model of the ARVS vector control system, which is made in accordance with the structure (Fig. 4) and fully corresponds to the proposed operation algorithm.

Verification of the operation of the model (Fig. 5) with the vector control system (Fig. 6) showed the ability of the converter to maintain the specified voltage at the output and to form the source current close to a sinusoid, which has a zero or 180 degree shift angle with respect to the phase voltage in the entire range of the change in the circuit power, which is consumed or generated by the load.

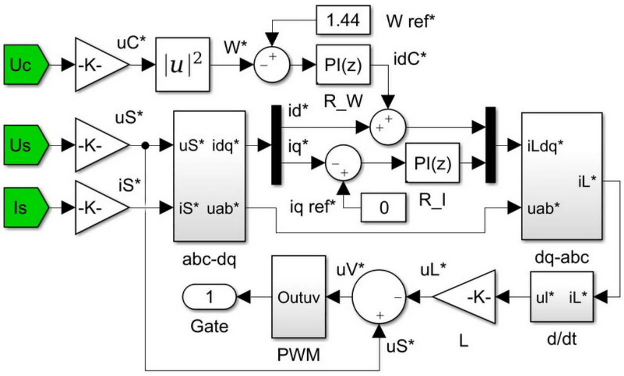

Fig. 6. MATLAB model of the ARVS control system

Figures 7, *a-d* are machine diagrams illustrating the operation of the circuit and its control system during a single time interval of 5 s when the load power changes in both directions.

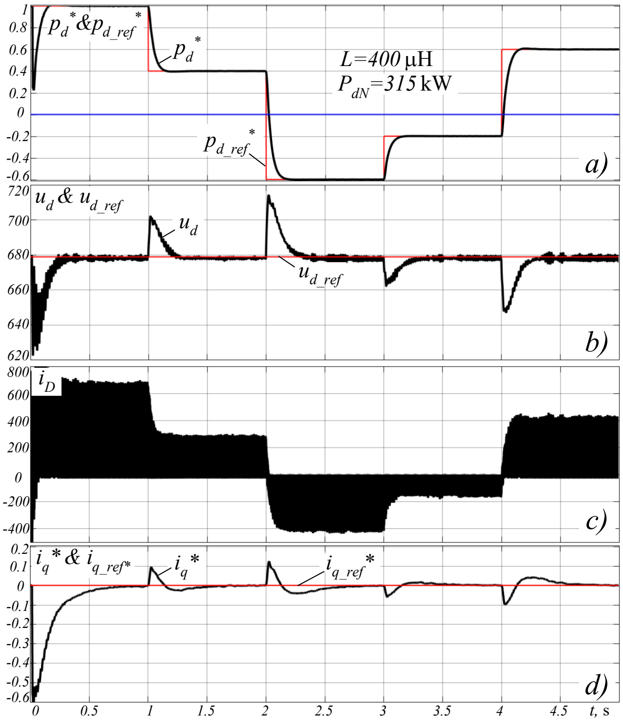

Fig. 7. Machine diagrams of the operation of the ARVS circuit

Figure 7,*a* shows the current value of the relative instantaneous power of the load and the step-changing task signal with different polarities. It can be seen that the power regulator performs the task correctly.

Figure 7,*b* shows the task signal and the current instantaneous value of the voltage of the DC link. It can be seen that in the steady state, the voltage regulator maintains its level exactly in accordance with the task, and the deviation of the instantaneous voltage level in transient modes does not exceed 8 % of the set value. The voltage task on the capacitor is selected at a level that exceeds the nominal amplitude of the line voltage of the power source by 20 %, which at given line voltage of 400 V is 678.8 V.

Figure 7,*c* shows the instantaneous value of the current at the ARVS output. It can be seen that it is modulated by high frequency and changes its polarity when the sign of the load power changes.

Figure 7,*d* shows the relative instantaneous value of the q-component of the ARVS network current i_q^*. It can be seen that in the steady state, its value tends to zero, that is, the level set by the regulator, which indicates the absence of consumption or generation of reactive power by the circuit, regardless of the value and sign of the power in the load.

Figures 8,*a*,*b* show the instantaneous values of the current and voltage of phase *A* in the mode of consumption (Fig. 8,*a*) and recovery (Fig. 8,*b*) of the load power at the level ±180 kW.

It can be seen that the phase current has a sinusoidal shape and is in phase or in antiphase with the source voltage in the steady state.

Machine diagrams shown in Fig. 7, 8, testify to the correct operation of the ARVS with fixed modulation frequency and the proposed control system in all permissible operating modes.

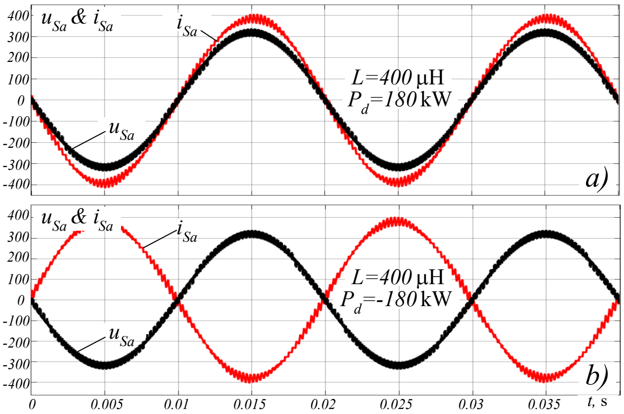

Fig. 8. Machine diagrams of current and voltage of phase *A* of ARVS

With the help of the model (Fig. 5), the dependencies of the total harmonic distortion coefficient of the current (THD_I) and voltage (THD_U) of the phase at the input of the converter on the relative value of the power of the circuit, which is consumed or generated by the load, are obtained. The studies were carried out for two values of the inductance of the ARVS input reactor. The obtained results are shown in the Table 1.

Table 1

Experimental research data

P_d^*	THD_I, %		THD_U, %	
	L=200 µH	*L*=400 µH	*L*=200 µH	*L*=400 µH
1	4.2	2.46	10.24	5.46
0.8	5.3	3.1	10.25	5.47
0.6	7.1	4.1	10.25	5.48
0.4	10.1	5.7	10.23	5.49
0.2	20.5	11.2	10.22	5.5
0	–	–	10.2	5.48
–0.2	21.8	12.2	10.16	5.46
–0.4	11.0	5.9	10.14	5.44
–0.6	7.2	3.9	10.12	5.42
–0.8	5.7	3.1	10.11	5.39
–1	4.5	2.5	10.07	5.35

According to the Table 1 graphical dependencies of THD_I and THD_U at the connection point of the converter on the relative value of the power of the circuit, which is consumed or generated by the load, which are shown in Fig. 9 are built. Also in Fig. 9, the dashed line shows the acceptable values of THD_I and THD_U, which are 5 % and 8 %, respectively, according to the norms [17].

From the obtained graphical dependencies (Fig. 9), it can be concluded that with the input inductance *L* taken at the level of 400 µH, the values of THD_I and THD_U correspond to the established standards in the entire range of changes in the power of the circuit, which is consumed or generated by the load. When reducing the value of the input inductance, to obtain the required THD_I and THD_U indicators it is necessary to install an additional input filter.

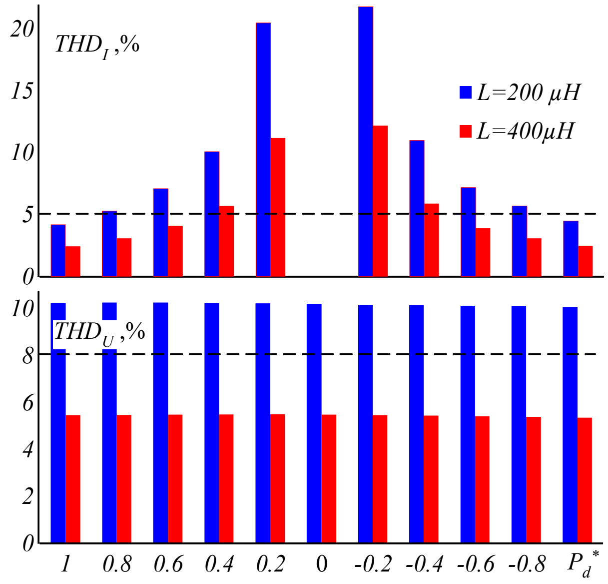

Fig. 9. Graphic dependencies of THD_I and THD_U

Conclusions.

1. The article proposes a new vector control system for an active rectifier-voltage source operating in the mode of bidirectional energy flow with fixed modulation frequency. It ensures stable and correct operation of the converter and has significant advantages compared to known vector control systems, namely: it reduces the number of regulators in the system to two; does not require calculation of *d-q* voltage components; does not require the calculation of trigonometric functions when transforming coordinates.

2. The article examines in detail the physical prerequisites for the operation of the power circuit and the ARVS vector control system with fixed modulation frequency proposed by the authors, as well as the principles of forming signals operating within it.

3. Mathematical modelling of the converter with the proposed vector control system in the MATLAB/Simulink software environment showed that the ARVS circuit allows maintaining a close to sinusoidal current of the power supply network and a set value of the output voltage with zero reactive power consumption in the steady state for a wide range of changes in the value and sign of the load power. The obtained machine diagrams allow to verify the correctness of the operation of the power circuit and the control system, which ensures minimal deviations from the specified parameters during transient processes.

Conflict of interest. The authors of the article declare that there is no conflict of interest.

REFERENCES

1. Kolar J.W., Friedli T. The Essence of Three-Phase PFC Rectifier Systems – Part I. *IEEE Transactions on Power Electronics*, 2013, vol. 28, no. 1, pp. 176-198. doi: https://doi.org/10.1109/TPEL.2012.2197867.

2. Nandhini E., Sivaprakasam A. A Review of Various Control Strategies Based on Space Vector Pulse Width Modulation for the Voltage Source Inverter. *IETE Journal of Research*, 2022, vol. 68, no. 5, pp. 3187-3201. doi: https://doi.org/10.1080/03772063.2020.1754935.

3. Jalnekar R.M., Jog K.S. Pulse-Width-Modulation Techniques: A Review. *IETE Journal of Research*, 2000, vol. 46, no. 3, pp. 175-183. doi: https://doi.org/10.1080/03772063.2000.11416153.

4. Krylov D.S., Kholod O.I. Determination of the input filter parameters of the active rectifier with a fixed modulation frequency. *Electrical Engineering & Electromechanics*, 2022, no. 4, pp. 21-26. doi: https://doi.org/10.20998/2074-272X.2022.4.03.

5. Kim H., Sul S.-K. A novel filter design for output LC filters of PWM inverters (2011) Journal of Power Electronics, 11 (1), pp. 74-81. doi: 10.6113/JPE.2011.11.1.074.

6. Yazdavar A.H., Azzouz M.A., El-Saadany E.F. Harmonic Analysis of Three-Phase Diode Bridge Rectifiers Under Unbalanced and Distorted Supply. *IEEE Transactions on Power Delivery*, 2020, vol. 35, no. 2, pp. 904-918. doi: https://doi.org/10.1109/TPWRD.2019.2930557.

7. Premkumar K., Kandasamy P., Vishnu Priya M., Thamizhselvan T., Ron Carter S.B. Three-phase rectifier control techniques: A comprehensive literature survey. *International Journal of Scientific and Technology Research*, 2020, vol. 9, no. 1, pp. 3183-3188.

8. Dwivedi A., Tiwari A.N. Analysis of three-phase PWM rectifiers using hysteresis current control techniques: a survey. *International Journal of Power Electronics*, 2017, vol. 8, no. 4, pp. 349-377. doi: https://doi.org/10.1504/IJPELEC.2017.085201.

9. Krylov D., Kholod O., Radohuz S. Active rectifier with different control system types. *2020 IEEE 4th International Conference on Intelligent Energy and Power Systems (IEPS)*, 2020, pp. 273-278. doi: https://doi.org/10.1109/IEPS51250.2020.9263226.

10. Soeiro T.B., Friedli T., Kolar J.W. Design and Implementation of a Three-Phase Buck-Type Third Harmonic Current Injection PFC Rectifier SR. *IEEE Transactions on Power Electronics*, 2013, vol. 28, no. 4, pp. 1608-1621. doi: https://doi.org/10.1109/TPEL.2012.2209680.

11. Wang Y. *Analysis of three-phase rectifier via three different control methods and switch power loss comparison*. Mankato, Minnesota State University, 2021. 93 p.

12. Krylov D.S., Kholod O.I. The efficiency of the active controlled rectifier operation in the mains voltage distortion mode. *Electrical Engineering & Electromechanics*, 2021, no. 2, pp. 30-35. doi: https://doi.org/10.20998/2074-272X.2021.2.05.

13. Zhang C., Yu S., Ge X. A Stationary-Frame Current Vector Control Strategy for Single-Phase PWM Rectifier. *IEEE Transactions on Vehicular Technology*, 2019, vol. 68, no. 3, pp. 2640-2651. doi: https://doi.org/10.1109/TVT.2019.2895290.

14. Liu C., Luo Y. Overview of advanced control strategies for electric machines. *Chinese Journal of Electrical Engineering*, 2017, vol. 3, no. 2, pp. 53-61. doi: https://doi.org/10.23919/CJEE.2017.8048412.

15. Kumar R., Gupta R.A., Bhangale S.V. Vector control techniques for induction motor drive: a review. *International Journal of Automation and Control*, 2009, vol. 3, no. 4, pp. 284-306. doi: https://doi.org/10.1504/IJAAC.2009.026778.

16. Zhemerov G.G., Tugay D.V. *Coordinates transformation of general vectors of voltages and currents for a three-phase power supply system*. Kharkiv, O.M. Beketov NUUE Publ., 2020. 200 p.

17. *IEEE Std 519-2014. IEEE Recommended Practice and Requirements for Harmonic Control in Electric Power Systems*, 2014, pp. 1-29. doi: https://doi.org/10.1109/IEEESTD.2014.6826459.

Received 05.03.2023
Accepted 08.05.2023
Published 02.11.2023

D.S. Krylov[1]*, PhD, Assistant Professor,*
O.I. Kholod[1]*, PhD, Senior Lecturer,*
[1] National Technical University «Kharkiv Polytechnic Institute», 2, Kyrpychova Str., Kharkiv, 61002, Ukraine,
e-mail: Denis.Krylov@khpi.edu.ua (Corresponding Author); Olha.Kholod@khpi.edu.ua

How to cite this article:
Krylov D.S., Kholod O.I. Active rectifier with a fixed modulation frequency and a vector control system in the mode of bidirectional energy flow. *Electrical Engineering & Electromechanics*, 2023, no. 6, pp. 48-53. doi: https://doi.org/10.20998/2074-272X.2023.6.08

UDC 621.314 https://doi.org/10.20998/2074-272X.2023.6.09

A. Namoune, R. Taleb, N. Mansour, M.R. Benzidane, A. Boukortt

Integrated through-silicon-via-based inductor design in buck converter for improved efficiency

Introduction. *Through-silicon-via (TSV) is one of the most important components of 3D integrated circuits. Similar to two-dimensional circuits, the performance evaluation of 3D circuits depends on both the quality factor and inductance. Therefore, accurate TSV-inductor modeling is required for the design and analysis of 3D integrated circuits.* ***Aim.*** *This work proposes the equivalent circuit model of the TSV-inductor to derive the relations that determine both the quality factor and the inductance by Y-parameters.* ***Methods.*** *The model developed was simulated using MATLAB software, and it was used to evaluate the effect of redistribution lines width, TSV radius, and the number of turns on inductance and quality factor. Additionally, a comparative study was presented between TSV-based inductors and conventional inductors (i.e., spiral and racetrack inductors).* ***Results.*** *These studies show that replacing conventional inductors with TSV-inductors improved the quality factor by 64 % compared to a spiral inductor and 60 % compared to a racetrack inductor. Furthermore, the area of the TSV-inductor was reduced up to 1.2* mm^2*. Using a PSIM simulator, the application of an integrated TSV-inductor in a buck converter was studied, and the simulation gave very good results in 3D integration compared to 2D integration. Moreover, the simulation results demonstrated that using a TSV-inductor in a buck converter could increase its efficiency by up to 15 % and 6 % compared to spiral and racetrack inductors, respectively.* References 21, tables 3, figures 8.

Key words: **through-silicon-via-based inductor, 3D integration, buck converter, efficiency.**

Вступ. *Наскрізне з'єднання кремнію (TSV) є одним з найважливіших компонентів тривимірних інтегральних схем. Подібно до двовимірних схем, оцінка продуктивності тривимірних схем залежить як від добротності, так і від індуктивності. Тому для проєктування та аналізу тривимірних інтегральних схем необхідне точне моделювання TSV-індуктора.* ***Мета***. *У цій роботі пропонується еквівалентна модель схеми TSV-індуктора для виведення співвідношень, що визначають як добротність, так і індуктивність за Y-параметрами.* ***Методи***. *Розроблена модель була змодельована з використанням програмного забезпечення MATLAB та використана для оцінки впливу ширини ліній перерозподілу, радіусу TSV та кількості витків на індуктивність та добротність. Крім того, було представлено порівняльне дослідження між індукторами на основі TSV та звичайними індукторами (тобто спіральними та індукторами типу бігова доріжка).* ***Результати***. *Ці дослідження показують, що заміна звичайних індукторів на TSV-індуктори покращила добротність на 64 % порівняно зі спіральним індуктором і на 60 % порівняно з індуктором типу бігова доріжка. Крім того, площа TSV-індуктора була зменшена до 1,2* $мм^2$*. За допомогою симулятора PSIM було вивчено застосування вбудованого дроселя TSV в знижувальному перетворювачі, і моделювання дало дуже хороші результати при 3D-інтеграції порівняно з 2D-інтеграцією. Більш того, результати моделювання показали, що використання TSV-індуктора в понижувальному перетворювачі дозволяє підвищити його ефективність до 15% та 6 % порівняно зі спіральними індукторами та індукторами типу бігова доріжка відповідно.* Бібл. 21, табл. 3, рис. 8.

Ключові слова: **індуктор на основі кремнію, 3D-інтеграція, знижуючий перетворювач, ефективність.**

Introduction. In recent years, technological advancements have enabled several functions to be combined into one chip by increasing passive components while maintaining the same chip area [1-3]. However, the scaling process in 2D technology has the effect of wasting energy for the integrated passive components, resulting in an inefficient system [4]. It is possible to resolve this latter issue using 3D integration due to its superior performance in comparison to 2D [5, 6]. 3D integration is a new technical approach to scientific progress that distinguishes itself from its 2D counterpart by its high efficiency, smaller area, and lower cost [7]. Several technologies including 3D integration exist, with the most important being integrated circuits based on through-silicon-via (TSV). As a solution to the aforementioned problems associated with planar inductors, a TSV-inductor is suggested in a buck converter [8]. The structure of TSV-based inductors is the most compact in design with fewer parasites and is used in a wide variety of applications [9].

To address the problems encountered with 2D inductors, several studies have been conducted in the literature to exploit TSVs. These studies include Zhang et al. (2010) [10], Bontzios et al. (2011) [11], and Feng et al. (2012) [12]. In 2013, Tida et al [13] attempted to employ TSVs in vertical inductors for radio frequency applications.

The main contributions of this article are as follows: we are the first to study the behavior of TSV-inductors at high frequencies. Additionally, we compare the effects of 3D inductors with 2D inductors on the efficiency of the buck micro-converter.

This work is organized as follows: first, a theoretical study of the TSV-inductor is presented, highlighting its equivalent electrical circuit. Second, simulation results are presented, showing the influence of the geometric parameters of the 3D inductor. Finally, this paper concludes by demonstrating how the efficiency of the buck converter can be improved using the proposed TSV-inductor and comparing it with two other inductors.

Design and modeling TSV-inductor. There is a strong relationship between the performance of the TSV-inductor and its geometric parameters.

Figure 1 shows the typical structure of a TSV-based 3D inductor, which consists of three basic parts: the TSV, which is cylindrical in shape, and the upper and lower redistribution lines (RDLs) that's have rectangular forms.

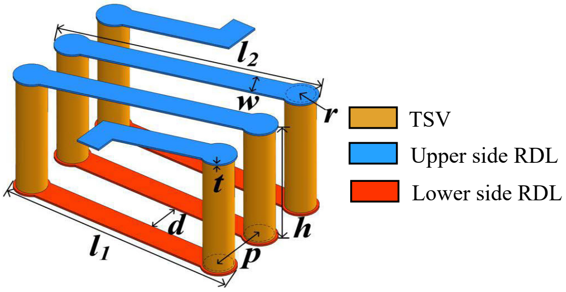

Fig. 1. Typical structure of TSV-inductor

The variables defining the geometry are the height h and radius r of the TSV, the length l, the width w, and the thickness t of each conductor, and the spacing d and the number of turns N. Copper is used as the metal material for these elements, and SiO_2 is used as the insulating material between the substrate and the copper lines.

Table 1 summarizes all geometric parameters that are essential factors in the performance of the TSV-inductor.

Table 1
Geometrical parameters of TSV-inductor

Parameter	Value
TSV height *h*, μm	80
TSV radius *r*, μm	12
Number of turns *N*	3
RDL length *l*, μm	150
RDL width *w*, μm	20
RDL thickness *t*, μm	6
Spacing between RDLs *d*, μm	15

The structure has two positive features: it greatly reduces the inductor printing space (lowering costs), and the design is greatly simplified. There are many equivalent circuit models for on-chip spiral inductors, but these models are rarely applied to inductors with TSVs.

As shown in Fig. 2,*a*, a π-equivalent circuit model has been developed for the higher frequency ranges [14]. The parameters of this model are: the capacitance between the redistribution lines adjacent C, the inductance series of the redistribution lines L_s, the resistance series of the redistribution lines R_s, the capacitance between the TSV and the substrate C_{ox}, the capacitance of the substrate C_{sub} and the resistance of the substrate R_{sub}, which represent the resistance, inductance, and capacitance characteristics of RDL and TSV [15, 16]. As shown in Fig. 2,*b*, these parameters of the circuit model can be derived from the Y-parameters: elements of admittance series Y_a and the elements of admittance shunt Y_b, and Y_c [17].

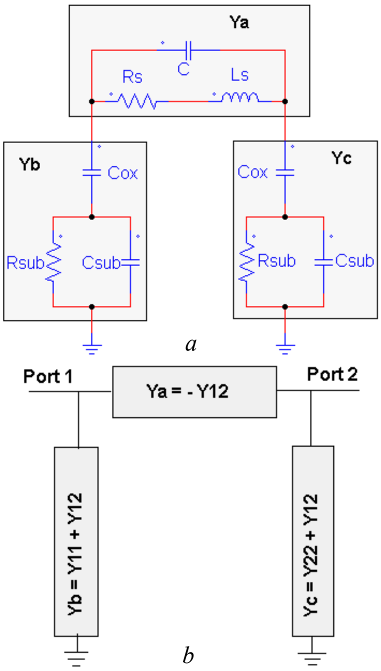

Fig. 2. *a* – equivalent circuit model of TSV-inductor;
b – π-model of two-port network

The definition of TSV-inductors is mainly based on two parameters; quality factor Q and inductance L. These latter are given by the Y parameters through the following equations [18, 19]:

$$L = \frac{\mathrm{Im}(1/\mathrm{Y}_{11})}{\omega}, \tag{1}$$

where $\omega = 2\pi f$ and f is the frequency,

$$Q = \frac{\mathrm{Im}(1/\mathrm{Y}_{11})}{\mathrm{Re}(1/\mathrm{Y}_{11})}. \tag{2}$$

Simulation and results. In this study, we simulated the proposed design using MATLAB software. The simulation results show a parametric study of conductor width *w*, the radius *r* of the TSV, and the number of turns *N*, to verify the extent to which structural parameters affect the electrical response of solenoid inductors. For a detailed examination of the effects of geometric parameters, we chose the frequency range 1–10 GHz as it includes the peak values of the electrical parameters (i.e., inductance and quality factor).

RDL width. As shown in Fig. 3, widening the width of RDL increases the quality factor with decreasing the value of the inductance due to the low resistance. At 6 GHz, the RDL width of 25 μm gives a maximum quality factor 50 and a minimum inductance 8,4 nH. Compared to a RDL width of 15 μm, it shows a 36 % variation in inductance and the *Q* factor decreases by 18 %.

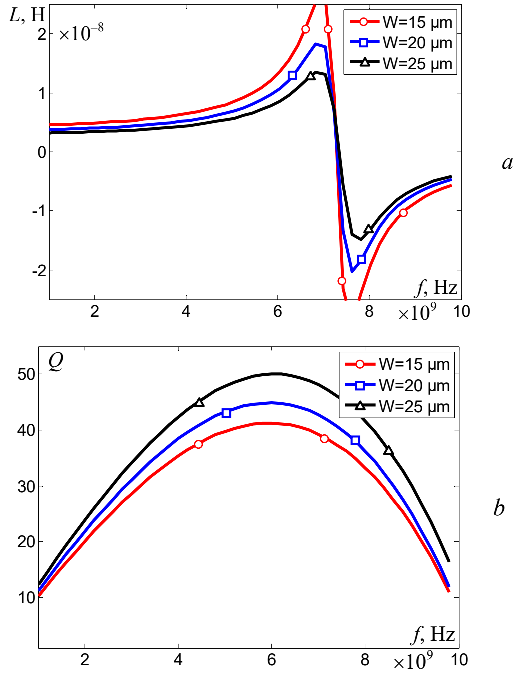

Fig. 3. Inductance (*a*) and quality factor (*b*) of TSV-inductor for different widths of RDL

Radius of TSV. Figure 4 shows the effect of changing the radius of the TSV while holding all other geometric parameters constant.

At 2 GHz, the smallest radius of 10 μm shows an inductance of 4.8 nH with a maximum difference of 31 %. The highest *Q* factor is observed in the largest diameter of 14 μm, which shows an improvement of 14 % compared to the smallest diameter. Therefore, to achieve a high inductance value with a high-quality factor, an optimum radius should be chosen.

Number of turns. Figure 5 shows the effect of changing *N* on inductance and quality factor while keeping all geometric parameters constant.

The inductance at 3 GHz is about 3.5 nH when the number of turns is 2 and increases to 5 nH when $N = 4$. With increasing frequency, we notice that there is a significant increase in inductance.

The quality factor peak at 49 when the number of turns is 2 at 7 GHz, for $N = 3$ the peak is 45 at 6.5 GHz, and for $N = 4$, is 42 at 6 GHz, respectively.

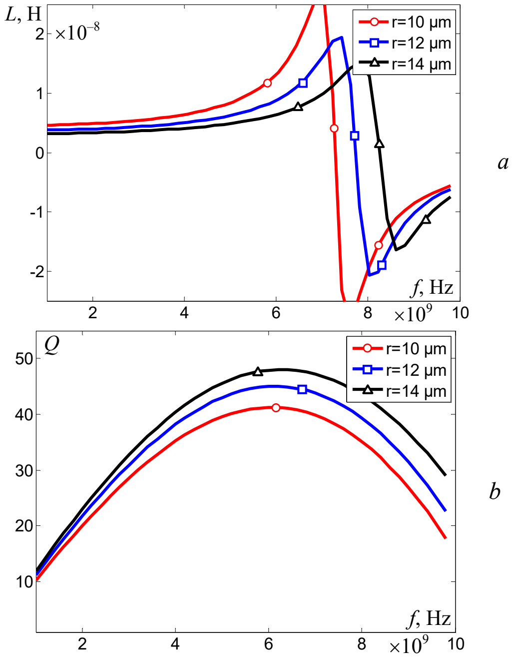

Fig. 4. Effect of changing the radius of TSV on inductance (*a*) and quality factor (*b*)

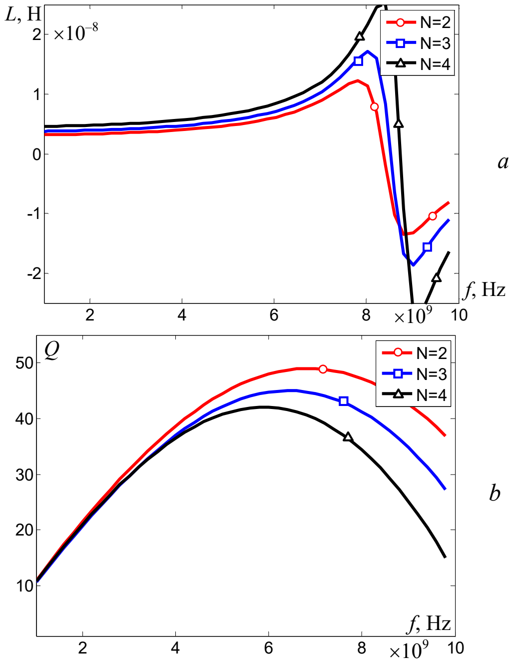

Fig. 5. Inductance (*a*) and quality factor (*b*) for TSV-inductor against frequency from 2 to 4 turns

Comparison and application in buck converter. The results obtained from the proposed TSV-inductor are compared with the 2D inductors in Table 2.

Table 2
Comparison between spiral inductor, racetrack inductor and TSV-inductor

Reference	Type	Size, mm^2	L, nH	Q_{max}
[20]	Spiral inductor	26	13,84	16
[21]	Racetrack inductor	22,7	8,89	18
This work	TSV-inductor	**1,2**	**4,2**	**45**

It is clear that the proposed TSV-inductor in our work presents a higher quality factor compared to other conventional inductors. The low Q of the 2D inductors is caused by the large substrate loss. As shown in Table 2, the achieved quality factor in this work is greater than that obtained in [20], [21] by 64,4 % and 60 %, respectively. The proposed inductor is considerably smaller than those of the other two types by about 95 %.

In order to compare the performance of the TSV-inductor with the other two types above, we applied each of them to a buck converter design with the same design specifications given in Table 3.

Table 3
Design specifications for the buck converter

V_{in}, V	V_{out}, V	f, MHz	Max load, A
1,5	0,8	500	0,5

Using a model of the TSV-inductor studied in the first part of this work in a buck converter gives the results obtained by the PSIM simulator. Figure 6 shows the output current of the buck converter at the frequency 500 MHz, which is stable at the value of 0,5 A after an initial period of about 2 ms. We also observe the same behavior for the output voltage shown in Fig. 7. It is noticeable that the input voltage decreased from 1.5 V to 0.8 V.

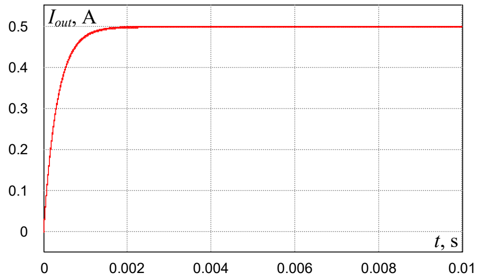

Fig. 6. Current output of a buck converter using a TSV-inductor

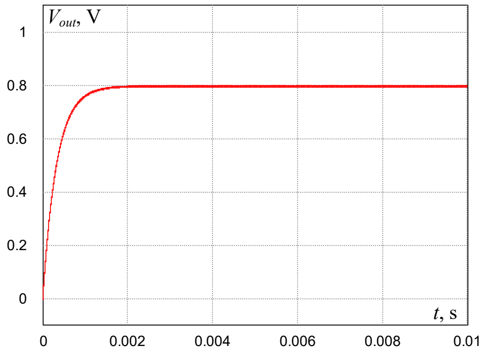

Fig. 7. Voltage output of a buck converter using a TSV-inductor

A study of the effects of load current on the efficiencies of three designs was conducted. Figure 8 shows that all three designs achieve approximately the same efficiency between 0 and 100 mA, but the difference between them increases slightly after 150 mA and reaches 500 mA, which is the maximum load. As expected, the TSV-inductor improves its efficiency by up to 15 % and 6 % compared to the spiral inductor and racetrack inductor, respectively.

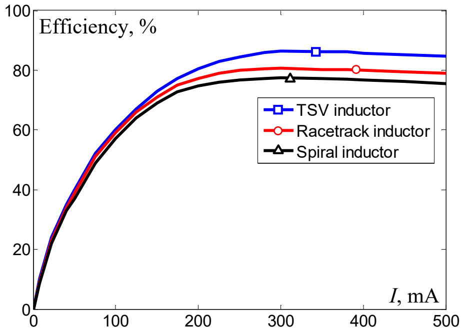

Fig. 8.Variation of buck converter efficiency as a function of load current for three inductors' different

Conclusions. In this article, a simple model of the through-silicon-via (TSV) inductor has been derived from the physical layout. Then, the effect of various geometric parameters such as the width of redistribution lines, the radius of TSV, and the number of turns was analyzed in detail using MATLAB simulations to determine the optimal TSV-indicator geometry parameters. Furthermore, we demonstrated the efficiency of the 3D TSV-inductor structure compared to other conventional 2D inductors in buck converter designs of the integrated circuit. According to simulations, the use of a TSV-inductor in a buck converter improves its efficiency by 15 % and 6 % compared to the spiral inductor and racetrack inductor, respectively. The results show that the TSV-inductor is a very promising approach for the integration of DC-DC converters.

Conflict of interest. The authors of the article declare that there is no conflict of interest.

REFERENCES

1. Namoune A., Taleb R., Mansour N. Design and modeling of solenoid inductor integrated with FeNiCo in high frequency. *TELKOMNIKA (Telecommunication Computing Electronics and Control)*, 2020, vol. 18, no. 4, pp. 1746-1753. doi: https://doi.org/10.12928/telkomnika.v18i4.12139.

2. Namoune A., Taleb R., Derrouazin A., Belboula A., Hamid A. Integrated square shape inductor with magnetic core in a buck converter DC-DC. *Przegląd Elektrotechniczny*, 2019, vol. 95, no. 9, pp. 57-61. doi: https://doi.org/10.15199/48.2019.09.11.

3. Baazouzi K., Bensalah A.D., Drid S., Chrifi-Alaoui L. Passivity voltage based control of the boost power converter used in photovoltaic system. *Electrical Engineering & Electromechanics*, 2022, no. 2, pp. 11-17. doi: https://doi.org/10.20998/2074-272X.2022.2.02.

4. Mimouni A., Laribi S., Sebaa M., Allaoui T., Bengharbi A. A. Fault diagnosis of power converters in a grid connected photovoltaic system using artificial neural networks. *Electrical Engineering & Electromechanics*, 2023, no. 1, pp. 25-30. doi: https://doi.org/10.20998/2074-272X.2023.1.04.

5. Hamdi R., Hadri Hamida A., Bennis O. On modeling and real-time simulation of a robust adaptive controller applied to a multicellular power converter. *Electrical Engineering & Electromechanics*, 2022, no. 6, pp. 48-52. doi: https://doi.org/10.20998/2074-272X.2022.6.08.

6. Benzidane M.R., Melati R., Benyamina M., Meskine S., Spiteri P., Boukortt A., Adda Benattia T. Miniaturization and Optimization of a DC–DC Boost Converter for Photovoltaic Application by Designing an Integrated Dual-Layer Inductor Model. *Transactions on Electrical and Electronic Materials*, 2022, vol. 23, no. 5, pp. 462-475. doi: https://doi.org/10.1007/s42341-021-00370-9.

7. Wang F., Ren R., Yin X., Yu N., Yang Y. A transformer with high coupling coefficient and small area based on TSV. *Integration*, 2021, vol. 81, pp. 211-220. doi: https://doi.org/10.1016/j.vlsi.2021.07.003.

8. Zhi C., Dong G., Zhu Z., Yang Y. A TSV-Based 3-D Electromagnetic Bandgap Structure on an Interposer for Noise Suppression. *IEEE Transactions on Components, Packaging and Manufacturing Technology*, 2022, vol. 12, no. 1, pp. 147-154. doi: https://doi.org/10.1109/TCPMT.2021.3131317.

9. Wu H., Dong G., Xiong W., Zhi C., Li S., Zhu Z., Yang Y. Accurate Magnetic Coupling Coefficient Modeling of 3-D Transformer Based on TSV. *IEEE Microwave and Wireless Components Letters*, 2022, vol. 32, no. 12, pp. 1419-1422. doi: https://doi.org/10.1109/LMWC.2022.3195193.

10. Zhang B., Xiong Y.-Z., Wang L., Hu S., Shi J., Zhuang Y.-Q., Li L.-W., Yuan X. 3D TSV transformer design for DC-DC/AC-DC converter. *2010 Proceedings 60th Electronic Components and Technology Conference (ECTC)*, 2010, pp. 1653-1656. doi: https://doi.org/10.1109/ECTC.2010.5490761.

11. Bontzios Y.I., Dimopoulos M.G., Hatzopoulos A.A. Prospects of 3D inductors on through silicon vias processes for 3D ICs. *2011 IEEE/IFIP 19th International Conference on VLSI and System-on-Chip*, 2011, pp. 90-93. doi: https://doi.org/10.1109/VLSISoC.2011.6081657.

12. Feng Z., Lueck M.R., Temple D.S., Steer M.B. High-Performance Solenoidal RF Transformers on High-Resistivity Silicon Substrates for 3D Integrated Circuits. *IEEE Transactions on Microwave Theory and Techniques*, 2012, vol. 60, no. 7, pp. 2066-2072. doi: https://doi.org/10.1109/TMTT.2012.2195026.

13. Tida U.R., Zhuo C., Shi Y. Through-silicon-via inductor: Is it real or just a fantasy? *2014 19th Asia and South Pacific Design Automation Conference (ASP-DAC)*, 2014, pp. 837-842. doi: https://doi.org/10.1109/ASPDAC.2014.6742994.

14. Xiong W., Dong G., Zhu Z., Yang Y. Compact and Physics-Based Modeling of 3-D Inductor Based on Through Silicon Via. *IEEE Electron Device Letters*, 2021, vol. 42, no. 10, pp. 1559-1562. doi: https://doi.org/10.1109/LED.2021.3107320.

15. Namoune A., Taleb R., Benzidane M.R. Design and simulation of integrated spiral inductor a boost converter for photovoltaic application. *Ingeniería Energética*, 2023, vol. 44, no. 1, pp. 1-12.

16. Liu Y., Zhu Z., Liu X., Lu Q., Yin X., Yang Y. Physics based scalable inductance model for three-dimensional solenoid inductors. *Microelectronics Journal*, 2020, vol. 103, art. no. 104867. doi: https://doi.org/10.1016/j.mejo.2020.104867.

17. Chen B., Zhuo C., Shi Y. A physics-aware methodology for equivalent circuit model extraction of TSV-inductors. *Integration*, 2018, vol. 63, pp. 160-166. doi: https://doi.org/10.1016/j.vlsi.2018.07.002.

18. Namoune A., Taleb R., Mansour N., Belboula A. Design and modeling of integrated octagonal shape inductor with substrate silicon in a buck converter. *Indonesian Journal of Electrical Engineering and Informatics (IJEEI)*, 2019, vol. 7, no. 3, pp. 527-534. doi: https://doi.org/10.52549/ijeei.v7i3.942.

19. Pulijala V., Syed A. Comparison of the effects of 60 nm and 96 nm thick patterned permalloy thin films on the performance of on-chip spiral inductors. *Journal of Magnetism and Magnetic Materials*, 2016, vol. 419, pp. 245-248. doi: https://doi.org/10.1016/j.jmmm.2016.06.031.

20. Meere R., Wang N., O'Donnell T., Kulkarni S., Roy S., O'Mathuna S.C. Magnetic-Core and Air-Core Inductors on Silicon: A Performance Comparison up to 100 MHz. *IEEE Transactions on Magnetics*, 2011, vol. 47, no. 10, pp. 4429-4432. doi: https://doi.org/10.1109/TMAG.2011.2158519.

21. Anthony R., Wang N., Casey D.P., O'Mathuna C., Rohan J.F. MEMS based fabrication of high-frequency integrated inductors on Ni–Cu–Zn ferrite substrates. *Journal of Magnetism and Magnetic Materials*, 2016, vol. 406, pp. 89-94. doi: https://doi.org/10.1016/j.jmmm.2015.12.099.

Received 13.02.2023
Accepted 14.04.2023
Published 02.11.2023

Abdelhadi Namoune[1]*, Associate Professor,*
Rachid Taleb[2]*, Professor,*
Noureddine Mansour[3]*, Associate Professor,*
Mohammed Ridha Benzidane[4]*, Doctor of Electrical Engineering*
Abdelkader Boukortt[4]*, Professor,*
[1] Department of Electrotechnical & Automatic Engineering,
Relizane University, Laboratoire Génie Industriel et
Développement Durable (GIDD), Relizane, Algeria,
e-mail: namoune.abdelhadi@gmail.com (Corresponding Author)
[2] Electrical Engineering Department,
Laboratoire Génie Electrique et Energies Renouvelables (LGEER),
Hassiba Benbouali University of Chlef, Algeria,
e-mail: rac.taleb@gmail.com
[3] College of Engineering, University of Bahrain, Bahrain,
e-mail: nmansour@uob.edu.bh
[4] Electrical Engineering Department,
Abdelhamid Ibn Badis University, Mostaganem, Algeria,
e-mail: ridha.benzidane.etu@univ-mosta.dz;
abdelkader.boukort@univ-mosta.dz

How to cite this article:

Namoune A., Taleb R., Mansour N., Benzidane M.R., Boukortt A. Integrated through-silicon-via-based inductor design in buck converter for improved efficiency. *Electrical Engineering & Electromechanics*, 2023, no. 6, pp. 54-57. doi: https://doi.org/10.20998/2074-272X.2023.6.09

UDC 621.314 https://doi.org/10.20998/2074-272X.2023.6.10

E. Parimalasundar, S. Muthukaruppasamy, R. Dharmaprakash, K. Suresh

Performance investigations of five-level reduced switches count H-bridge multilevel inverter

Introduction. *This research paper describes a simple five-level single-phase pulse-width modulated inverter topology for photovoltaic grid applications. Multilevel inverters, as opposed to conventional two-level inverters, include more than two levels of voltage while using multiple power switches and lower-level DC voltage levels as input to produce high power, easier, and less modified oscillating voltage. The H-bridge multilevel inverter seems to have a relatively simple circuit design, needs minimal power switching elements, and provides higher efficiency among various types of topologies for multi-level inverters that are presently accessible. Nevertheless, using more than one DC source for more than three voltage levels and switching and conduction losses, which primarily arise in major power switches, continue to be a barrier. The* ***novelty*** *of the proposed work consists of compact modular inverter configuration to connect a photovoltaic system to the grid with fewer switches.* ***Purpose.*** *The proposed system aims to decrease the number of switches, overall harmonic distortions, and power loss. By producing distortion-free sinusoidal output voltage as the level count rises while lowering power losses, the constituted optimizes power quality without the need for passive filters.* ***Methods.*** *The proposed topology is implemented in MATLAB/Simulink with gating pulses and various pulse width modulation technique.* ***Results****. With conventional topology, total harmonic distortion, power switches, output voltage, current, power losses, and the number of DC sources are investigated.* ***Practical value.*** *The proposed topology has proven to be extremely useful for deploying photovoltaic-based stand-alone multilevel inverters in grid applications.* References 18, table 2, figures 15.

Key words: **H-bridge multilevel inverter, pulse width modulation, switching losses, total harmonic distortion.**

Вступ*. У цій дослідницькій статті описується проста топологія п'ятирівневого однофазного інвертора із широтно-імпульсною модуляцією для фотоелектричних мереж. Багаторівневі інвертори, на відміну від звичайних дворівневих інверторів, включають більше двох рівнів напруги при використанні кількох перемикачів потужності та рівнів постійної напруги нижчого рівня на вході для створення більш потужної, простішої і менш модифікованої коливальної напруги. Багаторівневий інвертор з Н-мостом, мабуть, має відносно просту схему, вимагає мінімальної кількості елементів, що перемикають, і забезпечує більш високу ефективність серед різних типів топологій багаторівневих інверторів, які доступні в даний час. Тим не менш, використання більше одного джерела постійного струму для більш ніж трьох рівнів напруги, а також втрати на перемикання та провідність, які в першу чергу виникають в основних силових перемикачах, як і раніше, залишаються перешкодою.* ***Новизна*** *запропонованої роботи полягає у компактній модульній конфігурації інвертора для підключення фотоелектричної системи до мережі з меншою кількістю перемикачів.* ***Мета****. Пропонована система спрямована на зменшення кількості перемикачів, загальних гармонічних спотворень та втрат потужності. Створюючи синусоїдальну вихідну напругу без спотворень у міру збільшення рівня та одночасно знижуючи втрати потужності, перетворювач оптимізує якість електроенергії без необхідності використання пасивних фільтрів.* ***Методи****. Запропонована топологія реалізована в MATLAB/Simulink з використанням стробуючих імпульсів та різних методів широтно-імпульсної модуляції.* ***Результати****. За традиційної топології досліджуються загальні гармонічні спотворення, силові ключі, вихідна напруга, струм, втрати потужності та кількість джерел постійного струму.* ***Практична цінність****. Запропонована топологія виявилася надзвичайно корисною для розгортання автономних багаторівневих інверторів на фотоелектричній основі у мережних додатках.* Бібл. 18, табл. 2, рис. 15.

Ключові слова: **багаторівневий інвертор Н-мосту, широтно-імпульсна модуляція, комутаційні втрати, загальні гармонічні спотворення.**

1. Introduction. Multilevel inverters (MLIs) have become widely used as power converters for DC-AC power conversion in medium and high voltage/power applications, including those involving renewable energy sources, motor drives, and power systems like flexible AC transmission system and high voltage DC transmission systems. The MLI has gained acceptance as a result of its many benefits. These benefits include wider effects voltage, lower output voltage harmonic distortion, less voltage stress on the switches, low voltage ratings for high voltage applications, and smaller filters, to name a few. Most residential or low-power applications with power ranges under 10 kW use single-phase grid-connected inverters [1]. Numerous single-phase grid-connected inverter types have been the subject of studies [2].

Conventional MLI topologies include the cascaded H-bridge (CHB), flying capacitor (FC), and diode-clamped. However, these topologies have a greater number of components and more levels of capacitor voltage balancing. There have, however, been a number of MLI topologies with fewer switches proposed [3, 4]. The majority of renewable energy sources have had low output voltages. The boosting has traditionally been a crucial component of topologies used in higher voltage applications. The capacitor voltage disparity flaw affects both neutral point clamped (NPC) and FC configurations. As a result, balancing the voltages of capacitors requires the use of an auxiliary stability circuit, a sophisticated control algorithm, current/voltage sensors, and a recognition circuit. When their output reaches the desired level and a rapid increase in the number of power switches, power diodes, and capacitors used, the cost and regulate difficulty will be very high. In comparison to FC and NPC topologies, the conventional CHB topology can produce a significant output level with module cascading, and the voltage balance of the capacitor can be avoided because multiple symmetric/asymmetric DC sources are synthesized and used in the multilevel output. Finding enough unbiased sources is a major issue for the majority of practical uses [5, 6].

Single-phase MLIs can play an important role in this area, converting the photovoltaic (PV) system's DC voltage into a continuous AC signal accessible by loads as well as the gird significantly fewer harmonic filters and increased performance. The seven-level power conditioning unit inverter has been proposed for this purpose, with appealing features such as low number of switches and the ability to generate multiple voltage ranges at the result [7, 8].

Recently, it has been shown that five-level switched capacitor-based inverters are capable of producing higher voltage progress [9-12]. In [13] authors give an example based on an extendable switched capacitor module. Compared to inverters from [14, 15], all of which do not use diodes, it induces low voltages on its switches. Use of the diodes [16-18] can reduce the number of switches. The previous discussions suggest that there is a trade-off with switched capacitor-based boost MLIs. To put it another way, using low-voltage switches typically requires using more switches and the gate-driver circuits that go with them, whereas having a high switch count requires the use of high-voltage switches. These MLIs require a greater number of switches, DC sources, diodes, and capacitors as the number of output levels rises. Increased control complexity, system size, and installation space are the results of this. Consequently, the cost of the entire system rises.

The previous drawbacks are addressed by implementing modified MLI designs based on fewer circuit elements. The following noteworthy advantages of the topology are not in any specified sequence: The output voltage amplitude in the suggested topology can rise by as much as 4 times the magnitude of the DC source voltage. Designing switching patterns for power electronic switches involves the widely used multicarrier pulse width modulation (PWM) technique. Investigations have been made into the effects of variable loads on the current and voltage total harmonic distortion (THD) values. The five-level inverter has a significantly lower component count when compared to other inverters. Adding a suitable RL load have been assist in reducing the circuit's output voltage ripple.

Depending on the output voltage level, different common MLI configurations require different amounts of components. This suggests that the quantity of components will increase along with the output voltage levels. The main structural components of the multilevel converters are switches and related gate drive circuits. Size, cost, and control complexity of the inverter circuit all increase as the number of components does. In Fig. 1 a MLI with a PV application is illustrated. The proposed topology of five-level inverters and five power semiconductor switches is shown in Fig. 2.

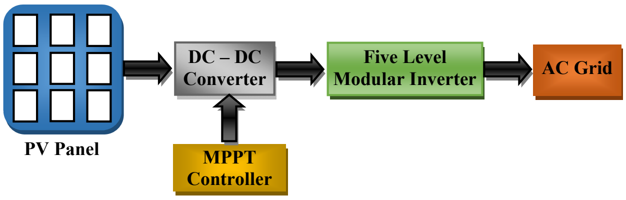

Fig. 1. PV fed proposed five-level MLI to AC grid integration

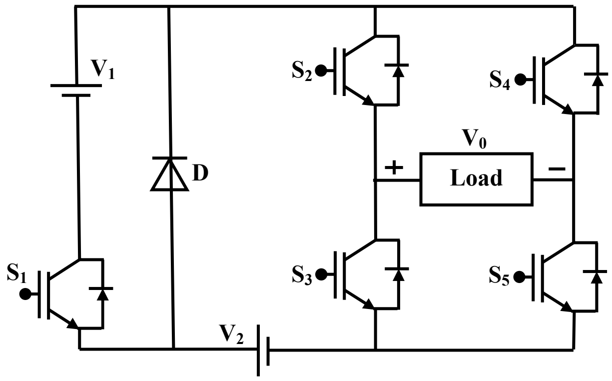

Fig. 2. Proposed topology of five-level MLI

2. Proposed topology and modes of operation. Power semiconductors are used in a MLI to create a staircase waveform from various DC levels. The 8 IGBT switches on the five-level output voltages of conventional MLI have been designed. The newly proposed topology with a reduced switch count of 5 IGBT switches is further discussed in this article. Figure 3 depicts the switching process of the proposed MLI, which results in a $+2V_{dc}$ output voltage. Similar to $+V_{dc}$, $0V_{dc}$, $-V_{dc}$, and $-2V_{dc}$ output voltages, which are depicted in Fig. 4-7 respectively, switching patterns of MLI are used to determine these voltages. Figure 8 illustrates the sinusoidal PWM used to generate switching patterns based on a signal with one reference wave and 4 carriers.

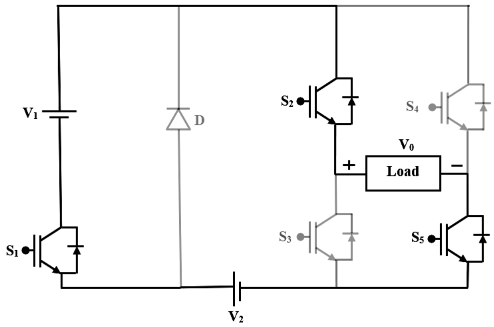

Fig. 3. Mode-I operation

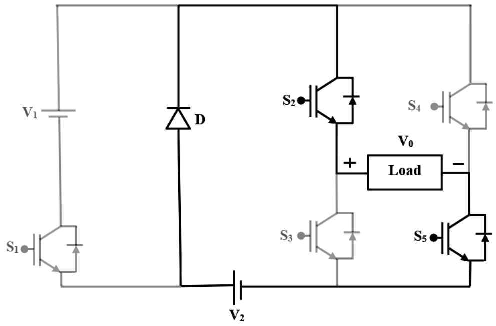

Fig. 4. Mode-II operation

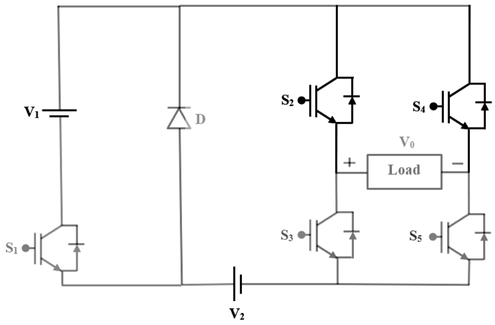

Fig. 5. Mode-III operation

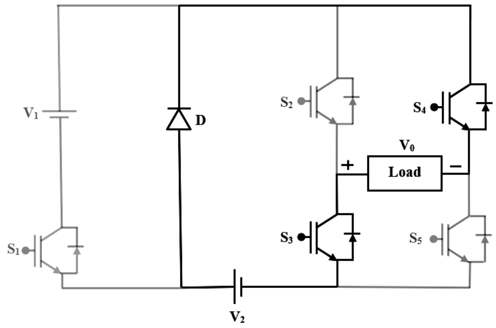

Fig. 6. Mode-IV operation

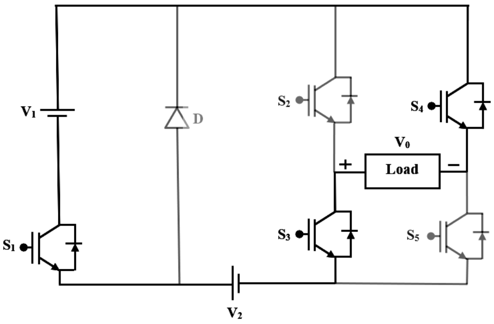

Fig. 7. Mode-V operation

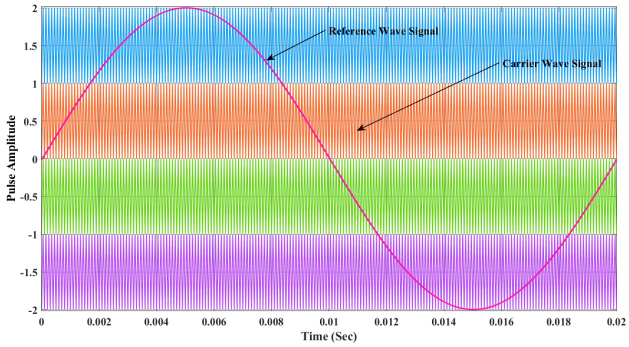

Fig. 8. Sinusoidal PWM for generating switching patterns

3. Results and discussion. Figure 9 shows the output voltage and current of the suggested MLI for a resistive load, which provides a 220V staircase five-level output voltage and current patterns which complement the output voltage patterns of resistive load. The output voltage and current of the proposed MLI for a resistive load are shown in Figure 10, which produces a 220V staircase output voltage but almost sinusoidal current patterns owing to the inductive load. Figure 11 has shown a THD analysis of the proposed MLI's output voltage under a resistive load. The output current of the proposed MLI under a resistive load is shown in THD analysis in Fig. 12. Figure 13 has shown a THD analysis of the proposed MLI's output current under a resistive and inductive load.

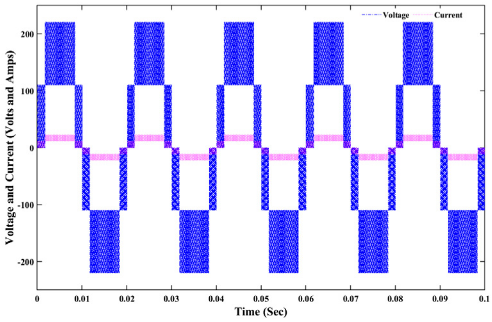

Fig. 9. Output voltage and current of proposed MLI for resistive load

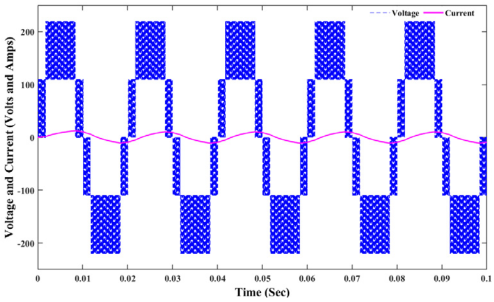

Fig. 10. Output voltage and current of proposed MLI for RL load

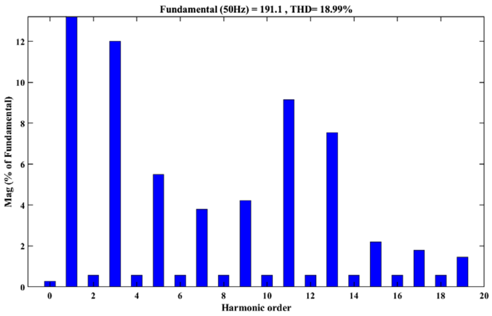

Fig. 11. THD analysis of output voltage of proposed MLI during R load

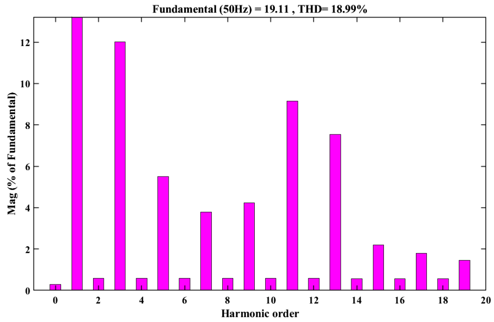

Fig. 12. THD analysis of output current of proposed MLI during R load

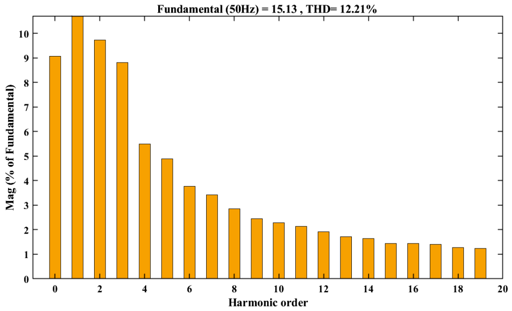

Fig. 13. THD analysis of output current of proposed MLI during RL load

4. Power loss and comparative analysis. The losses in the developed proposed structure are mostly intense on 3 main power losses, specifically losses during switching ($W_{Switching}$) and conduction ($W_{conduction}$). Then overall power loss (W_{Loss}) of MLI is written as:

$$W_{Loss} = W_{Switching} + W_{Conduction} \,. \tag{1}$$

Conduction loss of power semiconductor devices is calculated as:

$$W_{Conduction} = \int_{0}^{T_0/2} \left\{ \begin{array}{l} \left[V_{CE0} + r i_p \sin(\omega t)\right] \times \\ \times\, i_p \sin(\omega t) \left[\frac{1}{2}\left(1 + A_m \sin(\omega t + \varphi)\right]\mathrm{d}t\right. \end{array} \right\},$$

after simplification of above equation:

$$W_{Conduction} = \frac{1}{2} \left\{ \begin{array}{l} \left(V_{CEO} \cdot \frac{i_p}{\pi} + r \cdot \frac{i_p^2}{4} \right) + \\ + \left(A_m \cdot \cos\varphi \cdot V_{CEO} \cdot \frac{i_p}{8} \right) + \left(\frac{1}{3\pi} \cdot r i_p^2 \right) \end{array} \right\}, \tag{2}$$

where V_{CEO} is the zero-current collector to emitter voltage; r is the collector to emitter on-state resistance; A_m is the modulation index; i_p is the peak current of IGBT device.

Switching loss is expressed as the integration of all the turn-on and turn-off switching energies at the switching instants. In the equation, variable switching time is considered and integrated as:

$$W_{Switching} = f_{sw} \frac{1}{T_0} \int_0^{T_0/2} \left(E_{on} + E_{off}\right) \cdot \left(t, i_p\right) \mathrm{d}t \,, \qquad (3)$$

where T_0 is the switching time period; f_{sw} is the switching frequency; E_{on} is the on-state voltage drop; E_{off} is the off-state voltage drop.

The efficiency of MLI is calculation as:

$$Efficiency = \frac{P_{Output}}{P_{Output} + W_{Loss}} \cdot 100\% \,. \qquad (4)$$

Table 1 shows the results of various power loss and efficiency calculations based on mathematical expressions.

Table 1

THD, power loss and conduction loss parameters of proposed five-level MLI

Parameters	Conventional H-bridged topology	Proposed H-bridged topology
No. input DC supply (symmetrical)	2	2
DC voltage (magnitude), V	110	110
RMS output voltage, V	220	220
No. of IGBTs	8	5
No. gating circuits	8	5
Carrier frequency, kHz	2	2
THD current (RL load), %	18.99	12.21
$W_{switching\ loss}$, W	0.32	0.24
$W_{conduction\ loss}$, W	48.25	45.31
W_{Loss}, W	48.81	45.55
Efficiency, %	91.63	95.52

Table 2 depicts the fundamental parameters of conventional and proposed MLI.

Table 2

Parameters of conventional and proposed MLI

Parameters	DC	FC	CHB	Proposed MLI
DC supply	1	1	2	2
Switches	8	8	8	5
Diodes	12	–	–	1
DC bus capacitors	4	4	–	–
Balancing capacitors	0	6	–	–

Figure 14 has shown a THD analysis of the output current of the proposed MLI under a resistive load, and Figure 15 illustrates an efficiency comparison between the proposed and conventional MLI.

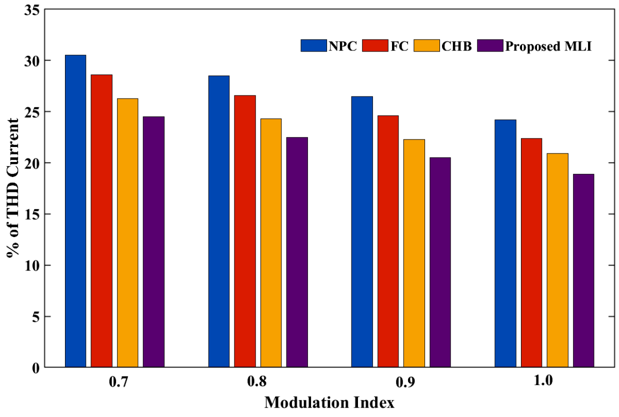

Fig. 14. THD analysis of output current of proposed MLI during resistive load

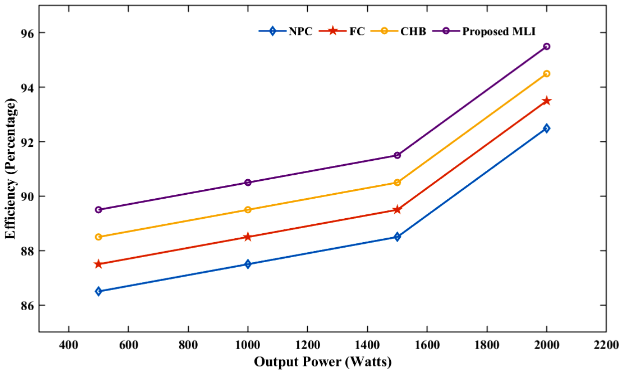

Fig. 15. Efficiency analysis of conventional and proposed MLI

5. Conclusions. It is observed that a five-level converter that is able to reconfigure and makes use of fewer power switches satisfies multilevel inverter requirements. The used five-level inverter produced 5 levels of RMS output staircase voltage when the power switches were given the proper pulse width modulation signal in a logical manner. Using the MATLAB/Simulink, total harmonic distortion values between 12.21 % distances with various loads were obtained and examined. The proposed converter is 95.52 % efficient when input, output, and power losses are taken into account. Comparisons show that the suggested single-phase five-level inverter performs significantly better than traditional converters.

Conflict of interest. The authors declare that they have no conflicts of interest.

REFERENCES

1. Odeh C., Lewicki A., Morawiec M., Kondratenko D. Three-Level F-Type Inverter. *IEEE Transactions on Power Electronics*, 2021, vol. 36, no. 10, pp. 11265-11275. doi: https://doi.org/10.1109/TPEL.2021.3071359.

2. Parimalasundar E., Kumar N.M.G., Geetha P., Suresh K. Performance investigation of modular multilevel inverter topologies for photovoltaic applications with minimal switches. *Electrical Engineering & Electromechanics*, 2022, no. 6, pp. 28-34. doi: https://doi.org/10.20998/2074-272X.2022.6.05.

3. Parimalasundar E., Senthil Kumar R., Chandrika V.S., Suresh K. Fault diagnosis in a five-level multilevel inverter using an artificial neural network approach. *Electrical Engineering & Electromechanics*, 2023, no. 1, pp. 31-39. doi: https://doi.org/10.20998/2074-272X.2023.1.05.

4. Sonti V., Jain S., Bhattacharya S. Analysis of the Modulation Strategy for the Minimization of the Leakage Current in the PV Grid-Connected Cascaded Multilevel Inverter. *IEEE Transactions on Power Electronics*, 2017, vol. 32, no. 2, pp. 1156-1169. doi: https://doi.org/10.1109/TPEL.2016.2550206.

5. Suresh K., Parimalasundar E. IPWM Based IBMSC DC-AC Converter Using Solar Power for Wide Voltage Conversion System. *IEEE Canadian Journal of Electrical and Computer Engineering*, 2022, vol. 45, no. 4, pp. 394-400. doi: https://doi.org/10.1109/ICJECE.2022.3207873.

6. Meneses D., Blaabjerg F., Garcia O., Cobos J.A. Review and Comparison of Step-Up Transformerless Topologies for Photovoltaic AC-Module Application. *IEEE Transactions on Power Electronics*, 2013, vol. 28, no. 6, pp. 2649-2663. doi: https://doi.org/10.1109/TPEL.2012.2227820.

7. Mhiesan H., Wei Y., Siwakoti Y.P., Mantooth H.A. A Fault-Tolerant Hybrid Cascaded H-Bridge Multilevel Inverter. *IEEE Transactions on Power Electronics*, 2020, vol. 35, no. 12, pp. 12702-12715. doi: https://doi.org/10.1109/TPEL.2020.2996097.

8. Jahan H.K., Panahandeh F., Abapour M., Tohidi S. Reconfigurable Multilevel Inverter with Fault-Tolerant Ability.

IEEE Transactions on Power Electronics, 2018, vol. 33, no. 9, pp. 7880-7893. doi: https://doi.org/10.1109/TPEL.2017.2773611.

9. Suresh K., Parimalasundar E. Design and Implementation of Universal Converter. *IEEE Canadian Journal of Electrical and Computer Engineering*, 2022, vol. 45, no. 3, pp. 272-278. doi: https://doi.org/10.1109/ICJECE.2022.3166240.

10. Siddique M.D., Mekhilef S., Rawa M., Wahyudie A., Chokaev B., Salamov I. Extended Multilevel Inverter Topology with Reduced Switch Count and Voltage Stress. *IEEE Access*, 2020, vol. 8, pp. 201835-201846. doi: https://doi.org/10.1109/ACCESS.2020.3026616.

11. Saeedian M., Adabi M.E., Hosseini S.M., Adabi J., Pouresmaeil E. A Novel Step-Up Single Source Multilevel Inverter: Topology, Operating Principle, and Modulation. *IEEE Transactions on Power Electronics*, 2019, vol. 34, no. 4, pp. 3269-3282. doi: https://doi.org/10.1109/TPEL.2018.2848359.

12. Suresh K., Parimalasundar E., Jayakumar S., Ravikumar R. Encapsulated 3Ø converter for power loss minimization in a grid-connected system. *Automatika*, 2023, vol. 64, no. 1, pp. 189-197. doi: https://doi.org/10.1080/00051144.2022.2119501.

13. Sandeep N., Yaragatti U.R. Design and Implementation of a Sensorless Multilevel Inverter with Reduced Part Count. *IEEE Transactions on Power Electronics*, 2017, vol. 32, no. 9, pp. 6677-6683. doi: https://doi.org/10.1109/TPEL.2017.2681739.

14. Parimalasundar E., Jayakumar S., Ravikumar R., Suresh K. Investigation analysis of open circuit and short circuit fault on cascaded H-bridged multilevel inverter using artificial neural network approach. *International Journal of Electrical and Electronics Research*, 2022, vol. 10, no. 2, pp. 320-326. doi: https://doi.org/10.37391/ijeer.100243.

15. Maalandish M., Hosseini S.H., Jalilzadeh T. High step-up dc/dc converter using switch-capacitor techniques and lower losses for renewable energy applications. *IET Power Electronics*, 2018, vol. 11, no. 10, pp. 1718-1729. doi: https://doi.org/10.1049/iet-pel.2017.0752.

16. Parimalasundar E., Suresh K., Sindhuja R., Manikandan K. A Performance Investigations of Modular Multilevel Inverter with Reduced Switch Count. *2022 International Conference on Intelligent Innovations in Engineering and Technology (ICIIET)*, 2022, pp. 83-87. doi: https://doi.org/10.1109/ICIIET55458.2022.9967595.

17. Belbachir N., Zellagui M., Settoul S., El-Bayeh C.Z., Bekkouche B. Simultaneous optimal integration of photovoltaic distributed generation and battery energy storage system in active distribution network using chaotic grey wolf optimization. *Electrical Engineering & Electromechanics*, 2021, no. 3, pp. 52-61. doi: https://doi.org/10.20998/2074-272X.2021.3.09.

18. Parimalasundar E., Jayanthi R., Suresh K., Sindhuja R. Investigation of efficient multilevel inverter for photovoltaic energy system and electric vehicle applications. *Electrical Engineering & Electromechanics*, 2023, no. 4, pp. 47-51. doi: https://doi.org/10.20998/2074-272X.2023.4.07.

Received 30.01.2023
Accepted 27.04.2023
Published 02.11.2023

Ezhilvannan Parimalasundar[1], *Professor,*
S. Muthukaruppasamy [2], *Professor,*
R. Dharmaprakash[3], *Professor,*
Krishnan Suresh[4], *Associate Professor,*
[1] Department of Electrical & Electronics Engineering,
Mohan Babu University (Erstwhile Sree Vidyanikethan Engineering College), Tirupati, AP – 517102, India,
e-mail: parimalasundar.e@vidyanikethan.edu (Corresponding Author)
[2] Electrical and Electronics Engineering,
Velammal Institute of Technology,
Anna University, Panchetti, TN – 601204, India,
e-mail: mksamy14@yahoo.com
[3] Department of Electrical and Electronics Engineering,
Panimalar Engineering College, Chennai – 600123, India,
e-mail: rdharmaprakash@yahoo.co.in
[4] Department of Electrical and Electronics Engineering,
Christ (Deemed to be University), Bangalore, India,
e-mail: sureshk340@gmail.com

How to cite this article:
Parimalasundar E., Muthukaruppasamy S., Dharmaprakash R., Suresh K. Performance investigations of 5-level reduced switches count H-bridge multilevel inverter. *Electrical Engineering & Electromechanics*, 2023, no. 6, pp. 58-62. doi: https://doi.org/10.20998/2074-272X.2023.6.10

UDC 621.314 https://doi.org/10.20998/2074-272X.2023.6.11

V.Y. Romashko, L.M. Batrak, O.O. Abakumova

Features of the work of pulse regulators in the maximum power transmission mode, with the presence of an accumulator at their output

Introduction. *For the efficient use of non-traditional and renewable sources of electrical energy, it is necessary to ensure their operation at the maximum power point, which is possible if the load resistance is equal to the output resistance of the source. To match the load resistance with the output impedance of the source, a matching switching regulator is connected between the source and the load. Very often, the amount of energy received from such sources depends on external conditions. To ensure a uniform supply of electrical energy to the load, a battery operating in buffer mode is connected at the output of the switching regulator.* ***Problem.*** *In this case, the load of the switching regulator is the battery, and the input impedance of the regulator will perform the role of the load of the power source. This resistance depends on the voltage of the battery, the type of switching regulator and its mode of operation. In such cases, the maximum power extraction mode from the source can be provided by selecting the appropriate operating mode of the switching regulator. The* ***aim*** *of the work is to analyze the conditions and determine the modes under which the transfer of the maximum possible amount of electrical energy from the source to the battery is ensured, as well as the features of the switching regulator in these modes.* ***Methods.*** *For this purpose, the regulating characteristics of step-up and step-down switching regulators were determined and analyzed, taking into account the presence of an accumulator at their output. Taking into account that in the maximum power transmission mode, the output resistance of the source and the load resistance are of the same order of magnitude, when determining the regulating characteristics, the internal resistance of the source was taken into account.* ***Results.*** *As a result of the analysis of the obtained regulating characteristics, the conditions were determined under which the transfer of energy from the source to the battery is ensured, and the parameters of the operating mode of the switching regulator were determined, under which the maximum power will be taken from the source of electrical energy.* ***Novelty****. The originality of the work is the consideration of the internal resistance of the source of electrical energy in determining the regulating characteristics of pulse regulators.* ***Practical value****. The obtained results made it possible to indicate the appropriate range of battery voltages for different types of pulse regulators, as well as to give practical recommendations for choosing the mode of operation of the pulse regulator depending on its type, as well as the amount of voltage on the battery.* References 17, tables 1, figures 4.

Key words: **source output impedance, matching switching regulator, battery operation, maximum power transmission.**

Для ефективного використання нетрадиційних та відновлюваних джерел електричної енергії необхідно забезпечувати їх роботу в точці максимальної потужності, що можливо при рівності опору навантаження та вихідного опору джерела. Для узгодження опору навантаження з вихідним опором джерела між джерелом та навантаженням підключають узгоджувальний імпульсний регулятор. Досить часто кількість енергії, що отримують від подібних джерел, залежить від зовнішніх умов. Щоб забезпечити більш рівномірне надходження електричної енергії до навантаження, на виході імпульсного регулятора підключають акумулятор, що працює в буферному режимі. За таких умов навантаженням імпульсного регулятора є акумулятор, а роль навантаження джерела живлення виконуватиме вхідний опір регулятора. Цей опір залежить від величини напруги на акумуляторі, типу імпульсного регулятора та режиму його роботи. У таких випадках режим відбору максимальної потужності джерела може бути забезпечений шляхом вибору відповідного режиму роботи імпульсного регулятора. ***Метою*** *роботи є аналіз умов та визначення режимів, за яких забезпечується передача від джерела в акумулятор максимально можливої кількості електричної енергії, а також особливостей роботи імпульсного регулятора у зазначеному режимі. З цією метою було визначено та проаналізовано регулювальні характеристики імпульсних регуляторів підвищувального та понижувального типів з урахуванням наявності акумулятора на їх виході. Враховуючи, що у режимі передавання максимальної потужності вихідний опір джерела та опір навантаження є величинами одного порядку, при визначенні регулювальних характеристик враховувався внутрішній опір джерела. В результаті аналізу отриманих регулювальних характеристик було визначено умови, за яких забезпечується передавання енергії від джерела до акумулятора, а також визначено параметри режиму роботи імпульсного регулятора, за яких від джерела електричної енергії буде відбиратися максимальна потужність.* ***Оригінальністю*** *роботи є врахування внутрішнього опору джерела електричної енергії при визначенні регулювальних характеристик імпульсних регуляторів. Одержані* ***результати*** *дали можливість вказати доцільний діапазон напруг акумулятора для різних типів імпульсних регуляторів, а також дати практичні рекомендації щодо вибору режиму роботи імпульсного регулятора у залежності від його типу, а також величини напруги на акумуляторі.* Бібл. 17, табл. 1, рис. 4.

Ключові слова: **вихідний опір джерела, узгоджувальний імпульсний регулятор, робота на акумулятор, передавання максимальної потужності.**

Introduction. In connection with the significant spread of non-traditional and renewable sources, the task of obtaining the maximum possible amount of electrical energy from them arises. For this, the operating point of the power source must be at the maximum power point (MPP). As is known [1-4], such a mode of operation of the source will be provided under the condition that the resistance of the load R coincides with the output resistance of the source r. If $R \neq r$, in order to ensure the possibility of taking maximum power from the source, a pulse regulator (PR) is switched on between the source and the load, which matches the resistance of the load with the output resistance of the source. Today, the main method of taking maximum power from non-traditional and renewable sources is the use of various algorithms to search for MPP of the source [5-10]. Most of these algorithms consist in periodically changing the duration of the locked state of the PR key and, depending on the consequences of such a change, adjusting this duration in the direction of decrease or increase. The main disadvantage of such methods is that at the time of start-up or a sudden change in external conditions, when the coordinates of the MPP are unknown, its search may take a certain amount of time, during which a certain amount of energy will not be received from the source. Moreover, in the process of searching for MPP, there may be cases when the duration of the locked state of the key will change in the opposite direction from the required one, which will increase the amount of under-received energy. Supplementing the existing algorithms with analytical methods for determining the MPP makes it possible to significantly speed up its search and reduce the amount of electricity not received from the source.

Quite often, the amount of energy coming from non-traditional and renewable sources depends on external conditions. Therefore, to ensure a more uniform supply of energy to the load, a battery is connected to the PR output, which operates in buffer mode [11-13]. In such cases, the PR load will be the battery itself, and the role of the source load will be performed by the input resistance of the regulator. The mode of selection from the source of maximum power can be ensured by selecting the appropriate operating mode of the PR.

The goal of the work is to analyze the conditions under which it is possible and expedient to transfer the maximum possible amount of electrical energy from the power source to the battery, as well as the features of PR operation in this mode.

To do this, it is necessary to determine and analyze the control characteristics of the regulator, taking into account the internal resistance of its power source. Let's consider these questions on the example of PR circuits of step-down and step-up types, which are most often used to match the output resistance of the power source with the load resistance.

Determination and analysis of regulatory characteristics. Since we are interested in extracting the maximum power from the power source, we will consider those variants of PR circuits that provide this possibility [14]. The corresponding circuits of step-down and step-up regulators are presented in Fig. 1, 2.

We will assume that the internal resistance of the source r is linear, and the internal resistance of the battery is much smaller compared to the internal resistance of the source. We will determine and analyze the control characteristics of the regulator circuits presented in Fig. 1, 2.

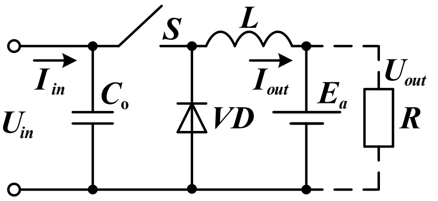

Fig. 1. Circuit of the step-down regulator

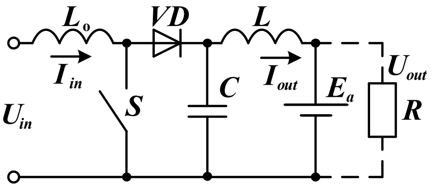

Fig. 2. Circuit of the step-up regulator

Step-down type regulator. If losses in the elements of the PR circuit are not taken into account, for the regulator (Fig. 1) in the mode of continuous inductance current, the conditions will always be fulfilled [15]

$$U_{out} = U_{in}t^* \text{ ; } I_{out} = I_{in}/t^* \text{ ,} \tag{1}$$

where $t^* = t_c/T$ is the relative time of the locked state of the key *S*.

Taking into account that the internal resistance of the battery is much smaller than the internal resistance of the source, we can assume that during the adjustment process the output voltage of the regulator remains almost unchanged and is equal to $U_{out} = E_a$. Therefore, in order for the system to be in a state of equilibrium in the process of regulation, the input voltage of the regulator must be

$$U_{in} = U_{out}/t^* = E_a/t^* \text{ .} \tag{2}$$

In real power sources, due to the presence of internal resistance in them, the input voltage of the regulator will change due to changes in the current consumed by the source. In the case of linear internal resistance of the source, its output voltage (PR input voltage U_{in}) will be determined by the output characteristic of the source

$$U_{in} = U_{oc} - I_{in}r \text{ ,} \tag{3}$$

where U_{oc} is the open-circuit voltage of the power source.

Therefore, in the state of equilibrium, (2), (3) must be fulfilled simultaneously

$$U_{oc} - I_{in}r = E_a/t^* \text{ ,} \tag{4}$$

or in relative units [15]

$$1 - I^*_{in} = E^*_a/t^* \text{ ,} \tag{5}$$

where $I^*_{in} = I_{in}/I_{sc}$; $U^* = U/U_{oc}$; $E^*_a = E_a/U_{oc}$; $I_{sc} = U_{oc}/r$ is the short-circuit current of the source.

Taking into account that the open-circuit voltage of the source, as well as the battery voltage, are fixed values, as a result of changes in the parameter t^*, the input and, accordingly, the output current of the regulator will be adjusted

$$I^*_{in} = \left[1 - E^*_a/t^*\right]. \tag{6}$$

Taking into account (1)

$$I^*_{out} = I^*_{in}/t^* = \left[1 - E^*_a/t^*\right] \cdot \frac{1}{t^*}. \tag{7}$$

Therefore, the control characteristics of PR (Fig. 1) are described by (6), (7). Let's analyze the obtained characteristics.

According to (6), to ensure the transfer of energy from the power source to the battery ($I_{in} > 0$), the condition must be fulfilled

$$\left[1 - E^*_a/t^*\right] > 0 \text{ ,} \tag{8}$$

or

$$t^* > E^*_a \text{ .} \tag{9}$$

Considering the physical content of the parameter t^*, we conclude that it can vary within a limited range

$$1 \ge t^* > E^*_a \text{ ,} \tag{10}$$

and the battery voltage cannot be greater than the open-circuit voltage of the power source. The lower the battery voltage E^*_a, the wider the permissible range of adjustment of the parameter t^*.

As is known [16], in the case of linear internal resistance of the source, its MPP has coordinates $I^* = 0,5$; $U^* = 0,5$. Taking into account that $I^* = I_{in}^*$ of the regulator, the condition for taking the maximum power from the source according to (6), takes the form

$$\left[1 - E_a^*/t^*\right] = 0,5 . \qquad (11)$$

Thus, the maximum power from the source to the battery will be transferred provided that $t^* = t_{MP}^*$, where

$$t_{MP}^* = 2E_a^* . \qquad (12)$$

Taking into account that t^* = [0...1], we conclude that the maximum power from the source to the battery can be transferred only if

$$E_a^* \leq 0,5 . \qquad (13)$$

Step-up type regulator. For this regulator (Fig. 2), in the mode of continuous inductance current, the following relations are valid

$$U_{out} = U_{in}/t^* \ ; \ \ I_{out} = I_{in}t^* , \qquad (14)$$

where $t^* = t_{open} / T$; t_{open} is the duration of the unlocked state of the key S on the period T. So, in steady state, the input voltage of the regulator should be

$$U_{in} = U_{out}t^* = E_a t^* . \qquad (15)$$

The system will be in a state of equilibrium under the condition

$$E_a t^* = U_{sc} - I_{in} r . \qquad (16)$$

In relative units, this condition will look like

$$E_a^* t^* = 1 - I_{in}^* . \qquad (17)$$

Therefore, the control characteristics of the PR of the step-up type (Fig. 2) will be as follows

$$I_{in}^* = \left[1 - E_a^* \cdot t^*\right]; \qquad (18)$$

$$I_{out}^* = \left[1 - E_a^* \cdot t^*\right] t^* . \qquad (19)$$

According to (18), the condition of energy transfer from the source to the battery ($I_{in}^* > 0$) will have the form

$$I_{in}^* = \left[1 - E_a^* \cdot t^*\right] > 0 , \qquad (20)$$

that is, the parameter t^* can vary in the range

$$0 < t^* < 1/E_a^* . \qquad (21)$$

So, for this regulator, the battery voltage, theoretically, can be both higher and lower than the open-circuit voltage of the source. However, in the case of $E_a^* > 1$, the permissible range of adjustment of the parameter t^* will be limited. The stronger the inequality $E_a^* > 1$ is fulfilled, the narrower the permissible parameter t^* adjustment range will be.

The condition of taking from the source of maximum power will be as follows

$$\left[1 - E_a^* t^*\right] = 0,5 . \qquad (22)$$

So,

$$t_{MP}^* = 1/2E_a^* . \qquad (23)$$

Taking into account (23), the maximum power can be taken from the source only if

$$E_a^* \geq 0,5 , \qquad (24)$$

that is, the battery voltage can be both higher and lower than the open-circuit voltage of the source. Figures 3, 4 present graphs of the family of control characteristics of the considered regulators for different values of the relative voltage on the battery E_a^* . These graphs confirm the results of the analysis carried out.

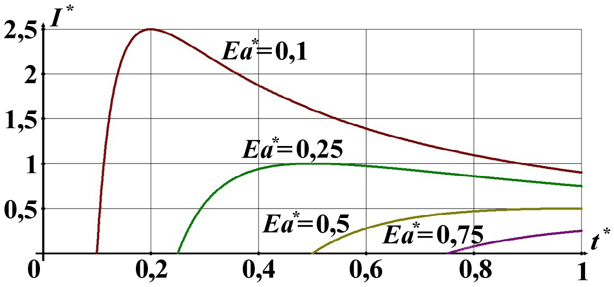

Fig. 3. Regulatory characteristics of the step-down regulator for different values of the relative voltage on the battery

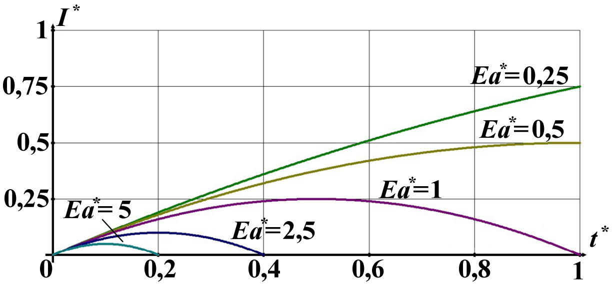

Fig. 4. Regulatory characteristics of the step-up regulator for different values of the relative voltage on the battery

Table 1 shows the conditions under which it is possible to transfer energy from the power source to the battery in the case of PR operation in the mode of *continuous* inductance current.

The parameter t_{MP}^* for which the maximum power is taken from the power source is provided, as well as the reasonable range of changing the parameter E_a^* is suggested.

Table 1

Pulse regulator	The condition for energy taking from the source	The condition for taking the maximum power	Appropriate range of change in E_a^*
Step-down type (Fig. 1)	$t^* > E_a^*$	$t_{MP}^* = 2E_a^*$	$0,1 \leq E_a^* \leq 0,5$
Step-up type (Fig. 2)	$t^* < 1/E_a^*$	$t_{MP}^* = 1/2E_a^*$	$0,5 \leq E_a^* \leq 5$

In the case of switching the regulator to the *intermittent* inductance current mode, it becomes possible to adjust the parameter t^* in the full range [0...1]. However, in this mode, the battery charging current is insignificant [17]. Therefore, it is advisable not to use this mode for charging the battery, but to compensate for its self-discharge in the charged state.

Conclusions.

1. If there is a battery at the output, the PR will operate in the input and, accordingly, output current (battery charging current) regulator mode.

2. The regulatory characteristic of the current will depend on the ratio of the numerical values of the battery voltage and the open-circuit voltage of the source E_a^*.

3. In the mode of continuous inductance current, the permissible range of adjustment of the parameter t^* is limited and depends on the type of regulator, as well as the numerical value of the parameter E_a^*.

4. The output current of the regulator (output power of the source) reaches its maximum value at a certain value of the parameter $t^* = t_{MP}^*$, which is a function of the parameter E_a^*, as well as the type of PR.

Conflict of interest. The authors of the article declare that there is no conflict of interest.

REFERENCES

1. Twaha S., Zhu J., Yan Y., Li B., Huang K. Performance analysis of thermoelectric generator using DC-DC converter with incremental conductance based maximum power point tracking. *Energy for Sustainable Development*, 2017, vol. 37, pp. 86-98. doi: https://doi.org/10.1016/j.esd.2017.01.003.

2. Danandeh M.A., Mousavi G. Comparative and comprehensive review of maximum power point tracking methods for PV cells. *Renewable and Sustainable Energy Reviews*, 2018, vol. 82, part 3, pp. 2743-2767. doi: https://doi.org/10.1016/j.rser.2017.10.009.

3. Claude Bertin N.F., Kamta M., Wira P. A comprehensive assessment of MPPT algorithms to optimal power extraction of a PV panel. *Journal of Solar Energy Research*, 2019, vol. 4, no. 3, pp. 172-179. doi: https://doi.org/10.22059/jser.2019.287029.1126.

4. Mohamed S.A., Abd El Sattar M. A comparative study of P&O and INC maximum power point tracking techniques for grid-connected PV systems. *SN Applied Sciences*, 2019, no. 1, art. no. 174. doi: https://doi.org/10.1007/s42452-018-0134-4.

5. Yahya K., Bilgin M.Z., Erfidan T. Practical Implementation of Maximum Power Tracking Based Short-Current Pulse Method for Thermoelectric Generators Systems. *Journal of Power Electronics*, 2018, vol. 18, no. 4, pp. 1201-1210. doi: https://doi.org/10.6113/JPE.2018.18.4.1201.

6. Karthikeyan V., Vijayalakshmi V.J., Vinod A., Vanitha U., Jeyakumar P., Ramarajan M. Step and search control method to track the maximum power in wind energy conversion systems - A study. *International Review on Modelling and Simulations*, 2013, vol. 6, no. 4, pp. 1205-1211.

7. Rajabi M., Hosseini S.M.H. Maximum power point tracking in photovoltaic systems under different operational conditions by using ZA-INC algorithm. *SN Applied Sciences*, 2019, vol. 1, no. 12, art. no. 1535. doi: https://doi.org/10.1007/s42452-019-1536-7.

8. Saad W., Hegazy E., Shokair M. Maximum power point tracking based on modified firefly scheme for PV system. *SN Applied Sciences*, 2022, vol. 4, no. 4, art. no. 94. doi: https://doi.org/10.1007/s42452-022-04976-3.

9. Louarem S., Kebbab F.Z., Salhi H., Nouri H. A comparative study of maximum power point tracking techniques for a photovoltaic grid-connected system. *Electrical Engineering & Electromechanics*, 2022, no. 4, pp. 27-33. doi: https://doi.org/10.20998/2074-272X.2022.4.04.

10. Saeed H., Mehmood T., Khan F.A., Shah M.S., Ullah M.F., Ali H. An improved search ability of particle swarm optimization algorithm for tracking maximum power point under shading conditions. *Electrical Engineering & Electromechanics*, 2022, no. 2, pp. 23-28. doi: https://doi.org/10.20998/2074-272X.2022.2.04.

11. Anandhi T.S., PremKumar S. Application of DC-DC boost converter for solar powered traffic light with battery backup. *Indian Journal of Science and Technology*, 2015, vol. 8, no. 32, pp. 1-5. doi: https://doi.org/10.17485/ijst/2015/v8i32/84408.

12. Krieger E.M., Arnold C.B. Effects of undercharge and internal loss on the rate dependence of battery charge storage efficiency. *Journal of Power Sources*, 2012, vol. 210, pp. 286-291. doi: https://doi.org/10.1016/j.jpowsour.2012.03.029.

13. Vieira J.A.B., Mota A.M. Implementation of a stand-alone photovoltaic lighting system with MPPT battery charging and LED current control. *2010 IEEE International Conference on Control Applications*, 2010, pp. 185-190. doi: https://doi.org/10.1109/CCA.2010.5611257.

14. Batrak L.M., Romashko V.Y. Switching Regulators Features in the Matching Mode Operation. *Microsystems, Electronics and Acoustics*, 2021, vol. 26, no. 1, pp. 232833-1 – 232833-7. (Ukr). doi: https://doi.org/10.20535/2523-4455.mea.232833.

15. Goncharov Y.P., Budonny O.V., Morozov V.G., Panasenko M.V., Romashko V.Y., Rudenko V.S. *Power conversion equipment. Text book. Part 2.* Kharkiv, Folio Publ., 2000. 360 p. (Ukr).

16. Bessonov L.A. *Theoretical Foundations of Electrical Engineering. In 2 vols. Vol. 1. Electric circuits: textbook for universities*. Moscow, Yurayt Publ. House, 2021. 831 p. (Rus).

17. Romashko V.Y., Batrak L.M. Features of the Switching Regulator Operation on a Rechargeable Battery. *Microsystems, Electronics and Acoustics*, 2018, vol. 23, no. 4, pp. 22-30. doi: https://doi.org/10.20535/2523-4455.2018.23.4.131272.

Received 05.01.2023
Accepted 24.03.2023
Published 02.11.2023

V.Y. Romashko[1]*, Doctor of Technical Science, Professor,*
L.M. Batrak[1]*, PhD, Assistant Professor,*
O.O. Abakumova[1]*, PhD, Assistant Professor,*
[1] National Technical University of Ukraine
«Igor Sikorsky Kyiv Polytechnic Institute»,
37, Prospect Beresteiskyi, Kyiv-56, 03056, Ukraine,
e-mail: rvy90593-eds@lll.kpi.ua;
batrakln5@gmail.com (Corresponding Author);
e.o.abakumova@gmail.com

How to cite this article:
Romashko V.Y., Batrak L.M., Abakumova O.O. Features of the work of pulse regulators in the maximum power transmission mode, with the presence of an accumulator at their output. *Electrical Engineering & Electromechanics*, 2023, no. 6, pp. 63-66. doi: https://doi.org/10.20998/2074-272X.2023.6.11

UDC 621.318 https://doi.org/10.20998/2074-272X.2023.6.12

Yu.V. Batygin, O.F. Yeryomina, S.O. Shinderuk, E.O. Chaplygin

The mutual influence of exciting and induced currents in the circular solenoid – massive conductor system

Problem. *The flow of currents in the conductive elements of electrical systems is accompanied by the excitation of electromagnetic fields and the occurrence of induced currents. The excitation of the induced signals, in turn, leads to a change in the parameters of the actual exciting currents. The* ***purpose*** *of the work is to obtain analytical expressions for the quantitative analysis of the results of the mutual influence of the exciting and induced currents and to calculate their ratio depending on the geometric characteristics of the inductor systems.* ***Methodology***. *The analysis of the processes of mutual influence is carried out on the example of a widespread inductor system, where a flat circular solenoid is placed above the surface of a massive conductor. Analytical expressions for eddy currents excited in a massive conductor and numerical estimates of the effect of induced currents on exciting currents in a solenoid are obtained.* ***Results***. *It is shown that the influence of the induced current on the current in the solenoid is very significant at small distances between the solenoid and the surface of the massive solenoid. It has been found that an increase in the width of the solenoid winding leads to a significant increase in the influence of the induced current on the excitation current in the solenoid. It is shown that the inductance of the «circular solenoid - massive conductor» system drops with a decrease in the distance between the solenoid and the massive conductor and an increase in the radial dimensions of the solenoid, which requires an increase in the amplitude of the exciting current to maintain a given value of the magnetic flux in the system.* ***Originality***. *The scientific novelty of this work lies in the proposal of an analytical approach and obtaining numerical estimates of the mutual influence of conductors with exciting and induced currents.* ***Practical value***. *Estimates of the mutual influence of conductors with currents are of interest for the practice of designing structures of electrical systems for various purposes. Very promising in the direction further research is seen as carrying out experiments with measurements of the quantitative characteristics of the mutual influence of exciting and induced currents in various designs of electrical systems.* References 20, figures 3.

Key words: **circular solenoid, massive conductor, inductor system, eddy currents, inductance.**

В роботі одержано аналітичні вирази для кількісного аналізу результатів взаємного впливу збуджуючих та індукованих струмів і числові оцінки їх співвідношення в залежності від геометричних характеристик індукторної системи. Аналіз результатів взаємного впливу проведено на прикладі широко поширеної індукторної системи, де плоский круговий соленоїд є розташованим над поверхнею ідеалізованого масивного провідника, що подається моделлю з нескінченою електропровідністю. Показано, що вплив індукованого струму на струм у соленоїді зростає при зменшенні відстані між соленоїдом та поверхнею масивного провідника і збільшенні ширини обмотки соленоїда, що вимагає підвищення амплітуди збуджуючого струму для збереження заданої величини магнітного потоку в системі. Бібл. 20, рис. 3.

Ключові слова: **круговий соленоїд, масивний провідник, індукторна система, вихрові струми, індуктивність.**

Introduction. Common to all known electrotechnical systems, regardless of their design, is the presence of conductive elements, the flow of currents in which is accompanied by the excitation of the corresponding electromagnetic fields. The latter, from a physical point of view, is a material substance with the help of which energy is exchanged between conductive elements where currents flow. It should be emphasized that the mentioned process is a process of mutual influence determined by M. Faraday's well-known law of electromagnetic induction. The interpretation of this law in relation to the process of mutual influence shows that the fields of induced currents lead to a change in the parameters of the actual exciting currents. On the other hand, physically, the mutual influence and related corresponding changes in the electrodynamic characteristics of the ongoing processes can also be explained by the principles of the law of conservation of energy [1-3].

Problem definition. Modern requirements for energy saving require mandatory numerical estimates of the parameters of the processes taking place, taking into account the mutual influence of exciting and induced currents, which is necessary for the design of electrical devices of any purpose.

Literature review. As an object of research, it is possible to consider the tools of electromagnetic technologies of metal processing, called in the special literature «inductor systems» [4, 5]. The latter are designs of circular solenoids placed above conductive objects [6, 7].

Thus, multi-turn inductor systems in the classic magnetic pulse processing of metals, which became widespread in the second half of the last century, carried out effective deformation of massive metal workpieces. In the case of a sharp skin effect (high frequencies of active fields), production operations such as «crimping», «dispensing» and «flat stamping» have been successfully implemented [8-10]. It should be emphasized that the principle of operation of the presented electromagnetic technologies is based on the natural repulsion of conductors from the sources of the external magnetic field, which manifests itself as the so-called «magnetic pressure» [4, 11].

The tools of magnetic pulse attraction are single-turn inductor systems, the principle of operation of which is based on the suppression of Lorentz repulsion forces in low-frequency modes of excited fields, the use of magnetic properties of processed metals and Ampere's law on the force interaction of parallel currents [5, 12, 13]. The authors presented [14] various designs of tools, power sources and technological equipment of magnetic pulse attraction systems, protected by Ukrainian patents.

Inductor systems for induction heating of metal samples are presented in [5]. An analysis of the processes of excitation of electromagnetic fields by a cylindrical solenoid, in the inner cavity of which a massive conductive object is placed, was analyzed here.

Separation of tasks to be solved. A general drawback of the cited works, as well as recent publications based on calculation methods, for example [11, 15-17], should be considered the solution of the tasks in the approximation of the «given current», when the excited electromagnetic fields do not affect the characteristics of the sources, which are considered constant. This makes it possible to single out a significant part of the problems that need their solution and are dedicated to the study of the formation of exciting currents and voltages taking into account the action of excited fields [3, 7, 18].

The goal of the work is to obtain analytical expressions for the quantitative analysis of the results of the mutual influence of the exciting and induced currents and to calculate their ratio depending on the geometric characteristics of the inductor systems.

Basic ratios, analytical dependencies. The calculation model of the inductor system is shown in Fig. 1.

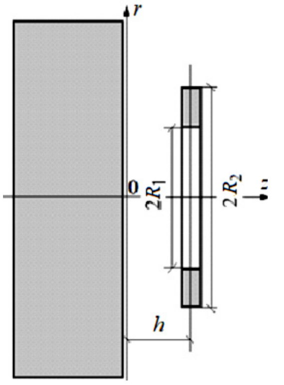

Fig. 1. Model of the inductor system with flat circular solenoid placed parallel to the surface of the massive conductor

Problem definition and assumptions to solving the problem:

1. A cylindrical coordinate system is acceptable.

2. We consider a massive conductor as one that conducts perfectly, which is practically admissible at sufficiently high frequencies of the active fields, and which can be realistically evaluated similarly to widely known works [1, 4, 16, 17].

3. The geometric dimensions of a massive conductor in $r \in [0, \infty)$ and $z \in (-\infty, 0]$ are infinite.

4. The solenoid is assumed to be axially symmetrical, i.e. $\partial/\partial\varphi = 0$, where φ is the azimuthal angle.

5. The azimuthal harmonic current $J(t) = J_m\sin(\omega t)$ flows in the solenoid winding with cyclic frequency ω that does not violate the accepted idealization of the conductor and with arbitrary amplitude J_m.

Note. Since an idealized model is adopted according to item 2, all characteristics of electromagnetic processes will be harmonic in time [16, 17].

6. According to the accepted geometric shape of the exciting current, the azimuthal component of the electric field strength $E_\varphi(t,r,z) \neq 0$, as well as the radial r and normal z components of the magnetic field strength vector $H_r(t,r,z) \neq 0$, $H_z(t,r,z) \neq 0$, respectively, are excited in the system [1, 2, 16, 17].

7. The evaluation of the characteristics of the mutual influence of the induced and exciting currents can be carried out, assuming that when the distance between the solenoid and the surface of the conductor varies, the average values of the normal components of the magnetic flux density, which are excited in the internal window of the solenoid, remain unchanged.

First, the relationships of a general nature.

The average value of the normal component of the magnetic flux density vector in the inner window of the solenoid, located at a distance h from the surface of the massive conductor, is described by the well-known relationship [18]:

$$\overline{B}_h = \Phi_h / S = \left(J_h \cdot L_h\right)/S\,, \tag{1}$$

where Φ_h is the magnetic flux, S is the area of the internal window, J_h is the current in the winding, L_h is the inductance of the solenoid winding, which takes into account the presence of a massive conductor.

According to the accepted problem definition, the influence of the induced current on the excitation processes of the electromagnetic field can be determined by the value of the average magnetic flux density from (1). The obvious statement is that the induced current has no effect if the massive conductor is «conditionally removed to infinity». In this case, the average magnetic flux density in the inner window of the actual solenoid depends on (1) at $h \to \infty$

$$\overline{B}_\infty = \Phi_\infty / S = \left(J_\infty \cdot L_\infty\right)/S\,, \tag{2}$$

where Φ_∞ and L_∞ are the magnetic flux and inductance of the solenoid winding without a massive conductor, J_∞ is the current in the winding.

Now the equality of the averaged magnetic flux density values in (1), (2) allows finding the ratio between the currents in the solenoid winding in the presence of a conductive object and in its absence. In fact, this ratio determines the effect of the induced current on the current in the solenoid winding.

So,

$$\overline{B}_h = \overline{B}_\infty;\quad J_h / J_\infty = L_\infty / L_h;\quad J_0 = \left(L_\infty / L_h\right) - 1, \tag{3}$$

where $J_0 = \Delta J / J_\infty$ and $\Delta J = J_\infty - J_h$ are the relative and absolute variations of the current in the solenoid winding due to the influence of the induced current.

The results in (3) are consistent with known dependencies. Indeed, the amplitudes of the currents in the windings are inversely proportional to their inductances [16].

In accordance with the set goal, let's turn to the calculation model in Fig. 1, for which we write down the system of Maxwell equations in the space of Laplace images [1, 2, 16, 17]:

$$\begin{cases} \dfrac{\partial E_\varphi(p,r,z)}{\partial z} = \mu_0 p H_r(p,r,z); \\ \dfrac{1}{r} \cdot \dfrac{\partial}{\partial r} \cdot \left(r \cdot E_\varphi(p,r,z)\right) = -\mu_0 p H_z(p,r,z); \\ \dfrac{\partial H_r(p,r,z)}{\partial z} - \dfrac{\partial H_z(p,r,z)}{\partial r} = j_{\varphi 0}(p,r,z), \end{cases} \tag{4}$$

where $E_\varphi(p,r,z) = L\{E_\varphi(g(t)t,r,z)\}$; $H_{r,z}(p,r,z) = L\{H_{r,z}(t,r,z)\}$; $j_{\varphi 0}(p,r,z) = \{j_{\varphi 0}(t,r,z)\}$, $j_{\varphi 0}(t,r,z)$ is the current density in the solenoid, $j_{\varphi 0}(t,r,z) = j_m \cdot g(t) \cdot f(r) \cdot \delta(z-h)$, $g(t)$ is the dependence in time, $f(r)$ is the radial dependence, $\delta(z-h)$ is the Dirac function [19].

Note. The system of Maxwell equations (4) is fundamental as the basic basis of problems in applied electrodynamics, but in combination with the also well-known relationships (1) – (3) it makes it possible to study the mutual influence of exciting and induced currents in the elements of inductor systems, which is necessary for the design of effective tools in magnetic pulse processing of metals.

Further solution of the given task will be carried out according to the adopted calculation model. The geometry of the inductor system and the accepted assumptions make it possible to apply the Fourier-Bessel integral transformation [19, 20]. For the *L*-image of the strength of the excited electric field $E_\varphi(p,r,z)$ we write that

$$\begin{cases} E_\varphi(p,r,z)=\int\limits_0^\infty E_\varphi(p,\lambda,z)\cdot\lambda\cdot J_1(\lambda r)\mathrm{d}\lambda; \\ E_\varphi(p,\lambda,z)=\int\limits_0^\infty E_\varphi(p,r,z)\cdot r\cdot J_1(\lambda r)\mathrm{d}r; \end{cases} \tag{5}$$

where $E_\varphi(p,\lambda,z)$ is the image of the electric field strength in the Fourier-Bessel space, λ is the integral transformation parameter, $J_1(\lambda r)$ is the Bessel function of the first order.

Omitting the intermediate mathematical transformations, from the system (4), using the integral representation (5), we write the differential equation for the azimuthal component of the strength of the excited electric field [19, 20]:

$$\frac{\partial^2 E_\varphi(p,\lambda,z)}{\partial z^2}-\lambda^2\cdot E_\varphi(p,\lambda,z)=K(p,\lambda)\cdot\delta(z-h), \tag{6}$$

where $K(p,\lambda)=\mu_0\cdot p\cdot j_m\cdot g(p)\cdot f(\lambda)$; $j_m = J_m / (R_2 - R_1)$ is the excitation current density;

$$g(p)=L\{g(t)\};\quad f(\lambda)=\int\limits_{R_1}^{R_2} f(r)\cdot r\cdot J_1(\lambda r)\mathrm{d}r\,.$$

The general solution of the ordinary differential equation (6) can be represented by an expression of the form [19, 20]:

$$\begin{aligned} E_\varphi(p,\lambda,z)&=C_1\cdot e^{\lambda z}+C_2\cdot e^{-\lambda z}+\\ &+\frac{K(p,\lambda)}{\lambda}\cdot\eta(z-h)\cdot\mathrm{sh}(\lambda\cdot(z-h)), \end{aligned} \tag{7}$$

where $C_{1,2}$ are the arbitrary integration constants, $\eta(z-h)$ is the Heaviside step function.

Satisfying the boundary conditions at $z = 0$ ($E_\varphi(p,\lambda, z = 0) = 0$) and $z\to\infty$ ($E_\varphi(p, \lambda, z\to\infty) = 0$), we find a partial solution of equation (6). By substituting the coordinate $z = h$ into the obtained expression, we obtain an image of the electric field strength excited in the inner window of a flat circular solenoid:

$$E_\varphi(p,\lambda,z=h)=-\frac{K(p,\lambda)}{2\lambda}\cdot\left(1-e^{-2\lambda\cdot h}\right). \tag{8}$$

The integral representation of (5) taking into account (8) takes the form:

$$E_\varphi(p,r,z)=-\int\limits_0^\infty\frac{K(p,\lambda)}{2}\cdot\left(1-e^{-2\lambda\cdot h}\right)\cdot J_1(\lambda r)\mathrm{d}\lambda\,. \tag{9}$$

The connection of the *L*-image of the normal component of the magnetic field strength, which is excited, in the internal window of the solenoid in the presence of a massive conductor, with the $E_\varphi(p,\lambda,z)$ is found using the second equation from system (4):

$$H_z(p,r,z=h)=-\frac{1}{\mu_0 p}\cdot\frac{1}{r}\cdot\frac{\partial}{\partial r}\cdot\left(r\cdot E_\varphi(p,r,z=h)\right). \tag{10}$$

By integrating expression (10), we determine the dependence for the *L*-image of the magnetic flux:

$$\begin{aligned} \Phi_h(p)&=2\pi\mu_0\cdot\int\limits_0^{R_1}H_z(p,r,z=h)r\mathrm{d}r=\\ &=-\frac{2\pi}{p}\cdot\left(r\cdot E_\varphi(p,r,z=h)\right)\Big|_0^{R_1}. \end{aligned} \tag{11}$$

Substituting (9) into (11) and opening $K(p,\lambda)$ from (6), we obtain that

$$\begin{aligned} \Phi_h(p)&=J_m\cdot\frac{\mu_0\pi R_1}{(R_2-R_1)}\cdot g(p)\times\\ &\times\int\limits_0^\infty f(\lambda)\cdot\left(1-e^{-2\lambda\cdot h}\right)\cdot J_1(\lambda R_1)\mathrm{d}\lambda. \end{aligned} \tag{12}$$

Since the time dependence of the magnetic flux, as follows from (12), is determined by the function $g(p)=L\{g(t)=\sin(\omega t)\}$, then $\Phi_h(t)\sim\sin(\omega t)$. And, therefore, expression (12) can be interpreted as a relationship between the amplitude values of the exciting current and the excited magnetic flux. That is,

$$\Phi_h=J_m\frac{\mu_0\pi R_1}{(R_2-R_1)}\int\limits_0^\infty f(\lambda)\left(1-e^{-2\lambda\cdot h}\right)J_1(\lambda R_1)\mathrm{d}\lambda\,. \tag{13}$$

The inductance of the analyzed system is defined as the ratio of the magnetic flux to the excitation current [16].

After introducing a new integration variable $y=\lambda R_1$ and the necessary identical transformations, we obtain the formula for the inductance at an arbitrary distance from the inductor to the massive conductor:

$$L_h=\frac{\mu_0\pi R_1^2}{(R_2-R_1)}\int\limits_0^\infty f(y,R_{1,2})\frac{1-e^{-y\cdot\left(\frac{2h}{R_1}\right)}}{y^2}J_1(y)\mathrm{d}y, \tag{14}$$

where $f(y,R_{1,2})=\int\limits_y^{y\cdot\frac{R_2}{R_1}}x\cdot J_1(x)\mathrm{d}x$

The limit transition in (14) at $h\to\infty$ gives an expression for the inductance of the actual inductor winding without a massive conductor:

$$L_\infty\approx\frac{\mu_0\pi R_1^2}{(R_2-R_1)}\int\limits_0^\infty\frac{f(y,R_{1,2})}{y^2}J_1(y)\mathrm{d}y\,. \tag{15}$$

Let's return to the relative value of the current change in the solenoid winding under the influence of induction effects in a massive conductor. Substitute dependencies (14), (15) into the corresponding formula from the set of relationships (3). We obtain an expression that quantifies the effect of the induced current on the exciting current in the solenoid winding:

$$J_0 = \frac{\Delta J}{J_\infty} = \left(\frac{L_\infty}{L_h} - 1\right), \qquad (16)$$

where
$$\frac{L_\infty}{L_h} = \frac{\int\limits_0^\infty \frac{f(y, R_{1,2})}{y^2} \cdot J_1(y) \mathrm{d}y}{\int\limits_0^\infty f(y, R_{1,2}) \frac{\left(1 - e^{-y \cdot \frac{2h}{R_1}}\right)}{y^2} \cdot J_1(y) \mathrm{d}y}.$$

Analysis of the effect of the induced current on the exciting current in the solenoid. Numerical evaluations by the found analytical expressions were obtained using standard programs (in particular, NIntegrate) from the Wolfram Mathematics – 7.10 package.

Graphs illustrating the functional dependence (16) are shown in Fig. 2.

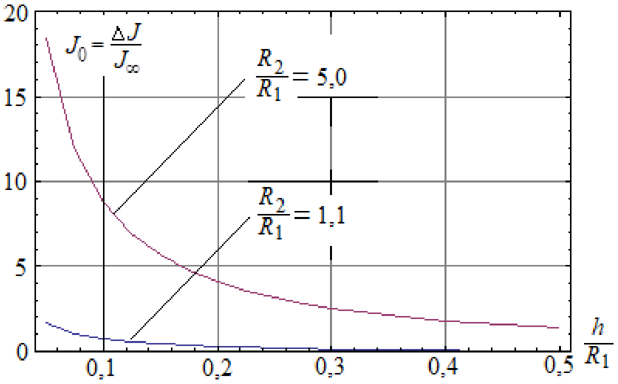

Fig. 2. Dependence of the current increase in the solenoid on the distance between it and the surface of the massive conductor

The results of the calculations showed that the influence of the induced current on the value of the current in the solenoid winding is mainly determined by the following factors:

- the influence on the exciting current increases when the distance between the solenoid and the massive conductor decreases and falls when the latter increases, which is fully consistent with a qualitative physical representation of the electromagnetic processes taking place;
- the influence of the excitation current largely depends on the geometry of the solenoid, that is, on the ratio between its external and internal dimensions;
- for a fairly thin solenoid ($R_2/R_1 \approx 1.1$) when $h/R_1 > 0.3$ the influence of the induced current is very insignificant, but when $h/R_1 < 0.05$ the influence of the induced current leads to an almost twofold increase in the current in the solenoid;
- an increase in the width of the solenoid winding leads to a significant increase in the influence of the induced current on the excitation current;
- a comparison of the calculation results for a «thin» and «wide» solenoid shows that an increase in the width of the winding leads to a significant distortion of the excitation current for fairly small and practically the most interesting ratios of the distance between the solenoid and its internal size.

Finally, we present the results of numerical estimates of the inductance of the «circular solenoid – massive conductor» system with normalization to the value of the inductance of a single isolated solenoid. The estimation data, as well as the results of direct calculations for currents, are also quantitative indicators of the influence of induction effects on the ongoing electromagnetic processes.

The results of calculations of the inductance of the «circular solenoid – massive conductor» system are presented in Fig. 3.

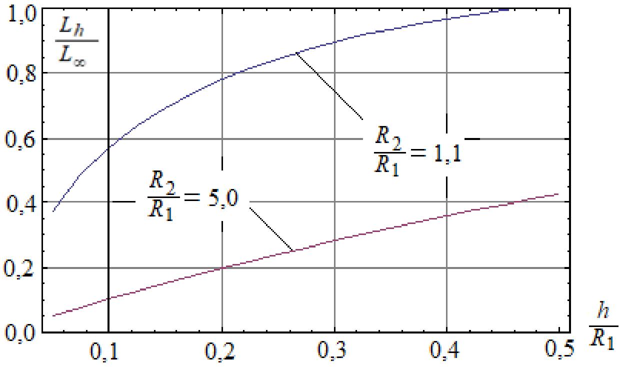

Fig. 3. Inductance of the «circular solenoid – massive conductor» system

It follows from the calculations that the inductance, as a proportionality factor between the excited magnetic flux and its exciting current, falls when the distance between the solenoid and the massive conductor decreases. Its largest value occurs at $h/R_1 \to \infty$ (single solenoid). It should also be noted that the inductance increases with an increase in its width.

As a result, these facts mean the need to increase the amplitude of the current feeding the solenoid winding, in order to maintain the constant value of the magnetic flux while reducing the distance between the solenoid and the massive conductor.

From a physical point of view, the obtained results can be explained by the superposition of oppositely directed fields of the source current and the current induced in an ideal conductor. Moreover, the value of the «counter current» in the solenoid winding naturally decreases compared to the source current, which is due to the presence of the distance between the solenoid and the metal h. Obviously, when $h \to 0$, the superposition of the source current and the «counter current» gives a zero result and the inductance of the system under study is $L_{(h \to 0)} \to 0$. The latter means the need for a significant increase in the source current to maintain a constant value of the excited magnetic flux.

Conclusions.

A theoretical analysis of the processes of excitation of eddy currents in a massive conductor by the field of a flat circular solenoid was carried out, numerical estimations of the influence of induced currents on the excitation currents in the solenoid were performed.

It is shown that the influence of the induced current on the current in the solenoid is very significant at small distances between the solenoid and the surface of the massive conductor.

It was found that an increase in the width of the solenoid winding leads to a significant increase in the influence of the induced current on the excitation current in the solenoid.

It is shown that the inductance of the «circular solenoid – massive conductor» system decreases with a decrease in the distance between the solenoid and the massive conductor and an increase in the radial dimensions of the solenoid, which requires an increase in the amplitude of the exciting current to maintain the given value of the magnetic flux in the system.

Conducting experiments with measurements of quantitative characteristics of the mutual influence of exciting and induced currents in various designs of electrical engineering systems is seen as a promising direction for further research.

Acknowledgments. The work was carried out and financed within the scope of research work under the state budget topic, state registration No. 0121U109610, code for program classification of expenditures and crediting 2201040: «Development of an energy-efficient machine complex for the transport support of the Armed Forces and the National Guard of Ukraine».

Conflict of interest. The authors declare no conflict of interest.

REFERENCES

1. Yavorskii B.M., Detlaf A.A., Lebedev A.K. *Physics handbook for engineers and students of universities*. Moscow, Oniks Publ., 2006. 1056 p. (Rus).

2. Benenson W., Harris J.W., Stöcker H., Lutz H. *Handbook of Physics*. Springer Nature Switzerland AG, 2002. 1190 p. doi: https://doi.org/10.1007/0-387-21632-4.

3. Gray Dwight E. (Ed.) *American Institute of Physics Handbook.* McGraw-Hill Book Company Inc., 1957. 1541 p.

4. Belyi I.V., Fertik S.M., Khimenko L.T. *Handbook of magnetic-pulse processing of metals*. Kharkiv, Vyshcha Shkola Publ., 1977. 189 p. (Rus).

5. Psyk V., Risch D., Kinsey B.L., Tekkaya A.E., Kleiner M. Electromagnetic forming – A review. *Journal of Materials Processing Technology*, 2011, vol. 211, no. 5, pp. 787-829. doi: https://doi.org/10.1016/j.jmatprotec.2010.12.012.

6. Batygin Y.V., Shinderuk S.O., Chaplygin E.O., Yeryomina O.F. Electromagnetic processes in a flat circular system with an inductor between thin bifilar coils. *Technical Electrodynamics*, 2020, no. 4, pp. 19-24. (Ukr). doi: https://doi.org/10.15407/techned2020.04.019.

7. Batygin Y.V., Shinderuk S.O., Chaplygin E.O. Mutual influence of currents in plane inductor system with solenoid between two massive conductors. *Electrical Engineering & Electromechanics*, 2021, no. 6, pp. 25-30. doi: https://doi.org/10.20998/2074-272X.2021.6.04.

8. Bay F., Jeanson A.-C., Zapata J.A. Electromagnetic Forming Processes: Material Behaviour and Computational Modelling. *Procedia Engineering*, 2014, no. 81, pp. 793-800. doi: https://doi.org/10.1016/j.proeng.2014.10.078.

9. Ouyang S., Li C., Du L., Li X., Lai Z., Peng T., Han X., Cao Q., Li L. Electromagnetic forming of aluminum alloy sheet metal utilizing a low-frequency discharge: A new method for attractive forming. *Journal of Materials Processing Technology*, 2021, vol. 291, art. no. 117001. doi: https://doi.org/10.1016/j.jmatprotec.2020.117001.

10. Altenbach H., Konkin V., Lavinsky D., Morachkovsky O., Naumenko K. Verformungsanalyse elektrisch leitender metallischer Bauteile bei Magnetimpulsbearbeitung. *Forschung im Ingenieurwesen*, 2018, vol. 82, no. 4, pp. 371-377. (Ger). doi: https://doi.org/10.1007/s10010-018-0285-x.

11. Kudasov Y.B., Surdin O.M., Platonov V.V., Kozabaranov R.V., Maslov D.A., Makarov I.V., Svetlov A.S., Popov E.Y. Metal plate deformation under magnetic field pulse of complex shape. *Journal of Applied Physics*, 2019, vol. 126, no. 8, p. 084901. doi: https://doi.org/10.1063/1.5108823.

12. Lavinskii D.V., Morachkovskii O. K. Elastoplastic Deformation of Bodies Interacting Through Contact Under the Action of Pulsed Electromagnetic Field. *Strength of Materials*, 2016, vol. 48, no. 6, pp. 760-767. doi: https://doi.org/10.1007/s11223-017-9822-3.

13. Du L., Li X., Xia L., Zhang X., Lai Z., Han X., Li L., Cao Q. Numerical and experimental verification of an iterative coupling method for analyzing the Lorentz-force-driven sheet metal stamping process. *The International Journal of Advanced Manufacturing Technology*, 2021, vol. 115, no. 7-8, pp. 2161-2173. doi: https://doi.org/10.1007/s00170-021-07268-z.

14. Batygin Y.V., Chaplygin E.A., Shinderuk S.A., Strelnikova V.A. The main inventions for technologies of the magnetic-pulsed attraction of the sheet metals. a brief review. *Electrical Engineering & Electromechanics*, 2018, no. 3, pp. 43-52. doi: https://doi.org/10.20998/2074-272X.2018.3.06.

15. Fireteanu V., Tudorache T. Electromagnetic forces in transverse flux induction heating. *IEEE Transactions on Magnetics*, 2000, vol. 36, no. 4, pp. 1792-1795. doi: https://doi.org/10.1109/20.877791.

16. Demirchyan K.S., Neiman L.R., Korovkin N.V., Chechurin V.L. *Theoretical foundations of electrical engineering. 4th ed. vol. 3*. St. Petersburg, Peter Publ., 2006. 318 p. (Rus).

17. Muller-Kirsten H.J.W. *Electrodynamics. 2nd Ed.* World Scientific Publishing Company, 2011. 632 p.

18. Isaev Yu., Vasilieva O. *Methods for calculating electromagnetic fields*. LAP Lambert Academic Publ., 2012. 172 p. (Rus).

19. Korn H., Korn T. *Mathematical Handbook*. Moscow, Nauka Publ., 1973. 831 p. (Rus).

20. Kreyszig E. *Advanced Engineering Mathematics. 10th ed.* Wiley Publ., 2011. 1283 p.

Received 05.03.2023
Accepted 09.05.2023
Published 02.11.2023

Yu.V. Batygin[1], *Doctor of Technical Science, Professor,*
O.F. Yeryomina[1], *PhD, Assistant Professor,*
S.O. Shinderuk[1], *PhD, Assistant Professor,*
E.O. Chaplygin[1], *PhD, Assistant Professor,*
[1] Kharkiv National Automobile and Highway University,
25, Yaroslava Mudrogo Str., Kharkiv, 61002, Ukraine,
e-mail: yu.v.batygin@gmail.com;
elena.yeryomina@gmail.com (Corresponding Author);
s.shinderuk.2016102@ukr.net; chaplygin.e.a@gmail.com

How to cite this article:
Batygin Yu.V., Yeryomina O.F., Shinderuk S.O., Chaplygin E.O. The mutual influence of exciting and induced currents in the circular solenoid – massive conductor system. *Electrical Engineering & Electromechanics*, 2023, no. 6, pp. 67-71. doi: https://doi.org/10.20998/2074-272X.2023.6.12

UDC 621.316 https://doi.org/10.20998/2074-272X.2023.6.13

Š. Gans, J. Molnár, D. Kováč

Estimation of electrical resistivity of conductive materials of random shapes

Introduction. *Electrical resistivity is an important material characteristic in the field of electrical engineering and material science. There are several methods that can be used to measure resistance, like the 4-wire method which relates the resistance to a voltage drop at a given current flow, but to define the resistivity from the resistance value requires an analytical expression for the given system which requires a sufficient mathematical apparatus for describing complicated shapes. Therefore we use finite element method computations to compute the resistivity of a metal material. This approach has been already used for different materials like concrete and aluminum in the past. We then compare this method with an analytical expression that due to intuition could approximate the solution sufficiently. After that, the same material is used again to test the electrical isotropy of the sample.* ***Novelty.*** *A method is developed by combining the results of experimental studies and the results of mathematical modelling of the process of determining the electrical conductivity of metals. The* ***goal*** *is to describe and employ a method of measuring the electrical resistivity of metal objects of random shapes. Using this method, it is possible to measure the resistivity of materials without the need to manufacture them into wires or ribbons.* ***Methods.*** *The solution to the problem was carried out by the finite element method via the COMSOL Multiphysics 5.6 simulation program in a cartesian coordinate system and the resistance between two points of the metal sample was measured by the 4-wire method.* ***Results.*** *A similar resistance value was obtained when the measuring terminals were placed in different places. The difference between them was within 1,5 % and the obtained values were close to the values given by the literature for the electrical resistivity of electrical steels. Terminal size influences the measured conductivity and a max error of 5,2 % was estimated.* ***Practical value.*** *A method of estimating the resistivity of materials without the need to manufacture them into specific shapes, like wires or ribbons, for which analytical expressions between resistivity and resistance are easily derived.* References 18, tables 7, figures 12.

Key words: **electrical resistivity, finite element method, electrical resistivity measurements, numerical simulation.**

Вступ*. Питомий електричний опір є важливою характеристикою матеріалу в галузі електротехніки та матеріалознавства. Існує кілька методів, які можна використовувати для вимірювання опору, наприклад, 4-провідний метод, який пов'язує опір з падінням напруги при заданому струмі, але для визначення питомого опору за значенням опору потрібен аналітичний вираз для даної системи, який вимагає достатнього математичного апарату для опису складних форм. Тому ми використовуємо розрахунки методом скінченних елементів до розрахунку питомого опору металевого матеріалу. Цей підхід вже використовувався в минулому для різних матеріалів, таких як бетон та алюміній. Потім ми порівнюємо цей метод з аналітичним виразом, який завдяки інтуїції може достатньо апроксимувати рішення. Після цього матеріал знову використовується для перевірки електричної ізотропії зразка.* ***Новизна****. Розроблено метод шляхом поєднання результатів експериментальних досліджень та результатів математичного моделювання процесу визначення електропровідності металів.* ***Мета*** *– описати та застосувати метод вимірювання питомого електичного опору металевих предметів довільної форми. Використовуючи цей метод, можна вимірювати питомий опір матеріалів без необхідності виготовлення дротів або стрічок.* ***Методи****. Розв'язання задачі здійснювалося методом скінченних елементів за допомогою програми моделювання COMSOL Multiphysics 5.6 у декартової системі координат, а опір між двома точками металевого зразка вимірювався 4-провідним методом.* ***Результати****. Отримано аналогічне значення опору під час розміщення вимірювальних клем у різних місцях. Різниця між ними знаходилася в межах 1,5% і отримані значення були близькими до наведених у літературі значень електричного опору електротехнічних сталей. Розмір клеми впливає на провідність, що вимірюється, максимальна похибка становить 5,2 %.* ***Практична цінність****. Метод оцінки питомого опору матеріалів без необхідності надання їм певної форми, наприклад, дроту або стрічок, для якого легко отримати аналітичні вирази між питомим опором та опором.* Бібл. 18, табл. 7, рис. 12.

Ключові слова: **електричний опір, метод скінченних елементів, вимірювання питомого електричного опору, чисельне моделювання.**

Introduction. Electrical resistivity is an important material characteristic. The theory of its measurement is well established and commonly used measurement techniques like the 2-wire or 4-wire method are used in praxis [1]. Because metals are usually very good conductors the measurement of their resistivities can be difficult [2, 3]. A similar problem of measuring the material resistivity of samples with different shapes was worked on in the study [4].

Resistivity defines the power losses of electrical conductors and in addition to parasitic capacitances and inductances, it can determine the transient behavior of circuits. It determines the skin depth of the magnetic and electric skin effect [5, 6]. The measurement of conductivity is also important in sensing the progress of concrete curing [7, 8] and also important in estimating its durability [9]. Not all metal materials can be measured this way and different techniques are used for porous materials [10]. Resistance measurements also yield structural information [11]. Most magnetic metals have a grain structure that experiences specific effects on resistivity [12]. Measuring the electrical resistance is done relative to two arbitrary points. In this work, it consists of connecting the points (terminals) to a power supply and measuring the current flowing from the power supply and the voltage difference between the two points. The resistance is then given by Ohm's law. However, calculating the resistivity based on resistance can be challenging especially when dealing with irregularly shaped objects. Then numerical methods can be employed to compute the electrical field distribution throughout the object. The current then flows in the direction of the electric field vectors (if we assume electric isotropy). The measurement of anisotropic materials has been done in the past, but in this work, the material is considered to be isotropic which will be tested [13].

After the resistance of the material is measured, the resistivity is computed from numerical analysis of the system by fitting the resistivity to fit the simulated voltage drop to the measured one.

The goal of the paper is to describe and test a method of electrical resistivity measurement of metal objects of non-standard shapes. Using it, it is possible to measure the resistivity of materials without the need to manufacture them into wires or ribbons.

The subject of investigations. This paper defines the used equations for the systems. The mathematics used is well-known in the field of electrical engineering.

After defining the problem and choosing a shape of interest, the numerical computation is done with the aid of the finite element method, which computes the discretized approximation of the system. After doing one simulation with a random resistivity value, the real value is computed which fits the simulation to the experiment. Because the chosen shape resembles a bus bar, the difference between an analytic expression and the simulation result of the conductivity is calculated. The terminal size influence is analyzed.

Theory and basic formulas. The equations governing electrostatics describe the electric field in a medium that arises due to static electrical charges. Via the material equations the relationship between the electric field $\boldsymbol{E}$ and current density $\boldsymbol{J}$ is established (1), which is the Ohm's law in differential form [14]. Throughout the paper we assume electrical isotoptropy of the medium so only scalar material characteristics are considered [15]:

$$\boldsymbol{J} = \sigma \boldsymbol{E}, \tag{1}$$

where σ is the conductivity of the material, which we want to estimate.

Electrical voltage is the potential difference between two points marked T1 and T2 in Fig. 1. The flowing current and voltage difference is expressed by (2) where the integration surface S is marked on the picture as well [16].

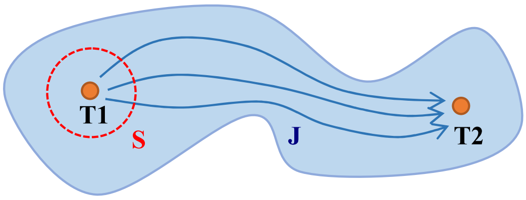

Fig. 1. A suitable integration surface for determining the current flowing through the body of the object. The integration surface S contains one terminal (T1) of the connected power supply

The current flowing through a medium is the flux of the current density vectors through a given surface. This surface should be suitably chosen like an enclosing sphere around one terminal of the object as it is shown in Fig. 2 [17].

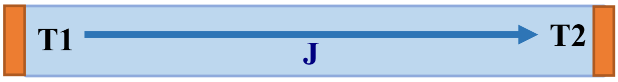

Fig. 2. A wire of uniform cross-section as a special case of the system

Equation (2) defines the resistance and so the relationship between the electric field and a corresponding current flow. The proportionality constant is the conductivity. By changing the conductivity at a given current we can fit the voltage drop from experiments and so the best-fit value will represent the conductivity of the material:

$$R = \frac{U}{I} = \frac{\int_{T1}^{T2} \boldsymbol{E} \mathrm{d}l}{\sigma \int_{S} \boldsymbol{E} \mathrm{d}S}. \tag{2}$$

Special case. One frequently used shape for which electrical resistance is computed is a long thin cylinder like it is in the case of an electrical wire.

The integrals from (2), because the wire is assumed to be uniform throughout its length becomes (3). Using Ohm's law we can obtain an analytic solution of (2) for simple wire-like objects (their length is the only significant dimension) [15]:

$$R = \frac{U}{I} = \frac{\boldsymbol{E} \cdot l}{I \cdot S} = \frac{1}{\sigma} \cdot \frac{l}{S}. \tag{3}$$

Material sample. A transformer steel strip was selected for the measurement (Fig. 3). The sheet's dimensions are 96 × 16,5 × 0,3 mm and two holes with a diameter of 5 mm are located near its ends. The holes were sanded, and two copper wires were soldered to their inner halves, which represent the two terminals of the object.

Fig. 3. The transformer sheet whose conductivity is the subject of determination

Based on this a 2D model was created in the Fusion 360 software that was extruded to 3D by giving the 2D plane a thickness of 0,3 mm (Fig. 4).

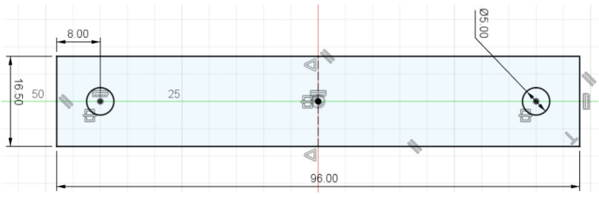

Fig. 4. Fusion 360 model of the steel strip

The model was imported into COMSOL Multiphysics modeling software as a .dxf file and an external domain representing an infinite air domain was added (Fig. 5). The air domain and the material were given a relative permittivity ε_r of 1. Air was given a conductivity σ of 10^{-10} S·m^{-1} (because 0 makes the model not converge) and the metal conductivity was set to $2 \cdot 10^6$ S·m^{-1}.

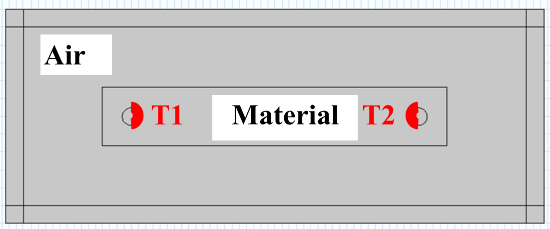

Fig. 5. COMSOL Multiphysics model of the system

Measurement. The measurement setup is shown in Fig. 6. It consisted of a constant current source (R&S HMP4040) and a voltmeter (RIGOL DM 3068), which measured the voltage difference between the terminals of the object.

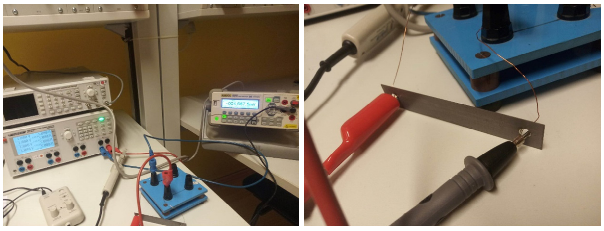

Fig. 6. Left – the measurement setup;
right – placement of the voltage meter probes

The voltage measurement was done at currents in the range of 1 to 5 A with a step of 1 A. The obtained values are shown in Table 1. The measurement method used is the 4-wire resistance measurement method [1].

Table 1
Measured values of voltage at a given current

Current, A	Voltage, mV	Resistance of strip, mΩ
1	7,0798	7,0798
2	14,1352	7,0676
3	21,135	7,045
4	28,2366	7,05915
5	35,3046	7,06092

The average value of the resistance was taken using an arithmetic mean (4). So a resistance of 7,0625 mΩ was computed:

$$\overline{R} = \frac{1}{5}\cdot\sum_{i=1}^{5} R_i = 7{,}0625\ \text{m}\Omega . \tag{4}$$

Simulation. The simulated system's terminals were connected to a 1 A constant current source and the output of the simulation was the voltage difference between the terminals that the current creates (Fig. 7, 8). The original guess of material conductivity $\sigma = 2\cdot 10^6$ S·m^{-1} was not correct, because the computed voltage drop was 9,5032 mV. The resistance of an object is inversely dependent on its conductivity, therefore linearly dependent on its resistivity ρ_R (ρ was used for volumetric charge density earlier). Two points in the resistivity/voltage drop graph define the linear relationship. At zero resistivity the voltage drop will be always zero so only one point is needed. The point coordinates are shown in Table 2.

Table 2
Two points from the resistivity/voltage drop space

Resistivity, Ω·m	Voltage, V
0	0
$5\cdot 10^{-7}$	0,016107

From them, we can define the voltage drop U as a function of resistivity. The expression is:

$$U = 16107\cdot\rho_R . \tag{5}$$

The desired voltage drop at 1 A is 7,0625 mV, so the material resistivity is fit as the value $4{,}38\cdot 10^{-7}$ Ω·m. When this value is set as the material resistivity in the simulation program, the computed voltage drop has the same value as the experimental one.

Comparison with the special case equation. The current density (Fig. 7–9) seems to be uniformly distributed through the middle part of the sheet. This may suggest that the analytical approach from the chapter «Special case» could be used with enough precision because the sheet has a long uniform middle section. The sheet cross-section in the middle is a rectangle that has dimensions of 0,3×16,5 mm. For the «wire length» we take the shortest path between the terminals, which is the strip axis between the holes (75 mm). Inserting these values into (3) returns a conductivity of $2{,}145\cdot 10^6$ S·m^{-1}.

When computing the relative error between these two approaches formula (6) yields a relative error of approx. 6 % which is to be decided by the application if it is tolerable:

$$\delta_\sigma = \left|\frac{\sigma_{eq} - \sigma_{sim}}{\sigma_{sim}}\right|\cdot 100\% = 5{,}932\ \% . \tag{6}$$

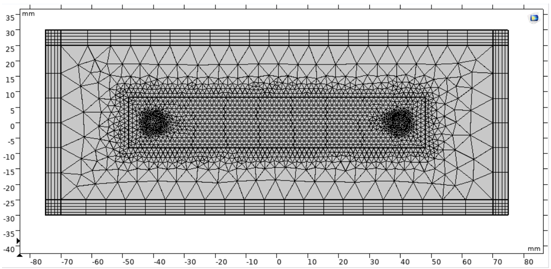

Fig. 7. The mesh generated for the given system

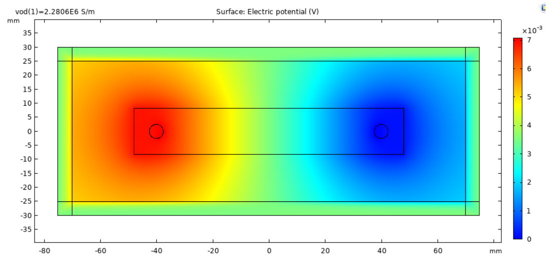

Fig. 8. The electrical potential at points of the system

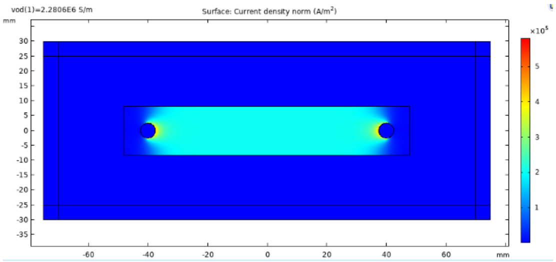

Fig. 9. The current density norm at points of the system

Measurement and simulation of resistivity at different terminals. The measurement and simulation were executed again at different points of the same sheet to test the obtained results. The tested terminal placements are shown in Fig. 10, 11. The lengths of the terminals were 5 mm in case *a*) and 2 mm in case *b*).

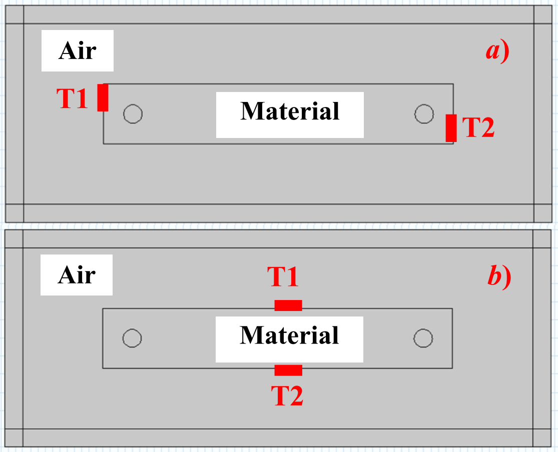

Fig. 10. Simulated samples of sheets

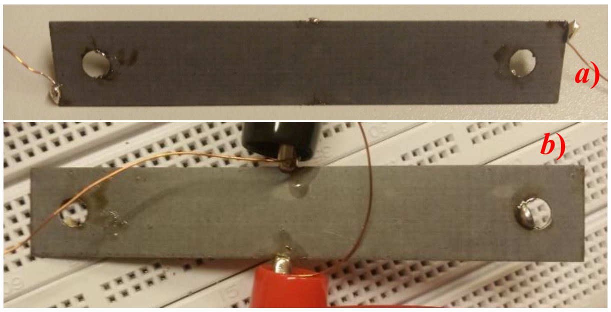

Fig. 11. The sheet samples to which wires were soldered as terminals as it was shown in Fig. 10

After the same process of measurement was repeated for sheets *a*) and *b*), the obtained results are shown below. After the resistance values were averaged from 5 current values (Table 3), the relative errors between the voltage drops if the same resistance value is used as the estimated one are shown in Table 4. The relative error was computed in the same way as in (6), but the *eq* index was replaced by *measurement*.

The resistances that would be obtained from such measurements are shown in Table 5. The error is again computed similarly as in (6) and relative to the original estimated sheet conductivity. The sheet seems to be electrically isotropic as it was expected.

Table 3
Measured values of sheet resistance

Sheet	Resistance of strip, mΩ
a)	10,5784
b)	2,7606

Table 4
Measured and simulated values of voltage drop at the given current

Sheet	Voltage drop at 1 A – measurement, mV	Voltage drop at 1 A – simulation, mV	Relative error, %
a)	10,5784	10,525	0,51
b)	2,7606	2,7857	0,9

Table 5
Measured and simulated values of voltage drop at the given current

Sheet	Resistivity, Ω·m	Error compared to the original sheet, %
Original	$4{,}385\cdot10^{-7}$	0
a)	$4{,}452\cdot10^{-7}$	1,52
b)	$4{,}429\cdot10^{-7}$	1,01

The effect of contact properties of probes to the surface of the sheet. The contacts that the probes make with the sheet affect the measured voltage drop. The transformer sheet was covered in an electrically isolating warnish that was removed in the places of probe connection and the sanded length was measured to correspond with the simulations. A simple ruler was used for the measurement with a resolution of 1 mm. To estimate how this affects the computed values of conductivity due to terminal size uncertainty the simulation was recomputed. Multiple terminal lengths from the interval of ±1 mm centered around the desired value were used. It is evident (Fig. 12) that the voltage drop monotonically decreases with terminal size. When computing the resistivity it can be seen that it increases monotonically with terminal size.

The main reason behind such large differences between the error values (Table 6) is the proximity of the measuring terminals, which was substantially lower in the case of *b*). The closer they are, the larger measuring uncertainty of resistivity can be expected, because at small distances it affects the electric field distribution the most. Also the solder connection resistance was not controlled and therefore also affects the measurement to some extent, since the solder conductivitiy is comparable to the sheet's conducitivity. The best method to suppress the effect of the connections' resistances is to place the terminals as far apart as possible in order to make the electric field lines between terminals as long as possible. This will render the resistance of the terminal connections as small as possible compared to the resistance of the sheet between the terminals and so the measured voltage drop will be mostly due to the sheet's resistance between the two terminals.

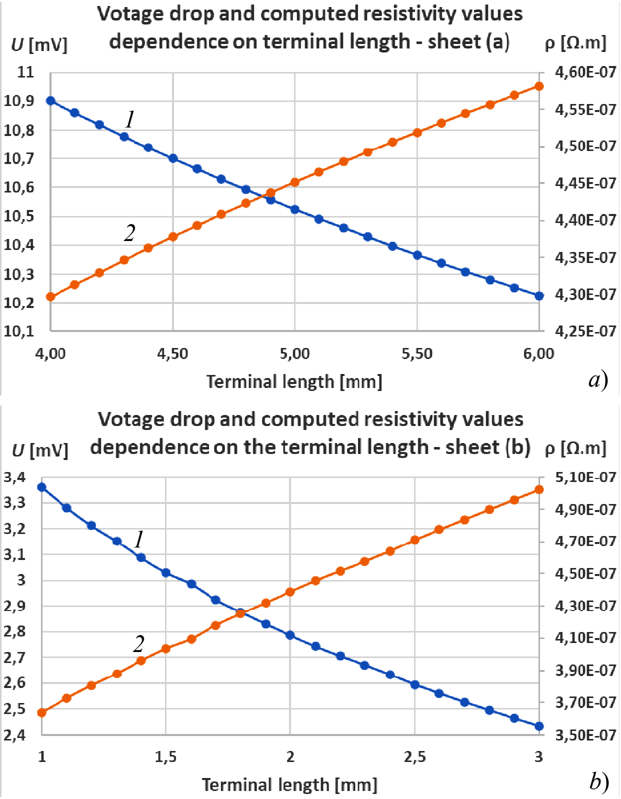

Fig. 12. Voltage drop dependence on terminal length when a conductivity of $2.25\cdot10^6$ S/m was used for the simulation on sheets (*a*) and (*b*) – blue graph *1* and the corresponding computed resistivity value to match experiments – orange graph *2*

Table 6
Calculated conducitivty interval due to a 1 mm terminal measuring error

Sheet	Lowest ρ, Ω·m	Largest ρ, Ω·m	Max error compared to Table 5, %
a)	$4{,}298\cdot10^{-7}$	$4{,}582\cdot10^{-7}$	3,47
b)	$3{,}638\cdot10^{-7}$	$5{,}022\cdot10^{-7}$	17,85

Uncertainty of the resistance measurement. The uncertainty values of measurements were calculated from the datasheet values of the used devices. The voltage drop was measured by the RIGOL DM 3068 multimeter which on the smallest 200 mV range has a 0,002 % error of reading and a 0,002 % error of range. The R&S HMP4040 current source has a regulation error consisting of a 0,01 % error of regulation and a 250 μA offset error. When setting a DC current value of 1 A, the current accuracy is 1 ± 0,00035 A. The voltage accuracies can be seen in Table 7.

Because the current and voltage were measured by two separate instruments, they are uncorrelated and because resistance is computed by division of these values, the resistance uncertainty is given as [18]:

$$u_R = \left(\frac{u_u}{U} + \frac{u_i}{I}\right)\cdot R\,, \tag{7}$$

where u_R is the resistance uncertainty, u_u and u_i are the voltage and current uncertainties, U and I are the measured voltage and current values and R is the computed resistance.

The resistance is then estimated as $R \pm u_R$ and is shown in Table 7. The relative resistance measurement uncertainty is 0,075 % for sheet *a*) and 0,182 % for sheet *b*) [18].

Table 7
Absolute uncertainty of the resistance measurement

Sheet	Absolute current uncertainty, A	Absolute voltage uncertainty, V	Absolute resistance uncertainty, Ω
a)	$3{,}5\cdot10^{-4}$	$4{,}212\cdot10^{-6}$	$7{,}914\cdot10^{-6}$
b)	$3{,}5\cdot10^{-4}$	$4{,}055\cdot10^{-6}$	$5{,}021\cdot10^{-6}$

When computing the resistance error due to terminal size uncertainty from Fig. 12 we obtain a relative uncertainty for sheet *a*) of 3,33 % and for sheet *b*) of 21,74 %. So the uncertainty in the connection parameters of the probes to the sheet strongly dominate the uncertainty of resistance measurement. The further apart the two terminals are, the smaller the error becomes.

Conclusions. The paper described a method of estimating the resistance of highly conductive materials of non-standard shapes. The method can estimate the conductivity of metals even when placed in different places of the object with a relative difference of approximately 1,5 %. However, because there is uncertainty in the terminal connection sizes and resistances, putting them too close together can yield very large uncertainty values. Terminals should be placed on opposite ends of the object to make these infuences as small as possible. Because there is no bounds of what object shapes could be used for the measurement the uncertainties of the given terminal placements should be computed for each case and decided if it is appropriate for the given application. The obtained results are similar to the resistivities of other metals of the same category. Because the measurement yielded a similar value of resistivity when the terminals were placed on the sheet axis (original measurement and sheet marked *a*)) and perpendicular to it (the sheet marked *b*)) we can assume that the electrical steel is electrically isotropic.

Conflict of interest. The authors of the article declare that there is no conflict of interest.

REFERENCES

1. Singh Y. Electrical resistivity measurements: a review. *International Journal of Modern Physics: Conference Series*, 2013, vol. 22, pp. 745-756. doi: https://doi.org/10.1142/S2010194513010970.

2. Zimmerman J.E. Measurement of Electrical Resistivity of Bulk Metals. *Review of Scientific Instruments*, 1961, vol. 32, no. 4, pp. 402-405. doi: https://doi.org/10.1063/1.1717387.

3. Rossiter P.L. *The Electrical Resistivity of Metals and Alloys*. Cambridge Solid State Science Series, 1991. 452 p.

4. Hájek M., Veselý J., Cieslar M. Precision of electrical resistivity measurements. *Materials Science and Engineering: A*, 2007, vol. 462, no. 1-2, pp. 339-342. doi: https://doi.org/10.1016/j.msea.2006.01.175.

5. Zhang D. Magnetic skin effect in silicon-iron core at power frequency. *Journal of Magnetism and Magnetic Materials*, 2000, vol. 221, no. 3, pp. 414-416. doi: https://doi.org/10.1016/S0304-8853(00)00414-5.

6. Wilmot-Smith A.L., Priest E.R., Hornig G. Magnetic diffusion and the motion of field lines. *Geophysical & Astrophysical Fluid Dynamics*, 2005, vol. 99, no. 2, pp. 177-197. doi: https://doi.org/10.1080/03091920500044808.

7. Sengul O., Gjorv O.E. Effect of Embedded Steel on Electrical Resistivity Measurements on Concrete Structures. *ACI Materials Journal*, 2009, vol. 106, no. 1, pp. 11-18. doi: https://doi.org/10.14359/56311.

8. Liang S., Du H., Zou N., Chen Y., Liu Y. Measurement and simulation of electrical resistivity of cement-based materials by using embedded four-probe method. *Construction and Building Materials*, 2022, vol. 357, art. no. 129344. doi: https://doi.org/10.1016/j.conbuildmat.2022.129344.

9. Azarsa P., Gupta R. Electrical Resistivity of Concrete for Durability Evaluation: A Review. *Advances in Materials Science and Engineering*, 2017, vol. 2017, art. no. 8453095. doi: https://doi.org/10.1155/2017/8453095.

10. Ma X., Peyton A.J., Zhao Y.Y. Eddy current measurements of electrical conductivity and magnetic permeability of porous metals. *NDT & E International*, 2006, vol. 39, no. 7, pp. 562-568. doi: https://doi.org/10.1016/j.ndteint.2006.03.008.

11. Liu X., Sun J., Wang H. Numerical simulation of rock electrical properties based on digital cores. *Applied Geophysics*, 2009, vol. 6, no. 1, pp. 1-7. doi: https://doi.org/10.1007/s11770-009-0001-6.

12. Nakamichi I. Electrical Resistivity and Grain Boundaries in Metals. *Materials Science Forum*, 1996, vol. 207-209, pp. 47-58. doi: https://doi.org/10.4028/www.scientific.net/MSF.207-209.47.

13. Montgomery H.C. Method for Measuring Electrical Resistivity of Anisotropic Materials. *Journal of Applied Physics*, 1971, vol. 42, no. 7, pp. 2971-2975. doi: https://doi.org/10.1063/1.1660656.

14. *OpenStax. 9.3 Resistivity and Resistance*. University Physics, 2023, vol. 2. Available at: https://openstax.org/books/university-physics-volume-2/pages/9-3-resistivity-and-resistance (accessed 01 March 2023).

15. *COMSOL Multiphysics Cyclopedia, Electrostatics, Theory. 2023.* Available at: https://www.comsol.com/multiphysics/electrostatics-theory?parent=electromagnetics-072-162 (accessed 01 March 2023).

16. Kováč D., Kováčová I., Kaňuch J. *EMC z hlediska teorie a aplikace*. Praha, BEN technická literatura, 2006.

17. *COMSOL Multiphysics Cyclopedia, Steady Currents. 2023.* Available at: https://www.comsol.com/multiphysics/steady-currents?parent=electromagnetics-072-502 (accessed 01 March 2023).

18. Taylor R.J. *An Introduction to Error Analysis: The Study of Uncertainties in Physical Measurements. 2nd Edition*. University Science Books, 1996. 327 p.

Received 16.03.2023
Accepted 28.04.2023
Published 02.11.2023

Šimon Gans[1]*, PhD Student,*
Ján Molnár[1]*, Associate Professor,*
Dobroslav Kováč[1]*, Professor,*
[1] Department of Theoretical and Industrial Electrical Engineering, Technical University of Košice, Slovakia,
e-mail: simon.gans@tuke.sk (Corresponding Author);
jan.molnar@tuke.sk; dobroslav.kovac@tuke.sk

How to cite this article:
Gans Š., Molnár J., Kováč D. Estimation of electrical resistivity of conductive materials of random shapes. *Electrical Engineering & Electromechanics*, 2023, no. 6, pp. 72-76. doi: https://doi.org/10.20998/2074-272X.2023.6.13

UDC 621.316.9 https://doi.org/10.20998/2074-272X.2023.6.14

A.V. Krasnozhon, A.O. Kvytsynskyi, R.O. Buinyi, I.V. Dihtyaruk, O.V. Krasnozhon

Study of the influence of the parameters of modern grounding wires on the value of power losses in them for overhead power lines of 330-750 kV

Introduction*. The problem of estimating power losses in grounding wires with built-in fiber optic cable for overhead power lines of voltage class 330-750 kV is relevant, while it is obvious that the amount of losses depends on the chosen brand of wire.* ***Problem****. In the article, an analysis of the influence of the parameters of grounding wires on the amount of losses that occur in them in the normal mode of operation of the overhead power lines is carried out.* ***Goal****. The purpose of the work is to determine the criterion for the selection of grounding wires with a built-in optical fiber cable under the condition of increasing the energy efficiency of electricity transmission.* ***Methodology****. To calculate power losses in grounding wires, the methods of electromagnetic field theory were used, while taking into account the location of phase conductors on various types of towers of operating 330-750 kV overhead power lines and the possible current load of such lines.* ***Results****. The paper analyzed the dependence of losses in the grounding wires of the overhead power lines on the ratio of its active and reactive resistances, determined in which range of this ratio the losses will be close to the maximum. It is shown that the amount of specific power losses in the grounding wires of 330-750 kV overhead power lines in its normal operating modes can range from 1.6 kW/km for the 750 kV lines to hundreds of W/km for the 330 kV power lines.* ***Originality****. For the first time, it is recommended to use grounding wires with built-in fiber optic cable with running active resistance in the range of no more than 0.25 Ohm/km, which will minimize power losses and increase the energy efficiency of the 330-750 kV overhead power lines.* ***Practical value.*** *The obtained results can be applied at the stage of designing new or modernizing existing overhead power lines in order to reduce losses and increase the energy efficiency of lines.* References 27, tables 1, figures 5.

Key words: **overhead power line, lightning protection system, grounding wire, electricity losses, running active resistance.**

Досліджено втрати електроенергії в грозозахисних системах повітряних ліній електропередавання напругою 330-750 kV з грозозахисними тросами, що містять вбудований оптоволоконний кабель. Показано, що ці втрати є значними, залежать від взаємного розташування фаз та тросу, навантаження лінії за струмом та параметрів самого тросу (співвідношення його активного та реактивного опорів) і можуть становити від 1,6 kW/km для ліній 750 kV до сотень W/km для ліній 330 kV. Визначено, що грозозахисні троси з погонним активним опором в діапазоні від 0,32 Ω/km до 1,5 Ω/km будуть мати втрати, близькі до максимальних. Вперше рекомендовано використовувати грозозахисні троси, які містять вбудований оптоволоконний кабель, з погонним активним опором не більше 0,25 Ω/km, що дозволить зменшити втрати потужності та підвищити енергоефективність повітряних ліній електропередавання 330-750 kV. Бібл. 27, табл. 1, рис. 5.

Ключові слова: **повітряна лінія електропередавання, грозозахисна система, грозозахисний трос, втрати електроенергії, погонний активний опір.**

Introduction. In the modern world, overhead power lines (PLs) are increasingly equipped with lightning protection cables (LPCs) with built-in fiber optic cable (cables of the OPGW type). Such cables not only protect the PL phases from direct lightning strikes, but at the same time have built-in channels for transmitting information. The process of equipping PLs with such cables continues in Ukraine, primarily these are main PLs of the 220-400 kV voltage class. It should be noted that the lightning protection system of the PLs of the above voltage classes most often consists of two LPCs.

According to the requirements of the Electrical installation regulations [1], OPGW-type LPCs must be connected to each PL support, which, in turn, is grounded. Here, additional losses of electrical energy will occur in the PL lightning protection system in normal operation mode. The magnetic field of the PL phase wires forms an alternating magnetic flux coupled to the PL lightning protection system. This flow leads to the appearance of induced currents in the LPC and, as a result, energy losses for heating the LPCs themselves, which have a certain active resistance.

Review of publications. In [2], the approach to calculating power losses in the lightning protection system of the 330 kV PL, which has one LPC and is made on poles of the PS330-2 brand with a vertical arrangement of phases, is considered. The authors show that in the case of the use of the LPC of the OPGW type, the induced current in the LPC can lead to significant power losses. However, the majority of 330-750 kV PLs have horizontal wiring and two LPCs. It should be noted that most often in the course of the modernization of the mentioned PLs in Ukraine, only one of the two LPCs is replaced with OPGW: the other remains divided into segments by a steel rope, and each of the segments, in accordance with the Electrical installation regulations, is grounded at one point in order to prevent the flow of the induced current in such a LPC.

Studies of the modes of operation of high and ultra-high voltage lightning protection systems have a long history [3, 4]. However, the never-ending interest in these issues is due to both the use of new materials and the development of new types of PL supports, changes in the parameters of the LPCs themselves, changes in the PL load, etc. Issues of arrangement and modes of operation of lightning protection systems are considered in [5-7]. However, in them, attention is paid to multi-circuit PLs with one or two lightning protection cables [5] and vertical arrangement of phases. Here, the optimal mutual location of the phases of different circuits of such a PL is chosen in order to reduce power losses in its lightning protection system.

PLs of voltage classes 330-750 kV found on the territory of our country have horizontal arrangement of phases and are mostly single-circuit. A characteristic feature of Ukrainian PLs is the significant size of the supports and the distances between the phases and the LPC, therefore, the methods of reducing power losses in the lightning protection system given in [5-7] cannot be applied to them.

Many works, in particular [8-13], are dedicated to the reduction of power losses in electrical networks. However, most of these works are aimed at solving the problem of reducing technological losses of electrical energy in phase conductors of the electrical network and power transformers.

The issue of reducing losses is also relevant for cable lines, where currents are induced in the shields of single-core cables according to a similar mechanism of influence (if there are conditions for their flow) [1, 14-17].

The analysis of regulatory documents regarding the installation of fiber-optic communication lines (FOCL) on PLs showed that when choosing OPGW, their mechanical strength and resistance to lightning and short-circuit currents are taken into account, and power losses that occur in them in normal PL operation mode are not taken into account[1]. It is obvious that it is worth proposing additional criteria for the selection of LPC in order to reduce these losses.

The goal of the article is to find and justify the selection criterion for the OPGW for 330, 400, 500 and 750 kV PLs, which will ensure the reduction of power losses in the lightning protection systems of such PLs.

The main research materials. Below are the calculation method and numerical values of power losses in the lightning protection system of the 330-750 kV PLs using the example of supports of the PP-750, PP-500 and P330-9 brands (Fig. 1).

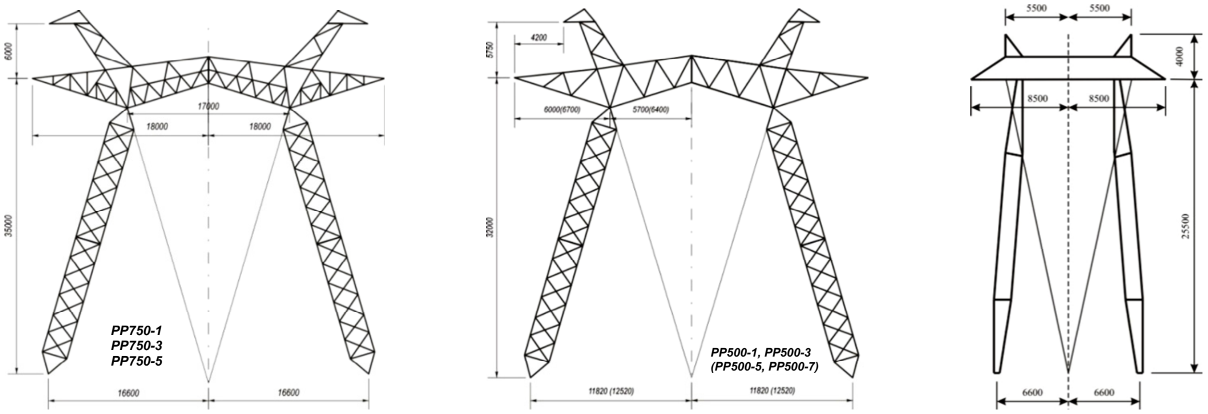

a *b* *c*

Fig. 1. External view and geometric dimensions of high-voltage PL supports: *a*) PP-750; *b*) PP-500; *c*) P330-9

For 750 kV PLs, which are built on supports of the PP-750 type (Fig. 1,*a*) [18], there will be the largest distances between the phases and the LPCs, which form the lightning protection system of the PL. Such PLs are designed to transport up to 2.25 GW of power (the current in a phase is approximately equal to 1.7 kA), and the load of PLs during the day, as a rule, changes insignificantly. In Ukraine, the indicated PLs most often have a load of up to 1 GW (the current in a phase is approximately equal to 770 A). All this means that it is in such PLs significant losses in the lightning protection system can occur. For example, the maximum annual losses in one LPC of the 750 kV PL with maximum load of 2,000 MW and the number of hours of use of the maximum load of 6,000 hours/year can reach 50,000 kW·h/km [4].

Let's find out for which LPCs the greatest losses will occur in the PL lightning protection system.

The currents induced in adjacent circuits from the OPGW grounded on each support, the body of the supports, and the ground, flow through the supports of the PL in opposite directions and compensate each other in the case of equality of the run lengths. It should also be noted that the resistance of one cable run is significantly lower than the grounding resistance of one PL support. Under such conditions, the currents from OPGW to the ground flow only from the terminal supports of the PL, the resistance of which is normalized in Table 2.5.29 of the Electrical installation regulations [1]. The circuit for the flow of this current has a certain active resistance R_{GW} and inductive resistance X_{GW}, which are determined by the parameters of the OPGW (provided that the grounding resistances of the terminal supports of the PL are small relative to R_{GW} and X_{GW} of the OPGW along the length of the PL).

Knowing the induced voltage U_{GW}, we can determine the induced current of I_{GW} by the formula:

$$I_{GW} = \frac{U_{GW}}{\sqrt{R_{GW}^2 + X_{GW}^2}}. \quad (1)$$

Losses of active power in the lightning protection system can be determined by the formula:

$$P_{GW} = I_{GW}^2 \cdot R_{GW} = U_{GW}^2 \cdot \frac{R_{GW}}{R_{GW}^2 + X_{GW}^2}. \quad (2)$$

The condition of maximum active losses can be found by determining the extremum of (2):

$$\frac{dP_{GW}}{dR_{GW}} = U_{GW}^2 \cdot \frac{\left(R_{GW}^2 + X_{GW}^2\right) - 2 \cdot R_{GW}^2}{\left(R_{GW}^2 + X_{GW}^2\right)^2} = 0. \quad (3)$$

It follows from (3) that the condition for maximum active losses in the LPC has the following form:

$$R_{GW} = X_{GW}. \quad (4)$$

It is obvious that the maximum power losses will be equal to:

$$P_{GW\max} == \frac{U_{GW}^2 \cdot X_{GW}}{X_{GW}^2 + X_{GW}^2} = U_{GW}^2 \cdot \frac{1}{2 \cdot X_{GW}}. \quad (5)$$

Let's determine the value of reduced losses in the form of the ratio of P_{GW} to $P_{GW\max}$:

$$\frac{P_{GW}}{P_{GW\max}} = \frac{2 \cdot R_{GW} \cdot X_{GW}}{R_{GW}^2 + X_{GW}^2}. \quad (6)$$

By dividing the numerator and denominator of (6) by the square of the reactive resistance, it is possible to obtain the value of the reduced losses in the lightning protection system as a function of the ratio of its active and reactive resistances:

$$\frac{P_{GW}}{P_{GW\max}} = f\left(\frac{R_{GW}}{X_{GW}}\right) = \frac{2 \cdot \dfrac{R_{GW}}{X_{GW}}}{1 + \left(\dfrac{R_{GW}}{X_{GW}}\right)^2}. \quad (7)$$

The dependence constructed according to (7) is shown in Fig. 2.

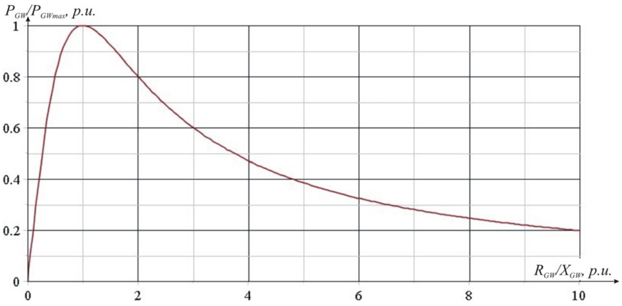

Fig. 2. Dependence of reduced losses of active power in the lightning protective cable of the PL on the ratio of its active and reactive resistances

It is obvious that in order to avoid maximum losses in the lightning protection system, one should choose such OPGW for which the ratio R_{GW}/X_{GW} will be either less than 1 or greater than one. So, in Fig. 2 it can be seen that under the condition of choosing OPGW, for which R_{GW}/X_{GW} = 0.5 or 2 p.u., we have a value of specific losses of 0.8 p.u., which means a reduction of losses relative to the maximum by only 20 %. Provided that $R_{GW}/X_{GW} \le 0.4$ or $R_{GW}/X_{GW} \ge 2.5$, we have a reduction in losses in the lightning protection system by more than 30 % in any operating mode of the PL. It is obvious that this criterion of the ratio R_{GW}/X_{GW} should be guided by the choice of OPGW for PL. Here, economic considerations should also be taken into account, because cables with a small ratio of active and reactive resistance have a larger diameter and mass per kilometer of length, as well as a higher price, but at the same time they will provide a better level of lightning protection and have greater resistance to lightning currents and short circuit (SC).

It should be noted that the above considerations are valid for the case when the resistance of the OPGW along the length of the entire PL is significantly greater than the resistances of the grounders of the terminal supports of the PL, which is actually performed for PLs of considerable length (in the case of short PLs, the above-mentioned resistances of the grounders should be taken into account).

Let's calculate the lossyi of active power in the lightning protection system of the PL under the condition of using different brands of OPGW. The mutual location of the phase conductors of the PL and the lightning protection cables with all the necessary distances is shown in Fig. 3.

Figure 3 shows the distance r_f between the phase and LPC1, as well as other distances necessary for the calculation. In cases where PLs are built on supports of the type:

- PP-750 (Fig. 1,*a*) – x_f = 18 m, x_t = 16.75 m, h_f = 15.9 m, H = 27.75 m;
- PP-500 (Fig. 1,*b*) – x_f = 11.7 m, x_t = 7.5 m, h_f = 17 m, H = 26.5 *m*;
- P330-9 (Fig. 1,*c*): x_f = 8.5 m, x_t = 5.5 m, h_f = 13.8 m, H = 20.25 m [18].

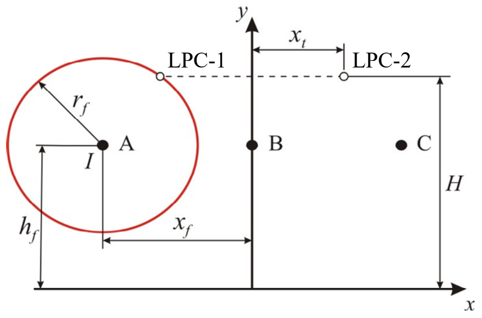

h_f – the height of the location of the phase conductors;
H – the height of the LPC location;
x_f – the distance from the vertical axis of symmetry of the support to the phases;
x_t – the corresponding distance to the LPC

Fig. 3. Geometric model of the PL for calculation

We assume that in Fig. 3 LPC1 is of the OPGW type, in which power losses should be determined. A steel rope divided into single-sided grounded segments is assumed as the LPC2.

It is also worth noting that the flow of current I in the PL phase will lead to the formation of the electromagnetic field around the conductor and, in the case of the passage of the PL along a residential building, create a harmful effect on the human body [19-23].

In Fig. 3 it can be seen that the distance between the PL phase and OPGW can be calculated by the formula:

$$r_f = \sqrt{\left(x_f - x_t\right)^2 + \left(H - h_f\right)^2}. \quad (8)$$

The depth of the current flow in the ground and the running voltage, in V/km, induced on the LPC1 of the OPGW type from the current of one phase of the PL, can be determined according to [4, 24] as:

$$D_{gr} = \frac{2{,}1}{\sqrt{f \cdot \gamma \cdot 10^{-5}}}; \quad (9)$$

$$U_{GW1P} = 0{,}1447 \cdot I \cdot \lg\left(D_{gr}/r_f\right), \quad (10)$$

where f is the current frequency; γ is the specific electrical conductivity of the soil (taken as equal to 0.01 S/m); I is the effective value of the current of one phase of the PL.

The running voltage from all phases of the PL induced on the OPGW will be determined as:

$$\dot{U}_{GW1} = U_{GW1A}\cdot e^{j\cdot 0} + U_{GW1B}\cdot e^{-j\cdot\frac{2\cdot\pi}{3}} + U_{GW1C}\cdot e^{j\cdot\frac{2\cdot\pi}{3}}. \quad (11)$$

The active and reactive resistances of one kilometer of the OPGW, taking into account the current in the ground, are equal to [4]:

$$R_{GW} = R_p + 0{,}05\,; \quad (12)$$

$$X_{GW} = 0{,}1447\cdot \lg\left(\frac{D_{gr}}{d/2}\right), \quad (13)$$

where R_p is the running active resistance of the OPGW of a certain brand; d is its diameter.

The current induced in the lightning protection system is calculated according to (1). Based on the known effective value of this current, losses in the lightning protection system of the PL can be found according to (2).

The passport parameters of OPGW of various brands, as well as the calculated running active and reactive resistances of lightning protection systems of PL 330, 500 and 750 kV and their ratios are given in Table 1 [25]. As can be seen in Table 1, the active resistance of the lightning protection system depends very much on the selected brand of OPGW, while the reactive resistance changes much less. Therefore, when choosing a brand of LPC, we need to focus, first of all, on its running active resistance.

Table 1

OPGW parameters for PL 330-750 kV

LPC brand	OPGW parameters		Running active and reactive resistances of OPGW of PL voltage 330-750 kV		R_{GW} / X_{GW}, p.u. for PL voltage 330-750 kV
	d, mm	R_p, Ω/km	R_{GW}, Ω/km	X_{GW}, Ω/km	
OPGW 426-AL1/56-A20SA	28,8	0,065	0,115	0,697	0,165
OPGW 264-AL3/29-A20SA	22,5	0,12	0,17	0,712	0,239
OPGW 34-AL3/34-A20SA	11,4	0,681	0,731	0,755	0,969
OPGW 11-AL3/15-A20SA	7,3	1,856	1,906	0,783	2,435
OPGW 27-A20SA	7,3	3,022	3,072	0,783	3,925

According to (1), (2), (8) – (13) for all cables specified in Table 1, the dependencies of the specific losses of active power in the lightning protection system on the current in the PL phase are plotted, shown in Fig. 4.

It is easy to see that the OPGW 34-AL3/34-A20SA type cable (curve 3 in Fig. 4) provides a significantly higher level of losses than other brands of OPGW. If the current value of the 750 kV PL phase is 770 A when using the OPGW 34-AL3/34-A20SA cable, the power losses in the 750 kV PL lightning protection system will be about 1.472 kW/km (see Fig. 4,*a*). With PL length of 500 km, the losses of active power over the entire length of the LPC will amount to 0.736 MW. The cost of such losses per year, under the condition of operation of the PL with constant load at the existing tariff for the transmission of electricity through main networks (397.85 UAH per MW·h. as of December 2022), will amount to 2.565 million UAH/year. It is obvious that the use of cables of other brands will allow to significantly save electricity, especially if we take into account the standard operating life of the PL, which according to current legislation is 40 years, as well as the fact that electricity prices are constantly increasing. For example, for the OPGW 426-AL1/56-A20SA brand cable with the same value of current, the power losses are 0.513 kW/km, while the cost of such losses during the year will be 0.893 million UAH/year.

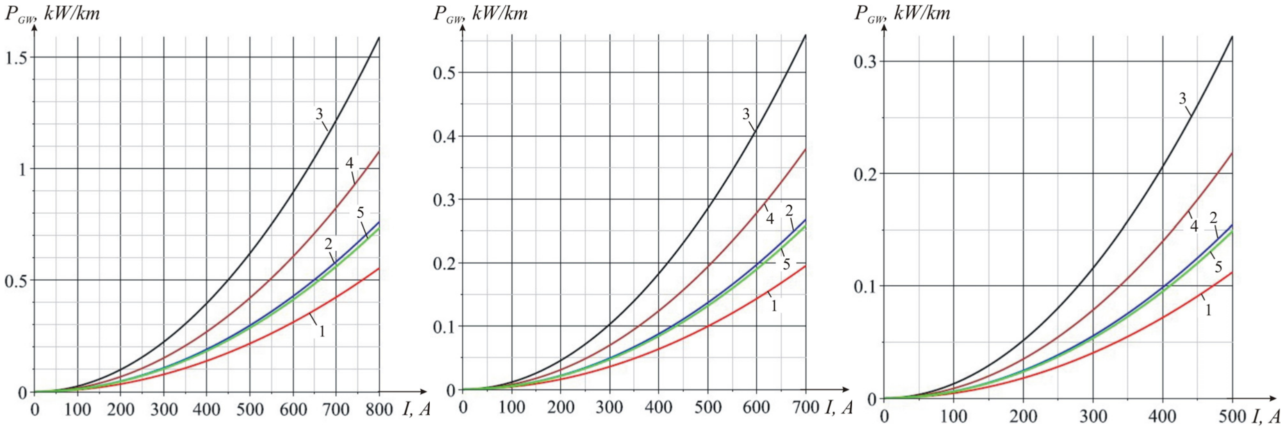

a) for PL 750 kV *b*) for PL 500 kV *c*) for PL 330 kV

Fig. 4. Dependencies of power losses in the 330-750 kV PL lightning protection system on the phase current for different brands of LPC:
1 – OPGW 426-AL1/56-A20SA; 2 – OPGW 264-AL3/29-A20SA; 3 – OPGW 34-AL3/34-A20SA;
4 – OPGW 11-AL3/15-A20SA; 5 – OPGW 27-A20SA

Figure 4,*b* shows that the power losses in the lightning protection system of the 500 kV PL can amount to hundreds of Watts per 1 km of its length. Such losses are also significant, especially considering the total length of the PL (for current of 500 A, losses in the lightning protection system of the PL with OPGW 34-AL3/34-A20SA brand cable can reach 0.285 kW/km). The correct choice of the LPC brand allows to reduce the value, and therefore the cost of such losses several times.

330 kV voltage class PLs are also of interest in the amount of losses in the lightning protection system. Such PLs also operate for a long time with significant current load. In Fig. 4,*c* it can be seen that the use of certain brands of OPGW allows to reduce losses to the value of tens of Watts per km of the length of the 330 kV PL (at current of 300 A, the losses in the lightning protection system of the PL with OPGW 34-AL3/34-A20SA cable can reach 116 W/km, and with OPGW 426-AL1/56-A20SA cable – only 40.5 W/km).

It should also be noted that when changing the OPGW brand, the reactive resistance of the lightning protection system changes significantly less than the active resistance (see Table 1), therefore, the value of the running active resistance of the OPGW should be the selection criterion in order to minimize power and electrical energy losses.

Analysis of the curves in Fig. 4 shows that cables with both low and high running active resistance on 330-750 kV PLs allow for a significant reduction in power losses in the lightning protection system, but at the same time, OPGWs with significant running active resistance have a smaller diameter, lower strength and thermal resistance to lightning currents and SC [26, 27].

According to Table 1 plots the dependencies of the ratio of active and reactive resistances R_{GW}/X_{GW} of the lightning protection system on the running active resistance R_p of the LPC are plotted (Fig. 5).

In Fig. 5 it can be seen that when using OPGW with running active resistance of 0.25 Ω/km, we have the value of R_{GW} / X_{GW} approximately equal to 0.4 p.u., which according to the curve in Fig. 2 provides a reduction of losses by 30 % from their maximum possible value. When choosing a LPC with lower values of the running active resistance, the losses in the lightning protection system of the 330-750 kV PL will be even smaller. Thus, when choosing an OPGW-type LPC for the considered PLs, it is worth choosing cables with running active resistance of no more than 0.25 Ω/km. Loss reduction can also be achieved by choosing cables with running active resistance greater than 1.85 Ω/km, corresponding to R_{GW} / X_{GW} of at least 2.45 p.u., which also provides a loss reduction of 30 % or more. However, such cables have a smaller cross-section, less mechanical strength and thermal resistance to lightning currents and SC, so it is not recommended to choose them.

It should also be noted that LPCs with running active resistance in the range from 0.32 Ω/km to 1.5 Ω/km are better not to be chosen at all, because it is for them that the R_{GW} / X_{GW} ratio varies from 0.5 to 2 p.u., that in accordance with Fig. 3 will ensure losses in the lightning protection system within 80-100 % of the maximum possible.

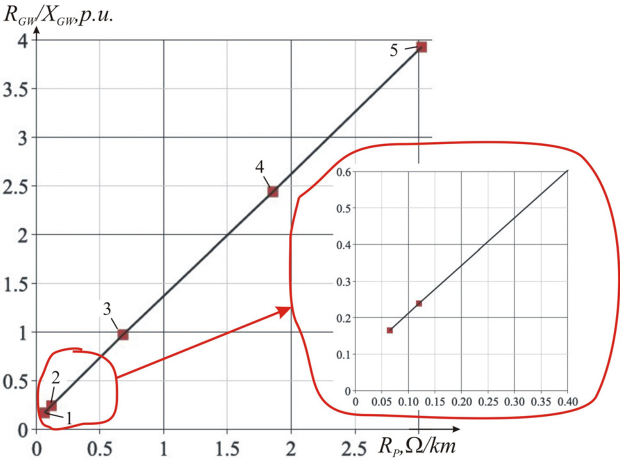

1 – OPGW 426-AL1/56-A20SA, 2 – OPGW 264-AL3/29-A20SA, 3 – OPGW 34-AL3/34-A20SA, 4 – OPGW 11-AL3/15-A20SA, 5 – OPGW 27-A20SA

Fig. 5. Dependencies of the R_{GW} / X_{GW} ratio on the running active resistance *Rp* of the LPC for lightning protection systems of the PL 330-750 kV

Conclusions.

It is shown that the value of specific power losses in lightning protection systems of 330-750 kV PLs in their normal modes of operation can range from 1.6 kW/km for 750 kV PLs to hundreds of W/km for 330 kV PLs and significantly depends on the mutual location of the phase wires and OPGW, PL load current and OPGW characteristics.

It has been determined that lightning protection cables with running active resistance in the range of 0.32 Ω/km to 1.5 Ω/km will have losses close to the maximum and should therefore be avoided. Smaller losses will be in the case of using OPGW with running active resistance of less than 0.25 Ω/km (usually of considerable value) or more than 1.85 Ω/km (usually of insufficient mechanical strength and thermal resistance to lightning currents and short circuit).

For the first time, it is recommended to use OPGW with running active resistance of no more than 0.25 Ω/km, which will allow to minimize power losses and increase the energy efficiency of 330-750 kV PLs at the stage of their design.

Conflict of interest. The authors declare no conflict of interest.

REFERENCES

1. *Electrical installation regulations*. Kharkiv, Fort Publ., 2017. 760 p. (Ukr).

2. Krasnozhon A.V., Buinyi R.O., Pentegov I.V. Calculation of active power losses in the grounding wire of overhead power lines. *Technical Electrodynamics*, 2016, no. 4, pp. 23-25. (Ukr). doi: https://doi.org/10.15407/techned2016.04.023.

3. Melnykov N.A., Rokotian S.S., Sherentsys A.N. *Design of the electrical part of overhead power lines 330-500 kV*. Moscow, Enerhyia Publ., 1974. 472 p. (Rus).

4. Bratslavskyi S.H., Hershenhorn A.Y., Losev S.B. *Special calculations of extra-high voltage power transmission*. Moscow, Enerhoatomyzdat Publ., 1985. 312 p. (Rus).

5. Hui Wang, Luyang Wang, Yufei Wang, Hua Xue, Changhui Yang, Tianyou Yan. The electric energy loss in overhead ground wires of 110kV six-circuit transmission line on the same tower. *IEEE PES Innovative Smart Grid Technologies*, 2012, pp. 1-5. doi: https://doi.org/10.1109/ISGT-Asia.2012.6303319.

6. Ning Zhou, Zhan Shu, Yongchun Su, Bo Chen, Zheng Cheng. Research on the selection method of phase sequence arrangement of double-circuit transmission lines on the same tower. *2016 IEEE PES Asia-Pacific Power and Energy Engineering Conference (APPEEC)*, 2016, pp. 2592-2596. doi: https://doi.org/10.1109/APPEEC.2016.7779958.

7. Taoning Jiang, Liang Xu, Peng Bian, Jia Jia, Dongsheng Kang, Chengqiu Sun, Jun Li. Effects of phase sequences and conductor transposition modes on the characteristics power loss of ground wire. *Electric Power Construction*, 2011, vol. 31, pp. 41-44.

8. Atteya I.I., Ashour H., Fahmi N., Strickland D. Radial distribution network reconfiguration for power losses reduction using a modified particle swarm optimisation. *CIRED - Open Access Proceedings Journal*, 2017, vol. 2017, no. 1, pp. 2505-2508. doi: https://doi.org/10.1049/oap-cired.2017.1286.

9. Lazzeroni P., Repetto M. Optimal planning of battery systems for power losses reduction in distribution grids. *Electric Power Systems Research*, 2019, vol. 167, pp. 94-112. doi: https://doi.org/10.1016/j.epsr.2018.10.027.

10. Kalantari Khandani M., Askarzadeh A. Optimal MV/LV transformer allocation in distribution network for power losses reduction and cost minimization: A new multi-objective framework. *International Transactions on Electrical Energy Systems*, 2020, vol. 30, no. 6, art. no. e12361. doi: https://doi.org/10.1002/2050-7038.12361.

11. Blinov I., Zaitsev I.O., Kuchanskyy V.V. Problems, Methods and Means of Monitoring Power Losses in Overhead Transmission Lines. *Studies in Systems, Decision and Control*, 2020, vol. 298, pp. 123-136. doi: https://doi.org/10.1007/978-3-030-48583-2_8.

12. Buinyi R.O., Krasnozhon A.V., Zorin V.V., Kvytsynskyi A.O. Justification for use of voltage class 20 kV in urban electrical networks. *Technical Electrodynamics*, 2019, no. 1, pp. 68-71. (Ukr). doi: https://doi.org/10.15407/techned2019.01.068.

13. Bezruchko V., Buinyi R., Bodunov V., Krasnozhon A., Miroshnyk O. Choosing the Cross-section of Cable Core for Wind Power Electrical Collector Network taking into account the economic factor. *2022 IEEE 8th International Conference on Energy Smart Systems (ESS)*, 2022, pp. 59-62. doi: https://doi.org/10.1109/ESS57819.2022.9969259.

14. Grinchenko V.S., Tkachenko A.O., Grinchenko N.V. Improving calculation accuracy of currents in cable shields at double-sided grounding of three-phase cable line. *Electrical Engineering & Electromechanics*, 2017, no. 2, pp. 39-42. doi: https://doi.org/10.20998/2074-272X.2017.2.06.

15. Al_Issa H.A., Qawaqzeh M., Khasawneh A., Buinyi R., Bezruchko V., Miroshnyk O. Correct Cross-Section of Cable Screen in a Medium Voltage Collector Network with Isolated Neutral of a Wind Power Plant. *Energies*, 2021, vol. 14, no. 11, art. no. 3026. doi: https://doi.org/10.3390/en14113026.

16. IEEE Guide for Bonding Shields and Sheaths of Single-Conductor Power Cables Rated 5 kV through 500 kV. *IEEE Std 575-2014 (Revision of IEEE Std 575-1988)*, 2014. 83 p. doi: https://doi.org/10.1109/IEEESTD.2014.6905681.

17. Li L., Yang Z., Luo Z., Liu K. Transient Disturbances Based Non-Intrusive Ageing Condition Assessment for Cross-Bonded Cables. *IEEE Access*, 2020, vol. 8, pp. 176651-176660. doi: https://doi.org/10.1109/ACCESS.2020.3026650.

18. Makarov Ye.F. *Reference book on electrical networks 0.4-35 kV and 110-1150 kV. In 4 vols. Vol. 2.* Moscow, Papirus Pro Publ., 2003.640 p. (Rus).

19. Krasnozhon A.V., Buinyi R.O., Dihtyaruk I.V., Kvytsynskyi A.O. The investigation of distribution of the magnetic flux density of operating two-circuit power line 110 kV «CHTPP-Chernihiv-330» in the residential area and methods of its decreasing to a safe level. *Electrical Engineering & Electromechanics*, 2020, no. 6, pp. 55-62. doi: https://doi.org/10.20998/2074-272X.2020.6.08.

20. Geri A., Locatelli A., Veca G.M. Magnetic fields generated by power lines. *IEEE Transactions on Magnetics*, 1995, vol. 31, no. 3, pp. 1508-1511. doi: https://doi.org/10.1109/20.376316.

21. Rozov V.Yu., Reutskyi S.Yu., Pelevin D.Ye., Yakovenko V.N. The research of magnetic field of high-voltage AC transmissions lines. *Technical Electrodynamics*, 2012, no. 1, pp. 3-9. (Rus).

22. Rozov V.Y., Grinchenko V.S., Pelevin D.Y., Chunikhin K.V. Simulation of electromagnetic field in residential buildings located near overhead lines. *Technical Electrodynamics*, 2016, no. 3, pp. 6-8. doi: https://doi.org/10.15407/techned2016.03.006.

23. Grinchenko V.S., Chunikhin K.V. Magnetic field normalization in residential building located near overhead line by grid shield. *Electrical Engineering & Electromechanics*, 2020, no. 5, pp. 38-43. doi: https://doi.org/10.20998/2074-272X.2020.5.06.

24. Kim I. A New Single-Logarithmic Approximation of Carson's Ground-Return Impedances – Part 1. *IEEE Access*, 2021, vol. 9, pp. 103850-103861. doi: https://doi.org/10.1109/ACCESS.2021.3097377.

25. *Optical cable in lightning wire*. Moscow, NKT Keibls Publ., 2014. 16 p. (Rus).

26. *State Standard HKD 34.48.151-2003 Design, construction and operation of fiber-optic communication lines over overhead power lines. Instruction*. (Ukr).

27. *State Standard STO 56947007-33.180.10.173-2014 Guidelines for calculating the thermal effects of short-circuit currents and thermal stability of lightning protection cables and optical cables*. (Rus).

Received 10.01.2023
Accepted 07.03.2023
Published 02.11.2023

A.V. Krasnozhon[1]*, PhD, Assistant Professor,*
A.O. Kvytsynskyi[2]*, PhD, Assistant Professor,*
R.O. Buinyi[1]*, PhD, Assistant Professor,*
I.V. Dihtyaruk[1]*, PhD,*
O.V. Krasnozhon[1]*, PhD,*
[1] Chernihiv Polytechnic National University,
95, Shevchenko Str., Chernihiv, 14035, Ukraine,
e-mail: red_john@ukr.net; buinyiroman@gmail.com;
dihtyaruk.ihor@gmail.com (Corresponding Author);
krasnozhon08@gmail.com
[2] Department of research support of regulatory support
of the NPC Ukrenergo,
11/8, Dorohozhytska Str., Kyiv, 04112, Ukraine,
e-mail: Kvytsynskyi.AO@ua.energy

How to cite this article:
Krasnozhon A.V., Kvytsynskyi A.O., Buinyi R.O., Dihtyaruk I.V., Krasnozhon O.V. Study of the influence of the parameters of modern grounding wires on the value of power losses in them for overhead power lines of 330-750 kV. *Electrical Engineering & Electromechanics*, 2023, no. 6, pp. 77-83. doi: https://doi.org/10.20998/2074-272X.2023.6.14

UDC 621.3 https://doi.org/10.20998/2074-272X.2023.6.15

M.A. Labed, M. Zellagui, M. Benidir, H. Sekhane, N. Tebbakh

Optimal hybrid photovoltaic distributed generation and distribution static synchronous compensators planning to minimize active power losses using adaptive acceleration coefficients particle swarm optimization algorithms

The paper ***aims*** *to identify the optimum size and location of photovoltaic distributed generation systems and distribution static synchronous compensators (DSTATCOMs) systems to minimize active power losses in the distribution network and enhance the voltage profile. The* ***methodology*** *employed in this article begins by thoroughly discussing various acceleration algorithms used in Particle Swarm Optimization (PSO) and their variations with each iteration. Subsequently, a range of PSO algorithms, each incorporating different variations of acceleration coefficients was verified to solve the problem of active power losses and voltage improvement. Simulation* ***results*** *attained on Standard IEEE-33 bus radial distribution network prove the efficiency of acceleration coefficients of PSO; it was evaluated and compared with other methods in the literature for improving the voltage profile and reducing active power.* ***Originality.*** *Consists in determining the most effective method among the various acceleration coefficients of PSO in terms of minimizing active power losses and enhancing the voltage profile, within the power system. Furthermore, demonstrates the superiority of the selected method over others for achieving significant improvements in power system efficiency.* ***Practical value*** *of this study lies on its ability to provide practical solutions for the optimal placement and sizing of distributed generation and DSTATCOMs. The proposed optimization method offers tangible benefits for power system operation and control. These findings have practical implications for power system planners, operators, and policymakers, enabling them to make informed decisions on the effective integration of distributed generation and DSTATCOM technologies.* References 30, table 3, figures 7.

Key words: **photovoltaic distributed generation, distribution static synchronous compensators, power losses, voltage profile, acceleration coefficients particle swarm optimization algorithms.**

Метою *статті є визначення оптимального розміру та розташування фотоелектричних систем розподіленої генерації та систем розподільних статичних синхронних компенсаторів (DSTATCOM) для мінімізації втрат активної потужності у розподільній мережі та покращення профілю напруги.* ***Методологія****, що використовується в цій статті, починається з детального обговорення різних алгоритмів прискорення, що використовуються в оптимізації рою частинок (PSO), та їх варіацій на кожній ітерації. Згодом було перевірено низку алгоритмів PSO, кожен з яких включає різні варіанти коефіцієнтів прискорення, для вирішення проблеми втрат активної потужності та покращення напруги.* ***Результати*** *моделювання, одержані на радіальній розподільній мережі шини стандарту IEEE-33, підтверджують ефективність коефіцієнтів прискорення PSO; він був оцінений та порівняний з іншими описаними в літературі методами покращення профілю напруги та зниження активної потужності.* ***Оригінальність****. Полягає у визначенні найбільш ефективного методу серед різних коефіцієнтів прискорення PSO з погляду мінімізації втрат активної потужності та покращення профілю напруги в енергосистемі. Крім того, демонструє перевагу обраного методу над іншими для досягнення значного підвищення ефективності енергосистеми.* ***Практична цінність*** *цього дослідження полягає у його здатності надати практичні рішення для оптимального розміщення та визначення розмірів розподіленої генерації та DSTATCOM. Запропонований метод оптимізації дає відчутні переваги для експлуатації та керування енергосистемою. Ці результати мають практичне значення для фахівців із планування енергосистем, операторів та розробників політики керування, дозволяючи їм приймати обґрунтовані рішення щодо ефективної інтеграції технологій розподіленої генерації та технологій DSTATCOM.* Бібл. 30, табл. 3, рис. 7.

Ключові слова: **фотоелектрична розподілена генерація, розподільні статичні синхронні компенсатори, втрати потужності, профіль напруги, коефіцієнти прискорення, алгоритми оптимізації рою частинок.**

1. Introduction. With the increasing demand for electricity and the share of distributed generation, including based on renewable energy sources, there is a need to solve a number of problems [1], power losses have become a significant concern for power system operators. In recent years, the deployment of distributed energy resources such as photovoltaic distributed generation (PVDG) systems and distribution static synchronous compensators (DSTATCOMs) has gained attention as a means to minimize power losses. PVDG systems generate electricity from solar energy and supply it to the distribution network, while DSTATCOMs provide reactive power compensation to increase the power quality of the network.

The incorporation of sustainable energy sources into the electrical grid has become increasingly important in latest years, due to the rising demand for clean energy and the need to reduce greenhouse gas emissions. Previously generation and transmission power systems were responsible for the power quality transmitted to customers [2], but currently, there is a significant focus on distribution networks, as they are prone to electrical breakdowns and considered a vulnerable point in the power grid. Among the Renewable Energy Sources (RES), PVDG systems have gained popularity due to their ease of installation and maintenance, low operating costs, and environmental benefits. However, the fitful nature of solar energy and the variability of the generated power can cause issues such as voltage fluctuations, power quality problems, and power losses in the distribution network.

In order to overcome these issues, DSTATCOMs can offer reactive power compensation and improve the quality of network. The effective integration of PVDG and DSTATCOM systems can enhance the dependability and stability of the power system while effectively harnessing RES. Therefore, the planning and optimization of PVDG and DSTATCOM systems have become crucial for the successful integrating of RES into the network.

It has been proven in the literature beyond any doubt that metaheuristic optimization algorithms perform well by optimally handling several versatile real-world optimization tasks [3].

Particle Swarm Optimization (PSO) is a powerful metaheuristic method for optimization derived from the demeanor of bird flocking or fish schooling. This approach involves a group of particles working to find the most optimal solution in a given problem space by iteratively adjusting their positions and velocities guided by their individual experience and the finest experiences of their neighbors. PSO has been widely applied in assorted domains, including engineering, finance, and science, due to its simplicity, flexibility, and ability to successfully tackle intricate optimization problems.

Different algorithms have been employed to investigate the suitable capacity and placement of Distributed Generation (DG) and DSTATCOM units are mentioned as follows: the Bacterial Foraging Optimization Algorithm (BFOA) [4], Multi-Verse Optimization Algorithm (MVOA) [5], Differential Evolution Optimization Algorithm (DEOA) [6], Slime Mould Algorithm [7], Multi-Objective Grasshopper Optimization Algorithm [8], Teaching Learning Based Optimization-Particle Swarm Optimization [9], Genetic Salp Swarm Algorithm [10], Northern Goshawk Optimization algorithm [11], Dwarf Mongoose Optimization Algorithm [12], Elitist Harris Hawks Optimization Algorithm [13], African Vultures Optimization Algorithm [14], Flower Pollination Algorithm [15], Butterfly-based PSO algorithm [16], hybrid Firefly PSO algorithms [17], Bald Eagle Search Algorithm [18], Modified Shuffled Frog Leaping Algorithm [19].

The goal of the paper is to identify the optimum placement and size of photovoltaic distributed generation and distribution static synchronous compensators on a radial distribution network according to the best-obtained result from the different particle swarm optimization applied algorithms and compare it to the other algorithms existing in the literature. The study was conducted using a standard IEEE-33 bus as the testing system by lessening active power dissipation and voltage profile enhancement.

2. Problem formulation.

2.1. Objective function. The primary aim of this paper has been to minimize the total active power losses, where the objective function is focused on achieving the least possible value of active power losses:

$$Ob = \min \sum_{i,j}^{N_b} P_{loss}\,, \tag{1}$$

where N_b is the number of busses; P_{loss} is the active power losses.

The following equation represents the branch power loss (P_{loss}) is:

$$P_{loss\,i,j} = \left(\frac{P_{i,j}^2 + Q_{i,j}^2}{V_i^2} \right) P_{i,j}\,, \tag{2}$$

where $R_{i,j}$, $P_{i,j}$, $Q_{i,j}$ are the resistance, active and reactive powers respectively from bus i to bus j; V_i is the voltage in the bus.

2.2. Constraints.

2.2.1. Distribution line constraints. The power conversation constraints [20-24]:

$$P_G + P_{DG} = P_D + P_{loss}; \tag{3}$$

$$Q_G + Q_{DSTATCOM} = Q_D + Q_{loss}, \tag{4}$$

where (P_{DG}, $Q_{DSTATCOM}$), (P_G, Q_G), (P_D, Q_D) are the active and reactive powers of PVDG and DSTATCOM, the generator and load respectively.

Bus voltage limits are:

$$V_{\min} \le |V_i| \le V_{\max}\,, \tag{5}$$

where $V_{\min}$, $V_{\max}$ are the predetermined minimum and maximum voltage values for the bus; V_i is the voltage magnitude at i^{th} bus in p.u.

Voltage drop limit is:

$$|1 - V_i| \le \Delta V_{\max}\,, \tag{6}$$

where $\Delta V_{\max}$ is the maximum permitted voltage drop at each branch.

Line capacity limit is:

$$|S_{ij}| \le |S_{\max}|\,, \tag{7}$$

where S_{ij}, $S_{\max}$ are the apparent and maximum apparent power in the line distribution between i and j bus.

2.2.2. DG constraints. The limitations of the DG unit are expressed through inequality constraints:

$$P_{DG}^{\min} \le P_{DG} \le P_{DG}^{\max}\,; \tag{8}$$

$$\sum_{i=1}^{N_{DG}} P_{DG}(i) \le \sum_{j=1}^{N_{bus}} P_{DG}(i); \tag{9}$$

$$2 \le DG_{position} \le N_{bus}\,; \tag{10}$$

$$N_{DG} \le N_{DG\max}\,; \tag{11}$$

$$\left(n_{DG,i} / Location \right) \le 1\,; \tag{12}$$

where $P_{DG}^{\min}$ and $P_{DG}^{\max}$ are the allowable range for power generation by the PVDG, encompassing both upper and lower limits; N_{DG} and $N_{DG\max}$ are the number and maximum number of PVDG, that are limited for one unit and location.

2.2.3. DSTATCOM constraints. The DSTATCOM unit's limits can be represented by inequality constraints formulated as follows:

$$Q_{DSTATCOM}^{\min} \le Q_{DSTATCOM} \le Q_{DSTATCOM}^{\max}\,; \tag{13}$$

$$\sum_{i=1}^{N_{DST}} Q_{DSTATCOM}(i) \le \sum_{j=1}^{N_{bus}} Q_D(i); \tag{14}$$

$$2 \le DSTATCOM_{position} \le N_{bus}\,; \tag{15}$$

$$N_{DSTATCOM} \le N_{DSTATCOM\max}\,; \tag{16}$$

$$\left(n_{DSTATCOM,i} / Location \right) \le 1\,, \tag{17}$$

where $Q_{DSTATCOM}^{\min}$ and $Q_{DSTATCOM}^{\max}$ are the allowable range for power generation by the DSTATCOM, encompassing both upper and lower limits; $N_{DSTATCOM}$ and $N_{DSTATCOM\max}$ are the number and maximum number of DSTATCOM, that are limited for one unit for one location.

3. Adaptive acceleration coefficients PSO algorithms.

PSO algorithm was first introduced in 1995, which can be seen as a global search technique. In this algorithm, each particle, denoted by i, has a velocity vector (V_i) and a position vector (X_i) [20]. It can be modeled by the following equations:

$$V_i^{k+1} = \omega V_i^k + c_1 r_1 \left[P_{best}^k - X_i^k \right] + c_2 r_2 \left[G_{best}^k - X_i^k \right]; \tag{18}$$

$$X_i^{k+1} = X_i^k + V_i^{k+1}\,, \tag{19}$$

where ω, r are the inertia weight and random values between 0 and 1 respectively; C_1, C_2 are the acceleration coefficients; G_{best} is the global best position; k is the iterations number.

This paper proposes novel PSO strategies that utilize time-varying acceleration coefficients (C_1 and C_2) to improve the global search performance. The primary concept behind employing PSO with time-varying acceleration coefficients is to increase the global search during the initial phase of the optimization process.

This is accomplished by altering C_1 and C_2 over time in such a way that the cognitive component decreases while the social component increases [25].

In this work, it should be noted that the names assigned to the various PSO methods are not mere abbreviations. Instead, they represent unique and distinct algorithms, each with its own set of characteristics and features. These names serve as identifiers for specific approaches in the field of PSO. The following equations show the acceleration formulas and their corresponding constants.

The Adaptive Accelerated Coefficients for the PSO algorithm (AAC PSO) and constants [26] are:

$$c_1 = c_{\min} + \left(c_{\max} - c_{\min}\right) e^{-\left(\frac{4k}{k_{\max}}\right)^2} ; \tag{20}$$

$$c_2 = c_{\max} - \left(c_{\max} - c_{\min}\right) e^{-\left(\frac{4k}{k_{\max}}\right)^2} , \tag{21}$$

with

$$c_{\min} = c_{\max} = 0.5 , \tag{22}$$

where $c_{\min}$, $c_{\max}$ are the constants of the AAC PSO method; k, $k_{\max}$ represent the iteration number and the maximum number of iterations, respectively.

The Autonomous Particles Groups for PSO (APG PSO) acceleration coefficient formula and constants [27] are:

$$c_1 = 1.95 - \left(\frac{2k^a}{k_{\max}^a}\right); \tag{23}$$

$$c_2 = 0.05 - \left(\frac{2k^a}{k_{\max}^a}\right), \tag{24}$$

with

$$a = 1/3, \tag{25}$$

where a is the constant of APG PSO method.

The Nonlinear Dynamic Acceleration Coefficients for PSO (NDAC PSO) acceleration coefficient formula and constants [28] are:

$$c_1 = -\left(c_f - c_i\right)\cdot\left(\frac{k}{k_{\max}}\right)^2 + c_f ; \tag{26}$$

$$c_2 = c_i \cdot \left(1 - \frac{k}{k_{\max}}\right)^2 + c_f \cdot \left(\frac{k}{k_{\max}}\right), \tag{27}$$

where the constants of this method c_i, c_f are:

$$c_i = 0.5, \tag{28}$$

$$c_f = 2.5, \tag{29}$$

The acceleration coefficient formula and constants for Sine Cosine Acceleration Coefficients for PSO (SCAC PSO) [29]:

$$c_1 = \partial \cdot \sin\left[\left(1 - \frac{k}{k_{\max}}\right)\cdot\frac{\pi}{2}\right] + \delta ; \tag{30}$$

$$c_2 = \partial \cdot \cos\left[\left(1 - \frac{k}{k_{\max}}\right)\cdot\frac{\pi}{2}\right] + \delta , \tag{31}$$

with the constants ∂, δ:

$$\partial = 2, \tag{32}$$

$$\delta = 0.5. \tag{33}$$

Finally, Time Varying Acceleration for PSO (TVA PSO) acceleration coefficient formula and constants [30] are:

$$c_1 = c_{1i} + \left(\frac{c_{1f} - c_{1i}}{k_{\max}}\right)\cdot k ; \tag{34}$$

$$c_2 = c_{2i} + \left(\frac{c_{2f} - c_{2i}}{k_{\max}}\right)\cdot k , \tag{35}$$

with

$$c_{1i} = c_{1f} = c_{2i} = c_{2f} = 0.5, \tag{36}$$

where k is the iterations number; c_{1i}, c_{2i}, c_{1f}, c_{2f} are the constants of the method.

Figure 1 displays diverse updating strategies for the C_1 and C_2 acceleration coefficients across the various PSO algorithms.

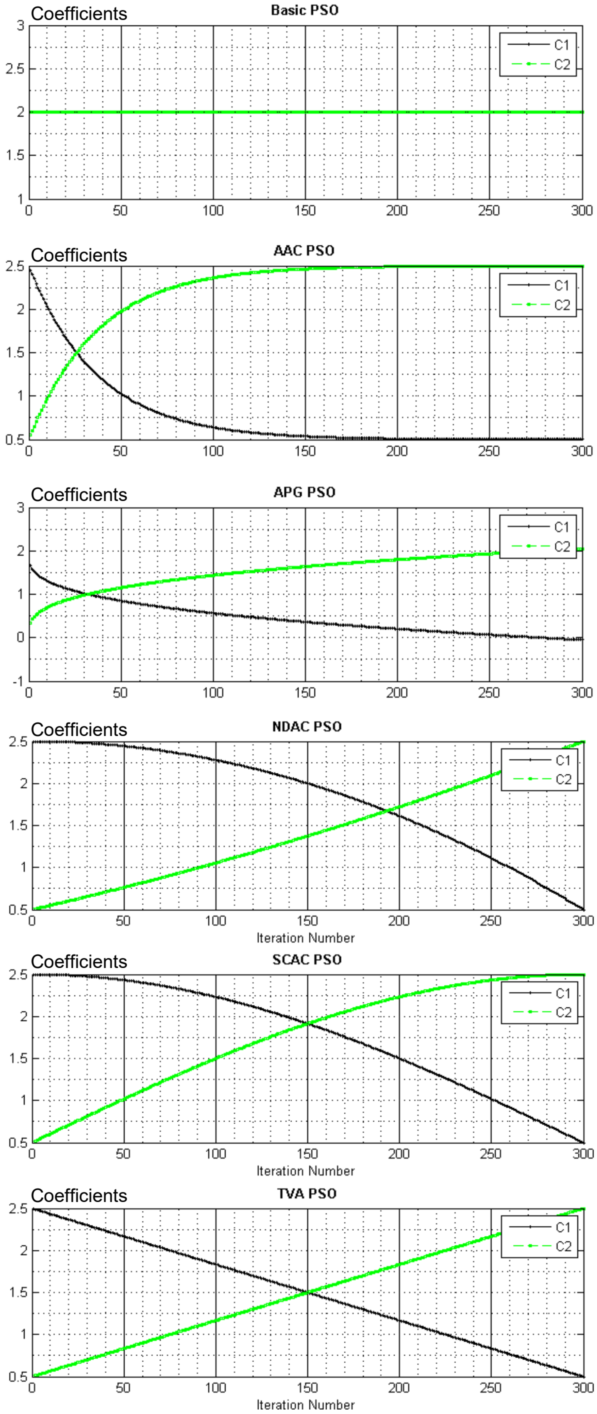

Fig. 1. Time-varying acceleration coefficients

In Fig. 1 the acceleration coefficients exhibit a varying trend with iterations, typically ranging from 0 to 2.5. The values of C_1 generally decrease over the iterations, whereas the values of C_2 tend to increase. These changes are dependent on the update function of C_1 and C_2, which can be linear, polynomial, or exponential. When C_1 is bigger than C_2, the particles conduct local search, whereas when C_2 is bigger than C_1, the particles conduct global search. The succeeding section will discuss the outcomes of these algorithms in achieving the efficient allocation of DG and DSTATCOM.

4. Test system, results and comparison. This section describes the test systems used for evaluation, results and comparison of various PSO algorithms applied to the IEEE 33 bus system for optimal planning of PVDG and DSTATCOM size and location.

The work's objective has been to enhance the voltage profile and reduce the active power losses of the system through the identification of the optimal locations and sizes of PVDG and DSTATCOM units. The presented Fig. 2 depicts the IEEE 33 bus radial distribution system, which serves as a widely adopted benchmark system for power system analysis that allows for fair comparison of different optimization algorithms. A range of PSO algorithms with different variations of the acceleration coefficients was applied and performance comparison of speed convergence, solution quality, and computational efficiency. The results are presented in terms of the total active power loss reduction, voltage profile improvement, and optimal locations and sizes of PVDG and DSTATCOM.

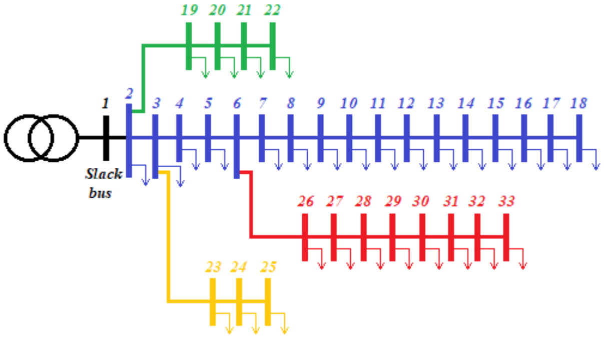

Fig. 2. IEEE 33 bus model

Finally, strengths and weaknesses of each PSO algorithm were analyzed and discussed as well as the comparison of the best method obtained from the different PSO coefficients with other algorithms existing in the literature. The comparison is performed in terms of the total active power loss reduction, voltage profile improvement, and computational efficiency. The results demonstrate the superiority of the suggested PSO algorithm and providing valuable insights into the optimal placement of PVDG and DSTATCOM units for power systems.

The results were obtained after 20 runs with 300 iterations each, using different PSO coefficients. It should be reminded that in the initial case, the active power losses were 210.987 kW and the initial $V_{\min}$ and $V_{\max}$ were 0.9038 p.u. and 1.000 p.u, respectively.

The results presented in Table 1, 2 suggest that the AAC PSO method outperforms the other PSO methods in terms of both active power losses reduction, with a reduction of 72.23 %, and voltage profile improvement, with a value of 0.95 for minimal voltage and 1.02 for maximal voltage.

Table 1

Test results in term of power losses

Method	P_{Loss}, kW	ΔP_{Loss}, %	PVDG		D-STATCOM	
			Bus location	P, kW	Bus location	Q, kVar
Basic PSO	59.00	72.03	6	2666.4	30	1358.7
AAC PSO	58.58	72.23	6	2437.2	30	1281.3
APG PSO	58.69	72.18	6	2502.3	30	1168.4
NDAC PSO	58.80	72.12	6	2370.1	30	1240.0
SCAC PSO	59.12	71.97	6	2390.2	30	1141.5
TVA PSO	59.45	71.82	6	2773.9	30	1173.4

Table 2

Test results in term of voltage profile improvement

Method	$V_{\min}$, p.u.	$V_{\max}$, p.u.	PVDG		D-STATCOM	
			Bus location	P, kW	Bus location	Q, kVar
Basic PSO	0.98	1.03	6	2666.4	30	1358.7
AAC PSO	0.95	1.02	6	2437.2	30	1281.3
APG PSO	0.95	1.02	6	2502.3	30	1168.4
NDAC PSO	0.95	1.00	6	2370.1	30	1240.0
SCAC PSO	0.95	1.01	6	2390.2	30	1141.5
TVA PSO	0.95	1.00	6	2773.9	30	1173.4

These results are attributed to the integration of a 2.43 kW DG unit at bus 6 and a 1.28 kW DSTATCOM at bus 30. The APG PSO and NDAC PSO methods also demonstrated good results regarding the reduction of active power losses.

It should be noted that, even with the same allocation of DG units and DSTATCOM, the AAC PSO method produced the best results. Therefore, it may be the most suitable choice for the simultaneous installation of PVDG and DSTATCOM in the IEEE 33-bus radial distribution system. However, further analysis is needed to confirm the robustness of the method under different conditions and constraints.

In order to gain a deeper insight into the behavior of the different PSO methods, the curves of active power losses versus the number of executions for each method were plotted.

Figure 3 shows clearly the obtained results, after 20 trials for each method, it is clear that the range of variation for the basic PSO, NDAC PSO, and TVA PSO is approximately between 59 kW and 64 kW, while the range of variation for AAC PSO and APG PSO is between 59 kW and 69 kW.

These results highlight the importance of selecting the appropriate PSO parameters and coefficients, as some methods converge faster and reach lower losses than others.

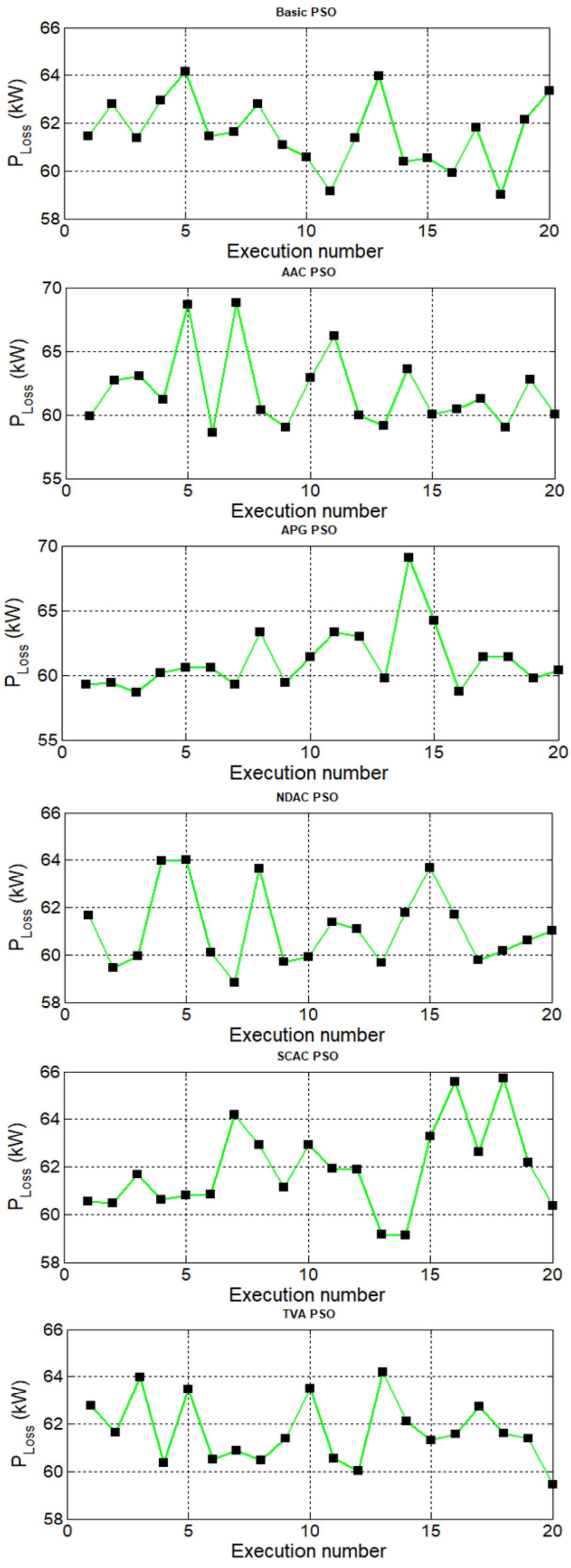

Fig. 3. Curves of active power losses versus the number executions

Figure 4 depicts the convergence curves of various algorithms applied to the simultaneous installation of DG and DSTATCOM, after 20 executions.

The results for the 33-bus system reveal that all algorithms converge at a total power loss reduction of 85 kW. Notably, the AAC PSO method shows superior convergence compared to the other PSO algorithms. It reaches a lower objective function value in less iteration, demonstrating its superior performance in optimizing the implementation of PVDG and DSTATCOM.

The AAC PSO method also achieves faster convergence and enhances the voltage profile, resulting in minimized active power losses.

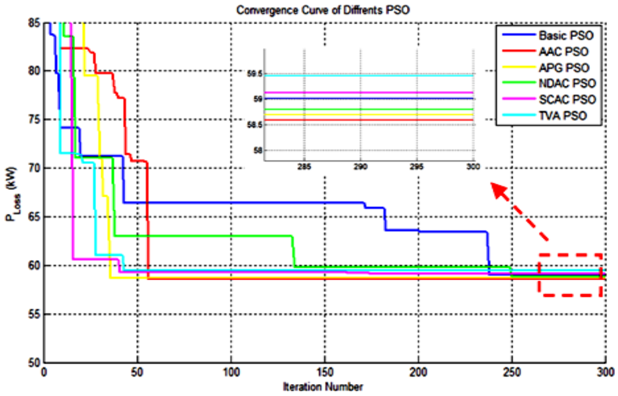

Fig. 4. Convergence curve of different PSO method

As seen in Fig. 5, the integrating of DG and DSTATCOM in simultaneous operation results in a significant improvement of the voltage profile compared to the base case. The implementation of DG and DSTATCOM together leads to a greater enhancement of the voltage profile, with the minimum voltage improving from 0.9038 to 0.9894 p.u.

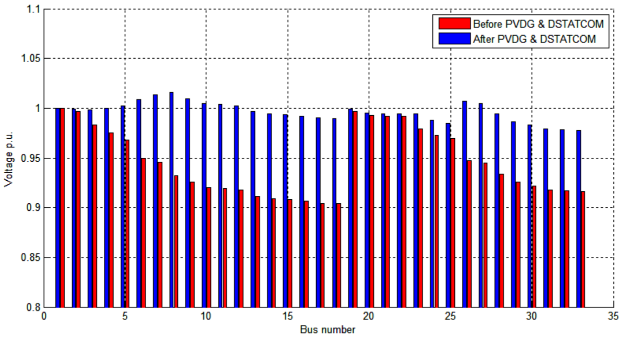

Fig. 5. Improved voltage profile with PVDG and DSTATCOM

The results from Table 3 manifest the efficiency and superiority of the AAC PSO algorithm over other algorithms in the literature for the simultaneous installation of DG and DSTATCOM for an IEEE 33 bus system, achieving the minimum active power losses and improving the optimum deployment of PVDG and DSTATCOM units.

Table 3

Comparison between our best method and others existing in the literature

Method	P_{Loss}, kW	ΔP_{Loss}, %	PVDG		D-STATCOM	
			Bus location	P, kW	Bus location	Q, kVar
AAC PSO	58.58	72.23	6	2437.2	30	1281.3
BFOA [3]	70.87	65	10	1239.8	30	1094.6
MVOA [4]	59.94	71.59	6	2848.8	30	1334.4
DEOA [5]	80.48	61.85	7	2327.5	26	1446.4

Figure 6 clearly shows that the proposed method resulted in a lower value of active power losses, with a value of 58.58 kW, which is superior to MVOA's value of 59.94 kW.

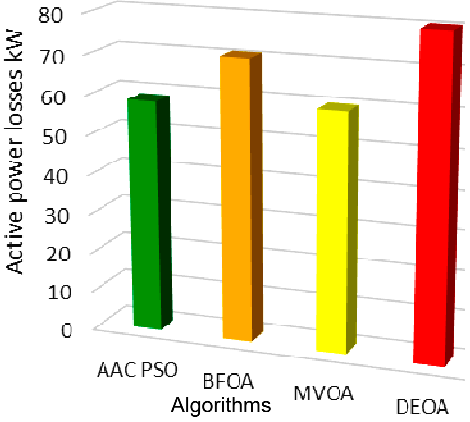

Fig. 6. Comparison between proposed method and others existing in the literature in term of active power losses

Figure 7 provides a visual representation of the percentage reduction in active power losses between the proposed method and the other method. The proposed method resulted in the highest reduction of active power, with a 27 % reduction compared to the other method.

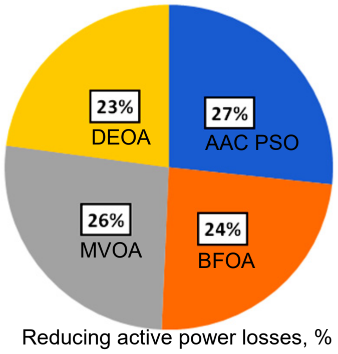

Fig. 7. Minimization rate of the active power losses for each method

Conclusions. The study aim has been to optimize the simultaneous implementation of photovoltaic distributed generation and distribution static synchronous compensator units in a standard IEEE 33-bus radial distribution system with the objective of reducing active power losses and enhancing the voltage profile.

Assorted particle swarm optimization methods with variable acceleration coefficients were applied, and the findings were evaluated against each other existing algorithms in the literature. The tables exhibited that the adaptive accelerated coefficients for particle swarm optimization method provided the best results in terms of active power loss reduction and voltage profile improvement, and the optimum size and location of the photovoltaic distributed generation and distribution static synchronous compensator. The figures demonstrated that the adaptive accelerated coefficients for particle swarm optimization method had the best convergence among the different particle swarm optimization algorithms and the losses curve according to the number of executions for each method.

Overall, the study demonstrated that the optimization of photovoltaic distributed generation and distribution static synchronous compensator installation using the adaptive accelerated coefficients for particle swarm optimization algorithm could significantly reduce active power losses and enhancement of voltage profile in the distribution system.

Conflict of interest. The authors of the article declare that there is no conflict of interest.

REFERENCES

1. Kyryk V.V., Bohomolova O.S. Justification of optimal location of connection of the distributed generation source and value of its power. *Electrical Engineering & Electromechanics*, 2019, no. 2, pp. 55-60. doi: https://doi.org/10.20998/2074-272X.2019.2.08.

2. Gopal Reddy S., Ganapathy S., Manikandan M. Power quality improvement in distribution system based on dynamic voltage restorer using PI tuned fuzzy logic controller. *Electrical Engineering & Electromechanics*, 2022, no. 1, pp. 44-50. doi: https://doi.org/10.20998/2074-272X.2022.1.06.

3. Gad A.G. Particle Swarm Optimization Algorithm and Its Applications: A Systematic Review. *Archives of Computational Methods in Engineering*, 2022, vol. 29, no. 5, pp. 2531-2561. doi: https://doi.org/10.1007/s11831-021-09694-4.

4. Devabalaji K.R., Ravi K. Optimal size and siting of multiple DG and DSTATCOM in radial distribution system using Bacterial Foraging Optimization Algorithm. *Ain Shams Engineering Journal*, 2016, vol. 7, no. 3, pp. 959-971. doi: https://doi.org/10.1016/j.asej.2015.07.002.

5. Hassan H.A., Zellagui M. MVO Algorithm for Optimal Simultaneous Integration of DG and DSTATCOM in Standard Radial Distribution Systems Based on Technical-Economic Indices. *2019 21st International Middle East Power Systems Conference (MEPCON)*, 2019, pp. 277-282. doi: https://doi.org/10.1109/MEPCON47431.2019.9007995.

6. Ibrahim K., Sirjani R., Shareef H. Performance Assesement of Pareto and Non-Pareto Approaches for the Optimal Allocation of DG and DSTATCOM in the Distribution System. *Technical Gazette*, 2020, vol. 27, no. 5, pp. 1654-1661. doi: https://doi.org/10.17559/TV-20181214103448.

7. Kouadri R., Slimani L., Bouktir T. Slime mould algorithm for practical optimal power flow solutions incorporating stochastic wind power and static VAR compensator device. *Electrical Engineering & Electromechanics*, 2020, no. 6, pp. 45-54. doi: https://doi.org/10.20998/2074-272X.2020.6.07.

8. Frahat M., Hatata A.Y., Saadawi M.M., Kaddah S.S. Grasshopper Optimization-based Optimal Sizing of DG/DSTATCOM in Distribution Networks. *Mansoura Engineering Journal*, 2022, vol. 47, no. 2, pp. 6-16. doi: https://doi.org/10.21608/bfemu.2022.238659.

9. Ansari A., Byalihal S.C. Application of hybrid TLBO-PSO algorithm for allocation of distributed generation and STATCOM. *Indonesian Journal of Electrical Engineering and Computer Science*, 2022, vol. 29, no. 1, pp. 38-48. doi: https://doi.org/10.11591/ijeecs.v29.i1.pp38-48.

10. Djabali C., Bouktir T. Simultaneous allocation of multiple distributed generation and capacitors in radial network using genetic-salp swarm algorithm. *Electrical Engineering & Electromechanics*, 2020, no. 4, pp. 59-66. doi: https://doi.org/10.20998/2074-272X.2020.4.08.

11. Manohara M., Veera Reddy V.C., Vijaya Kumar M. Northern Goshawk Optimization for Optimal Allocation of Multiple Types of Active and Reactive Power Distribution Generation in Radial Distribution Systems for Techno-Environmental Benefits. *International Journal of Intelligent Engineering and Systems*, 2023, vol. 16, no. 1, pp. 91-99. doi: https://doi.org/10.22266/ijies2023.0228.08.

12. Ferminus Raj A., Gnana Saravanan A. An optimization approach for optimal location & size of DSTATCOM and DG. *Applied Energy*, 2023, vol. 336, art. no. 120797. doi: https://doi.org/10.1016/j.apenergy.2023.120797.

13. Isha G., Jagatheeswari P., Jasmine Gnana Malar A. Elitist Harris Hawks Optimized Voltage Stability Enhancement in Radial Distribution System. *Journal of Electrical Engineering & Technology*, 2023, vol. 18, no. 4, pp. 2683-2693. doi: https://doi.org/10.1007/s42835-023-01375-5.

14. Pratap A., Tiwari P., Maurya R., Singh B. Minimisation of electric vehicle charging stations impact on radial distribution networks by optimal allocation of DSTATCOM and DG using African vulture optimisation algorithm. *International Journal of Ambient Energy*, 2022, vol. 43, no. 1, pp. 8653-8672. doi: https://doi.org/10.1080/01430750.2022.2103731.

15. Bharatbhai N.M., Gupta A.R. Active–Reactive Power Support with Optimal Allocation of DG and DSTATCOM in Distribution System Using Flower Pollination and Artificial Bee Colony Algorithm with Load Growth. *Lecture Notes in Electrical Engineering*, 2022, vol. 852, pp. 169-190. doi: https://doi.org/10.1007/978-981-16-9239-0_14.

16. Bhadoriya J.S., Gupta A.R. Techno-economic analysis of the DNO operated distribution system for active and reactive power support using modified particle swarm optimisation. *International Journal of Ambient Energy*, 2022, vol. 43, no. 1, pp. 7061-7076. doi: https://doi.org/10.1080/01430750.2022.2059779.

17. Zellagui M., Lasmari A., Settoul S., El-Sehiemy R.A., El-Bayeh C.Z., Chenni R. (2021). Simultaneous allocation of photovoltaic DG and DSTATCOM for techno-economic and environmental benefits in electrical distribution systems at different loading conditions using novel hybrid optimization algorithms. *International Transactions on Electrical Energy Systems*, 2021, vol. 31, no. 8, art. no. e12992. doi: https://doi.org/10.1002/2050-7038.12992.

18. Tebbakh N., Labed D., Labed M.A. Optimal size and location of distributed generations in distribution networks using bald eagle search algorithm. *Electrical Engineering & Electromechanics*, 2022, no. 6, pp. 75-80. doi: https://doi.org/10.20998/2074-272X.2022.6.11.

19. Ghatak S.R., Sannigrahi S., Acharjee P. Optimal Placement of DSTATCOM and DG using Modified SFLA based Technique for Techno-Economic and Environmental Benefits. *Recent Advances in Electrical & Electronic Engineering*, 2018, vol. 11, no. 3, pp. 334-347. doi: https://doi.org/10.2174/2352096511666180312155907.

20. Lasmari A., Zellagui M., Chenni R., Semaoui S., El-Bayeh C.Z., Hassan H.A. Optimal energy management system for distribution systems using simultaneous integration of PV-based DG and DSTATCOM units. *Energetika*, 2020, vol. 66, no. 1, pp. 1-14. doi: https://doi.org/10.6001/energetika.v66i1.4294.

21. Settoul S., Chenni R., Hasan H.A., Zellagui M., Kraimia M.N. MFO Algorithm for Optimal Location and Sizing of Multiple Photovoltaic Distributed Generations Units for Loss Reduction in Distribution Systems. *2019 7th International Renewable and Sustainable Energy Conference (IRSEC)*, 2019, pp. 1-6. doi: https://doi.org/10.1109/IRSEC48032.2019.9078241.

22. Settoul S., Zellagui M., Abdelaziz A.Y., Chenni R. Optimal Integration of Renewable Distributed Generation in Practical Distribution Grids based on Moth-Flame optimization Algorithm. *2019 International Conference on Advanced Electrical Engineering (ICAEE)*, 2019, pp. 1-5. doi: https://doi.org/10.1109/ICAEE47123.2019.9014662.

23. Abd Shukor S.F., Musirin I., Abd Hamid Z., Mohamad Zamani M.K., Zellagui M., Suyono H. Intelligent based technique for under voltage load shedding in power transmission systems. *Indonesian Journal of Electrical Engineering and Computer Science*, 2020, vol. 17, no. 1, pp. 110-117. doi: https://doi.org/10.11591/ijeecs.v17.i1.pp110-117.

24. Kellogg W.D., Nehrir M.H., Venkataramanan G., Gerez V. Generation unit sizing and cost analysis for stand-alone wind, photovoltaic, and hybrid wind/PV systems. *IEEE Transactions on Energy Conversion*, 1998, vol. 13, no. 1, pp. 70-75. doi: https://doi.org/10.1109/60.658206.

25. Chaturvedi K.T., Pandit M., Srivastava L. Particle swarm optimization with time varying acceleration coefficients for non-convex economic power dispatch. *International Journal of Electrical Power & Energy Systems*, 2009, vol. 31, no. 6, pp. 249-257. doi: https://doi.org/10.1016/j.ijepes.2009.01.010.

26. Ziyu T., Dingxue Z. A Modified Particle Swarm Optimization with an Adaptive Acceleration Coefficients. *2009 Asia-Pacific Conference on Information Processing*, 2009, pp. 330-332. doi: https://doi.org/10.1109/APCIP.2009.217.

27. Mirjalili S., Lewis A., Sadiq A.S. Autonomous Particles Groups for Particle Swarm Optimization. *Arabian Journal for Science and Engineering*, 2014, vol. 39, no. 6, pp. 4683-4697. doi: https://doi.org/10.1007/s13369-014-1156-x.

28. Chen K., Zhou F., Wang Y., Yin L. An ameliorated particle swarm optimizer for solving numerical optimization problems. *Applied Soft Computing*, 2018, vol. 73, pp. 482-496. doi: https://doi.org/10.1016/j.asoc.2018.09.007.

29. Chen K., Zhou F., Yin L., Wang S., Wang Y., Wan F. A hybrid particle swarm optimizer with sine cosine acceleration coefficients. *Information Sciences*, 2018, vol. 422, pp. 218-241. doi: https://doi.org/10.1016/j.ins.2017.09.015.

30. Ratnaweera A., Halgamuge S.K., Watson H.C. Self-Organizing Hierarchical Particle Swarm Optimizer With Time-Varying Acceleration Coefficients. *IEEE Transactions on Evolutionary Computation*, 2004, vol. 8, no. 3, pp. 240-255. doi: https://doi.org/10.1109/TEVC.2004.826071.

Received 22.03.2023
Accepted 13.06.2023
Published 02.11.2023

Mohamed Amir Labed[1]*, PhD Student,*
Mohamed Zellagui[2]*, Doctor, Associate Professor,*
Mohamed Benidir[3]*, Doctor, Professor,*
Hocine Sekhane[4]*, Doctor, Lecturer A,*
Noureddine Tebbakh[1]*, PhD Student,*
[1] LGEC Research Laboratory, Department of Electrical Engineering,
University of Constantine 1, Algeria,
e-mail: mohamedamir.labed@student.umc.edu.dz
(Corresponding Author); tebbakh.noureddine@yahoo.com
[2] Department of Electrical Engineering,
University of Batna 2, Algeria,
e-mail: m.zellagui@univ-batna2.dz
[3] Department of Transport Engineering,
University of Constantine 1, Algeria,
e-mail: mcbenidir@yahoo.fr
[4] LGEC Research Laboratory, Department of Electrical Engineering,
20 August 1955 University of Skikda, Algeria,
e-mail: docsekhoc@gmail.com

How to cite this article:
Labed M.A., Zellagui M., Benidir M., Sekhane H., Tebbakh N. Optimal hybrid photovoltaic distributed generation and distribution static synchronous compensators planning to minimize active power losses using adaptive acceleration coefficients particle swarm optimization algorithms. *Electrical Engineering & Electromechanics*, 2023, no. 6, pp. 84-90. doi: https://doi.org/10.20998/2074-272X.2023.6.15

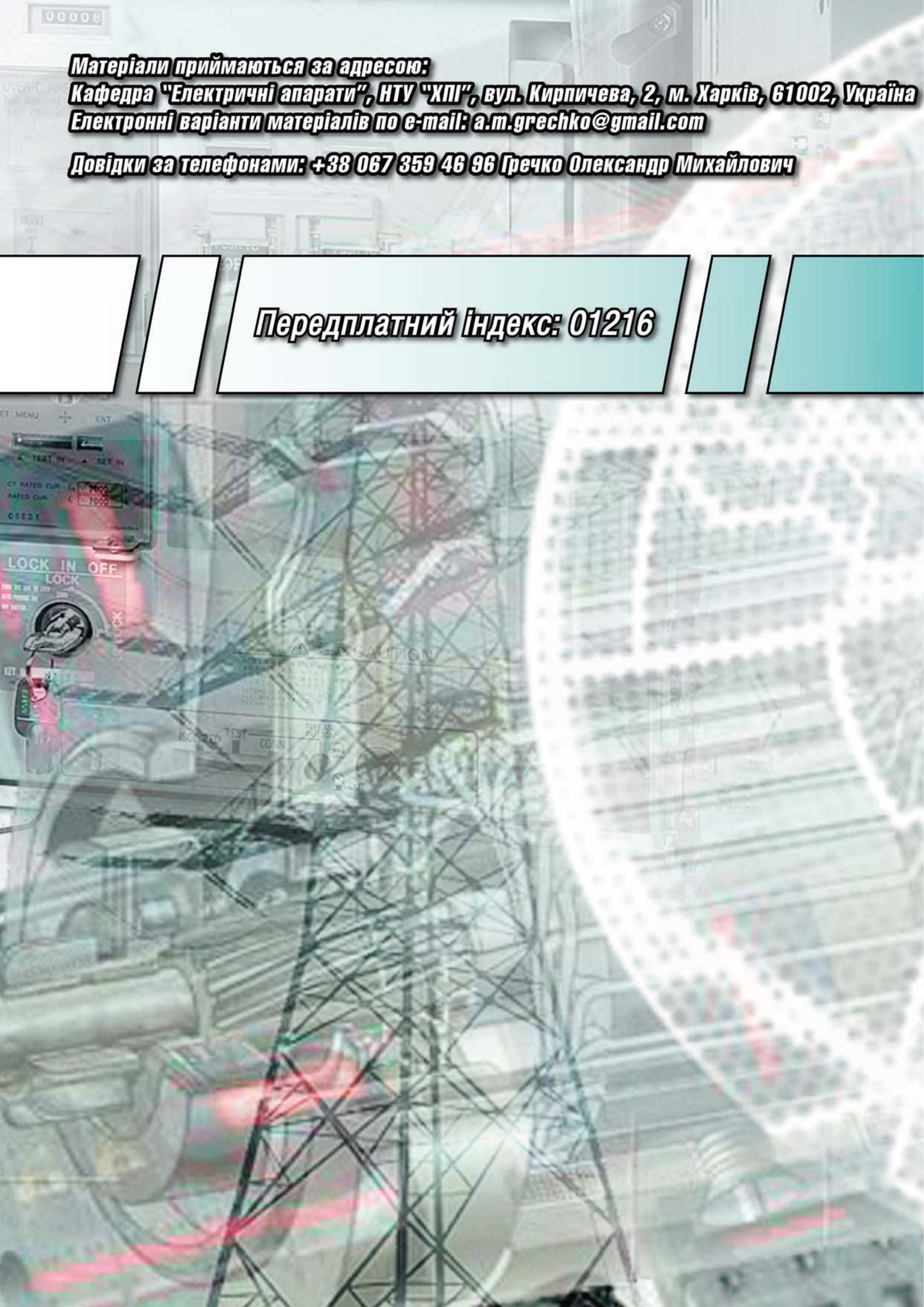

Матеріали приймаються за адресою:
Кафедра "Електричні апарати", НТУ "ХПІ", вул. Кирпичева, 2, м. Харків, 61002, Україна
Електронні варіанти матеріалів по e-mail: a.m.grechko@gmail.com

Довідки за телефонами: +38 067 359 46 96 Гречко Олександр Михайлович

Передплатний індекс: 01216